Lehrstuhl für Elektrische Antriebssysteme und Leistungselektronik
der Technischen Universität München

Sensorless Control of Synchronous Machines by Linear Approximation of Oversampled Current

Peter Landsmann

Vollständiger Abdruck der von der Fakultät für Elektrotechnik und Informationstechnik der Technischen Universität München zur Erlangung des akademischen Grades eines

Doktor-Ingenieurs

genehmigten Dissertation.

Vorsitzender: Univ.-Prof. Dr.-Ing. Hans-Georg Herzog

Prüfer der Dissertation:

1. Univ.-Prof. Dr.-Ing. Ralph Kennel
2. Univ.-Prof. Dr. techn. Manfred Schrödl
   (Technische Universität Wien/Österreich)

Die Dissertation wurde am 10.06.2014 bei der Technischen Universität München eingereicht und durch die Fakultät für Elektrotechnik und Informationstechnik am 14.09.2014 angenommen.

Preface

The present work examines the potential of current oversampling for the sensorless control of synchronous machines. Using linear regression, the current evolution during a switching state is approximated by a straight line. The approximated offset and slope represent low-noise current and current derivative values. Upon this basis, three position estimation techniques are developed and merged in two oppositional hybrid sensorless control methods which demonstrate the advantages of the oversampling.

The research behind those contents has been enabled by and carried out at the Institute for Electrical Drive Systems and Power Electronics of the Technische Universitaet Muenchen (Munich, Germany) in the period from 2012 to 2014 and under supervision of Prof. Ralph Kennel. At this point in time the required hardware components were significantly more expensive than conventional drive hardware. Hence, the reader is supposed to gain a preview of the opportunities that are going to emerge for sensorless control as soon as the prices of more elaborate components (e.g. DSP-FPGA combinations or magnetoresistive current transducers) will drop into a range relevant for series production.

For accomplishing this project, including all hardware and software development, within a period of 3 years the efficient collaboration with the following people has been essential: During the work of his Diploma thesis *Janos Jung* developed the real time system capable of current oversampling and the respective data processing. This development has been broadly supported by the scientific employee *Peter Stolze*. As a part of his studies *Mathias Kramkowski* implemented the recursive linear regression algorithm in VHDL which enabled the real time evaluation of the oversampling data. Based on the above works the former student *Tino Müller* manufactured and commissioned a portable and reliable test bench with which all experiments of this work have been realized.

Despite of the author's aim to investigate thoroughly and provide comprehensible deductions, he remains aware that no insight is ultimate - instead, the reader is welcome to comment, ask critically or discuss new experience.

Munich, January 2015

Peter Landsmann

Contents

Chapter 1

Introduction

The finite resources of our planet face a growing global development that already exceeds their sustainable limits [1]. The severity of the consequences of global resource over-exploitation makes profound political changes inevitable [2–4], of which the recent sustainability trend in industrialized nations, such as Germany, is just a beginning. Regarding energy production and consumption (as parts of the resource scarcity problem), we already note an increased currency of "green" technical products, but the required reduction of fossil fuel extraction and carbon emission is by far not reached yet [5]. A further reduction can be facilitated, inter alia, by the increasing electrification of applications and the improving efficiency of electro-mechanical power conversion.

Although power electronics and machine control strategies have made significant progress in the past three decades, in practice still a major part of the generated electric energy is used by machines in direct grid connection (Fig. 1.1(a)) - a simple operating mode with low efficiency. However, the installation of a more efficient drive system, consisting of inverter and machine, entails a higher initial investment. Especially when utilizing the potential of inverters to employ (more efficient) synchronous machines, the inverter requires the rotor position information.

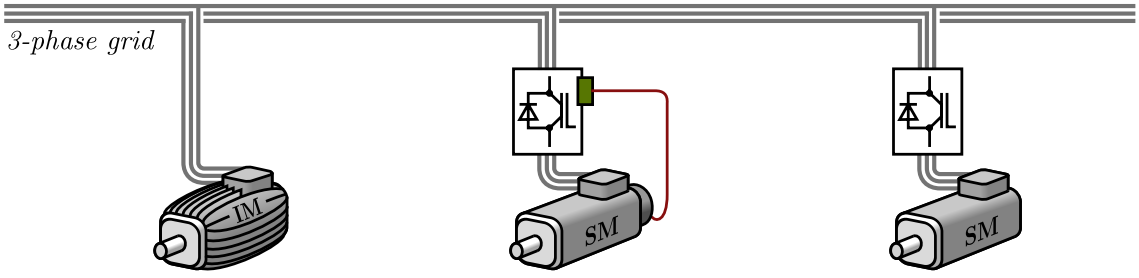

(a) grid connected machine (b) conventional drive system (c) sensorless drive system

Figure 1.1: *Machine operation topologies.*

This information is normally obtained by means of a rotor position sensor - a relatively expensive and sensitive component that demands a free shaft end, construction space on this side, an additional cable and an evaluation circuit (see Fig. 1.1(b)); and that increases the (often manual) installation effort and aggravates the overall fault probability of the drive system. This set of drawbacks obviously affects the attractiveness of inverter driven synchronous machines, and thereby motivates the development of control strategies that overcome the need for a position sensor (Fig. 1.1(c)).

In this sense, so called "sensorless control" strategies further the relevance and currency of synchronous machine drive systems, by making them cheaper, smaller, saver and more robust - and do hence, in a broader sense, give a small contribution to the overall electrification of applications and to the reduction of fossil energy consumption.

However, according to the state of the art in sensorless control, these strategies do also entail drawbacks, difficulties and limitations:

(1.) Due to internal or subsequent filtering, the estimation bandwidth of most sensorless methods is limited. Moreover, some injection-based methods require a reduction of the current controller bandwidth which propagates into all above cascades. Hence, a sensorless controlled drive will not fulfil very high dynamic requirements.

(2.) Sensorless control methods employ the machine as a sensor, despite its design for energy conversion. Hence, manufacturing tolerances, age and temperature dependences, nonlinearities and harmonics that may be negligible regarding energy conversion, limit the accuracy of the position estimate in comparison a sensor signal.

(3.) At low speed and standstill, the position information is commonly obtained from the anisotropy orientation, using signal injection techniques. Due to switching frequency limitation for drives larger than 1 kW, this injection is normally located in the audible frequency range, resulting in an acoustic noise emission at low speed.

(4.) The anisotropy, exploited for low speed position estimation, shows harmonic and load dependent deviations from the rotor position. Harmonics of very high magnitude, as for instance in discretely wound machines, and very high torques can both lead to an assignment problem between anisotropy and rotor position. Especially the latter cause is crucial, since it results in a general torque limitation for sensorless control techniques at low speed.

(5.) The transition between the techniques for low and for high speed angle estimation is based on the estimated speed, i.e. on the time derivative of the angle estimate,

resulting in non-smooth transitions (up to stability problems) during acceleration or deceleration processes.

(6.) Finally, most high speed schemes presume the preliminary knowledge of at least a few machine parameters, reaching up to multi-dimensional parameter curves. Low speed schemes comprise a set of filter parameters and gains that in some cases are machine parameter dependent and in most cases are complex to tune.

Those problems do still prevent the use of sensorless techniques in many applications where at least one of the above points hurts an essential requirement. Applications with close placement of the machine to the customer, for instance, are often not realizable because of the third reason, while the other reasons may be irrelevant. Hence, solving this one drawback, would already increase the number of possible applications of sensorless controlled synchronous machines.

To stay with this example, the particular extent of acoustic noise emission at low speed depends on the amount of injection required to identify the anisotropy orientation with sufficient signal quality. This identification is based on the relation between voltage and current time derivative, where the voltage is relatively well known from the pulse width reference. The current derivative, however, is not measured directly with a standard drive setup, but calculated from the difference between consecutive current samples. Hence, only a fraction of the current measurement range and resolution is utilized in this derivative calculation. Moreover, depending on the saliency ratio of the machine, only a fraction of the calculated current derivative is actually angle dependent. Hence, although the noise and quantization of the current measurement is sufficient for the current control, it may constitute the bottleneck for the anisotropy identification and for the desirable reduction of injection magnitude (i.e. acoustic noise emission).

On the other hand, the standard current sampling technique, referred to as synchronous current sampling (SCS), has been designed for the purpose of current control as well. By sampling in the centre of the passive switching state (once per PWM half-period), SCS aims to segregate the fundamental content of the current evolution from the pulse width modulation (PWM) induced harmonics [6]. However, conventional analogue to digital (A/D) converters are able to sample at a much higher rate than once per control interval. The respective gain in information, obtained without a change to the hardware configuration, could be employed for the purpose of sensorless control.

1.1 Contributions

This thesis deals with the development and assessment of sensorless control techniques that utilize the maximum A/D conversion frequency. The underlying idea herein is to approximate the oversampled current evolution during each switching state by a *straight line*. Using a least squares based technique (linear regression) for approximation, the resulting straight coefficients contain markedly less noise than single current samples. Moreover, the approximated straight slope provides a measure of the current derivative - the key information for anisotropy-based methods. Hence, the approximated straight slope and offset are employed to obtain low noise inductance and EMF information, allowing for the design of position estimation techniques for standstill and high speeds.

Beyond the noise reduction potential, this thesis shows that the approximated slope information can be utilized to develop an EMF based position estimator for surface mounted permanent magnet synchronous machines that does not involve any machine parameter. In order to realize this second advantage in a hybrid sensorless control scheme for the full speed range, two extensions are proposed: a parameter-free signal to noise ratio (SNR) based estimate fusion technique that, moreover, obviates the utilization of the estimated speed, and a q-axis pulse test for the identification of the load dependent anisotropy displacement.

A second (parameter involving) hybrid approach is developed in order to demonstrate the maximum achievable performance of oversampling based sensorless control, where the particular focus is on speed controller bandwidth and injection magnitude. It is shown that, in order to reach maximum bandwidth, non-static effects in the current-flux relation must be compensated.

By proposing and validating the above techniques, this work contributes to the solution of the problems (1.), (3.), (5.) and (6.) of the state of the art in sensorless control. Moreover, with the thorough analysis of the oversampled current response and its first utilization for the closed loop sensorless control of alternating current (AC) machines, this work provides deep insight into several effects in synchronous machine drive systems that are neglected in conventional models.

1.2 Related works

Current oversampling has been considered for sensorless control in a small number of other publications, however, using different approaches and attaining different results:

In 2010 the evaluation of switching transient by means of current oversampling has been

proposed by Wolbank et al. [7, 8]. In particular, the rarely documented machine winding recharge transient (discussed in Ch. 4.2.3) is captured by means of Rogovski-type current derivative sensors. By applying edge- and amplitude-detection techniques to the oversampled Rogovski-sensor signal, the anisotropy information is obtained from the current derivative oscillation. However, the placement of those sensors and the filtering of their output signal is not clear since, particularly, the significantly larger cable-related transients (discussed in Ch. 4.2.2) are not visible in the current derivative signal. Those normally dominating oscillations do not contain the position information, but would severely aggravate the proposed detection. Moreover, although in a later publication [9] the proposed technique has been implemented in a control system, a closed loop sensorless operation has not been presented for this approach.

In 2011 the evaluation of Rogovski-type current derivative sensors by averaging multiple high frequent samples has been proposed by Bolognani et al. [10]. In this way, the influence of parasitic effects related to this type of measurement could be minimized. However, as for this evaluation the above transient oscillations firstly need to settle [9], this technique requires relatively much injection magnitude. Moreover, both above approaches are based on current derivative sensors, i.e. additional hardware with respect to a conventional drive setup.

In 2012 the least squares based derivative approximation of oversampled current signals has been proposed theoretically by Sumner et al. [11], which is considered having the closest relation to the work of this thesis. The approximated current derivative during an active switching state (ASS) is approximated by a straight line, the slope of which is considered to provide the anisotropy information. The idea has been supported with simulation results, that did not contain parasitic effects. In practice, however, the current signal during ASSs of reasonable injection magnitudes is mostly described by the above mentioned transient oscillations, such that the approximation results are not usable. Due to this difficulty, Sumner et al. replaced the least squares based derivative approximation in 2013 by an artificial neuronal network (ANN) based slope identification [12] in order to still evaluate the oversampled current data during the ASS. Yet, the results showed only medium accuracy, while requiring relatively long ASSs, i.e. a relatively high injection magnitude.

In a broader sense, the term oversampling also includes methods that sample more than once per control interval, but obtain the time derivative of the current from the difference between two current samples. While some of these methods sample continuously and disregard unreasonable samples [13], other methods schedule the sampling instants

according to the switching pattern [14–16]. However, since these methods sample at a rate close to control frequency and employ the difference between two current samples, they are considered relating closer to conventional anisotropy-based methods than to the techniques proposed in this work.

1.3 Outline

After this introduction, the second chapter elucidates the underlying machine model, in order to agree on an understanding and a description of the electromagnetic relations and effects in synchronous machines. Moreover, extensions are added to the model to explain and predict parasitic effects discovered during the course of the thesis. Chapter 3 provides a brief review and classification of sensorless control techniques in literature, in order to describe the origin and illustrate the context of the techniques used in this thesis.

The following four chapters constitute a step-by-step development of the eventual current oversampling based hybrid sensorless control techniques. Firstly, Ch. 4 briefly describes the hardware setup designed for this thesis and provides an in-depth investigation of the oversampled current signal itself. Ch. 5 chapter focuses on the linear approximation of the oversampled current data, analyses the straight coefficients depending on several operating conditions, and compares the results to the theoretical expectation. Ch. 6 firstly contrasts reasonable ways to obtain the position information from the straight coefficients and proposes three position estimation techniques that are effective in different speed regions. Based on the experimentally determined properties of those position estimates, Ch. 7 finally concludes the development by proposing two oppositional fusion techniques, each aiming to support and work out one essential advantage of the oversampling-based position estimates.

Chapter 2

Drive model

A model, as a simplified description of reality, is helpful to segregate, understand and predict certain aspects of a real subject, but cannot give full evidence for the applicability of a method to the subject. In the context of sensorless control of synchronous machines, the purpose of this chapter is, hence, to agree on an underlying understanding of their electromagnetic behaviour, to set the foundation for theoretical descriptions and derivations, and to provide an explanation for particular effects found in practice, allowing for their prediction and compensation. The validation of approaches, however, will in this thesis only be performed by practical experiments and not by simulation.

After defining the nomenclature of this work, the space vector representation is derived and discussed briefly. Based on those mathematical conventions a generic nonlinear synchronous machine model is be derived, including a closer consideration of its anisotropic behaviour. From this generic model a linear permanent magnet synchronous machine (PMSM) and a linear reluctance synchronous machine (RSM) model are deduced as two special cases. Finally, a simple dynamic eddy current model will complement the overall machine model, such that most significant effects in the oversampled current responses can be emulated and partially predicted.

2.1 Nomenclature and definitions

This section provides a brief summary of the mathematical principles underlying the present work. Besides the usual work-specific choice of symbols for physical quantities that needs to be defined, the symbol font as well as super- and subscripts are employed to indicate certain properties of a quantity, such as dimension or reference frame. The condensed and centralized description allows to interpret all following parts of the thesis.

2.1.1 Quantities

Firstly, Tab. 2.1 shows the definition of the symbols for physical quantities. All quantities

Symbol	***Description***
u, ψ	voltage and flux linkage
i, ξ	current and current derivative
ν	normalized voltage / pulse width
γ	scaled current progression
R, L	resistance and inductance
Y, C	admittance and capacity
M, ω, θ	torque, speed and angle (electrical)
Θ, k_f	inertia and friction coefficient (electrical)
t, T	time and time constant
N	Gaussian noise

Table 2.1: *List of Quantities.*

will be quantified using SI units – with the following two exceptions:

(1.) A voltage or injection magnitude stated in percent (%) relates to the maximum vector length in the voltage hexagon of $\frac{2}{3}U_{dc}$ (ca. 373 V).

(2.) For comparability reasons, current slopes are stated in ampere per sampling interval A/T_s or milliampere per sampling interval mA/T_s.

2.1.2 Dimensions

Quantities with one dimension, i.e. scalars, are written in regular letters. Multidimensional quantities, such as vectors and matrices, are written in bold letters, where vectors are written in lower case and matrices are written in upper case. A summary of the dimension definitions with examples is given in Tab. 2.2.

Description	***Dimension***	***Character***	***Examples***
scalar	1	regular	R_s, M, θ
vector	n	bold, small	$\boldsymbol{i}_s^s$, $\boldsymbol{\psi}_s^s$
matrix	$m \times n$	bold, capital	$\mathbf{L}_s^s$, $\mathbf{T}$

Table 2.2: *Nomenclature of Dimensions*

2.1.3 Subscript

The subscript is used to specify the physical location or origin of a quantity. A few examples are given in order to circumscribe this notation: R_s is the resistance of the

stator windings, i_a is the current in phase winding a, i_α is the alpha component of the stator fixed current vector (see section 2.1.4) and ψ_{pm} is the flux linkage component caused by the permanent magnet. A list of the general subscripts used in this work and their respective description is given in Tab. 2.3

Subscript	***Description***
s	stator or sampling (in case of times)
r	rotor
pm	permanent magnet
dc	DC-link
ed	eddy current
a	anisotropy (used with vectors, matrices and angles)
a, b, c	stator phase windings (only scalars except angles)
u, v, w	inverter and motor terminals
α, β	stator fixed Cartesian axes
d, q	rotor fixed Cartesian axes
D, Q	anisotropy fixed Cartesian axes
x, y	voltage fixed Cartesian axes
Σ, Δ	specific average and difference
P, I	proportional and integral
z, p	active and passive switching state
$z+$, $z-$	positive and negative active switching state
0, 1, 2..	number of sampling interval in the past

Table 2.3: *List of Subscripts*

2.1.4 Reference frames (superscript)

The superscript (e.g. $\boldsymbol{i}^r$ or $\mathbf{L}^s$) is used to determine the reference frame in which a quantity[1] is described. The superscript "s" stands for stator fixed, "r" for rotor fixed, and "u" for voltage fixed reference frame. Each reference frame has a specific denotation for its axes which is summarized in Tab. 2.4.

Alignment	***Superscript***	***Abscissa***	***Ordinate***
stator	s	α	β
rotor	r	d	q
anisotropy	a	D	Q
voltage	u	x	y

Table 2.4: *Denotation of reference frames*

[1] Only vectors and matrices will have superscripts, since scalars do not have an orientation and are therefore not reference frame dependent.

As indicated in Fig. 2.1, the stator frame is spatially fixed and its α axis is aligned with the axis of the phase winding a. The rotor frame is fixed to the rotor, i.e. with

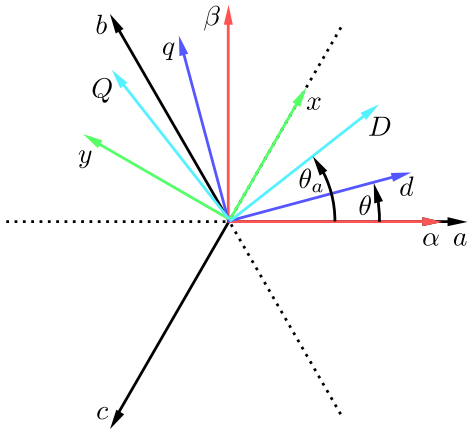

Figure 2.1: *Orientation of reference frames.*

respect to the stator fixed frame it is rotated by the rotor angle θ. For a given rotor speed the rotor frame is moving, which must be considered for derivations in this frame. The same applies for the anisotropy fixed reference frame that is rotated by the angle θ_a with respect to the stator fixed frame, and by $\Delta\theta_a = \theta_a - \theta$ with respect to the rotor fixed frame. The voltage fixed reference frame is aligned with the voltage (average voltage in a PWM interval), where in case of Fig. 2.1 a negative c phase voltage vector $-\boldsymbol{u}_c^s$ has been applied.

There are two other usages of superscripts: the mathematical operation "power of" (e.g. $\cos^2\theta$ or $\mathbf{T}^{-1}$) and the vector or matrix operation "transpose" (e.g. $\boldsymbol{i}_s^{s\top}\mathbf{J}\boldsymbol{\psi}_s^s$) which is denoted by a $\top$.

2.1.5 Transformations

The reference frames introduced in Ch. 2.1.4 have the same origin but a different orientation. Hence, a transformation of a vector from one into another reference frame is a rotation, realized by the matrix $\mathbf{T}$

$$\mathbf{T} = \mathbf{T}(\theta) = \begin{bmatrix} \cos\theta & -\sin\theta \\ \sin\theta & \cos\theta \end{bmatrix}. \tag{2.1}$$

Multiplying a vector by $\mathbf{T}$ results in a vector with the same magnitude, rotated by θ in mathematically positive direction, i.e. anticlockwise. The negative rotation is realized by

the inverse matrix $\mathbf{T}^{-1}$ which due to the orthogonality [17] of $\mathbf{T}$ is

$$\mathbf{T}^{-1} = \mathbf{T}^{\top} = \mathbf{T}(-\theta) = \begin{bmatrix} \cos\theta & \sin\theta \\ -\sin\theta & \cos\theta \end{bmatrix}. \tag{2.2}$$

Using $\mathbf{T}$ or $\mathbf{T}^{-1}$ in this particular way, without subscript, refers to a rotation by the rotor angle θ. In case another angle is used within $\mathbf{T}$, then the subscript of the angle is attached to $\mathbf{T}$, or $\mathbf{T}$ is expressed as a function of the angle

$$\mathbf{T}_1 = \mathbf{T}(\theta_1) = \begin{bmatrix} \cos\theta_1 & -\sin\theta_1 \\ \sin\theta_1 & \cos\theta_1 \end{bmatrix}. \tag{2.3}$$

In analogy to the complex notation the orthogonal rotation operator is referred to as matrix $\mathbf{J}$

$$\mathbf{J} = \mathbf{T}\left(\tfrac{\pi}{2}\right) = \begin{bmatrix} 0 & -1 \\ 1 & 0 \end{bmatrix}, \tag{2.4}$$

which for instance appears as a result of derivatives

$$\frac{\mathrm{d}\mathbf{T}}{\mathrm{d}t} = \frac{\partial \mathbf{T}}{\partial \theta}\frac{\mathrm{d}\theta}{\mathrm{d}t} = \mathbf{J}\omega\mathbf{T}. \tag{2.5}$$

Furthermore essential are the identity matrix $\mathbf{I}$ that does not influence a vector

$$\mathbf{I} = \begin{bmatrix} 1 & 0 \\ 0 & 1 \end{bmatrix} \tag{2.6}$$

and, in analogy to the complex conjugation, the matrix $\mathbf{X}$ that flips the second component of a vector

$$\mathbf{X} = \begin{bmatrix} 1 & 0 \\ 0 & -1 \end{bmatrix}. \tag{2.7}$$

Note that, in contrast to most other matrices, all rotation matrices are commutative

$$\mathbf{TJ} = \mathbf{JT}. \tag{2.8}$$

2.2 Space vector representation

Conventional AC machines are equipped with three terminals which give access to their three phase windings. Since this work addresses the sensorless control of synchronous machines, the phases are considered[2] being Y-connected (see Fig. 2.2). A coupling condition between the three phase currents restricts the electrical system to having only two degrees of freedom. This allows for a bijective transformation into a two dimensional, ideally decoupled reference system that simplifies the mathematical description of an AC machine.

This transformation, often referred to as Clarke-Transformation, is a commonly employed operation in most modern drive control techniques. The particular definitions in literature, however, involve different mathematical procedures and imply different assumptions. Most commonly, so-called space phasors are employed [18, p. 411][19, p. 9-16][20, p. 116] which are complex numbers with an interpreted spacial orientation. This representation originated from the early alternating current (AC) theory where AC machines were directly connected to the grid. In the grid-connected case, temporal and spatial quantities are sinusoidal and geometrically related.

In the highly dynamic and non-sinusoidal operation of controlled, voltage source inverter (VSI)-driven AC machines, however, a clear distinction between temporal and spacial relations is necessary in order to understand the dynamic system behaviour. Moreover, the description and handling of anisotropic relations (see. Ch. 2.3.2) that are essential within this thesis, is more restricted and often insufficient when using the complex description, as can be seen e.g. in [21, p. 175]. For these reasons, the vectorial notation [22, p. 30][23, p. 27] is used that provides clear segregation of spacial and temporal quantities and enables to efficiently process anisotropic relations by means of matrices.

Within the vectorial representation we find two conventions of the Clarke-Transformation [23, p. 27]:

(1.) The first retains the amplitude of currents and voltages, meaning that the magnitude of the current vector equals the amplitude of the phase currents (in sinusoidal operation). Then the resistances and inductances in space vector representation will be equal to the phase values. However, for energy-related equations, e.g. for torque production or electrical power consumption, a factor $\frac{2}{3}$ must be included.

(2.) The second convention is referred to as “energetically correct” and uses a different

[2]Delta connection is unusual for synchronous machines, as their third harmonic EMF component induces circular currents in this connection type.

scaling for the current in the transformation (but not for the voltage). Then the current vector magnitude is 1.5 times the amplitude of the phase currents and the resistance and inductance in space vector representation are only two thirds of the phase values. However, energy and power can be obtained directly from the vectorial quantities without using a correction factor.

Although in literature the first convention is used more often, the author decided to use the second one, i.e. the *energetically correct convention* of the Clarke transform. It should hence be noted that there will be no scaling factor in torque equations and the current graphs will be scaled 1.5 times larger. Yet, all other general relations remain unchanged.

Fig. 2.2 shows the phase configuration of an AC machine with three sets of windings a,

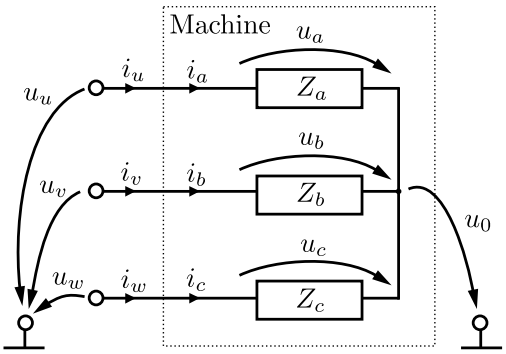

Figure 2.2: *Y-connection scheme for three phase AC machines .*

b and c in Y-connection with open neutral point that are connected to the three terminals u, v and w. The Y-connection results in the following relations between terminal and phase voltages

$$\begin{aligned} u_a &= u_u - u_0 \\ u_b &= u_v - u_0 \\ u_c &= u_w - u_0 \end{aligned} \tag{2.9}$$

and between terminal and phase currents

$$\begin{aligned} i_a &= i_u \\ i_b &= i_v \\ i_c &= i_w. \end{aligned} \tag{2.10}$$

The open neutral point results in a coupling condition between the terminal currents

$$i_u + i_v + i_w = 0, \tag{2.11}$$

providing only two degrees of freedom for the currents. Furthermore, only a voltage drop between the terminals will affect the machine currents, which provides two degrees of freedom for the actuating variable as well

$$u_{uv} = u_u - u_v, \qquad u_{vw} = u_v - u_w, \qquad u_{wu} = -u_{uv} - u_{vw}. \tag{2.12}$$

Hence, a three phase machine with open neutral point is a two dimensional system.

Seen from a physical perspective, the overall magnetomotive force $\boldsymbol{\mathcal{F}}_s^s$ in the machine results from the superposition of all single phase ampere-turns $\mathcal{F}_a$, $\mathcal{F}_b$ and $\mathcal{F}_c$. The 120°(electrical) spacial shift between the phase windings requires a respective vectorial summation, indicated in Fig. 2.3(a). Due to the proportional relation between current

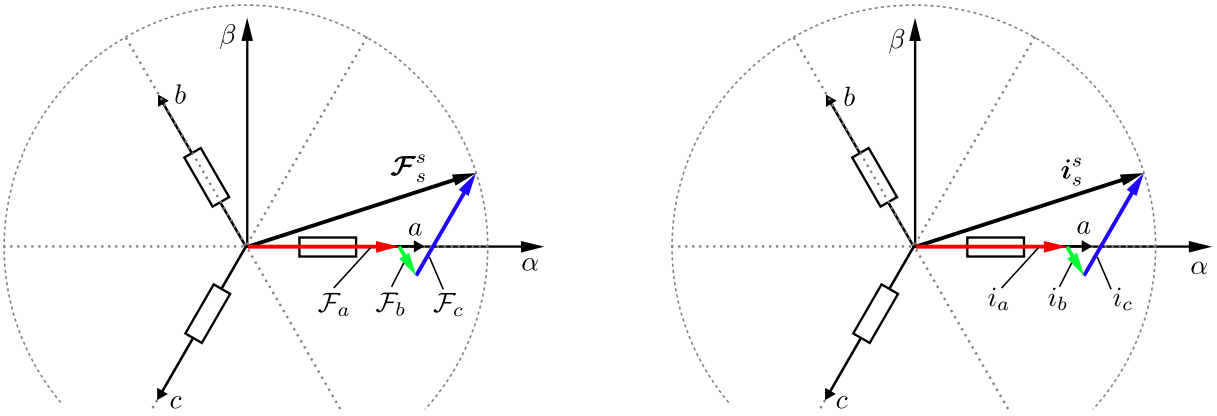

(a) Superposition of the phase ampere-turns.

(b) Superposition of the phase currents.

Figure 2.3: *Superposition of current related phase values to a vector in αβ-frame.*

and magnetomotive-force (by the number of turns per phase winding), the same vectorial summation is applied to the phase currents, such that the overall current vector $\boldsymbol{i}_s^s$, as a representation of the phase current composition, is interpreted having a spacial direction (see Fig. 2.3(b)).

The mathematical equivalent for this geometric superposition of current related phase quantities is the transformation matrix $\mathbf{Q}_i$

$$\mathbf{Q}_i = \begin{bmatrix} 1 & -\frac{1}{2} & -\frac{1}{2} \\ 0 & \frac{\sqrt{3}}{2} & -\frac{\sqrt{3}}{2} \end{bmatrix} \quad \text{, e.g.} \quad \begin{bmatrix} i_\alpha \\ i_\beta \end{bmatrix} = \mathbf{Q}_i \begin{bmatrix} i_u \\ i_v \\ i_w \end{bmatrix}. \tag{2.13}$$

The reverse transformation from a stator frame vector back to the phase quantities is

realized by the pseudo inverse of matrix $\mathbf{Q}_i$

$$\mathbf{Q}_i^+ = \frac{2}{3}\begin{bmatrix} 1 & 0 \\ -\frac{1}{2} & \frac{\sqrt{3}}{2} \\ -\frac{1}{2} & -\frac{\sqrt{3}}{2} \end{bmatrix} \quad \text{, e.g.} \quad \begin{bmatrix} i_u \\ i_v \\ i_w \end{bmatrix} = \mathbf{Q}_i^+ \begin{bmatrix} i_\alpha \\ i_\beta \end{bmatrix}. \tag{2.14}$$

The constraint (2.11) would allow to obtain the current vector $\boldsymbol{i}_s^s$ from only two phase sensors, which for the case of sensors being located in the lines u and v, would be realized by the following reduced transformation matrices

$$\mathbf{Q}_{i2} = \begin{bmatrix} \frac{3}{2} & 0 \\ \frac{\sqrt{3}}{2} & \sqrt{3} \end{bmatrix}, \qquad \mathbf{Q}_{i2}^{-1} = \frac{2}{3}\begin{bmatrix} 1 & 0 \\ -\frac{1}{2} & \frac{\sqrt{3}}{2} \end{bmatrix}. \tag{2.15}$$

For voltage related quantities (voltage, flux and flux linkage) a vectorial superposition does not apply, as the flux does not split up between the phase windings, but penetrates all phases – depending on its angle, however, to a different extent (see. Fig. 2.4). Hence, the

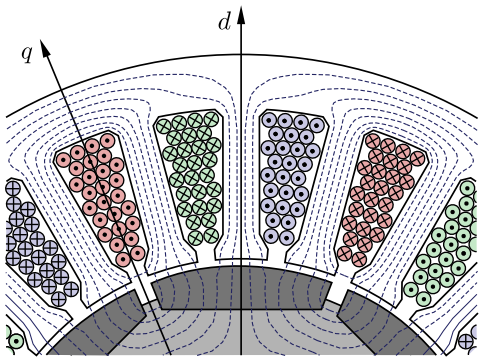

Figure 2.4: *Exemplary sketch of the flux distribution between the phase windings.*

overall flux vector must be projected onto all phase directions, in order to obtain the phase flux values, as indicated in Fig. 2.5(a). Due to the proportional relation between voltage and flux derivative (by the number of turns per phase winding), the same projection is applied to the voltage, such that also the voltage vector $\boldsymbol{u}_s^s$, as a representation of the phase voltage composition, is interpreted having a spacial direction (see Fig. 2.5(b)).

The mathematical analogue of this projection is the transformation matrix $\mathbf{Q}_{u,ph}^+$

$$\mathbf{Q}_{u,ph}^+ = \begin{bmatrix} 1 & 0 \\ -\frac{1}{2} & \frac{\sqrt{3}}{2} \\ -\frac{1}{2} & -\frac{\sqrt{3}}{2} \end{bmatrix} \quad \text{, e.g.} \quad \begin{bmatrix} u_a \\ u_b \\ u_c \end{bmatrix} = \mathbf{Q}_{u,ph}^+ \begin{bmatrix} u_\alpha \\ u_\beta \end{bmatrix}, \tag{2.16}$$

which determines the phase voltages u_a, u_b and u_c from the voltage vector $\boldsymbol{u}_s^s$. According

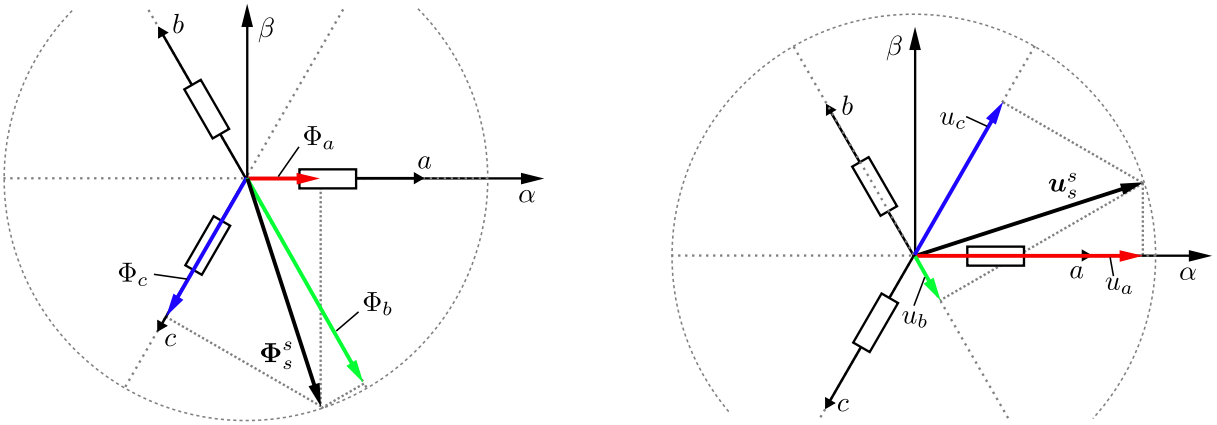

(a) Projection of the flux vector.

(b) Projection of the voltage vector.

Figure 2.5: *Projection of voltage related quantities on the phase axes.*

to (2.9), the terminal voltages u_u, u_v and u_w are obtained by adding the neutral point voltage u_0 to the phase voltages, resulting in the full inverse voltage transformation matrix $\mathbf{Q}_u^{-1}$

$$\mathbf{Q}_u^{-1} = \begin{bmatrix} 1 & 0 & 1 \\ -\frac{1}{2} & \frac{\sqrt{3}}{2} & 1 \\ -\frac{1}{2} & -\frac{\sqrt{3}}{2} & 1 \end{bmatrix} \quad \text{, e.g.} \quad \begin{bmatrix} u_u \\ u_v \\ u_w \end{bmatrix} = \mathbf{Q}_u^{-1} \begin{bmatrix} u_\alpha \\ u_\beta \\ u_0 \end{bmatrix}. \tag{2.17}$$

Since this added voltage offset u_0 does not cause a potential difference between the terminals, it has no effect on the currents in the machine. However, by varying it intelligently, the sinusoidal excitation range can be extended by about 15% [21, p. 31].

The reverse transformation of voltage related quantities from the terminals to the vectorial values is, hence, realized by the matrix $\mathbf{Q}_u$

$$\mathbf{Q}_u = \frac{2}{3} \begin{bmatrix} 1 & -\frac{1}{2} & -\frac{1}{2} \\ 0 & \frac{\sqrt{3}}{2} & -\frac{\sqrt{3}}{2} \end{bmatrix} \quad \text{, e.g.} \quad \begin{bmatrix} u_\alpha \\ u_\beta \end{bmatrix} = \mathbf{Q}_u \begin{bmatrix} u_u \\ u_v \\ u_w \end{bmatrix}, \tag{2.18}$$

where the voltage offset u_0 is not relevant and was therefore left out.

In conclusion, a three phase AC machine with open neutral point is a two dimensional system, enabling the description of its electromagnetic relations in a Cartesian reference frame where all electric or magnetic quantities are represented by space vectors with two components. The Clarke transformation links phase with vectorial quantities, where particularly its “energetically correct” definition is underlying this thesis.

2.3 Generic nonlinear synchronous machine model

Using this two dimensional representation, in the following section a generic nonlinear model of synchronous machines is derived. The particular structure and parametrization of the central key block in the model will then allow to emulate the characteristics of different kinds of synchronous machines, such as a surface mounted permanent magnet synchronous machine (SPMSM), an interior permanent magnet synchronous machine (IPMSM), a reluctance synchronous machine (RSM) or a permanent magnet assisted reluctance synchronous machine (PMARSM).

Firstly, the nonlinear electrical part of the model is derived in a relatively generic way, after which the anisotropic relations resulting from this derivation are analysed. Finally, the derivation of a simple mechanical model completes the system and allows to summarize all parts in a nonlinear model for simulation.

2.3.1 Electrical model

Despite the very different mechanical structure synchronous machines may have, their electrical behaviour can be described by a model that only differs in one component. As indicated in Fig. 2.6, the mechanical cross section of synchronous machines may show different winding schemes and rotor symmetries, leading to a different number of pole pairs

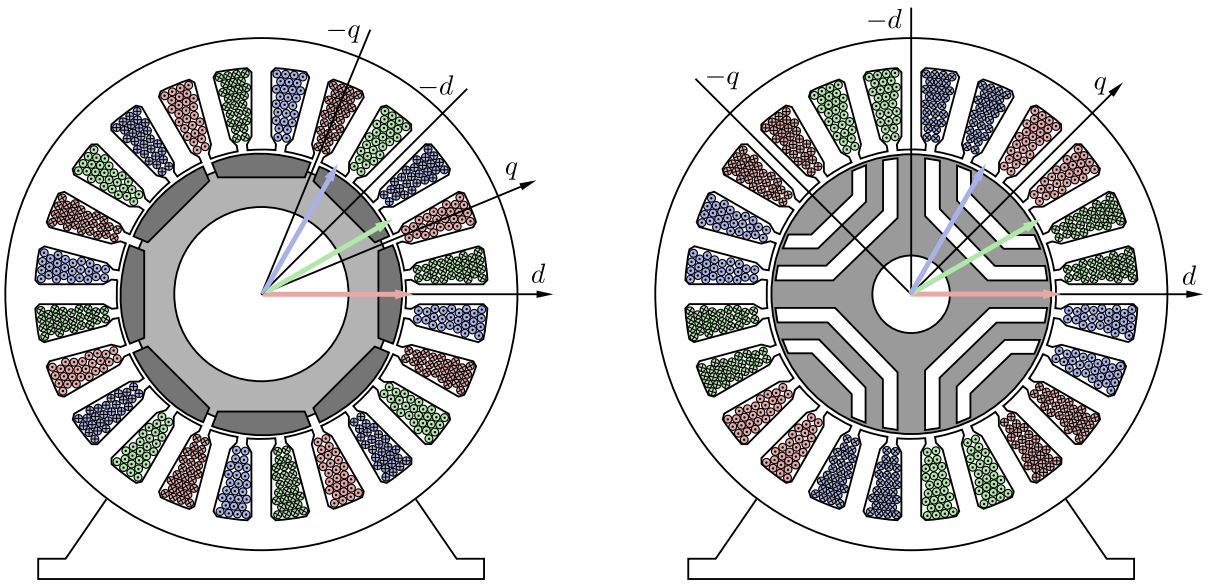

(a) SPMSM with 4 pole pairs.

(b) RSM with 2 pole pairs.

Figure 2.6: *Exemplary structural sketches of the mechanical cross section of different types of synchronous machines.*

z_p and hence to a different angular width of the mechanical projection of the rotor fixed frame. Moreover, the existence and placement of permanent magnets and flux barriers in the rotor, of which two extremes are indicated in Fig. 2.6, categorizes the machine type either as SPMSM (Fig. 2.6(a)), IPMSM, RSM (Fig. 2.6(b)) or PMARSM.

After the above described Clarke Transform, however, the particular winding scheme, the pole pairs, the stator and the rotor geometry are not noticeable anymore, such that any machine can be interpreted having the structure indicated in Fig. 2.7. There are two

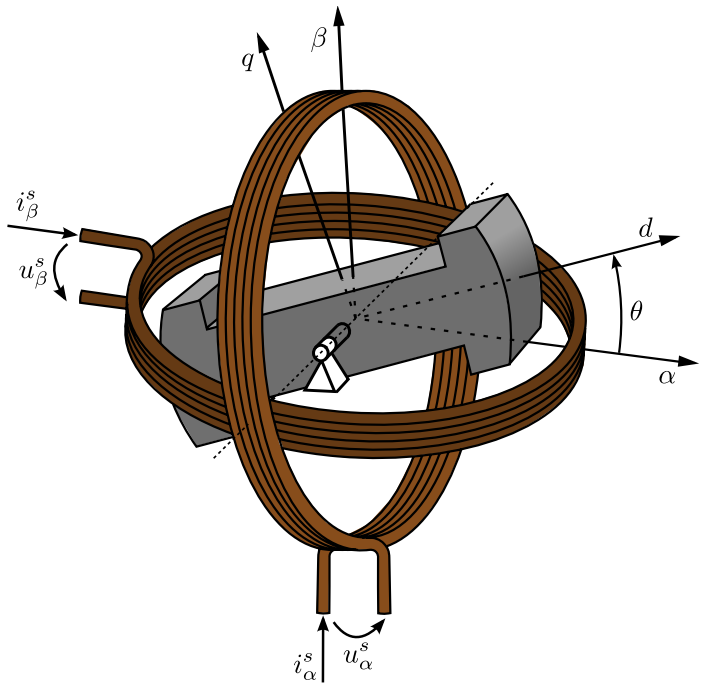

Figure 2.7: *Simplified structure of a synchronous machine in the electrical model.*

orthogonal windings α and β, within which a magnetic body rotates with the electrical rotor angle θ. The voltages u_α and u_β and the currents i_α and i_β are the components of the respective stator frame vectors $\boldsymbol{u}_s^s$ and $\boldsymbol{i}_s^s$, and the characteristics of the machine are represented by the magnetic properties of the rotating body, particularly its current-flux relation.

The mathematical derivation of the generic electrical model is started by considering that the voltage $\boldsymbol{u}_s^s = [u_\alpha \; u_\beta]^\top$ is the sum of the resistive voltage drop in the coils of Fig. 2.7 and the voltage induced by a variation of the flux linkage in each coil

$$\boldsymbol{u}_s^s = R_s \boldsymbol{i}_s^s + \frac{\mathrm{d}\boldsymbol{\psi}_s^s}{\mathrm{d}t}. \tag{2.19}$$

Since the resistive voltage is considered being isotropic, the stator resistance value R_s is a scalar.

In rotor fixed frame the flux linkage $\boldsymbol{\psi}_s^r$ is defined as a function of the current $\boldsymbol{i}_s^r$

$$\boldsymbol{\psi}_s^r = f_{\psi i}(\boldsymbol{i}_s^r) = \begin{bmatrix} \psi_d(i_d, i_q) \\ \psi_q(i_d, i_q) \end{bmatrix}. \tag{2.20}$$

In particular this function $f_{\psi i}(\cdot)$ is assumed to be a *bijective assignment* between a current vector $\boldsymbol{i}_s^r$ and a flux linkage vector $\boldsymbol{\psi}_s^r$ in rotor frame. Hence, $f_{\psi i}(\cdot)$ can be inverted to obtain the currents when knowing the flux linkage in rotor frame

$$f_{i\psi}(\cdot) = f_{\psi i}^{-1}(\cdot) \tag{2.21}$$

$$\boldsymbol{i}_s^r = f_{i\psi}(\boldsymbol{\psi}_s^r) = \begin{bmatrix} i_d(\psi_d, \psi_q) \\ i_q(\psi_d, \psi_q) \end{bmatrix}. \tag{2.22}$$

This function $f_{\psi i}(\cdot)$ is the characteristic element in the machine model, that identifies the machine type by defining whether the machine is linear or saturating, whether it is isotropic or salient, whether it is cross saturating and in case it is, $f_{\psi i}(\cdot)$ defines how the ratio and the orientation of the saliency are affected by the load current. Fig. 2.8 shows this function $f_{\psi i}(\cdot)$ for the above two machine type extremes SPMSM and RSM.

However, (2.20) also implies two major neglects:

(1.) By assuming that the function $f_{\psi i}(\cdot)$ does not depend on the rotor angle, a stator fixed anisotropy and slotting effects are not considered.

(2.) By assuming that the function $f_{\psi i}(\cdot)$ does not depend on its values in the past or on the current derivative, dynamic effects like hysteresis and eddy currents are not considered.

As the voltage equation (2.19) requires the flux linkage in stator frame, (2.20) must be transformed using the Park Transform. The result $\boldsymbol{\psi}_s^s$ depends on the rotor angle θ

$$\boldsymbol{\psi}_s^s = \mathbf{T} f_{\psi i}(\mathbf{T}^{-1} \boldsymbol{i}_s^s) \tag{2.23}$$

$$= \boldsymbol{\psi}_s^s(\boldsymbol{i}_s^s, \theta). \tag{2.24}$$

In particular, the voltage equation (2.19) requires the time derivative of the flux linkage in stator frame (2.23), in which both $\boldsymbol{i}_s^s$ and θ are time dependent

$$\frac{\mathrm{d}\boldsymbol{\psi}_s^s}{\mathrm{d}t} = \frac{\mathrm{d}}{\mathrm{d}t} \left(\mathbf{T} f_{\psi i}(\mathbf{T}^{-1} \boldsymbol{i}_s^s) \right). \tag{2.25}$$

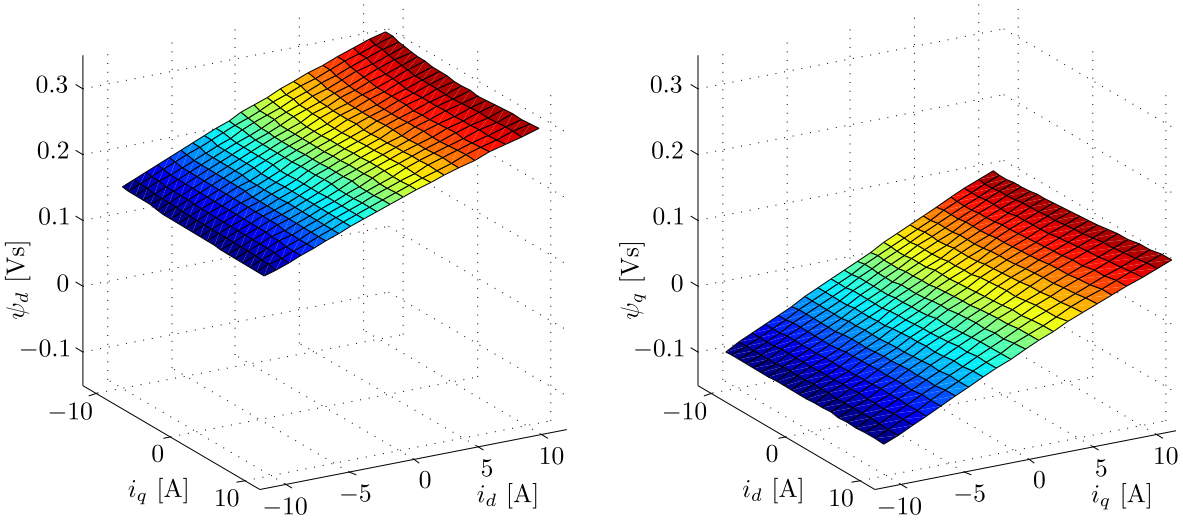

(a) 2.0 kW SPMSM Merkes MT4-0750 (SPM1).

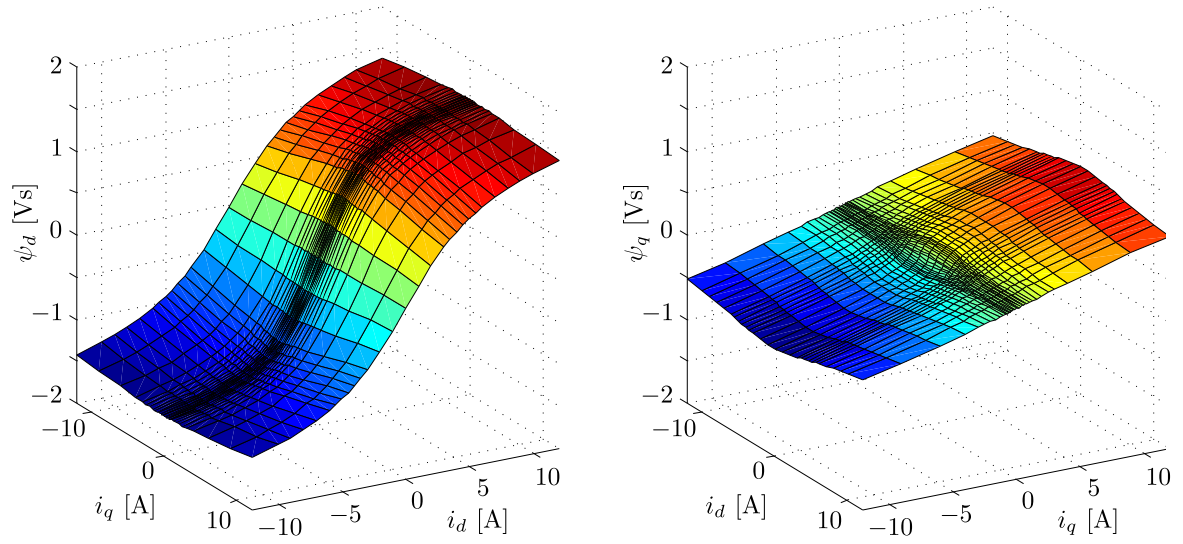

(b) 1.1 kW RSM Stellenbosch V1.0 (RSM1).

Figure 2.8: *Measured current-flux relation $f_{\psi i}(\cdot)$ of different types of synchronous machines.*

Deriving the product of $\mathbf{T}$ and $f_{\psi i}(\cdot)$ results in the summation

$$\frac{\mathrm{d}\boldsymbol{\psi}_s^s}{\mathrm{d}t} = \frac{\mathrm{d}\mathbf{T}}{\mathrm{d}t} f_{\psi i}(\mathbf{T}^{-1}\boldsymbol{i}_s^s) + \mathbf{T}\frac{\mathrm{d}f_{\psi i}(\mathbf{T}^{-1}\boldsymbol{i}_s^s)}{\mathrm{d}t}, \tag{2.26}$$

where the derivatives of $\mathbf{T}$ and $f_{\psi i}(\cdot)$ with respect to time are rewritten in partial form

$$\frac{\mathrm{d}\boldsymbol{\psi}_s^s}{\mathrm{d}t} = \frac{\partial\mathbf{T}}{\partial\theta}\frac{\mathrm{d}\theta}{\mathrm{d}t} f_{\psi i}(\mathbf{T}^{-1}\boldsymbol{i}_s^s) + \mathbf{T}\frac{\partial f_{\psi i}(\mathbf{T}^{-1}\boldsymbol{i}_s^s)}{\partial(\mathbf{T}^{-1}\boldsymbol{i}_s^s)}\frac{\mathrm{d}}{\mathrm{d}t}(\mathbf{T}^{-1}\boldsymbol{i}_s^s) \tag{2.27}$$

The derivative of the flux linkage $\boldsymbol{\psi}_s^r$ with respect to the current $\boldsymbol{i}_s^r$ in rotor frame is the

rotor fixed inductance $\mathbf{L}_s^r$

$$\frac{\partial f_{\psi i}(\mathbf{T}^{-1}\boldsymbol{i}_s^s)}{\partial(\mathbf{T}^{-1}\boldsymbol{i}_s^s)} = \frac{\partial \boldsymbol{\psi}_s^r}{\partial \boldsymbol{i}_s^r} = \mathbf{L}_s^r. \tag{2.28}$$

Since both the flux linkage and the current are vectorial quantities, $\mathbf{L}_s^r$ is a matrix

$$\mathbf{L}_s^r = \begin{bmatrix} L_{dd} & L_{dq} \\ L_{qd} & L_{qq} \end{bmatrix} = \begin{bmatrix} \frac{\partial \psi_d}{\partial i_d} & \frac{\partial \psi_d}{\partial i_q} \\ \frac{\partial \psi_q}{\partial i_d} & \frac{\partial \psi_q}{\partial i_q} \end{bmatrix}. \tag{2.29}$$

By using the derivative of the transformation matrix $\mathbf{T}$ given in (2.5) and the definition of the inductance matrix (2.28), the partial derivatives in (2.27) are substituted

$$\frac{\mathrm{d}\boldsymbol{\psi}_s^s}{\mathrm{d}t} = \mathbf{J}\omega\mathbf{T}\boldsymbol{\psi}_s^r + \mathbf{T}\mathbf{L}_s^r\frac{\mathrm{d}}{\mathrm{d}t}(\mathbf{T}^{-1}\boldsymbol{i}_s^s), \tag{2.30}$$

where the derivation of the product $(\mathbf{T}^{-1}\boldsymbol{i}_s^s)$ results in two terms

$$\frac{\mathrm{d}\boldsymbol{\psi}_s^s}{\mathrm{d}t} = \mathbf{J}\omega\mathbf{T}\boldsymbol{\psi}_s^r - \mathbf{T}\mathbf{L}_s^r\mathbf{T}^{-1}\mathbf{J}\omega\boldsymbol{i}_s^s + \mathbf{T}\mathbf{L}_s^r\mathbf{T}^{-1}\frac{\mathrm{d}\boldsymbol{i}_s^s}{\mathrm{d}t}. \tag{2.31}$$

Finally, the constellation of the matrices $\mathbf{T}$ and $\mathbf{T}^{-1}$ transforms the rotor frame quantities $\boldsymbol{\psi}_s^r$ and $\mathbf{L}_s^r$ to stator frame

$$\frac{\mathrm{d}\boldsymbol{\psi}_s^s}{\mathrm{d}t} = \mathbf{L}_s^s\frac{\mathrm{d}\boldsymbol{i}_s^s}{\mathrm{d}t} + \mathbf{J}\omega\boldsymbol{\psi}_s^s - \mathbf{L}_s^s\mathbf{J}\omega\boldsymbol{i}_s^s, \tag{2.32}$$

in which the stator frame inductance $\mathbf{L}_s^s$ has been introduced as

$$\mathbf{L}_s^s = \begin{bmatrix} L_{\alpha\alpha} & L_{\alpha\beta} \\ L_{\beta\alpha} & L_{\beta\beta} \end{bmatrix} = \begin{bmatrix} \frac{\partial \psi_\alpha}{\partial i_\alpha} & \frac{\partial \psi_\alpha}{\partial i_\beta} \\ \frac{\partial \psi_\beta}{\partial i_\alpha} & \frac{\partial \psi_\beta}{\partial i_\beta} \end{bmatrix} = \mathbf{T}\mathbf{L}_s^r\mathbf{T}^{-1} \tag{2.33}$$

$$L_{\alpha\alpha} = L_{dd}\cos^2\theta + L_{qq}\sin^2\theta - 2L_{dq}\sin\theta\cos\theta \tag{2.34}$$

$$L_{\alpha\beta} = (L_{dd} - L_{qq})\sin\theta\cos\theta + L_{dq}(\cos^2\theta - \sin^2\theta) = L_{\beta\alpha} \tag{2.35}$$

$$L_{\beta\beta} = L_{dd}\sin^2\theta + L_{qq}\cos^2\theta + 2L_{dq}\sin\theta\cos\theta. \tag{2.36}$$

Note that each of these values L constitutes a derivative of the flux linkage and does consequently depend on the current.

Finally, (2.32) is inserted into (2.19) to obtain the explicit voltage equation

$$\boldsymbol{u}_s^s = R_s\boldsymbol{i}_s^s + \mathbf{L}_s^s\frac{\mathrm{d}\boldsymbol{i}_s^s}{\mathrm{d}t} + \mathbf{J}\omega\boldsymbol{\psi}_s^s - \mathbf{L}_s^s\mathbf{J}\omega\boldsymbol{i}_s^s, \tag{2.37}$$

that can be solved for the current derivative

$$\frac{\mathrm{d}\boldsymbol{i}_s^s}{\mathrm{d}t} = \mathbf{L}_s^{s-1}(\boldsymbol{u}_s^s - R_s\boldsymbol{i}_s^s - \mathbf{J}\omega\boldsymbol{\psi}_s^s + \mathbf{L}_s^s\mathbf{J}\omega\boldsymbol{i}_s^s). \tag{2.38}$$

Those equations (2.37) and (2.38) constitute the generic nonlinear electrical model of a synchronous machine and form the basis of several derivations within this thesis.

2.3.2 Anisotropy consideration

As a consequence of the law of energy conversion, inductance matrices are symmetrical (e.g. $L_{dq} = L_{qd}$) and positive semi-definite (e.g $\boldsymbol{x}^\top\mathbf{L}_s^r\boldsymbol{x} \geq 0$, $\forall\boldsymbol{x} \in \mathbb{R}^2$) [24]. According to the principal axis transformation [17, p. 321], every real symmetrical matrix $\mathbf{A}$ can be transformed into a diagonal matrix $\mathbf{D}$ by means of an orthogonal matrix $\mathbf{U}$

$$\mathbf{D} = \mathbf{U}^\top\mathbf{A}\mathbf{U}, \tag{2.39}$$

where the diagonal entries of $\mathbf{D}$ are the eigenvalues of $\mathbf{A}$ and the columns of $\mathbf{U}$ are the respective normalized eigenvectors (which for symmetrical matrices must be orthogonal).

Within the range $\theta_x = -\pi \ldots \pi$ the columns of the transformation matrix $\mathbf{T}(\theta_x)$ represent all possible combinations of two normalized perpendicular vectors, meaning that $\mathbf{T}(\cdot)$ does (exactly) constitute the set of all possible matrices $\mathbf{U}$. Hence, there is an angle θ_a for which the inductance matrix in stator frame $\mathbf{L}_s^s$ can be transformed into a diagonal matrix $\mathbf{L}_s^a$

$$\mathbf{L}_s^a = \mathbf{T}_a\mathbf{L}_s^s\mathbf{T}_a^{-1} = \begin{bmatrix} L_D & 0 \\ 0 & L_Q \end{bmatrix}. \tag{2.40}$$

Since in particular (2.40) applies for four angles within $\theta_x = -\pi \ldots \pi$, we establish uniqueness of (2.40) by prescribing the order of the eigenvalues

$$L_D < L_Q \tag{2.41}$$

and by restricting the transformation angle to

$$-\frac{\pi}{2} < \theta_a \leq +\frac{\pi}{2}. \tag{2.42}$$

The physical interpretation of the above derivation is that every stator frame inductance matrix $\mathbf{L}_s^s$ can be transformed to an *anisotropy fixed reference frame* (see Ch. 2.1.4) which

is spanned by the eigenvectors of $\mathbf{L}_s^s$. Thus, in this frame vertical and horizontal voltages result in parallel current slopes.

In the anisotropy fixed reference frame the inversion required to obtain the admittance[3] matrix $\mathbf{Y}_s^a$ is simple

$$\mathbf{Y}_s^a = \begin{bmatrix} Y_D & 0 \\ 0 & Y_Q \end{bmatrix} \tag{2.43}$$

$$\overset{T_s \ll \frac{L_D}{R_s}}{\approx} (\mathbf{L}_s^a)^{-1}\, T_s = \begin{bmatrix} \frac{T_s}{L_D} & 0 \\ 0 & \frac{T_s}{L_Q} \end{bmatrix}, \tag{2.44}$$

with T_s being the sufficiently small[4] sampling time. According to (2.41), the order of the diagonal entries is

$$Y_D > Y_Q. \tag{2.45}$$

Starting from this anisotropy fixed reference frame, the following transformations can be carried out analogously for inductances and admittances. However, since for low speed sensorless control, where the current response to an imposed voltage is evaluated, the admittance has a higher relevance, the derivation steps for the inductance are not listed separately.

In order to separate the admittance into components with certain characteristics, the auxiliary quantities Y_Σ and Y_Δ and the angle dependent matrix $\mathbf{S}(\cdot)$ are introduced: The mean admittance Y_Σ is the average value of the diagonal entries of the admittance matrix (i.e. the self-admittances), independent of the reference frame used

$$Y_\Sigma = \frac{Y_D + Y_Q}{2} = \frac{Y_{dd} + Y_{qq}}{2} = \frac{Y_{\alpha\alpha} + Y_{\beta\beta}}{2}. \tag{2.46}$$

The differential admittance Y_Δ is defined as (half) the biggest possible difference between the diagonal entries that is obtained most easily from the anisotropy fixed reference frame

$$Y_\Delta = \frac{Y_D - Y_Q}{2}. \tag{2.47}$$

[3] In a strict sense, the usage of term "admittance" is wrong. Originating from AC theory it is an excitation frequency dependent complex conductance. However, in literature to sensorless control the term "admittance" is often employed to shorten the frequent usage of the long term "inverse inductance". Moreover, the definition (2.44) is similarly frequency dependent and shows for high frequencies (small T_s) a nearly inductive behaviour as well. For those reasons the author follows this terminology.

[4] If the sampling time T_s is much smaller than the smallest electrical time constant L_D/R_s, the resistive influence on the time-discretisation can be neglected, as the current evolution within T_s is nearly linear.

However, Y_Δ can also be calculated from any other reference frame by taking into account the mutual entries (e.g. Y_{dq})

$$Y_\Delta = \sqrt{\left(\frac{Y_{dd} - Y_{qq}}{2}\right)^2 + Y_{dq}^2} \tag{2.48}$$

$$= \sqrt{\left(\frac{Y_{\alpha\alpha} - Y_{\beta\beta}}{2}\right)^2 + Y_{\alpha\beta}^2}. \tag{2.49}$$

The matrix $\mathbf{S}(\cdot)$ is one of the essential tools for the derivation of the anisotropy-based sensorless control theory, as it segregates the rotor angle dependent behaviour of an anisotropic inductance

$$\mathbf{S}(\theta) = \begin{bmatrix} \cos 2\theta & \sin 2\theta \\ \sin 2\theta & -\cos 2\theta \end{bmatrix}. \tag{2.50}$$

Its effect on a vector is a vertical flip and a subsequent rotation with twice the rotor angle

$$\mathbf{S} = \mathbf{TTX}. \tag{2.51}$$

Using these three auxiliary quantities, Y_Σ, Y_Δ and $\mathbf{S}(\cdot)$, the admittance in stator frame $\mathbf{Y}_s^s$ is rewritten concisely in such a way

$$\mathbf{Y}_s^s = Y_\Sigma \mathbf{I} + Y_\Delta \mathbf{S}(\theta_a) \tag{2.52}$$

$$= \begin{bmatrix} Y_\Sigma + Y_\Delta \cos 2\theta_a & Y_\Delta \sin 2\theta_a \\ Y_\Delta \sin 2\theta_a & Y_\Sigma - Y_\Delta \cos 2\theta_a \end{bmatrix}, \tag{2.53}$$

that the anisotropic behaviour is split up into an isotropic, scaling part $Y_\Sigma \mathbf{I}$ and an angle dependent rotating part $Y_\Delta \mathbf{S}(\theta_a)$. When starting the derivation from rotor fixed frame[5], the less salient diagonal entries and the emerging mutual terms have to be considered, resulting in a more complex expression

$$\mathbf{Y}_s^s = Y_\Sigma \mathbf{I} + \left(\frac{Y_{dd} - Y_{qq}}{2}\ \mathbf{I} + Y_{dq}\ \mathbf{J}\right)\ \mathbf{S}(\theta). \tag{2.54}$$

As mentioned before, the derivation of the inductances would be carried out identically and results in analogous equations.

[5]For instance when not knowing the anisotropy angle, or when deriving the admittance from a flux-current look-up table (LUT).

2.3.3 Mechanical model

Since the focus of this work is not on plant or drive train related effects, the mechanical model is kept simple, comprising only of the torque generation and the integrations required to obtain speed and angle.

The torque equals the vector product of current and flux linkage which can be carried out in rotor frame

$$M = \boldsymbol{i}_s^{r\top} \mathbf{J} \boldsymbol{\psi}_s^r \tag{2.55}$$

as well as in stator frame

$$M = \boldsymbol{i}_s^{s\top} \mathbf{J} \boldsymbol{\psi}_s^s. \tag{2.56}$$

The rotor angle and speed are obtained by integrating the sum of all torques,

$$\frac{\mathrm{d}\omega}{\mathrm{d}t} = \frac{1}{\Theta}(M - k_f\omega - M_L) \tag{2.57}$$

$$\omega = \int \frac{\mathrm{d}\omega}{\mathrm{d}t}\, \mathrm{d}t \tag{2.58}$$

$$\theta = \int \omega\, \mathrm{d}t \tag{2.59}$$

where (2.57) exemplarily contains a linear friction term $k_f\omega$. If necessary, this can be replaced by any more sophisticated friction model which, however, is not the in focus of this work.

It is herein important to note that in the model the angle θ as well as the speed ω are electrical. In order to obtain the respective mechanical values θ_m and ω_m, both of them must be divided by the pole pair number z_p

$$\omega_m = \omega / z_p \tag{2.60}$$

$$\theta_m = \theta / z_p. \tag{2.61}$$

Hence, the inertia Θ and the friction coefficient k_{fr} are the electrical representations, obtained from the mechanical values by

$$\Theta = \Theta_m / z_p^2 \tag{2.62}$$

$$k_f = k_{fm} / z_p^2. \tag{2.63}$$

This electrically focused modeling has been chosen, since the work on sensorless control involves only minimal mechanical considerations. For comparability reasons, however, experimental results will show the mechanical values.

2.3.4 Nonlinear model for simulation

The nonlinear model derived in the previous sections 2.3.1 and 2.3.3 is the groundwork for further mathematical derivations. For the purpose of simulation in ©MATLAB/Simulink, however, the model is designed in an easier way while maintaining its transfer behaviour.

Firstly, the stator voltage equation (2.19) is integrated to obtain the flux linkage in stator frame

$$\boldsymbol{\psi}_s^s = \int (\boldsymbol{u}_s^s - R_s \boldsymbol{i}_s^s) dt. \tag{2.64}$$

Using the inverse function $f_{i\psi}(\cdot)$ defined in (2.21) and the rotor angle θ, a current vector in stator frame $\boldsymbol{i}_s^s$ is assigned to the flux linkage $\boldsymbol{\psi}_s^s$

$$\boldsymbol{i}_s^s = \mathbf{T} f_{i\psi}(\mathbf{T}^{-1} \boldsymbol{\psi}_s^s). \tag{2.65}$$

The function $f_{i\psi}(\cdot)$ can be realized using a two dimensional lookup table or an analytical approximation [25]. Due to its inherent energetical constraints, the source data should however be obtained from either flux measurements or finite element analysis (FEA).

In conclusion, these two vectorial equations (2.64) and (2.65) represent the entire nonlinear electrical model of a synchronous machine. The mechanical part is modelled by the equations (2.56) to (2.59).

Fig. 2.9 shows the block diagram of the model derived in this section which is used for simulation. The number of lines in a connector represents the dimension of the quantity.

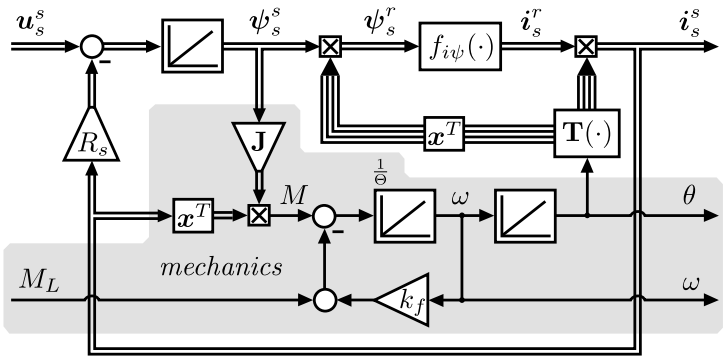

Figure 2.9: *Generic nonlinear model of synchronous machines.*

A single line represents a scalar, two lines represent a two dimensional vector and four lines represent a 2×2 matrix. The type of machine is characterized by the block $f_{i\psi}(\cdot)$ which accomplishes an interpolation in an LUT obtained from steady state flux measurements (examples indicated in Fig. 2.8).

2.4 Linear PMSM model

The term "linear" refers to the relation between rotor frame flux linkage $\boldsymbol{\psi}_s^r$ and current $\boldsymbol{i}_s^r$. Note that even if this condition is fulfilled, from a control point of view there are still nonlinearities in the model, due to the multiplication with the angle dependent matrix $\mathbf{T}$.

However, a linear relation between $\boldsymbol{\psi}_s^r$ and $\boldsymbol{i}_s^r$ leads to a constant inductance in rotor frame

$$\mathbf{L}_s^r = \frac{\partial \boldsymbol{\psi}_s^r}{\partial \boldsymbol{i}_s^r} = \text{const.} \,, \tag{2.66}$$

meaning that the inductance $\mathbf{L}_s^r$ can be used as a factor between flux and current. In a linear PMSM this current dependent flux is added to the permanent magnet flux ψ_{pm} which is aligned with the d-axis of the rotor frame

$$\boldsymbol{\psi}_s^r = \mathbf{L}_s^r \boldsymbol{i}_s^r + \boldsymbol{\psi}_{pm}^r \tag{2.67}$$

$$\boldsymbol{\psi}_{pm}^r = \begin{bmatrix} \psi_{pm} \\ 0 \end{bmatrix}. \tag{2.68}$$

The inductance may still be salient, but in linear case it is always (also under load) aligned with the rotor position

$$\mathbf{L}_s^r = \begin{bmatrix} L_d & 0 \\ 0 & L_q \end{bmatrix}. \tag{2.69}$$

The stator voltage equation (2.19) requires the time derivative of the flux linkage in stator frame which is obtained by transforming (2.67) to stator frame

$$\boldsymbol{\psi}_s^s = \mathbf{T}\mathbf{L}_s^r\mathbf{T}^{-1}\boldsymbol{i}_s^s + \mathbf{T}\boldsymbol{\psi}_{pm}^r \tag{2.70}$$

$$= \mathbf{L}_s^s \boldsymbol{i}_s^s + \boldsymbol{\psi}_{pm}^s \tag{2.71}$$

and deriving it with respect to time

$$\frac{\mathrm{d}\boldsymbol{\psi}_s^s}{\mathrm{d}t} = \frac{\mathrm{d}\mathbf{L}_s^s}{\mathrm{d}t}\boldsymbol{i}_s^s + \mathbf{L}_s^s\frac{\mathrm{d}\boldsymbol{i}_s^s}{\mathrm{d}t} + \frac{\mathrm{d}\boldsymbol{\psi}_{pm}^s}{\mathrm{d}t} \tag{2.72}$$

$$\overset{(2.5)}{=} (\mathbf{JTL}_s^r\mathbf{T}^{-1} - \mathbf{TL}_s^r\mathbf{T}^{-1}\mathbf{J})\omega\boldsymbol{i}_s^s + \mathbf{L}_s^s\frac{\mathrm{d}\boldsymbol{i}_s^s}{\mathrm{d}t} + \mathbf{J}\omega\boldsymbol{\psi}_{pm}^s \tag{2.73}$$

$$= (\mathbf{JL}_s^s - \mathbf{L}_s^s\mathbf{J})\omega\boldsymbol{i}_s^s + \mathbf{L}_s^s\frac{\mathrm{d}\boldsymbol{i}_s^s}{\mathrm{d}t} + \mathbf{J}\omega\boldsymbol{\psi}_{pm}^s. \tag{2.74}$$

Finally, inserting (2.74) into (2.19) leads to the specific stator voltage equation for a linear, salient PMSM

$$\boldsymbol{u}_s^s = R_s\boldsymbol{i}_s^s + \mathbf{L}_s^s\frac{\mathrm{d}\boldsymbol{i}_s^s}{\mathrm{d}t} + \mathbf{J}\omega\boldsymbol{\psi}_{pm}^s + (\mathbf{JL}_s^s - \mathbf{L}_s^s\mathbf{J})\omega\boldsymbol{i}_s^s. \tag{2.75}$$

The respective state equation is obtained by solving (2.75) for $\frac{\mathrm{d}\boldsymbol{i}_s^s}{\mathrm{d}t}$

$$\boxed{\frac{\mathrm{d}\boldsymbol{i}_s^s}{\mathrm{d}t} = \mathbf{L}_s^{s-1}(\boldsymbol{u}_s^s - R_s\boldsymbol{i}_s^s - \mathbf{J}\omega\boldsymbol{\psi}_{pm}^s - (\mathbf{JL}_s^s - \mathbf{L}_s^s\mathbf{J})\omega\boldsymbol{i}_s^s).} \tag{2.76}$$

The particular torque equation for a linear, salient PMSM is obtained by inserting the linear current-flux relation in rotor frame (2.67) into the general nonlinear torque equation (2.55)

$$M = \boldsymbol{i}_s^{r\top}\mathbf{J}\boldsymbol{\psi}_s^r \tag{2.77}$$

$$= \boldsymbol{i}_s^{r\top}\mathbf{J}(\mathbf{L}_s^r\boldsymbol{i}_s^r + \boldsymbol{\psi}_{pm}^r) \tag{2.78}$$

$$= (L_d - L_q)i_d i_q + \psi_{pm}i_q \tag{2.79}$$

which comprises both a reluctance torque and the permanent magnet torque. The other mechanical equations (2.57) to (2.59) remain unchanged.

2.5 Linear RSM model

The step from the linear salient PMSM to the reluctance synchronous machine (RSM) is done by eliminating the permanent magnet flux

$$\boldsymbol{\psi}_{pm}^s = \boldsymbol{\psi}_{pm}^r = \mathbf{0}. \tag{2.80}$$

Using (2.80), every equation of the last Ch. 2.4 can be transformed to an equation valid for the linear RSM. The resulting flux linkage in rotor and in stator frame is

$$\boldsymbol{\psi}_s^r = \mathbf{L}_s^r \boldsymbol{i}_s^r \tag{2.81}$$

$$\boldsymbol{\psi}_s^s = \mathbf{T}\mathbf{L}_s^r \mathbf{T}^{-1} \boldsymbol{i}_s^s = \mathbf{L}_s^s \boldsymbol{i}_s^s, \tag{2.82}$$

which leads to the particular voltage equation

$$\boldsymbol{u}_s^s = R_s \boldsymbol{i}_s^s + \mathbf{L}_s^s \frac{\mathrm{d}\boldsymbol{i}_s^s}{\mathrm{d}t} + (\mathbf{J}\mathbf{L}_s^s - \mathbf{L}_s^s \mathbf{J})\omega \boldsymbol{i}_s^s, \tag{2.83}$$

the electrical state equation

$$\frac{\mathrm{d}\boldsymbol{i}_s^s}{\mathrm{d}t} = \mathbf{L}_s^{s-1}(\boldsymbol{u}_s^s - R_s \boldsymbol{i}_s^s - (\mathbf{J}\mathbf{L}_s^s - \mathbf{L}_s^s \mathbf{J})\omega \boldsymbol{i}_s^s) \tag{2.84}$$

and the torque equation of a linear RSM

$$M = (L_d - L_q) i_d i_q. \tag{2.85}$$

The other mechanical equations are given by (2.57) to (2.59) as well.

2.6 Eddy current model

In the derivation of the generic machine model in Ch. 2.3 harmonics, hysteresis and eddy currents have been neglected. As will be shown in the later chapters, however, eddy currents play an important role within the scope of this work. Their influence can be observed in the oversampled current response, does thereby affect the current slope approximation and, hence, both the anisotropy-based and the fundamental model based position estimation. In order to verify the existence and the influence of eddy currents, the observed effects will be compared to an eddy current model in the respective parts of this thesis.

Most literature on eddy currents in AC machines focuses on the modelling of the losses in steady state operation [26–28], resulting in the well known squared frequency dependence. Dynamic eddy current simulations in literature are mostly based on finite element methods (FEM) [29–31] and, hence, very complex and computationally expensive. This work requires an eddy current model for two purposes: for the qualitative verification of the influence of eddy currents itself and for the compensation of a dynamic error in a flux estimator. In both cases a simple model is sufficient that must, however, be able to

emulate the transient behaviour. A model which matches these requirements will be derived in this section, where the focus is by trend on the high frequency behaviour.

As indicated in Fig. 2.10, the basic consideration of this derivation is that the stator flux $\boldsymbol{\psi}_s^s$ penetrates different paths within the machine[6], some of which are electrically

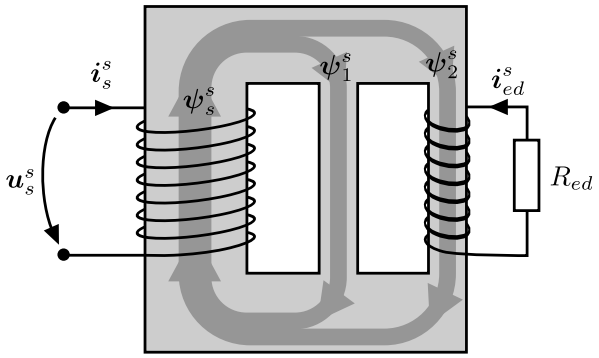

Figure 2.10: *Stator flux penetrating conducting and isolating paths.*

conducting (e.g. the permanent magnet), while others are isolating (e.g. laminated material). The stator flux $\boldsymbol{\psi}_s^s$, generated by (2.19), is hence considered to split up into two components $\boldsymbol{\psi}_1^s$ and $\boldsymbol{\psi}_2^s$

$$\boldsymbol{\psi}_s^s = \boldsymbol{\psi}_1^s + \boldsymbol{\psi}_2^s, \tag{2.86}$$

where $\boldsymbol{\psi}_1^s$ only penetrates the stator winding

$$\boldsymbol{\psi}_1^s = L_1 \boldsymbol{i}_s^s \tag{2.87}$$

and $\boldsymbol{\psi}_2^s$ penetrates an additional coil with the same number of turns as the stator winding that conducts the summarized eddy current $\boldsymbol{i}_{ed}^s$

$$\boldsymbol{\psi}_2^s = L_2 \left(\boldsymbol{i}_s^s - \boldsymbol{i}_{ed}^s \right). \tag{2.88}$$

L_1 and L_2 are the respective path inductances. As this second coil is shorted via the resistor R_{ed}, representing the electric resistivity of the material conducting the eddy currents, it is described by a voltage equation with zero excitation

$$0 = R_{ed} \boldsymbol{i}_{ed}^s - \frac{\mathrm{d}\boldsymbol{\psi}_2^s}{\mathrm{d}t}. \tag{2.89}$$

This is the basic set of equations for the simple eddy current model.

[6]Due to their proportionality, flux linkage is used instead of flux and current instead of penetration, such that both relate to each other by the inductance and not by the reluctances of the paths.

We firstly insert (2.87) and (2.88) into (2.86) and the time derivative of the result into the voltage equation (2.19)

$$\boldsymbol{\psi}_s^s = L_1 \boldsymbol{i}_s^s + L_2 \left(\boldsymbol{i}_s^s - \boldsymbol{i}_{ed}^s\right) \tag{2.90}$$

$$\boldsymbol{u}_s^s = R_s \boldsymbol{i}_s^s + L_1 \frac{\mathrm{d}\boldsymbol{i}_s^s}{\mathrm{d}t} + L_2 \frac{\mathrm{d}\boldsymbol{i}_s^s}{\mathrm{d}t} - L_2 \frac{\mathrm{d}\boldsymbol{i}_{ed}^s}{\mathrm{d}t}. \tag{2.91}$$

Secondly, the time derivative of (2.88) is inserted into (2.89) and rewritten as the eddy current state equation

$$0 = R_{ed} \boldsymbol{i}_{ed}^s - L_2 \frac{\mathrm{d}\boldsymbol{i}_s^s}{\mathrm{d}t} - L_2 \frac{\mathrm{d}\boldsymbol{i}_{ed}^s}{\mathrm{d}t} \tag{2.92}$$

$$\frac{\mathrm{d}\boldsymbol{i}_{ed}^s}{\mathrm{d}t} = \frac{\mathrm{d}\boldsymbol{i}_s^s}{\mathrm{d}t} - \frac{R_{ed}}{L_2} \boldsymbol{i}_{ed}^s. \tag{2.93}$$

Eq. (2.93) demonstrates the transformer effect of the eddy currents: the derivative is equal to $\frac{\mathrm{d}\boldsymbol{i}_s^s}{\mathrm{d}t}$, while the eddy currents gradually fade out. Now inserting (2.93) in (2.91)

$$\boldsymbol{u}_s^s = R_s \boldsymbol{i}_s^s + L_1 \frac{\mathrm{d}\boldsymbol{i}_s^s}{\mathrm{d}t} + L_2 \frac{\mathrm{d}\boldsymbol{i}_s^s}{\mathrm{d}t} - L_2 \left(\frac{\mathrm{d}\boldsymbol{i}_s^s}{\mathrm{d}t} - \frac{R_{ed}}{L_2} \boldsymbol{i}_{ed}^s \right) \tag{2.94}$$

$$= R_s \boldsymbol{i}_s^s + L_1 \frac{\mathrm{d}\boldsymbol{i}_s^s}{\mathrm{d}t} + R_{ed} \boldsymbol{i}_{ed}^s. \tag{2.95}$$

reveals that the high frequency response of the stator currents $\boldsymbol{i}_s^s$ is determined only by the inductance of the non-conducting path of L_1

$$\frac{\mathrm{d}\boldsymbol{i}_s^s}{\mathrm{d}t} = L_1^{-1} \left(\boldsymbol{u}_s^s - R_s \boldsymbol{i}_s^s\right) - \frac{R_{ed}}{L_1} \boldsymbol{i}_{ed}^s. \tag{2.96}$$

By substituting $\frac{\mathrm{d}\boldsymbol{i}_s^s}{\mathrm{d}t}$ in the eddy currents state equation (2.93) with (2.96), the explicit eddy current state equation is obtained

$$\frac{\mathrm{d}\boldsymbol{i}_{ed}^s}{\mathrm{d}t} = L_1^{-1} \left(\boldsymbol{u}_s^s - R_s \boldsymbol{i}_s^s\right) - \left(\frac{R_{ed}}{L_1} + \frac{R_{ed}}{L_2} \right) \boldsymbol{i}_{ed}^s \tag{2.97}$$

that describes the eddy currents as a result of a stator voltage excitation. Eq. (2.97) constitutes an eddy current model that can be integrated into the conventional machine model of Ch. 2.3 by first solving (2.91) for $\frac{\mathrm{d}\boldsymbol{i}_s^s}{\mathrm{d}t}$

$$\frac{\mathrm{d}\boldsymbol{i}_s^s}{\mathrm{d}t} = \underbrace{\frac{1}{L_1 + L_2}}_{L_s} \left(\boldsymbol{u}_s^s - R_s \boldsymbol{i}_s^s\right) + \frac{L_2}{L_1 + L_2} \frac{\mathrm{d}\boldsymbol{i}_{ed}^s}{\mathrm{d}t} \tag{2.98}$$

and then integrating (2.98) with respect to time

$$\boldsymbol{i}_s^s = \int \frac{\mathrm{d}\boldsymbol{i}_s^s}{\mathrm{d}t}\,\mathrm{d}t = \frac{1}{L_s}\int \left(\boldsymbol{u}_s^s - R_s\boldsymbol{i}_s^s\right)\,\mathrm{d}t + \frac{L_2}{L_1+L_2}\boldsymbol{i}_{ed}^s. \tag{2.99}$$

Hence, the summarized eddy current $\boldsymbol{i}_{ed}^s$ is simply scaled by the factor $\frac{L_2}{L_1+L_2}$ and added to the stator current of the conventional model that, in contrast to the high frequency response described by (2.96), is the result of the inductance of all paths $L_s = L_1 + L_2$.

However, considering the amount of parameters involved in (2.97) and (2.99) which can hardly be determined, the eventually simple model is obtained by means of a final simplifying summary. Firstly, the eddy current estimation equation is defined in a way that with respect to the state equation (2.96) is scaled by $\frac{L_2}{L_1+L_2}$

$$\frac{\mathrm{d}\hat{\boldsymbol{i}}_{ed}^s}{\mathrm{d}t} = \frac{L_2}{L_1+L_2}L_1^{-1}\left(\boldsymbol{u}_s^s - R_s\boldsymbol{i}_s^s\right) - \left(\frac{R_{ed}}{L_1}+\frac{R_{ed}}{L_2}\right)\hat{\boldsymbol{i}}_{ed}^s \tag{2.100}$$

$$\approx \underbrace{\frac{L_2}{L_1L_s}}_{Y_{ed}}\boldsymbol{u}_{hf}^s - \underbrace{\left(\frac{R_{ed}}{L_1}+\frac{R_{ed}}{L_2}\right)}_{\frac{1}{T_{ed}}}\hat{\boldsymbol{i}}_{ed}^s, \tag{2.101}$$

and where the term $(\boldsymbol{u}_s^s - R_s\boldsymbol{i}_s^s)$ has been replaced by the high pass filtered stator voltage

$$\boldsymbol{u}_{hf}^s = \mathrm{HPF}\left(\boldsymbol{u}_s^s\right). \tag{2.102}$$

Since the term $(\boldsymbol{u}_s^s - R_s\boldsymbol{i}_s^s)$ cannot have a constant offset (flux would drift away) and since mainly the high frequency behaviour of the eddy currents is relevant in this model, this substitution is valid and yields a higher independence of parameters and input signals.

The resulting scaled eddy current estimator

$$\boxed{\frac{\mathrm{d}\hat{\boldsymbol{i}}_{ed}^s}{\mathrm{d}t} = Y_{ed}\;\boldsymbol{u}_{hf}^s - \frac{\hat{\boldsymbol{i}}_{ed}^s}{T_{ed}}} \tag{2.103}$$

comprises only of two parameters, the eddy current admittance Y_{ed} and the eddy current fade out time constant T_{ed}, that both are to be tuned empirically in the application. This scaled eddy current value $\hat{\boldsymbol{i}}_{ed}^{\hat{s}}$ can then simply be added to the current of the conventional model

$$\boldsymbol{i}_s^s = \frac{1}{L_s}\int \left(\boldsymbol{u}_s^s - R_s\boldsymbol{i}_s^s\right)\,\mathrm{d}t + \hat{\boldsymbol{i}}_{ed}^{\hat{s}}. \tag{2.104}$$

Chapter 3

Sensorless control – state of the art

The goal of sensorless control is the regulation of the current and torque of an AC machine, based on an estimate of the electrical rotor position instead of an angle measurement by an encoder, a resolver or another position sensor. However, the so-called sensorless drive system must still be equipped at least with current sensors in order to estimate the rotor position. Most approaches also require a direct current (DC)-link voltage measurement and some methods even additional current derivative- [14, 32, 33], phase voltage- [34–36] or torque sensors [37]. Hence, referring to these solutions as "Sensorless" is – in a strict sense – incorrect terminology. At the other hand, alternative expressions like "Self-Sensing" or "Encoderless" that aim to be more correct, do still not succeed 20 years after their first appearance. Hence, for the sake of correct classification, this work uses the common terminology.

Beyond the current control, the rotor position estimate is also used as a feedback signal for outer control cascades like speed and position control. The rotor speed is obtained as the time derivative of the estimated rotor position signal. The resulting amplification of estimation noise can be damped by filtering which, however, leads to a time delay in the feedback signal. Hence, the speed controller is usually the most critical cascade in a sensorless drive and it is preferably used as a benchmark to demonstrate the dynamical capabilities of a sensorless method.

Within the variety of sensorless control techniques in literature two generally different approach categories are distinguished: fundamental model (FM)-based and anisotropy-based approaches. Reconsidering the explicit voltage equation of the nonlinear synchronous machine model (2.37)

$$\boldsymbol{u}_s^s = R_s \boldsymbol{i}_s^s + \mathbf{L}_s^s(\theta)\frac{\mathrm{d}\boldsymbol{i}_s^s}{\mathrm{d}t} + \mathbf{J}\omega\boldsymbol{\psi}_s^s(\theta) - \mathbf{L}_s^s(\theta)\mathbf{J}\omega\boldsymbol{i}_s^s \tag{3.1}$$

there are three angle dependent terms. The first term $\mathbf{L}_s^s(\theta)\frac{\mathrm{d}\boldsymbol{i}_s^s}{\mathrm{d}t}$ carries the position information of the anisotropic inductance and, apart from sufficient anisotropy magnitude, it requires (only) the presence of a current time derivative $\frac{\mathrm{d}\boldsymbol{i}_s^s}{\mathrm{d}t} \neq 0$. The second and third term $\mathbf{J}\omega\boldsymbol{\psi}_s^s(\theta) - \mathbf{L}_s^s(\theta)\mathbf{J}\omega\boldsymbol{i}_s^s$ are referred to as electromotive force (EMF) (or more precisely extended electromotive force (eEMF)) and constitute the source of information for fundamental model (FM)-based methods. As can be seen from these terms, the EMF scales with the rotor speed which for these methods results in the loss of position observability around standstill.

For this reason several hybrid sensorless strategies have been proposed [38–42] that utilize the EMF information at medium and high speed and employ signal injection techniques to utilize the anisotropy information at low speed. The challenge of this fusion, however, is the phase-over strategy between the two approaches [43], since it relies on the estimated speed.

In the following sections fundamental model-based and anisotropy-based position estimation will be introduced in more technical detail, where for each category a rough classification of approaches will be given.

3.1 Fundamental model based position estimation

In general, fundamental model (FM)-based sensorless techniques exploit the fact that the relation between current and flux in the machine is rotor position dependent which, as the precondition for the electro-mechanical energy conversion, is always given. Since, consequently, the rotor speed causes a time derivative of the flux, often the relation between current and induced voltage is employed in FM-based techniques.

In particular, for most synchronous machines the rotor frame d-axis is defined by the direction of the permanent magnet (PM) flux. Hence, when estimating the PM flux vector $\boldsymbol{\psi}_{pm}^s$, the angle of this estimate, $\arg(\hat{\boldsymbol{\psi}}_{pm}^{\hat{s}})$, will be the rotor angle. The induced voltage, as the time derivative of the PM flux, consequently shows a 90° phase advance with respect to the rotor angle. A reluctance synchronous machine (RSM), however, that does not have a rotor flux source, requires special consideration in order to evaluate its angle dependent current flux relation.

In this section the above mentioned three FM-based approaches will be described in terms of their basic structure and properties. Since for some of these approaches several particular ways of realization are available, this section aims to provide only a rough overview about the categories of FM-based techniques.

3.1.1 Electromotive force observers

The first category of FM-based sensorless techniques is the electromotive force (EMF) observer. EMF observers deduce the rotor position from the angle of the back EMF, for which a variety of different methods has been proposed. Well known examples are the (extended) Kalman Filter [39], the Luenberger Observer [38], the Sliding Mode Observer [44] and the model reference adaptive system (MRAS) [42]. Despite their very different structures, EMF observers can be interpreted to have a similarity in their approach: The EMF is seen as an unknown state in a machine model that leads to a model error, if not estimated correctly. This deviation between model and reality is, hence, employed to correct the estimation of the EMF.

In the following an exemplary way of realizing an EMF observer will be described which summarizes the above principle with similarity to Luenberger and Sliding Mode observers. A reduced electrical model of the machine that considers only the resistive and inductive behaviour

$$\frac{d}{dt}\hat{\boldsymbol{i}}_s^s = \frac{1}{L_s}\left(\boldsymbol{u}_s^s - R_s\boldsymbol{i}_s^s\right) \tag{3.2}$$

maps all influences on the current, except for the EMF. While calculating the current response by the above model, the real machine will (to the same voltage) produce a current response

$$\frac{d}{dt}\boldsymbol{i}_s^s = \frac{1}{L_s}\left(\boldsymbol{u}_s^s - R_s\boldsymbol{i}_s^s - \mathbf{J}\omega\boldsymbol{\psi}_{pm}^s\right) \tag{3.3}$$

which differs due to the presence of the EMF. This difference is forced to zero by adding a correcting voltage term $\boldsymbol{u}_{corr}^s$ to (3.2)

$$\frac{d}{dt}\hat{\boldsymbol{i}}_s^s = \frac{1}{L_s}\left(\boldsymbol{u}_s^s - R_s\boldsymbol{i}_s^s + \boldsymbol{u}_{corr}^s\right) \tag{3.4}$$

which is the output signal of a correction controller. This controller may be a proportional (P), a proportional-integral (PI), a Sliding Mode or another type of controller, which mainly affects the dynamic response of the observer. In steady state, however, the controller output voltage $\boldsymbol{u}_{corr}^s$ must match the actual EMF in order to keep the model deviation $\hat{\boldsymbol{i}}_s^s - \boldsymbol{i}_s^s$ zero.

Fig. 3.1 shows an exemplary structure of this approach. Since the actuating variable of the preferably fast controller (especially for Sliding Mode Observers) has a high noise content, some filtering must be applied to this signal before its evaluation. Eventually,

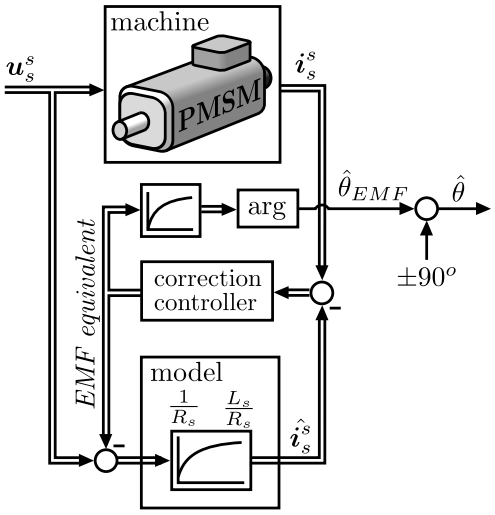

Figure 3.1: *Exemplary structure of an EMF observer.*

the 90° phase advance of the EMF with respect to the flux is subtracted in order to obtain the rotor angle estimate $\hat{\theta}$. For the direction of this subtraction the sign of the estimated speed must be taken into account.

Since at high speed the EMF is the strongest voltage component in (3.3), EMF observers provide a very clean and reliable estimation signal above medium speed. However, since the EMF is a derivative signal, the magnitude of flux harmonics is in the EMF scaled by the order of the respective harmonic. At low speed, when the EMF becomes weaker, the noise content of the angle estimate increases and a parameter error of the resistance[1] R_s and offsets in the voltage[2] $\boldsymbol{u}_s^s$ or the current[3] $\boldsymbol{i}_s^s$ lead to (low frequency) angle estimation errors.

3.1.2 Flux estimators

The second FM-based sensorless approach category is the flux estimator. In contrast to the EMF, the flux does not scale with rotor speed. Hence, the signal to noise ratio (SNR) is not a problem of this estimation approach and additional filtering of the position estimate is not necessary – a unique quality in sensorless control. However, as will be explained in this section, this FM-based technique leads to a different problem that is especially hard to cope with at low speed. In the following the most simple flux estimator for an SPMSM will be introduced to elucidate the principle. A method for different synchronous machine

[1]The resistance R_s depends on the phase winding temperature and can vary for more than 30% within ten seconds.

[2]The stator voltage measurement offset can be caused by an inaccurate DC link voltage measurement, the insulated gate bipolar transistor (IGBT) voltage drop and the inverter dead time.

[3]A current measurement offset can be caused e.g. by a pre-magnetization of the current transducer.

types can be found for instance in [45].

In flux estimators the general voltage equation in stator frame (2.19) is solved for the flux derivative and integrated with respect to time

$$\hat{\boldsymbol{\psi}}_s^s = \int \boldsymbol{u}_s^s - R_s \boldsymbol{i}_s^s \, dt, \tag{3.5}$$

where the stator resistance R_s is a required parameter. According to the linear PMSM flux equation (2.67), the PM flux vector $\boldsymbol{\psi}_{pm}^s$ is then obtained by subtracting the inductive term form the total flux $\boldsymbol{\psi}_s^s$,

$$\hat{\boldsymbol{\psi}}_{pm}^{\hat{s}} = \hat{\boldsymbol{\psi}}_s^s - L_s \boldsymbol{i}_s^s, \tag{3.6}$$

for which the inductance L_s must be known. Finally, the angle evaluation of the estimated PM flux $\arg\left(\hat{\boldsymbol{\psi}}_{pm}^{\hat{s}}\right)$ gives the rotor angle estimate $\hat{\theta}$ and completes the relatively simple estimation scheme indicated in Fig. (3.2).

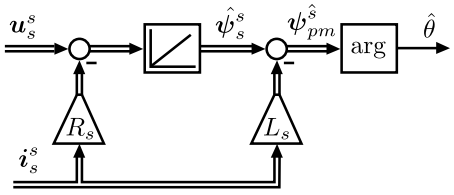

Figure 3.2: *Flux estimator for an SPMSM.*

The physically justified integration leads to a low noise content in $\boldsymbol{\psi}_s^s$ and hence also in $\boldsymbol{\psi}_{pm}^s$. However, a parameter error of the resistance R_s and offsets in the voltage $\boldsymbol{u}_s^s$ or the current $\boldsymbol{i}_s^s$ causes an offset at the integrator input which results in the integrator output drifting away from the origin – a common problem of an open integration. For this reason flux estimators require a feed back structure that compensates this drift. The most simple stabilizing feedback is achieved by adding a negatively scaled flux term in the integral of (3.5), resulting in the drift compensated flux estimation state equation

$$\frac{d}{dt}\hat{\boldsymbol{\psi}}_s^s = \boldsymbol{u}_s^s - R_s \boldsymbol{i}_s^s - k_d \hat{\boldsymbol{\psi}}_s^s \tag{3.7}$$

and the drift compensated flux estimation scheme indicated in Fig. 3.3. The tuning factor k_d adjusts the bandwidth of the drift compensation, where by trend higher values allow to compensate stronger and faster varying errors but impose more phase lag at low speed. Such incorrect influence of the drift compensation creates a limit of feasible operation for flux estimators at low speed.

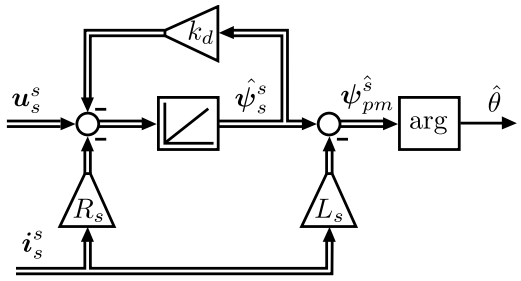

Figure 3.3: *Flux estimator for an SPMSM with simple drift compensation.*

The particular height of this speed limit depends on the intelligence of the feedback structure. While simple feedback techniques, targeting zero flux [46, 47] (as the above introduced), have a relatively high speed limit, the incorporation of the internal voltage[4] angle [45, 48] allows to operate at lower speeds. Incorporating the angle estimation of an anisotropy-based method [40, 49–51] extends the feasible operation down to standstill, which will be described in more detail in Ch. 7.2.

3.1.3 Fundamental model based position estimation for the RSM

The reluctance synchronous machine (RSM) constitutes a special case within fundamental model based position estimation techniques, since it does not have a rotor flux source that could be tracked. For this reason and because of its still sparse application in industry, FM-based solutions for the RSM are rare in literature. In [52] a method has been proposed that exploits the fundamental saliency of the RSM. The fundamental saliency causes a misalignment between flux linkage $\boldsymbol{\psi}_s^s$ and current $\boldsymbol{i}_s^s$. As shown in Fig. 3.4, the total flux linkage vector $\boldsymbol{\psi}_s^s$ can be separated into an isotropic part $\boldsymbol{\psi}_\Sigma^s$ that is aligned with

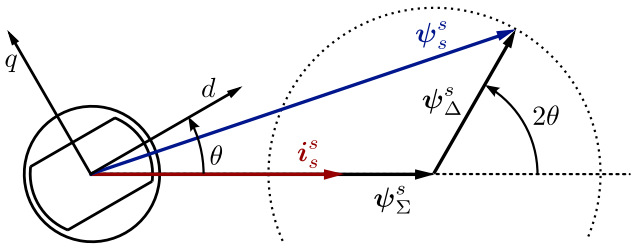

Figure 3.4: *Fundamental current and flux linkage vectors in an RSM.*

the current vector and a salient part $\boldsymbol{\psi}_\Delta^s$ that spans a circle around the isotropic part. The exact orientation of the salient part $\boldsymbol{\psi}_\Delta^s$ within the circle is determined by twice the angle between the current and the rotor position. Employing this relation in reverse, the

[4]The EMF is directly calculated from the voltage equation. The relatively high noise content of this estimate does not allow for it to be directly employed for the rotor position estimation, but it is sufficient for the drift compensation.

rotor angle θ can be obtained when knowing the current $\boldsymbol{i}_s^s$, the flux linkage $\boldsymbol{\psi}_s^s$ and the isotropic component $\boldsymbol{\psi}_\Sigma^s$.

The total flux linkage $\boldsymbol{\psi}_s^s$ is obteined by voltage integration, similar to (3.7). The isotropic component of the flux linkage is calculated as a function of the measured current $\boldsymbol{\psi}_\Sigma^s(\boldsymbol{i}_s^s)$, for instance by means of a look-up table (LUT)[5]. The content of this LUT is obtained from FEM results or flux measurements (as in Fig. 2.8) by using the following precept:

$$\psi_\Sigma(|\boldsymbol{i}_s^s|) = \frac{\psi_d(|\boldsymbol{i}_s^s|, 0) + \psi_q(0, |\boldsymbol{i}_s^s|)}{2}. \tag{3.8}$$

In order to align the respective vector $\boldsymbol{\psi}_\Sigma^s(\boldsymbol{i}_s^s)$, ψ_Σ is multiplied with the current direction

$$\boldsymbol{\psi}_\Sigma^s(\boldsymbol{i}_s^s) = \psi_\Sigma(|\boldsymbol{i}_s^s|)\frac{\boldsymbol{i}_s^s}{|\boldsymbol{i}_s^s|}. \tag{3.9}$$

Finally, the isotropic component $\boldsymbol{\psi}_\Sigma^s$ is subtracted from the total flux linkage $\boldsymbol{\psi}_s^s$ in order to obtain the angle dependent salient component

$$\boldsymbol{\psi}_\Delta^s = \boldsymbol{\psi}_s^s - \boldsymbol{\psi}_\Sigma^s, \tag{3.10}$$

which is tracked by a phase locked loop (PLL) structure in order to deduce the rotor angle θ. Fig. 3.5 shows the complete estimation scheme, where the drift compensation feedback targets the isotropic component $\boldsymbol{\psi}_\Sigma^s$ in order to minimize the before mentioned incorrect influence of the drift compensation on the flux estimator.

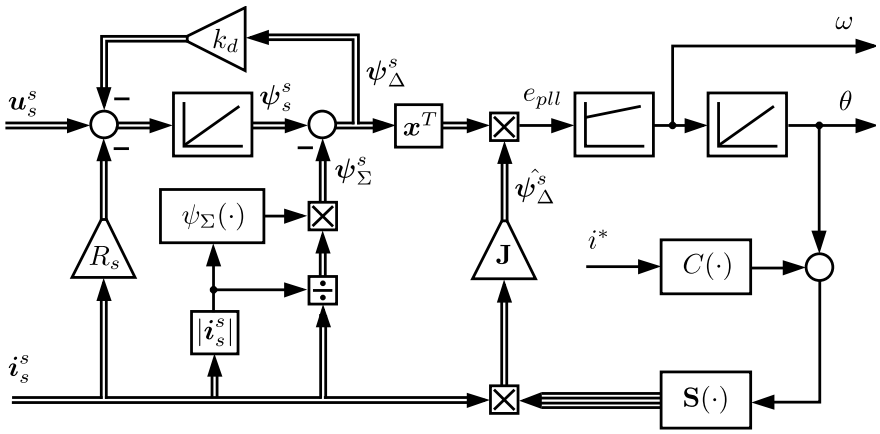

Figure 3.5: *Nonlinear fundamental model based position estimation scheme for RSMs.*

[5]Since efficiently dimensioned RSMs have a nominal operating point in deep magnetic saturation, while being unsaturated in idle condition, their overall current flux relation is strongly nonlinear.

Apart from the above flux-based fundamental saliency evaluation, also EMF-based sensorless techniques have been proposed for the RSM [53, 54].

3.2 Anisotropy-based position estimation

The incapacity of FM-based approaches to observe the rotor position around standstill has a physical reason and cannot be solved without employing a physically different source of information. Looking at the explicit voltage equation (3.1), the only angle dependent term that does not scale with the rotor speed is $\mathbf{L}_s^s(\theta)\frac{\mathrm{d}\boldsymbol{i}_s^s}{\mathrm{d}t}$ – the relation between voltage and current time derivative that is influenced by the so-called anisotropy.

To specify this terminology: Anisotropy is the opposite term of isotropy which means independence of direction. Hence, the term anisotropy describes a *dependence on direction* which in the specific technical context of AC machines refers to a property of the inductance $\mathbf{L}_s^s$: The way in which the current responds to a voltage depends on the direction in which the voltage is applied.

Anisotropy-based sensorless control methods have been developed assuming that the inductance anisotropy is rotor fixed, i.e. that the anisotropy is always aligned with the electrical rotor position. This assumption has been motivated by two thoughts:

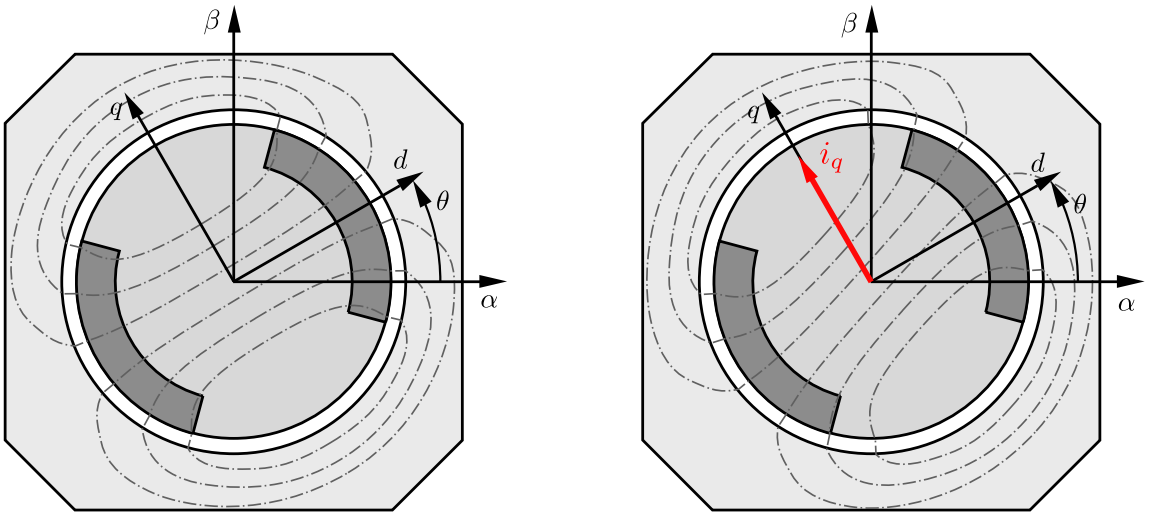

(a) Idle machine. (b) Loaded machine.

Figure 3.6: *Possible reasons for an inductance anisotropy.*

- **Geometry -** If the material in the rotor with high magnetic permeability inheres a rotatory asymmetry (see Fig. 3.6), the resulting flux paths with different reluctance can lead to a variation of the inductance of the stator windings. This geometrical

asymmetry is also referred to as saliency[6], and occurs in an IPMSM as a side effect (saliency ratio ≈20–30%), while in an RSM or PMARSM it is created intentionally for torque production (saliency ratio ≈50–80%).

- **Saturation -** Although SPMSMs are designed symmetrical, they still show a magnetic anisotropy of about 5–15% which, as indicated in Fig. 3.6(a), results from their strong permanent magnets saturating the stator iron. As under magnetic saturation a certain current causes less flux, the value of the inductance $L = d\Psi/di$ decreases. In PMSMs with geometrical saliency this saturation effect causes an additional drop of the d-axis inductance.

In practice, however, there are two neglects implied when assuming a rotor fixed anisotropy: Firstly, the influence of the current that contributes to the main field (see Fig. 3.6(b)) and hence to the saturation state of the machine. The result is a load-dependent steady deviation between the anisotropy orientation and the rotor angle [55]. Secondly, slotting effects, non-sinusoidally distributed windings or stator asymmetries cause harmonic deviations between the anisotropy orientation and the rotor angle [56]. We must therefore distinguish between

(1.) the identification of the anisotropy and

(2.) the assignment between anisotropy and rotor angle,

as they constitute two separate problems. Depending on the machine type and particular design, point (2.) may constitute a sophisticated challenge [57], but will not be focused in this thesis.

The anisotropy position information is contained in the relation between the inductive voltage and the time derivative of the current. The stator voltage is obtained precisely from the DC-link voltage and the pulse width. However, as the inductive voltage is only a part of the stator voltage, all other voltage components must firstly be eliminated. Moreover, the current derivative is not measured directly within a standard drive setup, but must be obtained from the difference between current samples from different time instants. The particular solution to those two challenges and the particular way to decrypt the anisotropy angle from the resulting quantities (inductive voltage and current derivative) is what distinguishes the anisotropy-based sensorless methods that have been proposed in literature.

[6]Although the term saliency originates from the geometrical shape of the rotor, it is often used in literature as a synonym for anisotropy.

Firstly, a pulse response technique has been proposed for the initial position detection at standstill in 1988 [58] which in later publications [14, 59–61] has been extended for low speed operation and referred to as Indirect Flux detection by online Reactance Measurement (INFORM). In this technique the field oriented current control is recurrently interrupted in order to apply three consecutive test pulses in the three phase directions. The resulting current responses are transformed and added in a particular way, such that a vector is yielded that represents the rotor position (with 180° modulo). The test pulse pattern is applied once per speed controller cycle, which if scheduled every 2ms results in a 500Hz acoustic noise. Since INFORM set the foundation of anisotropy-based sensorless control and does moreover work also with very simple current measurement (DC-link shunt), it is today the most well known anisotropy-based method and relatively wide spread in industry. However, according to [62], the estimation performance increases with the injection frequency, due to the ease of the filtering trade-off between bandwidth and SNR. An increase of the INFORM update rate, however, would affect the current controller through additional interruptions. Thus, the required estimation performance can only be gained by means of pulse magnitude, resulting in a relatively high acoustic noise emission.

Later, modulation-based techniques have been proposed which superimpose a continuous (mostly sinusoidal) signal on the field oriented control (FOC) voltage (without interrupting the controller) and demodulate the current response in order to extract the rotor position. Within the modulation-based techniques two branches can be distinguished: The first one is based on the injection of a rotating carrier voltage in stator frame (see Fig. 3.7(a)) and has firstly been proposed in [63]. The demodulation aims to find a counter injection wise rotating component in the current response, referred to as negative

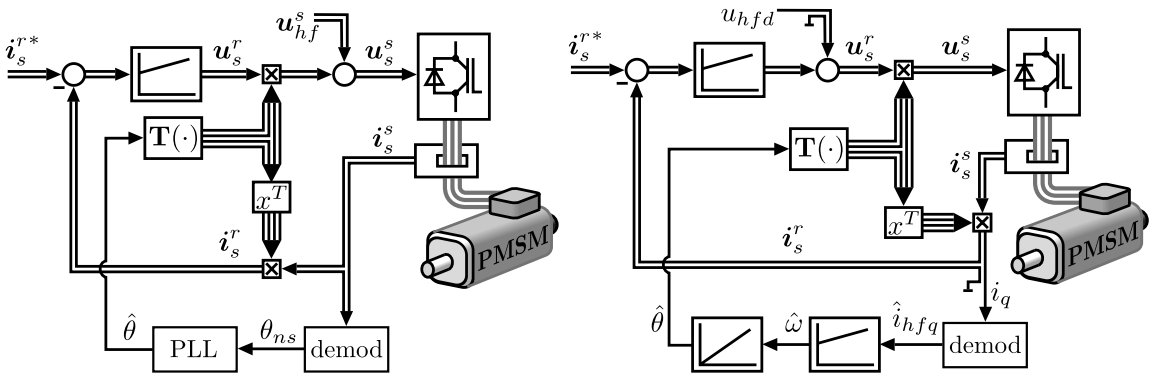

(a) Rotating Injection. (b) Alternating Injection.

Figure 3.7: *Modulation-based position estimation approaches.*

sequence component, the orientation of which reveals the rotor position (with 180° modulo). The second branch of modulation-based techniques is based on the injection of an alternating carrier voltage in estimated rotor frame and was first published in [38]. The demodulation aims to find a quadrature component (perpendicular to the injection) in the high frequency (HF) current response, being a measure for the misalignment between the estimated and the actual anisotropy reference frame. This quadrature component is consequently employed to correct the orientation of the estimated frame by creating a drive involving PLL structure (see Fig. 3.7(b)). However, in both branches a variety of demodulation techniques has been proposed, exhibiting different properties in terms of SNR, estimation bandwidth, robustness, stability and so forth. For instance within Alternating Injection the following (incomplete) list of demodulation techniques can be summarized:

- Sinusoidal injection with Fourier Analysis based demodulation [38, 64].
- Sinusoidal injection with band pass filter (BPF) and sign-multiplication based demodulation [65].
- Square wave injection with BPF and equation based demodulation [62].
- Square wave injection with matrix-based demodulation [66].
- Optimized pattern injection with matrix-based demodulation [50].

However, as a very general property, modulation-based techniques are reliant on the shape of the carrier signal they are defined for. Deviations from the expected injection shape affect the demodulation process and create artefacts in the position estimate. There are two main distortions to be noted: Firstly, the voltage limitation may clip the HF voltage component, if the voltage demanded by the FOC is too high. For this reason modulation-based methods are generally excluded from high speed. Secondly, modulation-based methods assume sufficient separation between the injected HF component and the actuation of the current controller, which requires a reduction of the current controller bandwidth and still leads to estimation error peaks during torque transients. Consequently, superordinate control cascades, as speed or position control, must also have a reduced bandwidth.

Recently, methods without a demand for a specific shape of injection have been proposed [16, 42, 67–71]. By considering the full machine model in their derivation, these methods can utilize any current derivative, regardless of its source, shape or frequency content, to deduce the anisotropy orientation (with 180° modulo). Hence, the FOC actuation voltage does not need to be filtered out, but it becomes a source of information as well. Moreover,

since these methods do not assume frequency separation, they work with high bandwidth current controllers and are insensitive to torque transients.

Around zero speed sufficiently much current ripple must be sustained by injecting a voltage signal. In contrast to modulation-based techniques, this injection signal can have various shapes without requiring an adaptation of the evaluation algorithm. However, a major restriction of all methods that aim to estimate the position through a direct resolution of the inductance matrix [42, 68–70] is that the underlying voltage vectors must be linearly independent (see Appx. C) – particularly the quality of the position estimate scales with the voltage direction difference. The consequent aim to maximize the angle between consecutive voltages and to avoid (anti-) parallel or steady excitation does not allow for an entirely arbitrary injection. For instance, the pure FOC voltage or an alternating injection shape could not be evaluated.

This restriction has been nearly overcome with [16, 71] as will be explained in the following section 3.2.1. After an injection based start-up these methods are able to utilize any voltage excitation, regardless of its linear dependence. Hence, these methods are referred to as *Arbitrary Injection* based and chosen for the evaluation of the oversampling data of this work.

3.2.1 Arbitrary Injection based anisotropy identification

This section explains the technical function of the anisotropy position estimation technique underlying this thesis. As the author contributed only partially to the development of this method, a respective explanation depth and placement within the thesis has been chosen.

One special aspect of Arbitrary Injection is that it is a model-based technique for anisotropy position estimation. The comparison of the measured machine behaviour with an isotropic machine model directly reveals the anisotropy information. The sophistication comes with the demand to have a parameter-free model in order to ensure accuracy and robustness under presence of saturation-, current-, voltage- and parameter-variation. The respective derivation in this section is a selection and rehashing of the information from [16] and [71] and starts with the consideration of the current time derivative in stator frame of a general synchronous machine (2.38). Hence, no assumption regarding linearity, saliency ratio or presence and strength of a permanent magnet is implied. Considering the sampling time of the digital control system T_s, (2.38) is rewritten in a discrete-time

form

$$\Delta \boldsymbol{i}_s^s = \mathbf{Y}_s^s \left(\boldsymbol{u}_s^s - R_s \boldsymbol{i}_s^s - \mathbf{J}\omega \boldsymbol{\psi}_s^s + \mathbf{L}_s^s \mathbf{J}\omega \boldsymbol{i}_s^s \right) \tag{3.11}$$

with $\mathbf{Y}_s^s$ being the admittance matrix in stator frame. According to Ch. 2.3.2, matrix $\mathbf{Y}_s^s$ is angle dependent and will, hence, be employed for the position estimation.

Regarding the frequency content of the terms, the current progression (3.11) is separated into two parts

$$\Delta \boldsymbol{i}_s^s = \mathbf{Y}_s^s \boldsymbol{u}_s^s - \mathbf{Y}_s^s \left(R_s \boldsymbol{i}_s^s + \mathbf{J}\omega \boldsymbol{\psi}_s^s - \mathbf{L}_s^s \mathbf{J}\omega \boldsymbol{i}_s^s \right), \tag{3.12}$$

where the right hand side only consists of parameters and state variables and is therefore relatively slowly changing over time. The left hand side, in contrast, might acquire a complete opposite value within one sampling cycle and is therefore relatively fast changing. Based on this consideration the component $\Delta \boldsymbol{i}_{FM}^s$ is introduced

$$\Delta \boldsymbol{i}_{s0}^s = \boldsymbol{i}_{s0}^s - \boldsymbol{i}_{s1}^s = \mathbf{Y}_s^s \boldsymbol{u}_{s1}^s - \Delta \boldsymbol{i}_{FM0}^s, \tag{3.13}$$

where now additionally the sampling cycle is denoted to which a quantity is assigned. In this notation the state values within the FM current progression $\Delta \boldsymbol{i}_{FM0}^s$ would, in a strict sense, have to be assigned to middle of the previous sampling period

$$\Delta \boldsymbol{i}_{FM0}^s = \mathbf{Y}_s^s \left(R_s \boldsymbol{i}_{s\frac{1}{2}}^s + \mathbf{J}\omega_{\frac{1}{2}} \boldsymbol{\psi}_{s\frac{1}{2}}^s - \mathbf{L}_s^s \mathbf{J}\omega_{\frac{1}{2}} \boldsymbol{i}_{s\frac{1}{2}}^s \right) \tag{3.14}$$

which, however, is unimportant as the following steps will show. In order to eliminate all unknown parameters and state variables contained in $\Delta \boldsymbol{i}_{FM}^s$, its slow change over time is employed to assume that it remains constant[7] over two sampling cycles

$$\Delta \boldsymbol{i}_{FM0}^s \approx \Delta \boldsymbol{i}_{FM1}^s. \tag{3.15}$$

Then, the difference between two current progressions $\Delta^2 \boldsymbol{i}_s^s$ becomes free of all resistive

[7] This assumption is sufficient for low rotor speed. When applying Arbitrary Injection for high speed as well, $\Delta \boldsymbol{i}_{FM}^s$ has to be considered linearly changing over time. The respective derivation is included in [16]. When utilizing current oversampling data, $\Delta \boldsymbol{i}_{FM}^s$ will be obtained in a different way.

or EMF related terms

$$\Delta^2 \boldsymbol{i}^s_{s0} = \Delta \boldsymbol{i}^s_{s0} - \Delta \boldsymbol{i}^s_{s1} \tag{3.16}$$

$$= (\mathbf{Y}^s_s \boldsymbol{u}^s_{s1} - \Delta \boldsymbol{i}^s_{FM0}) - (\mathbf{Y}^s_s \boldsymbol{u}^s_{s2} - \Delta \boldsymbol{i}^s_{FM1}) \tag{3.17}$$

$$\overset{(3.15)}{\approx} \mathbf{Y}^s_s \left(\boldsymbol{u}^s_{s1} - \boldsymbol{u}^s_{s2}\right) \tag{3.18}$$

$$= \mathbf{Y}^s_s(\theta_a)\ \Delta \boldsymbol{u}^s_{s1}. \tag{3.19}$$

Note that in (3.19) the angle dependent admittance matrix $\mathbf{Y}^s_s(\theta_a)$ is directly connecting a voltage with a current difference. This eases the admittance estimation problem, as both the applied voltage and the current difference are known.

Using the anisotropy angle θ_a, the angle dependence of the admittance shows the simple form of (2.53)

$$\mathbf{Y}^s_s(\theta_a) = Y_\Sigma\ \mathbf{I} + Y_\Delta\ \mathbf{S}(\theta_a) \tag{3.20}$$

$$= \begin{bmatrix} Y_\Sigma + Y_\Delta \cos 2\theta_a & Y_\Delta \sin 2\theta_a \\ Y_\Delta \sin 2\theta_a & Y_\Sigma - Y_\Delta \cos 2\theta_a \end{bmatrix}. \tag{3.21}$$

According to (3.21), the 4 entries of $\mathbf{Y}^s_s$ comprise 3 unknowns, Y_Σ, Y_Δ and θ_a. Thus, if one parameter Y_Σ or Y_Δ was known, the angle θ_a could be determined from a single (two dimensional) voltage-current-relation as in (3.19). Hence, in contrast to [42, 68–70] (see Appx. C) even linearly dependent consecutive voltages could be employed. The Arbitrary Injection scheme proposed in [16, 71] decouples the estimation of Y_Σ from the angle estimation. Only for updating Y_Σ linearly independent voltage vectors are required, which technically is only necessary in certain conditions.

By combining Eq. (3.19) and (3.20), Arbitrary Injection considers the EMF free current progression $\Delta^2 \boldsymbol{i}^s_s$ to consist of an isotropic and a rotating component

$$\Delta^2 \boldsymbol{i}^s_s = Y_\Sigma \Delta \boldsymbol{u}^s_s + Y_\Delta \mathbf{S}(\theta_a) \Delta \boldsymbol{u}^s_s, \tag{3.22}$$

where the sampling cycle assignment stays the same, but is not noted anymore. In order to segregate the rotating component, the isotropic component must be eliminated, which is done by the key idea of Arbitrary Injection: An isotropic prediction of the current

progression $\hat{Y}_\Sigma \boldsymbol{u}_s^s$ is subtracted from the measured current progression $\Delta^2 \boldsymbol{i}_s^s$

$$\boldsymbol{e}_{prd}^s = \Delta^2 \boldsymbol{i}_s^s - \hat{Y}_\Sigma \Delta \boldsymbol{u}_s^s \tag{3.23}$$

$$\overset{\hat{Y}_\Sigma \approx Y_\Sigma}{\approx} Y_\Delta \mathbf{S}(\theta_a) \Delta \boldsymbol{u}_s^s, \tag{3.24}$$

which is referred to as the *prediction error*. In case the mean admittance Y_Σ is sufficiently well represented by $\hat{Y}_\Sigma$, the prediction error $\boldsymbol{e}_{prd}^s$ forms a rotating vector, the orientation of which depends on (twice) the ansiotropy angle. The vector components of (3.24)

$$e_\alpha = Y_\Delta u_\alpha \cos 2\theta_a + Y_\Delta u_\beta \sin 2\theta_a \tag{3.25}$$

$$e_\beta = Y_\Delta u_\alpha \sin 2\theta_a - Y_\Delta u_\beta \cos 2\theta_a \tag{3.26}$$

constitute two equations with two unknowns Y_Δ and θ_a which can simply be solved for the anisotropy angle θ_a. The result is the direct anisotropy angle estimation equation of Arbitrary Injection

$$\hat{\theta}_a = \frac{1}{2} \mathrm{atan2}(u_\alpha e_\beta + u_\beta e_\alpha,\ u_\alpha e_\alpha - u_\beta e_\beta) \tag{3.27}$$

where the function $\mathrm{atan2}(y, x)$ calculates the angle of a vector $[x\ y]^\top$ within the range $-\pi \ldots \pi$. The vector composed by the arguments of (3.27) evolves on a circular trajectory (for negligible anisotropy harmonics) when the rotor moves. As voltage and prediction error are proportional (3.24), this circle would scale with the squared voltage, which is irrelevant for the evaluation of its angle by (3.27). However, while the noise in the prediction error $\boldsymbol{e}_{prd}^s$, imposed by the current measurement, is nearly constant, the noise in this circle would be scaled by the voltage. Hence, for later SNR considerations in Ch. 6.1 and 7.1 it is reasonable to define a circular moving vector $\Delta \boldsymbol{i}_a^s$ that contains a voltage independent noise

$$\Delta \boldsymbol{i}_a^s = \frac{1}{|\boldsymbol{u}_s^s|} \begin{bmatrix} u_\alpha e_\alpha - u_\beta e_\beta \\ u_\alpha e_\beta + u_\beta e_\alpha \end{bmatrix} \tag{3.28}$$

$$|\Delta \boldsymbol{i}_a^s| = \left|\Delta \boldsymbol{e}_{prd}^s\right| = Y_\Delta \left|\Delta \boldsymbol{u}_s^s\right|, \tag{3.29}$$

and consequently has the physical unit [A]. This vector will be referred to as anisotropic current progression.

A summary of the key steps of Arbitrary Injection is given by:

(1.) Eliminate the resistive and EMF related components in the current progression by

employing the difference between current progressions $\Delta^2 \boldsymbol{i}_s^s$ (3.19).

(2.) Subtract the isotropic current progression $\hat{Y}_\Sigma \boldsymbol{u}_s^s$ from $\Delta^2 \boldsymbol{i}_s^s$ in order to obtain a component rotating with twice the anisotropy angle.

(3.) Use Eq. (3.27) to directly calculate the anisotropy angle from this rotating component.

However, within this derivation we assumed in (3.23) that a sufficiently accurate estimate of the mean admittance $\hat{Y}_\Sigma$ is available, which still has to be obtained.

3.2.2 Mean admittance estimation

The above described angle estimation technique premises the knowledge of only one machine parameter, required for the elimination of the isotropic component of the current response in (3.23): the mean admittance

$$Y_\Sigma = \frac{1}{2}\left(\frac{1}{L_{dd}} + \frac{1}{L_{qq}}\right) T_s. \tag{3.30}$$

According to (2.46) and [72], Y_Σ could be deduced from the average parallel component of the current response to multiple equally long voltages vectors that are equidistantly distributed within (a modulus of) 180 electrical degrees. Several injection forms, like rotating or triangular injection, do fulfil this condition – in steady state. However, in order to allow for transient operation and for the general interference of a high bandwidth current controller, a more sophisticated approach is required that can obtain the mean admittance from an arbitrary combination of voltage vectors.

As a reflection of [71], in this section a mean admittance estimation technique is derived that is capable of working with arbitrary voltage excitation. Therefore firstly the anisotropic voltage-current relation is reconsidered from a certain perspective. Upon this groundwork, a geometrical approach is derived that is finally extended with machine background information in order to improve the performance of the technique.

3.2.2.1 Anisotropic voltage-current relation

The following consideration is based on the voltage frame, a Cartesian reference frame in which the x-axis is aligned with the previously applied voltage vector (see Fig. 2.1 in Ch. 2.1.4). In voltage frame the anisotropic current response $\Delta^2 \boldsymbol{i}_s^u$ (to a fixed voltage time expanse) is located on a circle. As shown in Fig. 3.8 the centre of this circle is specified

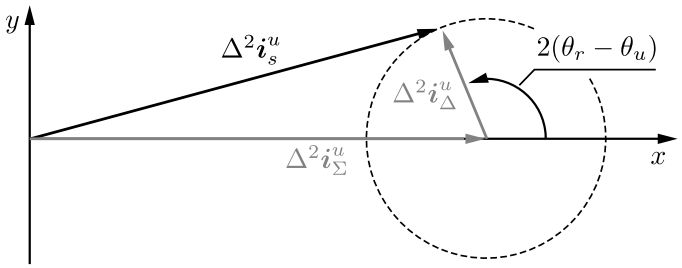

Figure 3.8: *Anisotropic current response in voltage frame.*

by the isotropic current response $\Delta^2 \boldsymbol{i}_\Sigma^u$ which is parallel to the applied voltage

$$\Delta^2 \boldsymbol{i}_\Sigma^u = Y_\Sigma \Delta \boldsymbol{u}_s^u. \tag{3.31}$$

The magnitude of the rotating component $\Delta^2 \boldsymbol{i}_\Delta^u$ scales with the saliency magnitude Y_Δ defined by (2.47) to (2.49). The direction of $\Delta^2 \boldsymbol{i}_\Delta^u$ is determined by twice the angle difference between anisotropy and voltage

$$\Delta^2 \boldsymbol{i}_\Delta^u = Y_\Delta \mathbf{S}(\theta_a - \theta_u) \Delta \boldsymbol{u}_s^u, \tag{3.32}$$

with $\mathbf{S}(\cdot)$ being the saliency matrix according to (2.50). Hence, the total anisotropic current response $\Delta^2 \boldsymbol{i}_s^u$ is the sum of both $\Delta^2 \boldsymbol{i}_\Sigma^u$ and $\Delta^2 \boldsymbol{i}_\Delta^u$

$$\Delta^2 \boldsymbol{i}_s^u = \left(Y_\Sigma \mathbf{I} + Y_\Delta \mathbf{S}(\theta_a - \theta_u)\right) \Delta \boldsymbol{u}_s^u. \tag{3.33}$$

3.2.2.2 Geometrical approach

When dividing the current progression in voltage frame $\Delta^2 \boldsymbol{i}_s^u$ by the magnitude of the respective voltage vector $|\Delta \boldsymbol{u}_s^s|$ we obtain the so-called admittance vector in voltage frame

$$\boldsymbol{\gamma}^u = \frac{\Delta^2 \boldsymbol{i}_{HF}^u}{|\Delta \boldsymbol{u}_s^s|}. \tag{3.34}$$

In a strict sense, $\boldsymbol{\gamma}^u$ is not an admittance, but a scaled current progression in voltage frame. However, $\boldsymbol{\gamma}^u$ is an important quantity because, independent of the applied voltage, this vector will always point at the edge of the circle in Fig. 3.9, the centre of which is located at $(Y_\Sigma, 0)$ – the mean admittance.

Using scalar and vector product related operations, this voltage frame vector $\boldsymbol{\gamma}^u$ is

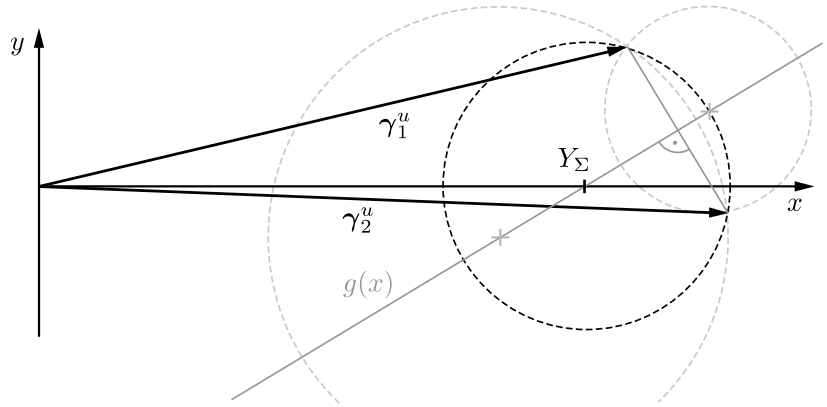

Figure 3.9: *Identification of the mean admittance Y_Σ with a geometrical approach.*

obtained from measured stator frame quantities

$$\boldsymbol{\gamma}^u = \begin{bmatrix} \gamma_x \\ \gamma_y \end{bmatrix}, \quad \gamma_x = \frac{\Delta^2 \boldsymbol{i}_s^{s\top} \Delta \boldsymbol{u}_s^s}{\Delta \boldsymbol{u}_s^{s\top} \Delta \boldsymbol{u}_s^s}, \quad \gamma_y = \frac{\Delta^2 \boldsymbol{i}_s^{s\top} \mathbf{J} \Delta \boldsymbol{u}_s^s}{\Delta \boldsymbol{u}_s^{s\top} \Delta \boldsymbol{u}_s^s}. \tag{3.35}$$

After two arbitrary voltages $\Delta \boldsymbol{u}_1^s$ and $\Delta \boldsymbol{u}_2^s$ (generated by FOC and/or injection) have been applied and the resulting current progressions $\Delta^2 \boldsymbol{i}_1^s$ and $\Delta^2 \boldsymbol{i}_2^s$ have been measured, two admittance vectors $\boldsymbol{\gamma}_1^u$ and $\boldsymbol{\gamma}_2^u$ are obtained through (3.35) which already comprise enough information to compute the value of the mean admittance:

Considering the fact that both vectors $\boldsymbol{\gamma}_1^u$ and $\boldsymbol{\gamma}_2^u$ must point to the edge of an unknown circle, there is an infinite amount of circles which would match this description, exemplified by the dashed circles in Fig. 3.9. However, since all points on the edge of a circle must have the same distance to its centre, the centre of all possible circles must be located on the straight $g(x)$ in Fig. 3.9. The respective straight equation is given by

$$g(x) = \frac{\gamma_{1x} - \gamma_{2x}}{\gamma_{2y} - \gamma_{1y}} \cdot \left(x - \frac{\gamma_{1x} + \gamma_{2x}}{2} \right) + \frac{\gamma_{2y} + \gamma_{1y}}{2}. \tag{3.36}$$

Within this infinite amount of circles there is only one with the y-component of its centre being equal to zero (Y_Σ describes the isotropic part of the current progression). Y_Σ is consequently found as the root of the straight $g(x)$

$$g(Y_\Sigma) = 0 \tag{3.37}$$

$$\hat{Y}_\Sigma = \frac{\gamma_{1y}^2 - \gamma_{2y}^2 + \gamma_{1x}^2 - \gamma_{2x}^2}{2(\gamma_{1x} - \gamma_{2x})}. \tag{3.38}$$

The result (3.38) is an explicit law for calculating the extended mean admittance Y_Σ from

the current response after applying two arbitrary voltages. Considering the denominator, however, it is clear that this approach will be sensitive to current measurement noise for cases in which the tips of the vectors $\boldsymbol{\gamma}_1^u$ and $\boldsymbol{\gamma}_2^u$ are vertical above one another. In these cases one would calculate the root of an almost horizontal straight $g(x)$. The simulation result in Fig. (3.10), including current sampling noise, shows that most of the connecting

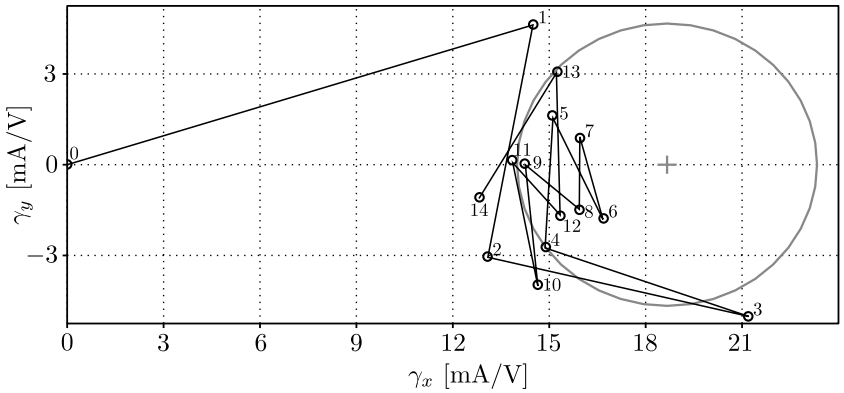

Figure 3.10: *Admittance vector $\boldsymbol{\gamma}_1^u$ calculation for 15 simulation steps.*

lines between two consecutive admittance vectors can happen to be rather vertical. For most of these points the straight $g(x)$ would be rather horizontal and consequently its root would be very sensitive to current sampling noise.

3.2.2.3 Extension with machine background information

By extending the geometrical approach with physical background information the sensitivity to current measurement noise can be reduced. According to Fig. 3.8, the orientation of the radial current response $\Delta^2\boldsymbol{i}_\Delta^u$ is defined by twice the angle difference between anisotropy and voltage $2(\theta_a - \theta_u)$. Hence, when applying two consecutive voltages $\Delta\boldsymbol{u}_1^s$ and $\Delta\boldsymbol{u}_2^s$ without a change in anisotropy position, the angle between both radial responses, $\Delta^2\boldsymbol{i}_{\Delta1}^u$ and $\Delta^2\boldsymbol{i}_{\Delta2}^u$, must be $2\Delta\theta_u$

$$2(\theta_a - \theta_{u1}) - 2(\theta_a - \theta_{u2}) = 2(\theta_{u2} - \theta_{u1}) = 2\Delta\theta_u. \tag{3.39}$$

As indicated in Fig. 3.11, the angle between the straight $g(x)$ and one radial component will therefore be equal to $\Delta\theta_u$, i.e. to the angle between the voltages $\Delta\boldsymbol{u}_1^s$ and $\Delta\boldsymbol{u}_2^s$ in stator frame. This defines the location of Y_Σ on the straight $g(x)$ just depending on the voltage angles (i.e. the pulse width references), i.e. independent of current measurement noise. Especially in the horizontal case this will markedly reduce the noise in the mean admittance information.

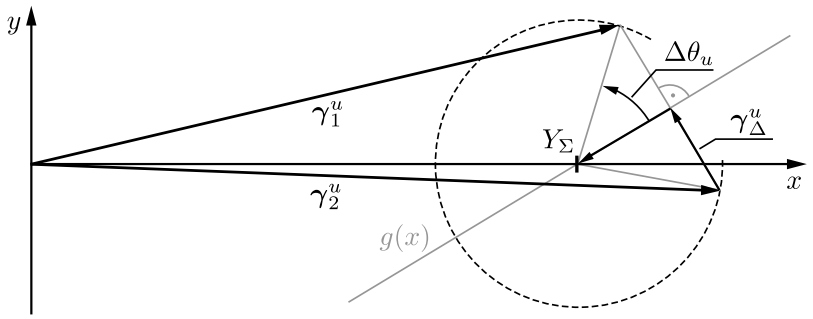

Figure 3.11: *Identification of mean admittance with machine background information.*

For the respective mathematical description, in a first step two elementary vectors $\boldsymbol{\gamma}_\Sigma^u$ and $\boldsymbol{\gamma}_\Delta^u$ are defined which represent the average of and the distance between the measured vectors $\boldsymbol{\gamma}_1^u$ and $\boldsymbol{\gamma}_2^u$

$$\boldsymbol{\gamma}_\Sigma^u = \frac{\boldsymbol{\gamma}_1^u + \boldsymbol{\gamma}_2^u}{2}, \qquad \boldsymbol{\gamma}_\Delta^u = \frac{\boldsymbol{\gamma}_1^u - \boldsymbol{\gamma}_2^u}{2}. \tag{3.40}$$

The average vector $\boldsymbol{\gamma}_\Sigma^u$ points at the middle between $\boldsymbol{\gamma}_1^u$ and $\boldsymbol{\gamma}_2^u$. Starting from this point, the circle centre is located in a direction perpendicular to the distance vector $\boldsymbol{\gamma}_\Delta^u$

$$\begin{bmatrix} \hat{Y}_\Sigma \\ 0 \end{bmatrix} - \boldsymbol{\gamma}_\Sigma^u = \lambda \, \mathbf{J} \frac{\boldsymbol{\gamma}_\Delta^u}{|\boldsymbol{\gamma}_\Delta^u|}, \tag{3.41}$$

where λ represents the distance between $\boldsymbol{\gamma}_\Sigma^u$ and the circle centre that is now gained through the machine background information. According to the relations in a right-angled triangle, this distance λ is represented by the length of the adjacent leg and $|\boldsymbol{\gamma}_\Delta^u|$ by the length of the opposite leg with respect to the angle $\Delta\theta_u$. Hence, λ can be rewritten by

$$\lambda = \tan(\Delta\theta_u) \, |\boldsymbol{\gamma}_\Delta^u| = \frac{\cos\Delta\theta_u}{\sin\Delta\theta_u} |\boldsymbol{\gamma}_\Delta^u|, \tag{3.42}$$

where the sine and cosine functions of the angle between the voltage vectors $\Delta\boldsymbol{u}_1^s$ and $\Delta\boldsymbol{u}_2^s$ can be obtained from scalar and vector product related operations

$$\cos\Delta\theta_u = \frac{\Delta\boldsymbol{u}_1^{s\top} \Delta\boldsymbol{u}_2^s}{|\Delta\boldsymbol{u}_1^s||\Delta\boldsymbol{u}_2^s|} \tag{3.43}$$

$$\sin\Delta\theta_u = \frac{\Delta\boldsymbol{u}_1^{s\top} \mathbf{J} \Delta\boldsymbol{u}_2^s}{|\Delta\boldsymbol{u}_1^s||\Delta\boldsymbol{u}_2^s|}. \tag{3.44}$$

Finally, by combining (3.42) to (3.44) the vectorial mean admittance estimation equation

is obtained

$$\begin{bmatrix} \hat{Y}_{\Sigma x} \\ \hat{Y}_{\Sigma y} \end{bmatrix} = \frac{\boldsymbol{\gamma}_1^u + \boldsymbol{\gamma}_2^u}{2} + \frac{\boldsymbol{u}_1^{s\top} \boldsymbol{u}_2^s}{\boldsymbol{u}_1^{s\top} \mathbf{J} \boldsymbol{u}_2^s} \mathbf{J} \frac{\boldsymbol{\gamma}_1^u - \boldsymbol{\gamma}_2^u}{2}, \tag{3.45}$$

in which, supposedly, the y-component should be zero $\hat{Y}_{\Sigma y} = 0$. As will be shown in Ch. 6.1, however, certain parasitic effects emerging at low injection magnitudes result in a vertical shift of the circle in Fig. 3.8 that is important to track in the mean admittance estimation.

When using standard synchronous current sampling (SCS) and hence usual injection magnitudes the circle centre is located nearly on the x-axis, such that only the x-component of (3.45) needs to be evaluated

$$\hat{Y}_{\Sigma} = \hat{Y}_{\Sigma x} = \frac{\gamma_{1x} + \gamma_{2x}}{2} + \frac{\boldsymbol{u}_1^{s\top} \boldsymbol{u}_2^s}{\boldsymbol{u}_1^{s\top} \mathbf{J} \boldsymbol{u}_2^s} \frac{\gamma_{1y} - \gamma_{2y}}{2}. \tag{3.46}$$

The noise sensitivity of the equations (3.45) and (3.46) depends on the vector product between the voltages $\boldsymbol{u}_1^{s\top} \mathbf{J} \boldsymbol{u}_2^s$, which from physical perspective is inevitable, since an angle difference between the voltages is the source of information. When finally low pass filtering the estimates $\hat{Y}_{\Sigma}$, or $\hat{Y}_{\Sigma x}$ and $\hat{Y}_{\Sigma y}$ in order to reduce noise, it is therefore reasonable to weight the low pass filter time constant with this vector product

$$\frac{\mathrm{d}}{\mathrm{d}t} \hat{Y}_{\Sigma,lpf} = k_{\Sigma} \boldsymbol{u}_1^{s\top} \mathbf{J} \boldsymbol{u}_2^s \left(\hat{Y}_{\Sigma} - \hat{Y}_{\Sigma,lpf} \right), \tag{3.47}$$

where the tuning parameter k_{Σ} influences the resulting overall bandwidth of $\hat{Y}_{\Sigma,lpf}$.

For some methods proposed in this work, an online estimation of the saliency magnitude Y_{Δ} is essential to achieve sufficient accuracy without preliminary knowledge of machine parameters. This value Y_{Δ} is simply the distance between each measured admittance vectors γ^u and the filtered mean admittance value $\hat{Y}_{\Sigma,lpf}$, which for noise reasons should also be low pass filtered

$$\frac{\mathrm{d}}{\mathrm{d}t} \hat{Y}_{\Delta,lpf} = k_{\Delta} \left(\sqrt{\left(\gamma_{1x} - \hat{Y}_{\Sigma x,lpf} \right)^2 + \left(\gamma_{1y} - \hat{Y}_{\Sigma y,lpf} \right)^2} - \hat{Y}_{\Delta,lpf} \right). \tag{3.48}$$

The tuning factor k_{Δ} allows the adjustment of the filter bandwidth.

Chapter 4

Current oversampling

In contrast to grid-connected machines, the current waveform in inverter driven AC machines is not sinusoidal, but consists of various frequencies. The pulse pattern, imposed by the discrete voltage states of the inverter, generates components with multiples of its repetition frequency. Since these frequencies exceed the current control cycle frequency, it is important to consider the Aliasing problem when sampling the current.

For most drive control techniques in literature the average current over one control cycle is relevant, since only this average value can directly be actuated through the pulse width and since this value corresponds to the generated shaft torque. Hence, the measured current value should ideally represent the average current over one control cycle. However, as averaging-based measurements [73, 74] are relatively complex and cost extensive, a technique referred to as synchronous current sampling (SCS) has been established in drive systems.

As indicated in Fig. 4.1, SCS is generally employed in combination with a symmetrical PWM structure [75], generated by a triangular PWM counter. The current sampling is

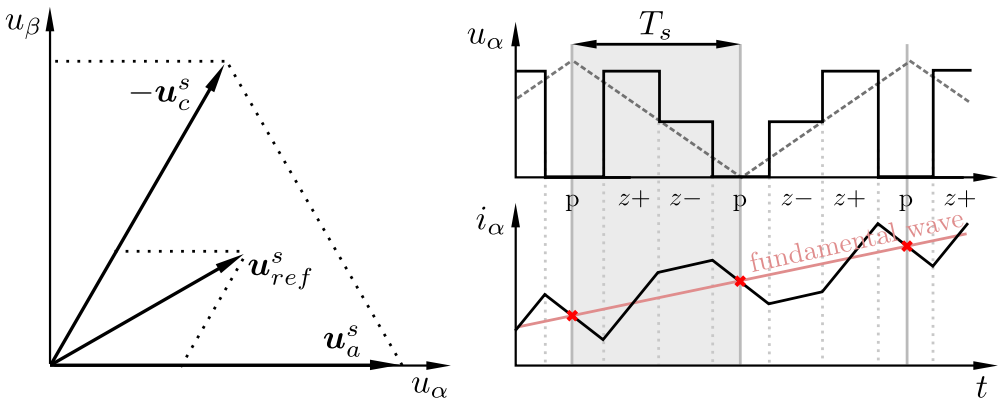

Figure 4.1: *PWM voltage synthesis and ideal current response.*

then triggered with the direction change of the counter, which is consequently located in the middle of each passive switching state (PSS). As indicated by the red crosses in Fig. 4.1, the current does at these instants match the average value over one control cycle – i.e. the fundamental wave without PWM-induced harmonics. The assumption implied in this conclusion is that the current evolves linearly during constant voltage phases. In literature, this assumption is considered to hold if only the sampling period is much shorter than the electrical time constant of the machine $T_s \ll L_s/R_s$ [6], such that only a small fraction of the normally exponential current response of an RL-load passed.

Exceeding the purposes of conventional drive control, sensorless control aims to gain additional information out of the current response that can be employed to deduce the rotor position without using a position sensor. Considering that the employed A/D converters are often able to sample at higher frequencies than given by the switching frequency limitation (and hence the control cycle), SCS neglects information that could be useful for the position estimation.

Instead of sampling only once per PWM half-period at a specific time, in this work the analogue to digital converter (ADC) is operated with a much higher frequency. The increased amount of data must be collected and pre-processed, such that its evaluation by a sensorless algorithm working at control frequency is possible.

In particular, we utilize the above assumption that during constant voltage phases a linear voltage evolution can be found – a constant slope that, according to (2.38), is described inter alia by the EMF and the anisotropy orientation. This supposedly linear evolution will be approximated by a straight, resulting in one slope and one offset value for each switching state. These low noise straight coefficients comprise both the anisotropy and the EMF information and do hence form the basis for the later sensorless evaluation.

In order to allow for the experimental investigation of this approach, a specific hardware setup has been designed and manufactured which will be described in the following section. The remaining parts of this chapter will provide an in-depth analysis of the current data obtained with this setup, in order to validate the above assumptions and to pre-asses potential sources of errors.

4.1 Test bench hardware setup

The test bench setup designed for this work employs an industrial 7.5 kW inverter (SEW MDS60A0075), modified in order to impose the IGBT switching signals. However, when providing a PWM signal, the 8 kHz switching frequency restriction must be respected.

The internal 3 phase diode bridge of the inverter rectifies the three phase low voltage grid into a 560 V DC-link voltage. Depending on the load, this voltage may decrease during motoring condition momentarily down to 484 V and increase during generating condition up to 800 V where the break chopper interferes. Due to this large possible variation, a DC-link voltage measurement is received from the inverter and considered in the control algorithms. Through standardized plugs the connected machine can quickly be replaced by another one, allowing for the development and investigation of generic control methods. The four machines used for the validation of the theory derived in this work are described in Tab. B.1 in Appx. B.

However, as indicated in Fig. 4.2, the speciality of the test bench setup is the self developed real time system (RTS) that provides a fast current measurement, while facilitating quick and easy prototyping of control algorithms. The core part is the field programmable

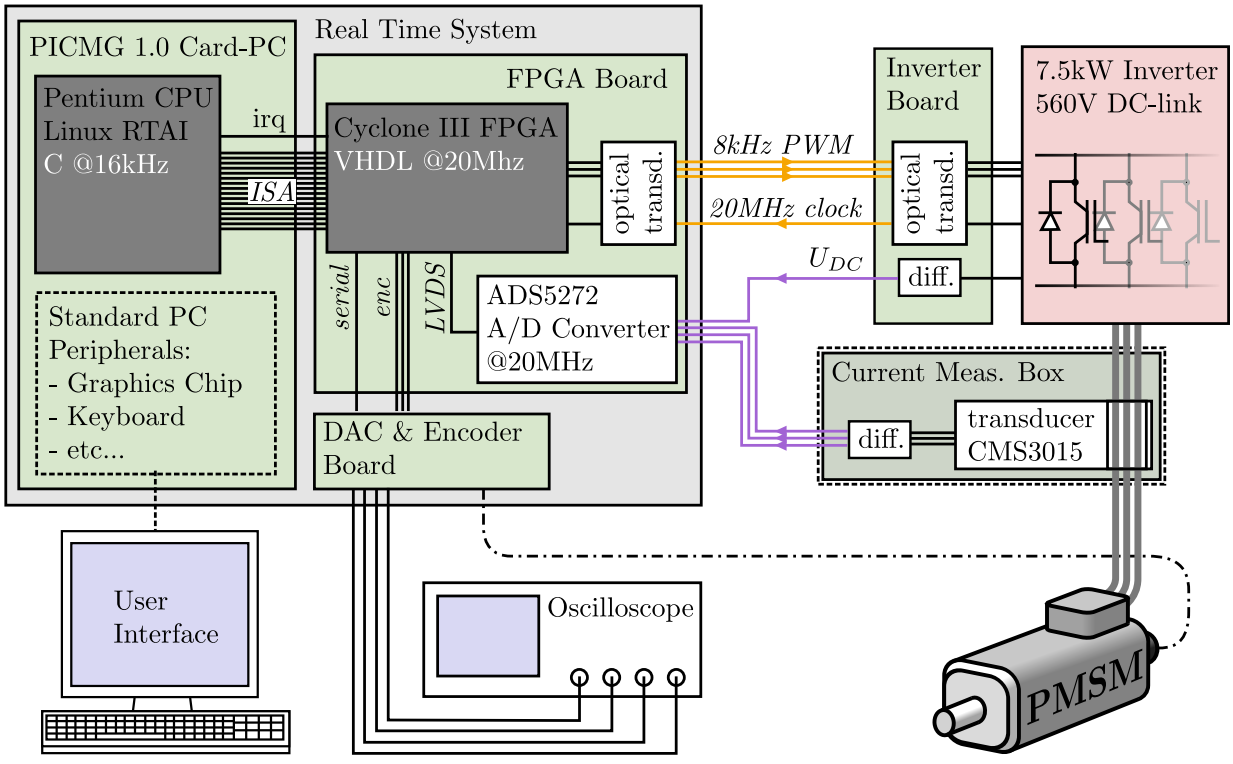

Figure 4.2: *Hardware setup underlying this thesis.*

gate array (FPGA)-Board which, among other components, houses a Cyclone III FPGA from Altera and a very fast 12 bit ADC from Analog Devices. Although both components could operate faster, they are triggered by the general board clock with 20 MHz which corresponds to 1250 current samples per 16 kHz control cycle (resulting from the switching frequency limitation). The 20 MHz clock, however, is provided by the inverters logical circuit, which pre-processes the commanded switching signals for safety reasons. Using

this unified 20 MHz clock, the FPGA generates the PWM with 8 kHz and the control interrupt (irq) with 16 kHz, such that all tasks in all discrete-time components of the test bench are executed synchronously and any jitter is avoided.

The FPGA, as the central component, executes a variety of tasks. Apart from the communication and data exchange with all peripheral components and the PWM- and control interrupt generation, this does (most importantly for this work) comprise the recursive linear regression (RLR) algorithm, described in section 5.2. Only in this way the extensive amount of oversampled current data could be processed and summarized into a few coefficients per control cycle which are manageable by the central processing unit (CPU). In the respective moment during the control process, the CPU requests these coefficients from the FPGA which will then provide these values via the ISA bus.

The 3 GHz ©Pentium CPU, as part of an entire personal computer (PC) on a slot card (PICMG 1.0), runs a mastering real time operating system that in its idle time allows a Linux operating system to execute its tasks. In this way both, the code development and code execution are done on the same hardware, while the execution has absolute priority.

Apart from the CPU, the FPGA boards communicates to 3 main peripheral boards:

(1.) A digital to analogue converter (DAC) & Encoder board is located within the RTS housing. The DAC data is transmitted to this board via a serial communication. The increment and index signals of the encoder are directly fed through (including potential insulation) and evaluated by the FPGA. The main purpose of the DAC is the visualization of physical and algorithmic quantities on an oscilloscope.

(2.) The inverter board is located directly at the inverter. It receives the IGBT switching signals and sends the 20 MHz clock both in optical form (orange colour in Fig. 4.2) in order to avoid electro magnetic interference (EMI). Especially momentary misinterpretations of a switching signal can markedly increase the switching frequency and thereby overload and destroy an IGBT. Furthermore, the DC-link voltage measurement, provided by the inverter, is converted to an analogue differential signal (purple colour in Fig. 4.2) in order to minimize the EMI during the (potentially long distance) transmission to the RTS. In this way the differential analog inputs of the ADC are utilized.

(3.) The current measurement box is a relatively important component of the test bench and has been redesigned in 3 iterations, using different current transducer types. Finally, the sensors CMS3015 from ©SENSiTEC have been selected, since these showed the most veridical output signal in an empirical comparison, compared to a

high bandwidth current measurement probe of an Oscilloscope. In contrast to the widespread Hall-compensation based current transduction principle, these transducers utilize a magneto-resistive principle which has just recently been realized in commercial current sensors for drive systems. Although their long-term behaviour is not entirely approved yet, these magneto-resistive sensors provide a higher quality signal than compensation-based transducers with a significantly higher bandwidth and less artefacts. Both points influence on the ability to evaluate the oversampling data. Generally, the attentive selection of an appropriate current sensor is a highly important part of the hardware design for high performance sensorless control, as will be concluded in Ch. 5.4.4. For the purpose of EMI minimization the current measurement box is shielded and the analogue output voltage is provided in differential form as well.

All in all this hardware setup shown in Fig. 4.3 that has been developed to investigate the potential of oversampling-based sensorless control, combines a very fast and high

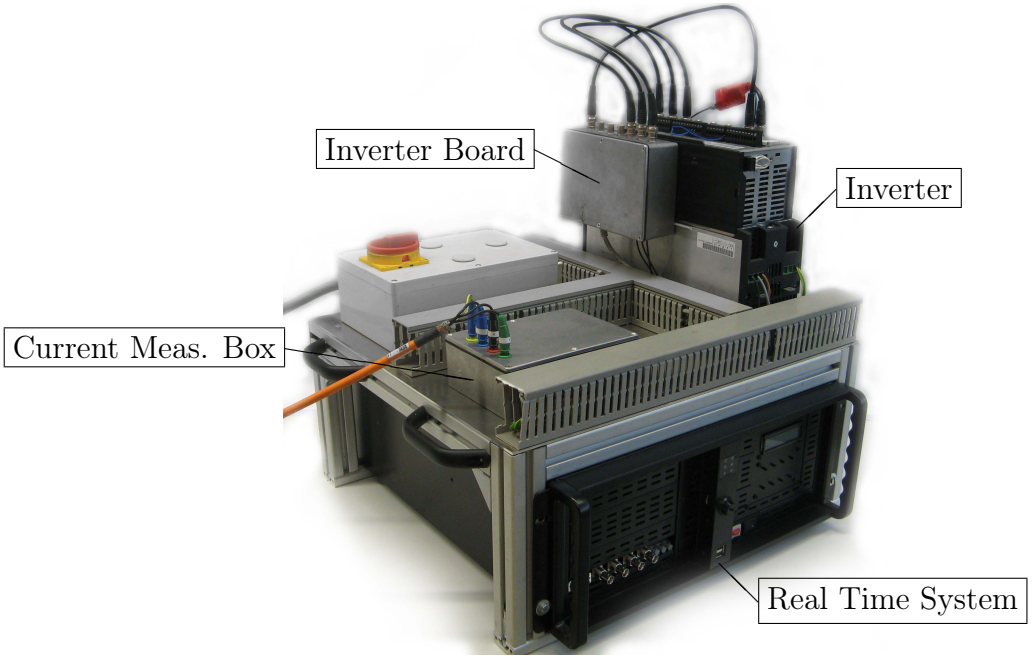

Figure 4.3: *Photo of the hardware setup underlying this thesis.*

quality current measurement and the individually programmable low-level pre-processing capabilities of an FPGA with the high computation power, the easy high-level C-code development and the convenient live data indication and logging facilities of the Linux-RTAI based PC. Although, for an RTS, the overall system cost is relatively cheap, the components involved are too expensive for industrial serial production. This dimensioning

has, however, been motivated by the thought that the purpose of this academic system is to asses the potential and the limits of an approach itself, instead of of the hardware.

4.2 Analysis of the oversampled current response

Using the above described hardware, all three phase currents are measured 20 million times per second, such that 1250 12 bit current samples per PWM half-period for each phase current are available for the control algorithms. Since this amount of data can neither be communicated to nor be processed by the CPU, it is summarized within the FPGA (see Ch. 5.2) and only a few resulting coefficients are subsequently transmitted to the CPU. Hence, all graphs within this work that directly show oversampled current data have been captured in and transmitted from the FPGA using the JTAG protocol.

Following the common assumptions in drive control that for instance also form the basis of synchronous current sampling (SCS), the current should evolve linearly during the application time of a switching state (see Fig. 4.1). Then, the oversampled current data can be approximated adequately by a straight, the slope of which contains information about the inductance and the EMF, and hence about the rotor position. However, the measured current oversampling data, shown in Fig. 4.4, reveals a notably more complex drive behaviour than described by the conventional machine equations. In the following section the major additional effects are analysed in order to scrutinize whether the above simplification can still be employed for a sensorless approach and whether adaptations are necessary.

4.2.1 Dead time

Fig. 4.4 shows the switching state command and the resulting α-axis current measured over one cycle of the triangular injection with 12% magnitude. There is an evident dead time between the command of a switching state and the first response in the current signal which is the result of several delays in the signal path. The major part is caused by the fixed IGBT interlock time, inherently programmed in the industrial inverter. Other delays like the gate recharging or the current path changing[1] time depend on the sign and the magnitude of the current in the switching IGBT and do therefore cause a variation of the overall delay. The resulting distribution of the total dead time is indicated in Fig. 4.5 which was obtained from more than 100,000 switching transitions. The machine has

[1]The switching of an IGBT forces the current to take a different path within one inverter half bridge, which due to parasitic inductances requires time.

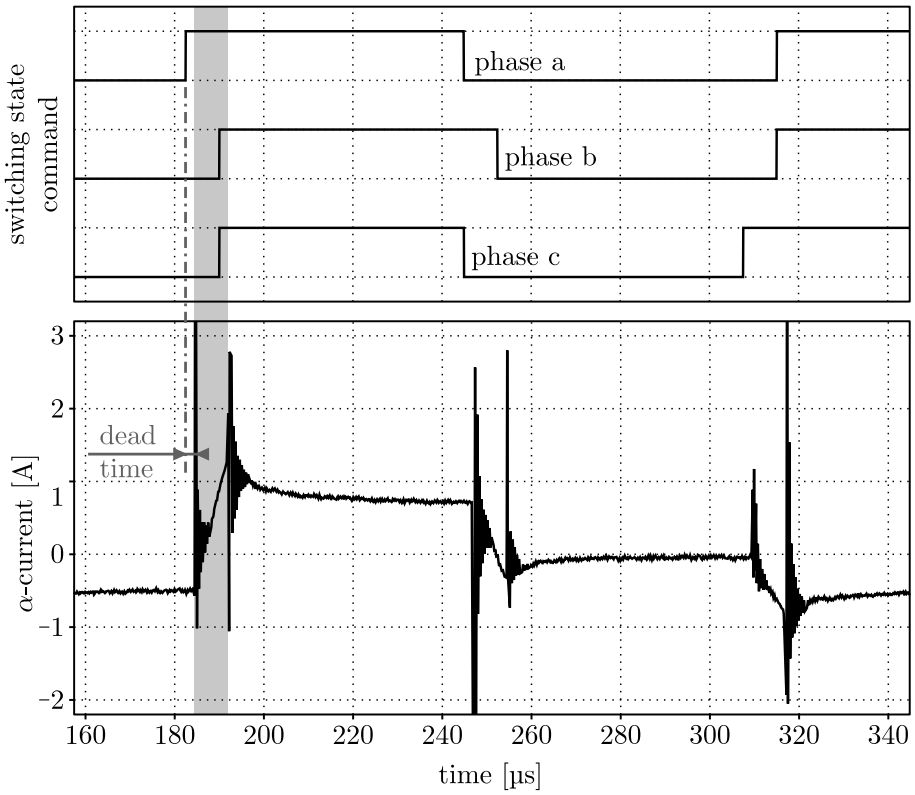

Figure 4.4: *Current response at 12% injection over one injection cycle.*

been load free while applying injection with 0.1% to 10% magnitude. Since the current value during the switching transitions increases with the injection magnitude, this analysis already includes a medium scale current variation (up to 20% rated current), which allows to deduce that the width of the distribution will remain within the scale of Fig. 4.5. All in all, this investigation is concluded to the dead time occurring with an average of 39 samples (1.95 µs) and a variation of ±1 sample (±0.05 µs).

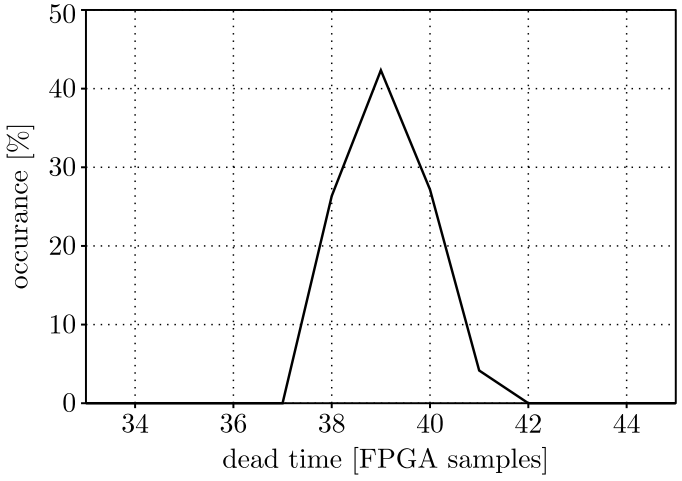

Figure 4.5: *Dead time occurrence distribution at idle machine.*

Thus, when deducing the location of the regression window (time range in which the current signal is analysed, grey area in Fig. 4.4) from the PWM reference signal, this dead time has to be taken into account. In particular, a reduced dead time value of 35 samples is parametrized in the regression algorithm in order to allow for some uncertainty. A reduction is preferable in this case since the dead time parameter only defines the end of the regression window directly where oscillations from the succeeding switching state must be omitted (see Ch. 4.2.2). However, as all delay components result from effects in the inverter and the controller, the uncertainty does not relate to the machine or cable configuration.

4.2.2 Cable recharging

A very obvious effect in Fig. 4.4 is the oscillation appearing after each switching state alteration, the peak of which may exceed rated current. These oscillations in the current signal appear on the inverter side end of the motor cable as a result of the cables specific impedance being excited by the high frequency contents of the PWM edges. The same oscillation appears on the motor side end of the cable in the voltage signal, severely aggravating ageing, robustness and temperature related issues of the winding insulation and the shaft bearings [76–81]. The current peaks on the inverter side end are less severe from physical perspective[2], but demand special considerations from control side: At high fundamental voltage (high speed), the short duration of the passive switching state (PSS) brings these transient oscillations into the SCS instants, severely distorting the measured current value. In order to obviate a voltage limitation, drive manufacturers shift the current measurement instant into a neighbouring active switching state (ASS), which in this case causes less distortion.

Within the scope of this work these switching transients in the current signal constitute a problem, as they distort the slope calculation to an unusable extent. Since a pure, average free oscillation should not have an effect on the slope calculation, the properties of the present oscillations are investigated in the following, in order to determine the reason of the distorting effect. Fig. 4.6 zooms into two consecutive switching instants from Fig. 4.4. A short time average filter with the window length of one oscillation period has been applied to the measured signal, resulting in the dotted red curve. As can be seen from the second half of each oscillation, the averaging over one period completely

[2]According to [76], the oscillation only appears when the IGBT switches faster than half the period of the oscillation, implying that the current peak is situated within the fully conducting state of the IGBT. Considering its short duration, the peak therefore results only in a minor contribution to the overall thermo-mechanical strain in the IGBT [82].

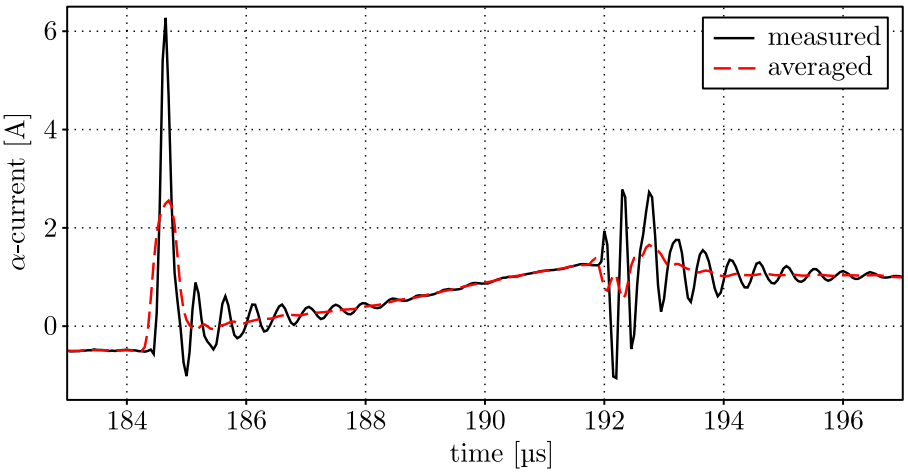

Figure 4.6: *Switching transients comprising cable recharging current.*

removes all content at the resonance frequency of the cable, and does therefore segregate any DC content within the transient that would distort the slope calculation. Those peaks in the red curve found at the very beginning of each transient represent the recharging processes of the parasitic line-to-line and line-to-earth capacitance of the cable, where the particular problem for the sensorless evaluation is the variation of their shape between the transients.

However, since this DC content is restricted to the very beginning of each switching state, it can simply be blinded out by ignoring the first few microseconds of each switching state. As will be determined in Ch. 5.4, a blind-out time of 6 µs results in the lowest noise content of the linear approximation and will therefore already be considered in the following figures and investigations of this section.

4.2.3 Machine recharging

Depending on the used cable type and length, the above analysed cable recharging oscillations are roughly in the scale of nominal current (for the machines of this work a few Amperes) and last for about five microseconds. When zooming in 50 times on the current axis, while zooming out 5 times on the time axis, a different oscillation becomes apparent which (because of its tiny scale) has rarely been documented in literature, yet [9, 83, 84].

Fig. 4.7 shows three exemplary measurements of this oscillation during a zero vector alteration (zero pulse with, all bridges switch from 0 V to U_{dc} at the same time), where the machine type and the cable length have been altered. Between the graphs with the same machine type but different cable length, only the initial high frequency oscillation differs, which affirms the assignment of this fast oscillation to the recharging of the cable. As

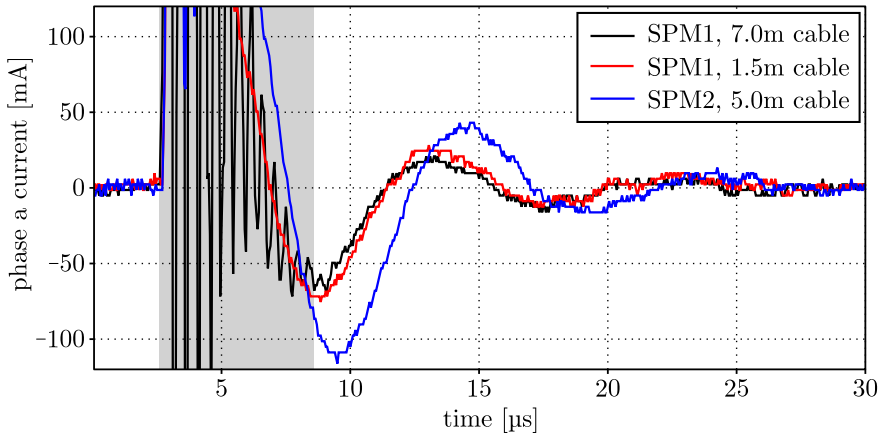

Figure 4.7: *Difference between cable and machine recharging oscillations.*

indicated by the light grey area in Fig. 4.7, this oscillation is almost completely blinded out even for the longer cable. However, the secondary slow oscillation which is roughly in the scale of 100 mA and has only about a hundredth of the frequency of the cable oscillation, is independent of the connected cable but evolves differently for different machine types. Since an oscillating behaviour requires the interaction of an inductance with a capacitance, the only explanation for this rarely documented phenomenon is a recharging process of the machine winding-to-case capacitance through the winding inductance.

It is moreover interesting to note that the particular shape of this oscillation depends on the rotor position. Fig. 4.8 shows two exemplary rotor positions and the resulting shape of the current oscillation over one PWM period. Since zero pulse width has been applied, all phases were excited identically and the resulting oscillation in the three phases seems nearly the same. However, after transforming the currents into stator frame (carried out in the FPGA before the linear approximation), the α and β component contain a projection of the phase oscillation, which implies that there is a difference between the individual phase responses. Moreover, a comparison between the left and the right graphs deduces that this difference between the phases varies with the rotor position.

Since from a physical perspective a rotor position dependent winding-to-case capacitance is implausible, an explanation of this rotor dependent oscillation shaping requires a closer investigation by means of the a high frequency model of the phase windings (implemented in MATLAB code). As indicated in Fig. 4.9, each phase winding is split up into multiple copies of an RLC-circuit, where a layer depth of $n = 15$ has been chosen as a compromise between accuracy and simulation time. The primed values are fractions or

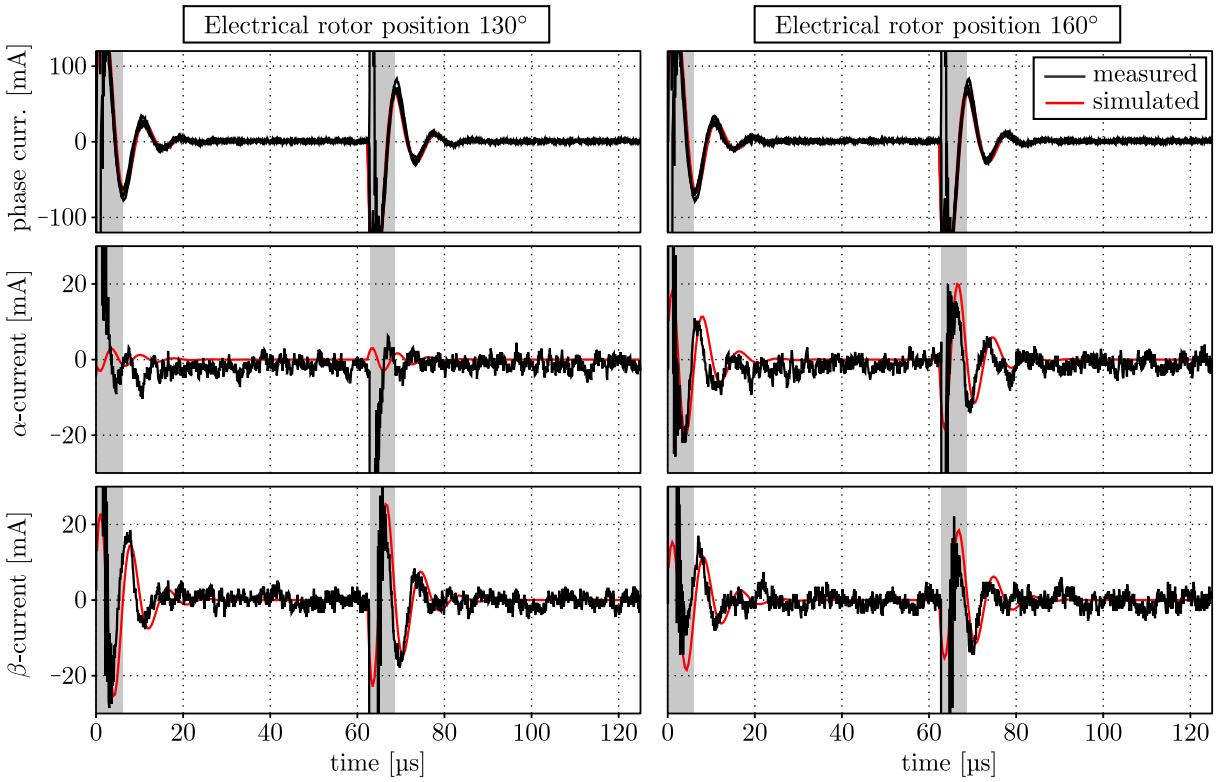

Figure 4.8: *Measured and simulated phase- and stator frame currents over one PWM period, resulting from zero voltage (all phases 50% pulse width).*

multiples of the respective overall phase values

$$L'_{a,b,c} = \frac{L_{a,b,c}}{n}, \qquad R'_{ph} = \frac{R_{ph}}{n}, \qquad R'_C = nR_C \quad \text{and} \quad C'_{ph} = \frac{C_{ph}}{n}, \tag{4.1}$$

where the phase resistance R_{ph} and the phase inductances $L_{a,b,c}$ have been parametrized according to the real machine values. The phase capacitance C_{ph} and the recharging resistance R_c have been tuned empirically to $C_{ph} = 0.8\,\text{pF}$ and $R_c = 1030\,\Omega$, such that the oscillation of the phase currents (upper graph in Fig. 4.8) matches the measurement. With this parametrization the simulation develops the same stator frame current oscillation (lower graphs in Fig. 4.8), with the same angle dependence. Through the above modelling and simulation it has been found that the appearance of the oscillation in stator frame is a result of the inductance anisotropy. A phase with lower inductance value recharges quicker with slightly higher peak currents and slightly shorter oscillation periods than a phase with higher inductance. The difference between those phase current evolutions projects into the stator frame current and forms an oscillation there as well which due to the saliency ratio ($\approx 15\%$) is markedly smaller than the phase current oscillation. The rotor position defines which phase inductance is higher and which is lower, and thereby

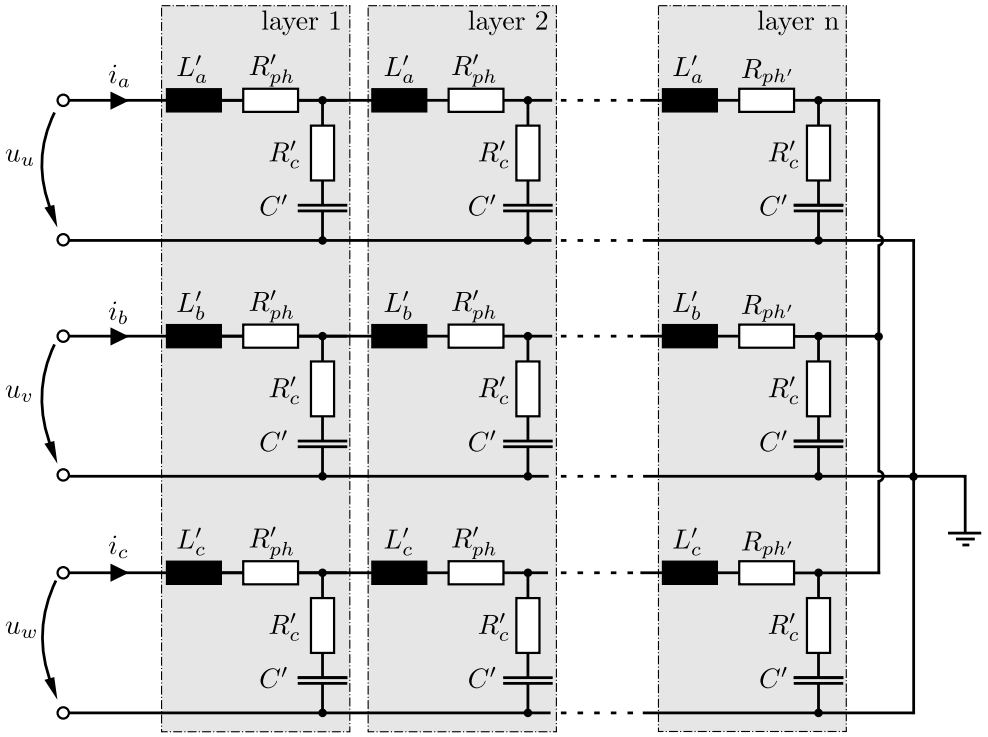

Figure 4.9: *High frequency model of the phase windings.*

also in which stator frame direction this oscillation appears.

Since the modelling has been straightforward with realistic parametrization, and since the resulting simulated currents match the measurement relatively well, this simulation affirms the assumption that a recharging distributed winding-case capacitance is the cause of this slow stator frame current oscillation that appears after the cable recharging.

As most of this oscillation is located outside of the blind-out window (light gray areas in Fig. 4.7 and Fig. 4.8), it is expected to have an effect on the linear approximation (see Ch. 5.4).

4.2.4 Eddy currents

The third effect, causing the current evolution during constant voltage phases to differ from a straight, can be seen after stator frame voltage alterations – i.e. for instance after the transition from an ASS to a PSS. Fig. 4.10 shows the measured α-current evolution during switching state alterations in black colour. The middle section belongs to a PSS where, according to the conventional machine model, the current should drop with the electrical time constant exponentially towards zero. The dotted blue curve shows a conventional model simulation, in which the current during constant voltage phases can indeed not be distinguished from a straight. However, the measured current shows an

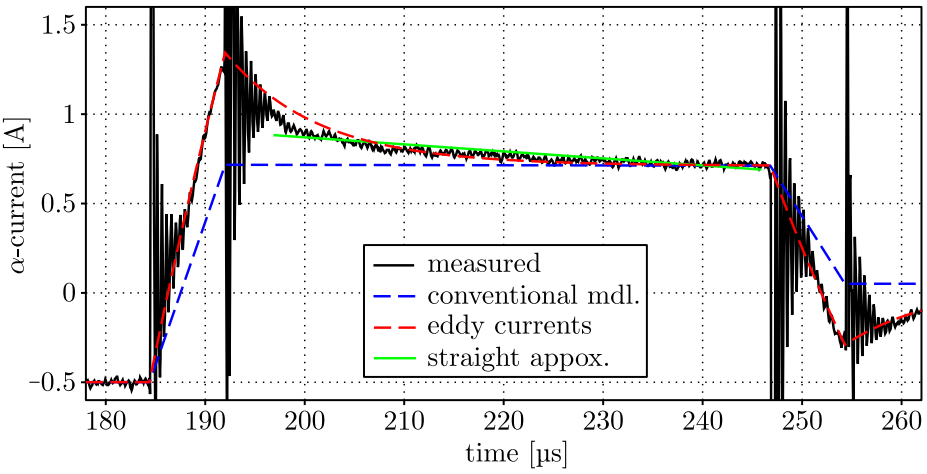

Figure 4.10: *Effect of eddy currents in measured current response.*

additional, much faster exponential behaviour that converges towards a point different from zero.

This behaviour can be emulated by means of the simple eddy current model introduced in Ch. 2.6, in which the eddy current admittance $\mathbf{Y}^s_{ed}$ has been set to $\frac{2}{3}Y_\Sigma$ and the eddy current time constant T_{ed} to 0.15 T_s (i.e. SCS captures less than 5% of the initial value). The combination of conventional and eddy current model according to Ch. 2.6 results in dotted red curve in Fig. 4.10 which resembles the measured current relatively well. Hence, it can be concluded that this deviation from the conventional model can be explained with eddy currents.

When approximating the measured data using linear regression (LR) (with blind-out time), the green straight in Fig. 4.10 is obtained which has a steeper slope and a slightly higher offset than the supposed blue curve. It can therefore be expected that eddy currents will influence the position estimation. However, since in Ch. 6 three position estimation techniques based on the oversampling data are proposed, the particular influence of the eddy currents on each technique will be analysed in the respective subsections.

4.2.5 Summary of the oversampled current response analysis

In this section 4 essential insights into the oversampled current data have been gained which shall be summarized in the following:

(1.) A dead time between the switching state reference and the current measurement of 39 ± 1 samples has been identified. This dead time is accounted for by shifting the regression window for 35 samples – which maintains the window length.

(2.) Within the first few microseconds of each switching state, the cable recharging oscillations contain a strong DC component that will distort the current slope approximation. Consequently, a blind-out time must be introduced – which shortens the regression window length.

(3.) After the cable recharging oscillations have disappeared, a much slower and weaker oscillation remains that is the result of an anisotropic machine recharging process. This weak oscillation is too long to be blinded out and will therefore slightly affect the linear approximation.

(4.) Stator frame voltage alterations induce an eddy current related overshoot in the measured stator frame current which affects the linear approximation. Potential effects of this phenomenon on the position estimation approaches will be analysed in the respective sections.

Chapter 5

Linear approximation

Following the understanding of conventional machine models (e.g. Ch. 2.3), the *current* and the *time derivative of the current* for a given voltage are rotor position dependent, as both are determined by the orientation of the anisotropy and the EMF. Accordingly, the key idea of this thesis is *the approximation of the current evolution during each switching state by a straight line* which will yield two position dependent coefficients, *offset* and *slope*. By employing a least squares based approximation method (linear regression), those coefficients will comprise minimal possible noise (see Ch. 5.3). Hence, the approximated straight coefficients of the current evolution during each switching state may not only improve the quality of the position estimation source signal – the current – but also provide a high quality signal for a position dependent quantity that is normally not measured – the current slope.

Although, according to Ch. 4.2, the shape of the current evolution during constant voltages phases in practice is not entirely linear, the analysis of terms of second or higher order in the approximation polynomial is not part of this thesis. Nevertheless, it should be noted that these terms could potentially be used to evaluate a possible position dependency of eddy current, hysteresis or winding capacitance related effects as described in Ch. 4.2.

This chapter starts with a brief description of the first order least squares method *linear regression*, after which its recursive implementation on an FPGA will be discussed. In the next step, the theoretical noise reduction potential of linear regression is discussed, in order to set a reference mark for the following experimental investigation. The resulting insights into the properties of the approximated straight coefficients under several operating conditions will eventually be compared to the initial theoretical expectation.

5.1 Linear regression

The method of least squares [85, p. 427] is a well-known approach for curve approximation of stochastic data. The optimal solution curve is obtained analytically, i.e. straightforward without iterative search loops and without the common optimization problem of local minima. A cloud of points $P(x_i, y_i)$, with $i = 1 \ldots n$ and n being the number of points in the cloud, is approximated by a polynomial $f(\cdot)$ of arbitrary order, the parameters of which are directly obtained in such a way that the sum of all squared vertical distances between the points and the polynomial is minimized.

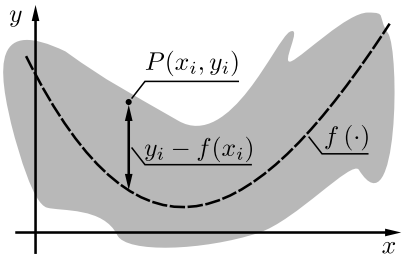

Figure 5.1: *Point cloud and approximation curve.*

The simplest realization of this general approach is referred to as linear regression (LR), where a first order polynomial – a straight – is used for approximation

$$f(x) = a_1 x + a_0. \tag{5.1}$$

As a least squares method, LR defines the error function N^2 as the sum of all squared vertical deviations between the cloud points $P(x_i, y_i)$ and the approximation curve $f(\cdot)$

$$N^2 = \sum_{i=1}^{n} \left(y_i - f(x_i)\right)^2 \tag{5.2}$$

$$= \sum_{i=1}^{n} \left(y_i - a_1 x_i - a_0\right)^2. \tag{5.3}$$

The optimal straight is described by that set of parameters a_1 and a_0 that minimizes the error N^2 – i.e. a_1 and a_0 are the roots of the partial derivatives of (5.3)

$$\frac{\partial N^2}{\partial a_1} = \sum_{i=1}^{n} -2\left(y_i - a_1 x_i - a_0\right) x_i = 0 \tag{5.4}$$

$$\frac{\partial N^2}{\partial a_0} = \sum_{i=1}^{n} -2\left(y_i - a_1 x_i - a_0\right) = 0. \tag{5.5}$$

By summarizing (5.4) and (5.5) and factoring out a_1 and a_0,

$$0 = a_1 \sum_{i=1}^{n} x_i^2 + a_0 \sum_{i=1}^{n} x_i - \sum_{i=1}^{n} y_i x_i \tag{5.6}$$

$$0 = a_1 \sum_{i=1}^{n} x_i + a_0 \; n - \sum_{i=1}^{n} y_i, \tag{5.7}$$

and by considering that all values x_i and y_i are known, a simple set of two equations with two unknowns is obtained. Solving this set of equations for a_1 and a_0 leads to the well known LR equations

$$a_1 = \frac{\sum_{i=1}^{n} (x_i y_i - \overline{xy})}{\sum_{i=1}^{n} (x_i^2 - \overline{x}^2)} \tag{5.8}$$

$$a_0 = \overline{y} - a_1 \overline{x}, \tag{5.9}$$

in which an overline indicates an average value, like for instance $\overline{x} = \frac{1}{n} \sum_{i=1}^{n} x_i$. The coefficients a_1 and a_0 describe the straight with the overall minimum quadratic deviations to all measured points $P(x_i, y_i)$.

The general least squares based solution that minimizes the squared deviations to a polynomial of arbitrary order is described for instance in [86], but is not considered within the scope of this work. In contrast to the above derived linear regression, general least squares methods involve matrix inversion which significantly increases the overall computational effort.

5.2 Recursive implementation on an FPGA

The present RTS provides current measurements with 20 MHz sampling rate, whereas the sensorless, current and speed control algorithms run twice per PWM period, i.e. at 16 kHz control update rate. Consequently, the system obtains 1250 current samples per control cycle for all phases. This sums up to 3750 12 bit integers that have to be processed within 62.5 µs (≈ 150 MB/s) in order to approximate the slope of the current evolution in real time. Concluding from practical implementations, this exceeds the capability even of the used Pentium 4 CPU by far. Yet, an FPGA (already included in the RTS, e.g. for the communication with the fast ADC) is capable of processing data at this rate which does, however, come at the cost of a higher implementation complexity.

Fig. 5.2 exemplifies the measurement data of the α-current over time, where each dot represents one current sample. Due to measurement noise and quantization, the measured current values form a point cloud around the actual current evolution which for the sake of clearness is illustrated in an exaggerated way.

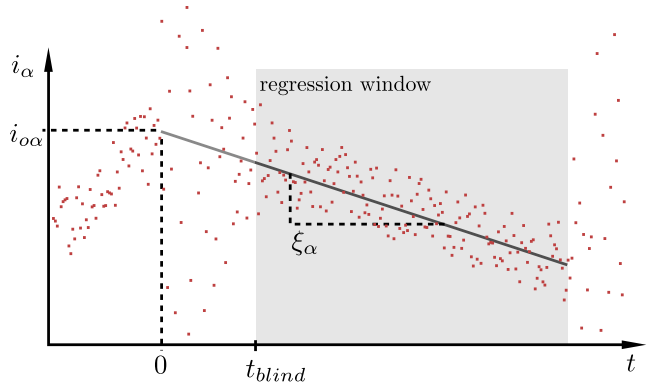

Figure 5.2: *Linear approximation of the current measurement point cloud.*

In spanning slightly more than one switching state, Fig. 5.2 shows only a fraction of a sampling period. The moment $t = 0$ represents the switching instance of the PWM reference signal delayed by $t_{dead} = 35\,\mathrm{FPGAsamples}$ (see Ch. 4.2.1). At this point the software time counter t is reset and starts to raise linearly over time. Between $t = 0$ and $t = t_{blind}$ all current samples are ignored in order to prevent the cable recharging currents (see Ch. 4.2.2) from affecting the slope calculation. In the following phase – the so-called *regression window* which starts at t_{blind} and ends with the next switching transition (also determined by the switching reference signal and the delay t_{dead}) – all measured current values are taken into account for the LR algorithm.

Considering both, the α- and the β-current, the specific implementation of LR approximates a vectorial straight $\boldsymbol{i}^s_{reg}(t)$, defined by

$$\boldsymbol{i}^s_{reg}(t) = \boldsymbol{\xi}^s_s t + \boldsymbol{i}^s_o, \tag{5.10}$$

where $\boldsymbol{\xi}^s_s = [\xi_\alpha\ \xi_\beta]^\top$ is the current slope over time and $\boldsymbol{i}^s_o = [i_{o\alpha}\ i_{o\beta}]^\top$ is the current offset at the switching instance $t = 0$. By applying the derivation from Ch. 5.1 to the vectorial case, the straight coefficients are obtained as

$$\boldsymbol{\xi}^s_s = \frac{\sum_{i=1}^{n} \left(\boldsymbol{i}^s_{si}\ t_i - \overline{\boldsymbol{i}^s_s}\ \bar{t} \right)}{\sum_{i=1}^{n} \left(t_i^2 - \bar{t}^2 \right)} \tag{5.11}$$

$$\boldsymbol{i}^s_o = \overline{\boldsymbol{i}^s_s} - \boldsymbol{\xi}^s_s\ \bar{t}. \tag{5.12}$$

However, this standard LR equation (5.11) can only be computed after all measurement data has been obtained, since the summations require the average values $\overline{\boldsymbol{i}_s^s}$ and $\bar{t}$. This means that n data samples (up to 3750 in the case of the present RTS) would have to be stored in memory first and then be processed at once after all data has been obtained.

In order to mitigate this intense computational effort, a recursive equivalent is derived from (5.11) which will be referred to as recursive linear regression (RLR). After splitting up the brackets of numerator and denominator

$$\boldsymbol{\xi}_s^s = \frac{\sum\limits_{i=1}^{n} \boldsymbol{i}_{si}^s \; t_i - \sum\limits_{i=1}^{n} \overline{\boldsymbol{i}_s^s} \; \bar{t}}{\sum\limits_{i=1}^{n} t_i^2 - \sum\limits_{i=1}^{n} \bar{t}^2}, \tag{5.13}$$

the expression within the right hand side summation of both is constant and can therefore simply be multiplied by n

$$\boldsymbol{\xi}_s^s = \frac{\sum\limits_{i=1}^{n} \boldsymbol{i}_{si}^s \; t_i - n \; \overline{\boldsymbol{i}_s^s} \; \bar{t}}{\sum\limits_{i=1}^{n} t_i^2 - n \; \bar{t}^2}. \tag{5.14}$$

Now, reducing both the numerator and the denominator by n

$$\boldsymbol{\xi}_s^s = \frac{\frac{1}{n}\sum\limits_{i=1}^{n} \boldsymbol{i}_{si}^s \; t_i - \overline{\boldsymbol{i}_s^s} \; \bar{t}}{\frac{1}{n}\sum\limits_{i=1}^{n} t_i^2 - \bar{t}^2}. \tag{5.15}$$

yields a left hand side expression that matches the arithmetic method of average calculation

$$\boldsymbol{\xi}_s^s = \frac{\overline{\boldsymbol{i}_s^s \; t} - \overline{\boldsymbol{i}_s^s} \; \bar{t}}{\overline{t^2} - \bar{t}^2}. \tag{5.16}$$

Considering the recursive way of average calculation

$$\overline{x}[i] = \overline{x}[i-1] + \frac{x[i] - \overline{x}[i-1]}{i} \tag{5.17}$$

with $i = 1 \ldots n$ (and $\overline{x}[0]$ being irrelevant), there are only 4 recursive average values $\bar{t}$, $\overline{\boldsymbol{i}_s^s}$, $\overline{t^2}$ and $\overline{\boldsymbol{i}_s^s \; t}$ to be computed and finally summarized by the non-iterative equations (5.16) and (5.12). In this way the approximated current slope $\boldsymbol{\xi}_s^s$ and the current offset at the switching instant $\boldsymbol{i}_o^s$ can be updated with every current sample, involving minimal

computational effort and allowing for a feasible realization in Very High Speed Integrated Circuit Hardware Description Language (VHDL).

Although the complete set of equations (2.13), (5.17), (5.16) and (5.12), necessary for the LR, appears quite simple, its particular implementation in VHDL required quadruple pipelining, an LUT storing 3000 integers and an overall delay of 27 FPGA cycles (1.35 µs). The result are four normalized 32 bit fixed point values for the slopes ξ_α and ξ_β and the offsets $i_{o\alpha}$ and $i_{o\beta}$ which are required to realize the accuracy potential of the LR approach. Each 32 bit value is split up into two 16 bit values in order be communicated through the 16 bit bus to the CPU where they are recomposed and converted to a floating point value in SI unit.

5.3 Noise suppression through linear regression

The specific implementation of linear regression used in this thesis constitutes a special case of combining stochastic data. Before evaluating the practical regression results, we will assess from a theoretical point of view to which extent this linear regression is able to reduce noise content.

Therefore we firstly assume that the measured current values contain white noise, such that each sample is a partially random value i. As indicated in Fig. 5.3, a large set of single values i will form a Gaussian distribution around the expected current value μ with a standard deviation σ

$$i = N(\mu, \sigma^2), \tag{5.18}$$

where $N(\cdot)$ is the function creating a random value with this probability distribution. Since the root mean square (RMS) value of the current noise equals the definition of σ, only σ and not μ is relevant for the analysis in this section.

When scaling a measured current sample i with a constant factor c, both the expected value μ and the standard deviation σ are scaled

$$ci = cN(\mu, \sigma^2) \tag{5.19}$$

$$= N\left(c\mu, (c\sigma)^2\right). \tag{5.20}$$

When adding two different current samples i_1 and i_2 which show the same Gaussian

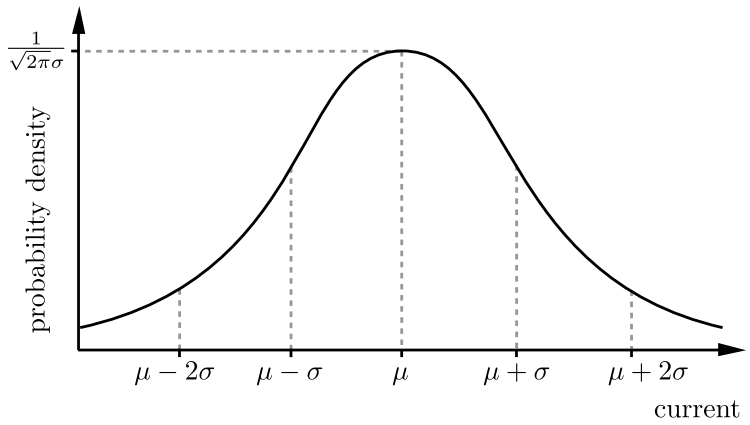

Figure 5.3: *Gaussian probability density distribution for the current measurement.*

properties σ and μ, the resulting value will have the following properties

$$i_1 + i_2 = N(\mu, \sigma^2) + N(\mu, \sigma^2) \tag{5.21}$$

$$= N(\mu + \mu, \sigma^2 + \sigma^2), \tag{5.22}$$

if i_1 and i_2 can be considered stochastically independent from another [87, p.176]. Note that in this stochastically independent case, not the standard deviation σ itself, but its squared value σ^2 is subject to the summation. Based on those two rules from probability theory, we will now derive to which extent the noise content from the current samples projects into the regression results.

Considering that n current samples $i_1 ... i_n$ are employed for the linear approximation, the straight offset $\bar{i}$ in the middle of the regression window (see explanation in Ch. 5.4.1) is obtained through a simple averaging process

$$\bar{i} = \frac{1}{n}\sum_{k=1}^{n} i_k = \frac{1}{n}\sum_{k=1}^{n} N(\mu, \sigma^2) \tag{5.23}$$

$$\text{indep. sum:} \qquad = \frac{1}{n} N(\sum_{k=1}^{n} \mu, \sum_{k=1}^{n} \sigma^2) = \frac{1}{n} N(n\mu, n\sigma^2) \tag{5.24}$$

$$\text{scaling:} \qquad = N\left(n\frac{\mu}{n}, n\left(\frac{\sigma}{n}\right)^2\right) = N\left(\mu, \left(\frac{\sigma}{\sqrt{n}}\right)^2\right), \tag{5.25}$$

in which the expected value μ is retained, but the noise RMS is lowered by factor $\frac{1}{\sqrt{n}}$. This result is part of the known properties of oversampling, e.g. described in [88, p.997].

The noise RMS of the slope coefficient, however, depends on the particular implementation of the LR and will therefore be derived specifically for the present conditions. Firstly, we must consider that the current samples i_k are equidistantly distributed in time. We

normalize the time axis with respect to the regression window length

$$t_k = \frac{k-1}{n-1} - \frac{1}{2} \qquad \text{with} \quad k = 1 \dots n, \tag{5.26}$$

such that the resulting slope values will be comparable to the current. The particular relation between the current slope and the current value is given by the factor $T_s/2$, as will be derived in Ch. 6.1.2. Hence, when interpreting the results in this section, the slope results will be halved for the comparison with the current offset.

Due to the symmetric definition of (5.26), the average time value is zero ($\bar{t} = 0$), which simplifies the slope approximation equation (5.16)

$$\xi = \frac{\overline{i\ t}}{\overline{t^2}}. \tag{5.27}$$

The denominator $\overline{t^2}$ is a noise-free value that only depends on the number of samples n

$$\overline{t^2} = \frac{1}{n} \sum_{k=1}^{n} \left(\frac{k-1}{n-1} - \frac{1}{2} \right)^2, \tag{5.28}$$

and that converges towards $\overline{t^2} = \frac{1}{12}$ with increasing n. Practically, for $n > 50$ (4% of the PWM half-period), it can be considered $\overline{t^2} \approx \frac{1}{12}$.

The numerator $\overline{i\ t}$ constitutes a summation of individually scaled noisy values i

$$\overline{i\ t} = \frac{1}{n} \sum_{k=1}^{n} t_k i_k = \sum_{k=1}^{n} \frac{1}{n} \left(\frac{k-1}{n-1} - \frac{1}{2} \right) N(-, \sigma^2) \tag{5.29}$$

$$\text{scaling:} \qquad = \sum_{k=1}^{n} N\left(-,\ \left[\frac{1}{n} \left(\frac{k-1}{n-1} - \frac{1}{2} \right) \sigma \right]^2 \right) \tag{5.30}$$

$$\text{indep. sum:} \qquad = N\left(-,\ \sum_{k=1}^{n} \left[\frac{1}{n} \left(\frac{k-1}{n-1} - \frac{1}{2} \right) \sigma \right]^2 \right) \tag{5.31}$$

$$= N\left(-,\ \frac{1}{n} \sum_{k=1}^{n} \left(\frac{k-1}{n-1} - \frac{1}{2} \right)^2 \frac{\sigma^2}{n} \right) \tag{5.32}$$

$$\overset{(5.28)}{=} N\left(-,\ \overline{t^2}\ \frac{\sigma^2}{n} \right), \tag{5.33}$$

in which the expected value μ is irrelevant for the noise consideration and has therefore been disregarded. When combining numerator (5.33) and denominator (5.28) in order to

obtain the current slope ξ, the denominator acts as a noise scaling factor

$$\xi = \frac{1}{\overline{t^2}}\ N\left(-,\ \frac{\overline{t^2}}{n}\sigma^2\right) \tag{5.34}$$

$$= N\left(-,\ \frac{\overline{t^2}}{n}\left[\frac{\sigma}{\overline{t^2}}\right]^2\right) \tag{5.35}$$

$$= N\left(-,\ \left[\frac{\sigma}{\sqrt{\overline{t^2}n}}\right]^2\right). \tag{5.36}$$

Hence, in the approximated slope the noise RMS is scaled by factor $\frac{1}{\sqrt{\overline{t^2}n}}$ with respect to the current samples which (because of the convergence of $\overline{t^2}$) for almost all switching state lengths is approximately factor $3.46\frac{1}{\sqrt{n}}$.

The above result implies that the varying number of samples n is equally distributed over the entire PWM half-period, which is especially relevant for an oversampling ratio (OSR) consideration. When the varying number of samples n, however, is a result of the shortened switching state at a fixed oversampling frequency, then the resulting slope value ξ_{pw} is scaled with the ratio between involved samples n and the number of samples in a full PWM half-period n_0

$$\xi_{pw} = \frac{n_0}{n}\ N\left(-,\ \left[\frac{\sigma}{\sqrt{\overline{t^2}n}}\right]^2\right) \tag{5.37}$$

$$= N\left(-,\ \left[\frac{n_0}{n}\frac{\sigma}{\sqrt{\overline{t^2}n}}\right]^2\right) \tag{5.38}$$

$$= N\left(-,\ \left[\frac{1}{n^{3/2}}\frac{n_0\sigma}{\sqrt{\overline{t^2}}}\right]^2\right). \tag{5.39}$$

Hence, in case of a (pulse width induced) switching state length variation, the noise RMS of the average value $\bar{i}$ still scales with $\frac{1}{\sqrt{n}}$, but the noise RMS of the slope ξ scales with $\frac{1}{n^{3/2}}$. When the switching state fills the complete PWM half-period, the slope noise is already 1.73 times stronger than the noise of the average value[1], and from this initial level it raises markedly quicker than the noise of the average value $\bar{i}$ when the switching state is shortened. This stronger increase is the result of two deteriorating facts coming together:

(1.) The number of current samples involved in the least squares method decreases pro-

[1]As will be shown in Ch. 6.1, the relevant factor between both quantities is $T_s/2$. Since for this derivation the factor T_s has been used the above factor 3.46 has to be divided by two.

portionally with the switching state length, which affects the average value noise the same way as the slope noise.

(2.) The overall distribution of the current samples over time shrinks with decreasing switching state length, which does not affect the average value but does affect the slope noise. According to (5.38), this loss of distribution has a stronger influence on the slope than the loss of involved samples.

Fig. 5.4 illustrates the above relations, where the upper edge of the frame represents the noise RMS of the current samples. The above analytical derivations are supported by the results of a numerical RMS computation based on the artificial generation of white noise with MATLAB. On the right hand side axis can be seen that, in ideal condition and if the

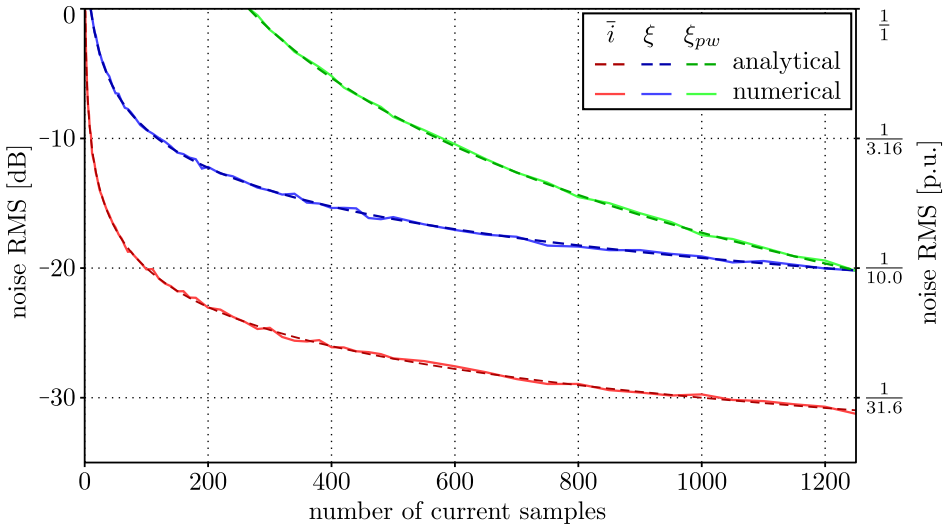

Figure 5.4: *Theoretical oversampling based noise reduction depending on involved number of current samples.*

switching state amounts the complete PWM half-period (1250 samples), the noise of the offset could be up to 33 times lower than the original noise in the current. The slope noise ends at factor 1/10 which according to Ch. 6.1.3 results in a noise reduction by factor 20, compared to the conventional current measurement. According to the green graph in Fig. 5.4, the slope approximation is not reasonable if the regression window amounts less than a fifth of the PWM half-period – i.e. including blind time, if the respective switching state is shorter than 30%.

Finally, Tab. 5.1 compares the white noise reduction potential of the least squares approximation (order 2) with the (iterative) linear approximation targeting the minimization of other error orders. Order 1, for instance, minimizes the mean absolute value of the error, whereas order 4 minimizes the mean fourth power error. Since order 2 shows the

Error order	1	2	3	4	5
Straight offset	27.4	33.2	30.7	26.3	21.6
Straight slope	8.2	10.5	9.5	8.0	6.5

Table 5.1: *White noise reduction factor depending on the order of the error, minimized in the linear approximation.*

highest noise reduction factors in both offset and noise, least squares based linear approximation is considered to be give the best possible approximation results, comprising minimal possible noise.

However, all above results constitute only the theoretical limits of noise reduction, assuming that the white (temperature) noise is the only distortion of the current signals. The next subsection comprises an experimental investigation of this subject, scrutinizing to which extent this theoretical potential of the linear approximation can be reached in practice.

5.4 Experimental validation of the linear approximation

As the least squares based linear approximation can employ more than a thousand current samples, the resulting noise content in the straight coefficients should be significantly lower than the noise in the synchronous current samples. Hence, the amount of signal content, required to extract the position information from the straight coefficients, is expected to be much lower as well. This section aims to validate this assumption and to moreover evaluate the extent to which the non-ideal effects discovered in Ch. 4.2 distort the expected current behaviour.

As determined in the previous section, the straight slope $\boldsymbol{\xi}_s^s$ should have a significantly higher noise content than the mean value of the samples $\overline{\boldsymbol{i}_s^s}$. Due to the equidistant distribution of the current samples over time, this mean value $\overline{\boldsymbol{i}_s^s}$ represents the straight offset in the middle of the regression window $\boldsymbol{i}_m^s$ which consequently is the point of the straight with the lowest overall noise content. According to (5.12), however, the straight offset value $\boldsymbol{i}_o^s$ provided by the RLR implementation refers to the beginning of the regression window and does hence contain a mixture of slope noise and mean value noise. Thus, in order to segregate slope and offset related effects, in all following sections the term *straight offset* will refer to the *middle* of the regression window and is calculated from the

regression results $\boldsymbol{\xi}_s^s$ and $\boldsymbol{i}_o^s$ by

$$\boldsymbol{i}_m^s = \boldsymbol{i}_o^s + \boldsymbol{\xi}_s^s \, \bar{t} = \overline{\boldsymbol{i}_s^s}. \tag{5.40}$$

5.4.1 Noise properties and components in idle condition

Fig. 5.5 shows a time plot of the SCS current and of the straight coefficients *slope* and *offset* during zero stator frame voltage (all phase pulse widths 50%). It can be seen

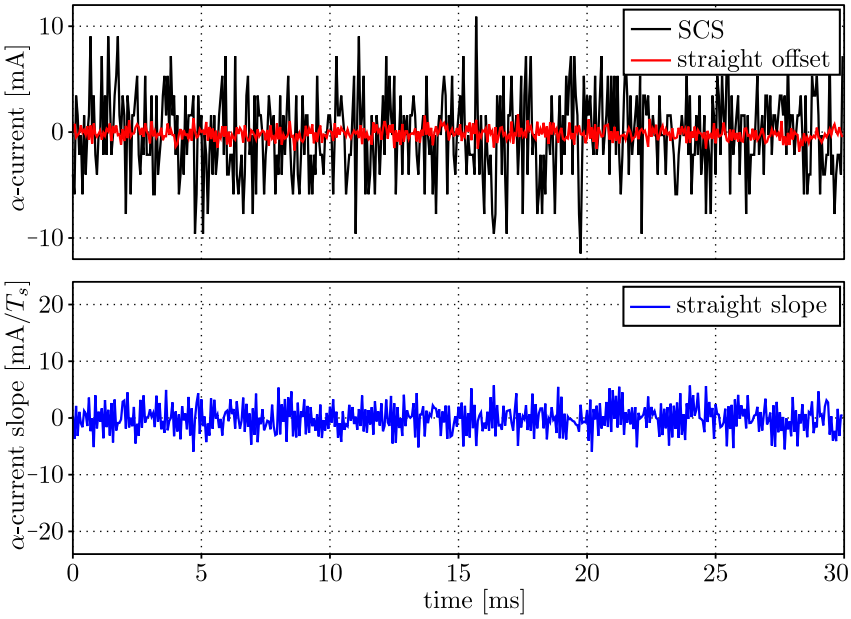

Figure 5.5: *Time plot of sampled current and approximated straight coefficients at zero stator frame voltage (each phase 50% pulse width).*

that all signals contain noise, where expectedly the noise of the straight coefficients is significantly lower. The scaling of the slope axis has been set according to the influence of the slope when it is eventually combined with the offset in equation 6.17. This scaling of 1:2 in between both graphs will be applied throughout the rest of this section in order to establish comparability for the slope results.

According to the frequency plot of the current and the straight coefficients, shown in Fig. 5.6, the noise type is *white* in all cases. White noise exhibits an equal power density over all relevant frequencies and forms the basis for various filter techniques. The later property is particularly important for the sensorless observer design.

In Fig. 5.7, the dark-red and -blue curves show that the distribution of the straight coefficients is roughly Gaussian. For comparability reasons, the height of each curve has been normalized to its maximal value. The distribution of the synchronous current samples exceeds the width of the plot, where the dull corners around 1.8 mA constitute

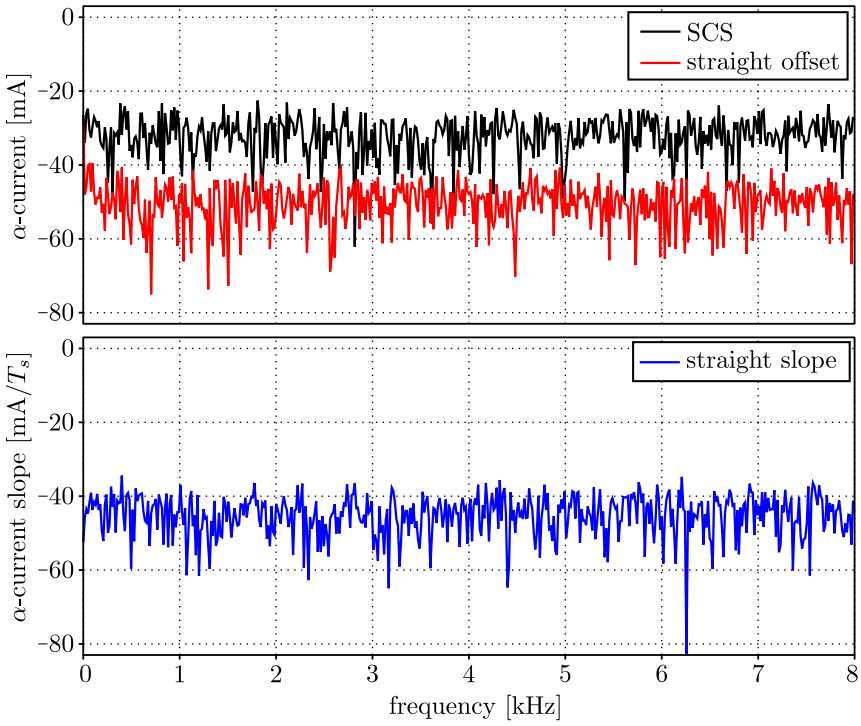

Figure 5.6: *Frequency plot of sampled current and approximated straight coefficients at zero stator frame voltage (each phase 50% pulse width).*

the projection of the ADC resolution in stator frame[2]. The RMS value of the SCS is 3.83 mA which is in the scale of the phase current resolution.

When analysing the straight offset values for their RMS, we obtain 0.62 mA which is 6.15 times smaller than the SCS value. However, the respective Gaussian curve with $\sigma = 0.62\,\mathrm{mA}$, indicated in grey colour, does not completely match the measured distribution and does hence point out its slight non-Gaussian shape. Even more distinct is this deviation for the slope which has an overall RMS value of $2.43\,\mathrm{mA}/T_s$.

The reason for this deviation can be found when analysing positive (all phases U_{DC}) and negative (all phases GND) PSSs separately. The resulting distribution curves are drawn in lighter colours and with respectively smaller height in both plots. The RMS value of those sub-quantities is 0.52 mA for the offset and $1.79\,\mathrm{mA}/T_s$ for the slope which corresponds to Gaussian curves (indicated dotted grey in Fig. 5.7) that match the measured distributions exactly. The expectations of both sub-distribution-curves lay at $\mu = \pm 0.34\,\mathrm{mA}$ for the offset and at $\mu = \pm 1.65\,\mathrm{mA}/T_s$ for the slope.

Hence, we must distinguish between an actual noise in the straight coefficients that shows all normal noise properties, and a component that alternates with PWM fre-

[2]The phase current resolution is 3.7 mA and the smallest factor within the Clarke transformation matrix (2.13) is 0.5.

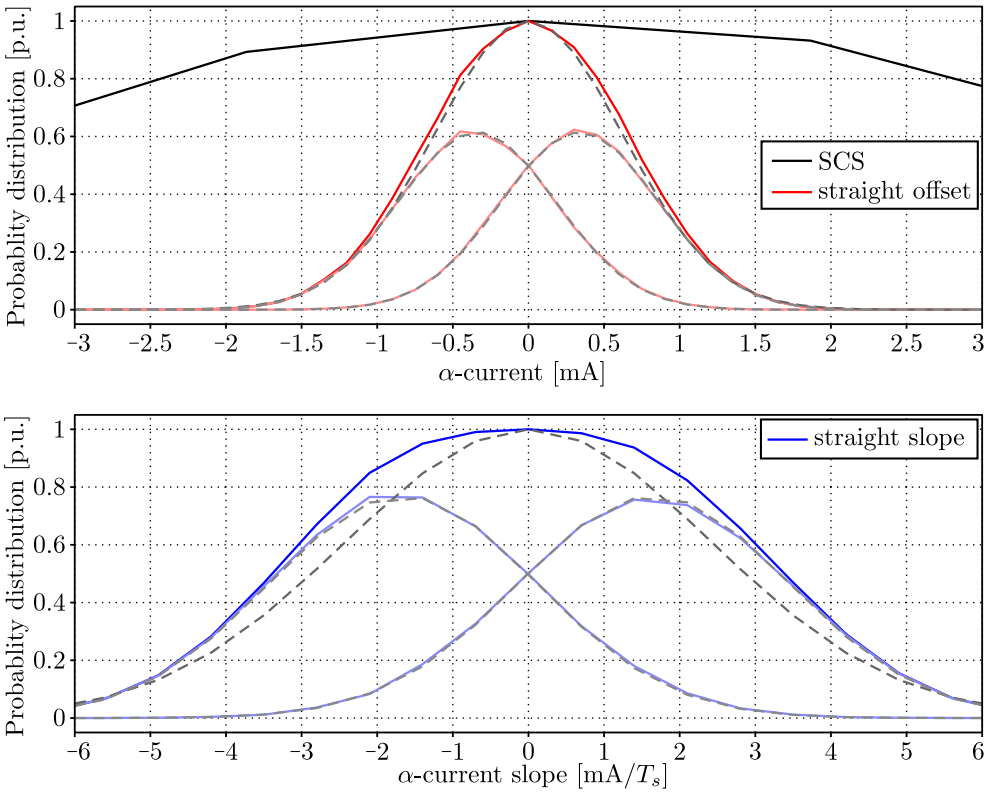

Figure 5.7: *Probability distribution of sampled current and approximated straight coefficients at zero stator frame voltage (each phase 50% pulse width).*

quency. The reason for this alternating component has been discovered and investigated in Ch. 4.2.3. It is the recharging process of the isotropic winding-to-case capacitance through the anisotropic phase inductances of the machine that consequently projects into stator frame. This relatively small scaled and rarely documented machine recharging process does affect the straight coefficients to a notable extent. Moreover, according to Ch. 4.2.3, the magnitude and more importantly the direction of this alternation depends on the rotor position, which raises the question whether this anisotropy-based information – that emerges already by pure transition between opposite zero vectors (i.e. without injection) – can be utilized for (absolutely silent) position estimation at standstill. Since first investigations, however, showed an increased entailed complexity of a respective approach, the realization will not be part of this thesis.

Fig. 5.8 shows the dependence of the noise and the alternation on the blind-out time. In this plot both noise and alternation are magnitude values of stator frame vectors, and hence scaled roughly by factor $\sqrt{2}$ with respect to the above plots. As shown in Ch. 4.2.2, the cable recharging oscillations are located within the first 100 samples and it is very interesting to note that these oscillations result in an increase of the alternation curves, but not of the noise. This means that the oscillations exhibit a precise repeatability and do

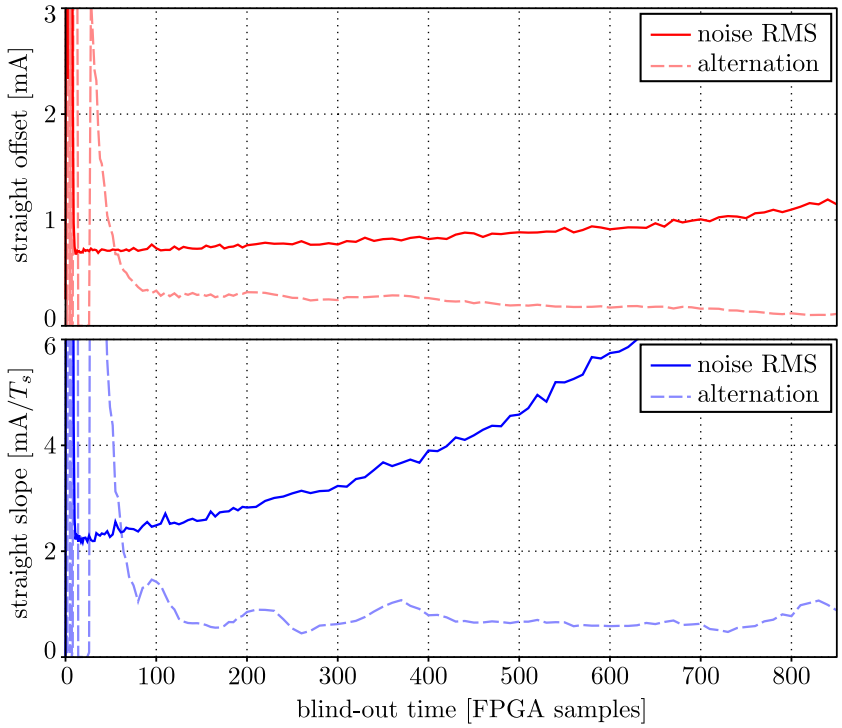

Figure 5.8: *Noise and alteration of straight coefficients over blind-out time.*

not appear as a random signal for the current oversampling. However, as also alternating straight coefficients do distort or complicate the position estimation, these oscillations have to be blinded out.

Furthermore, it can be seen from Fig. 5.8 that the noise content of the straight offset increases slightly and the noise content of the straight slope increases markedly with the blind-out time. It is consequently reasonable to keep the blind-out time as short as possible. Hence, the blind-out time is parametrized with a value slightly higher than the duration of the cable recharge oscillation (alteration fade out): 120 FPGA samples or 6 µs. This value has been and will be assumed for all other derivations and investigations of this work.

5.4.2 Linear approximation during injection

For the position estimation around standstill a triangular voltage injection will be applied to the machine and the resulting current response will be evaluated by means of the Arbitrary Injection method. Since especially under low injection magnitude the ASS is much shorter than the above defined blind-out time, only the PSS straight parameters can be evaluated. Fig. 5.9 shows the dependence of signal, noise and alternation of the approximated PSS straight coefficients on the injection magnitude. Expectedly, the sig-

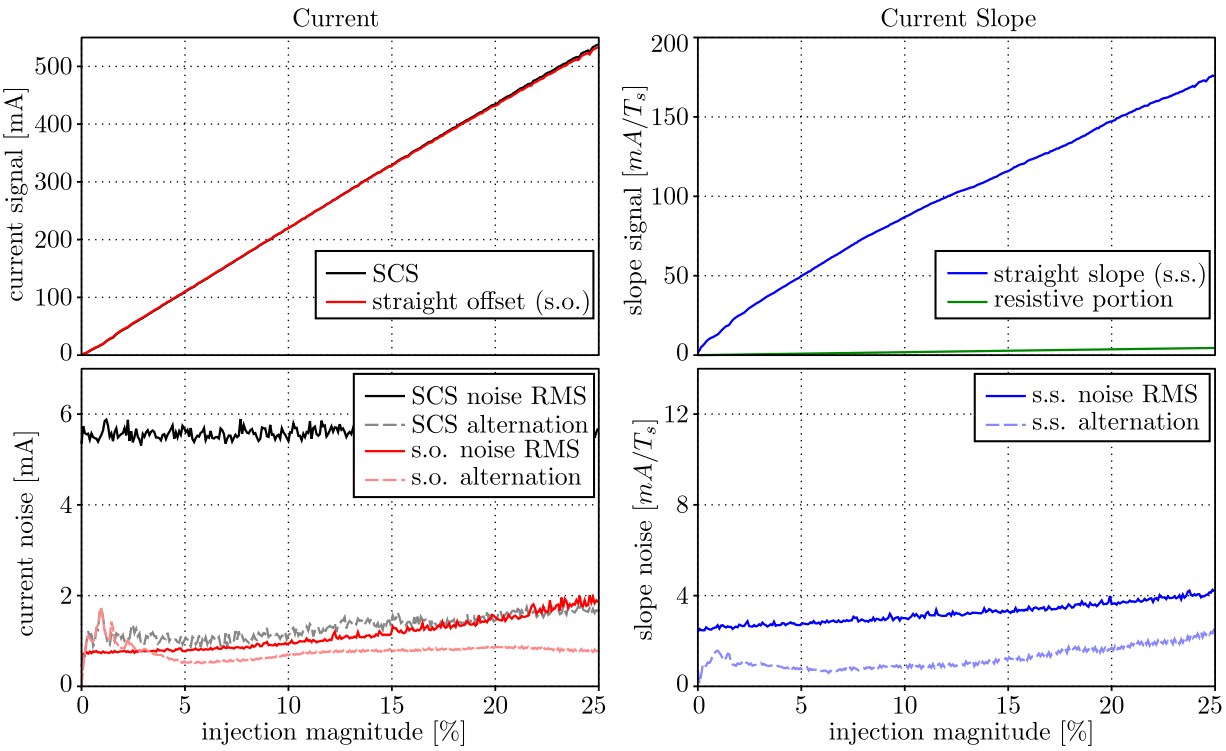

Figure 5.9: *Noise and alternation of the PSS straight coefficients depending on injection magnitude.*

nal content of the passive straight offset increases linearly over the injection magnitude. Although the noise content should not be directly influenced by the injection magnitude, the noise RMS of the straight offset increases slightly towards very high injection magnitudes. EMI and chaotic effects could be considered as reasons for this increase. However, since the oversampling-based anisotropy position estimation will require less than 10% injection magnitude, this effect does not play an important role.

It is more interesting to note that for low injection magnitudes the alternation becomes larger than the noise RMS and, hence, larger than the alternation value without injection (zero voltage). The reason for this lies in the now different instants at which the single phases switch. Hence, not only the anisotropic inductance causes a difference between the phase winding recharging processes, but the single phase winding capacitances are excited at slightly different times. As a result, a bigger part of the 100 mA phase winding recharging current (see Ch. 4.2.3) projects into stator frame and causes this increase in magnitude of the alternation.

In contrast to the noise, however, which according to Fig. 5.6 has equal power density in all frequencies, the alternation has only one frequency component: PWM frequency. Since this is the highest recognizable frequency, it is much easier to suppress this alternation by means of the subsequent filtering than to suppress the noise. The hence more crucial

noise content of the straight offset is significantly lower than the value of the SCS.

The noise RMS and the alternation of the approximated slope evolve similar to the offset, whilst the signal content of the slope exhibits a more interesting property. When calculating the straight slope according to the electrical time constant L_s/R_s of the machine and the actual current due to the injection (upper left hand side graph of Fig. 5.9), we obtain the slope value indicated by the green curve in Fig. 5.9. This value, which relates to the expected exponential fade out process of the current due to the winding resistance, is an almost negligible component within the measured current slope. Hence, the current slope during injection at standstill (zero EMF) is almost solely generated by eddy currents, the influence of which has already been disclosed in Ch. 4.2.4.

5.4.3 Linear approximation in the presence of rotor speed

At medium and high rotor speed the voltage required to counter the EMF is much higher, than the injection magnitude. Moreover, the major portion of the EMF-induced current response is angle dependent, while the angle dependent portion of the injection-based current response corresponds to the saliency ratio Y_Δ/Y_Σ, i.e. makes only $5-15\%$ of the total current response in an SPMSM. Thus, in the presence of rotor speed, the EMF-based current response is commonly employed for the rotor position estimation.

When utilizing current oversampling, the linear approximation data comprises the EMF information mainly within the slope coefficients. The straight offsets comprise this information only in the same indirect form as the synchronous current samples do. In order to investigate the new potential of current oversampling for sensorless control, this work only focuses on the development of current slope based EMF estimation techniques. Hence, within this subsection 5.4.3 the offset properties will not be investigated.

The left hand side graph of Fig. 5.10 displays the approximated current slope values of several hundred thousand PSSs which have been recorded while the machine was running at rated speed. The hexagon indicates the maximum current slopes that can be generated by the PWM and the machine admittance, i.e. the maximum EMF-induced PSS slope that could be countered.

Considering the whole set of measured slope values, comprising of both the orange and the light blue graph, the slope trajectory normally appears to have a relatively wide noise band. The orange and the light blue graphs have been segregated by distinguishing upper (all phases at U_{DC}) and lower (all phases at ground potential) PSSs. Then both graphs evolve different from another and have a markedly narrower noise band.

An alternating component in addition to the noise has been noted before in Ch. 5.4.1,

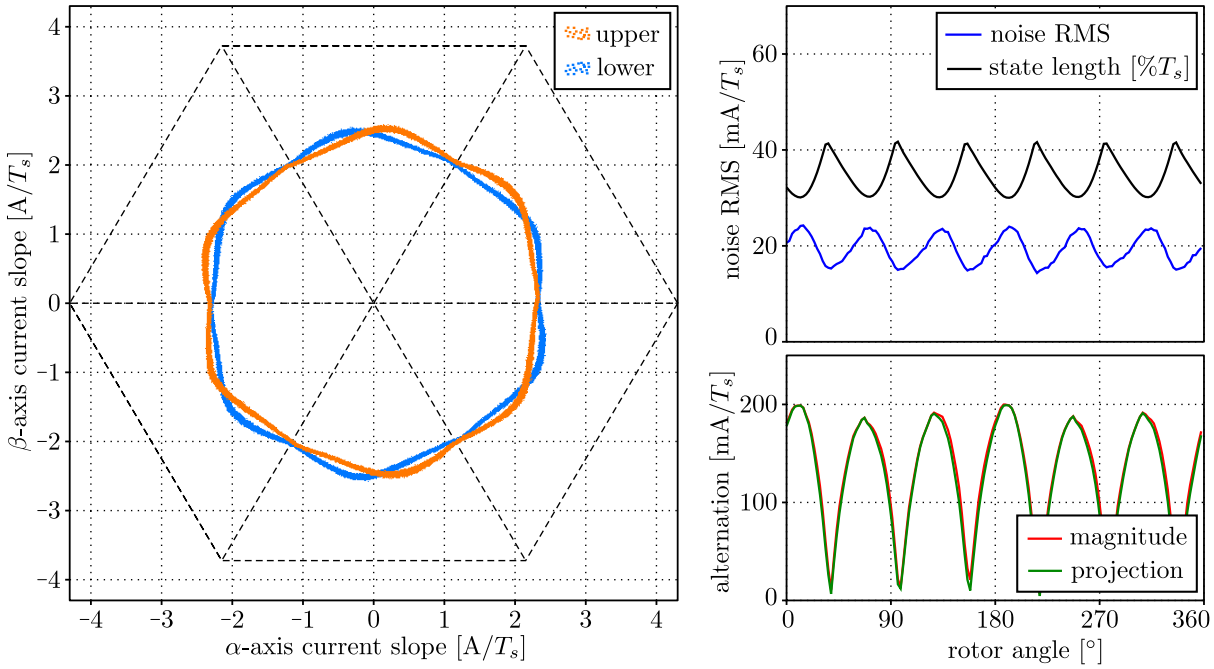

Figure 5.10: *PSS current slope due to EMF at nominal speed.*

but with a significantly smaller magnitude. As the blue and the red curve in the right hand side graphs of Fig. 5.10 show, the alternation magnitude in this case is up to 10 times larger than the noise RMS and generates up to 10% of the measured slope.

Generally, those right hand side plots show how noise and alternation evolve over one electrical rotor revolution. The noise content changes with the length (application time) of the PSS since the number of implied current samples changes. As indicated in black colour, this length naturally varies over rotor position, because the rotating voltage vector with (more or less) constant magnitude must be composed of different active vector directions.

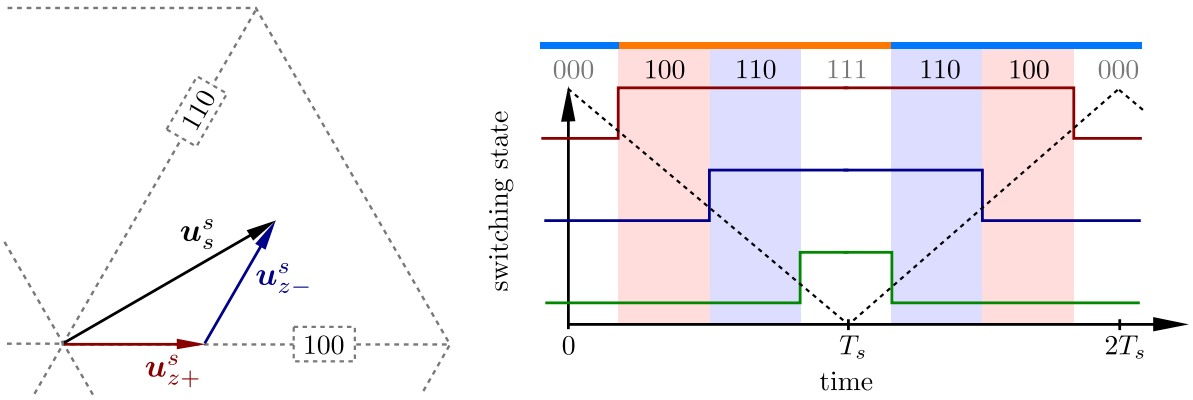

Figure 5.11: *Vector composition in SVM, resulting switching state sequence in symmetric PWM, and alternation colour (orange and light blue) assignment depending on counter direction.*

Fig. 5.11 exemplifies this composition of the stator frame voltage $\boldsymbol{u}_s^s$ by two ASS vectors $\boldsymbol{u}_{z+}^s$ and $\boldsymbol{u}_{z-}^s$, which forms the basis of SVM. The length of the coloured vectors represents the application time of their respective switching states (see right hand side of Fig. 5.11). Hence, for geometrical reasons, the same voltage magnitude $|\boldsymbol{u}_s^s|$ requires more overall active time in the sector middle than at the sector edge, which explains the varying PSS length. The strong variation of the alternation magnitude in Fig. 5.10 cannot be explained by the varying PSS length and will, hence, be investigated later.

Looking at the current slope of the positive ASS (one phase at U_{DC}, two at ground potential), indicated in Fig. 5.12, the alternation is much more obvious and the trajectories seem to burst at their ends. Here the alternation results from the difference between an

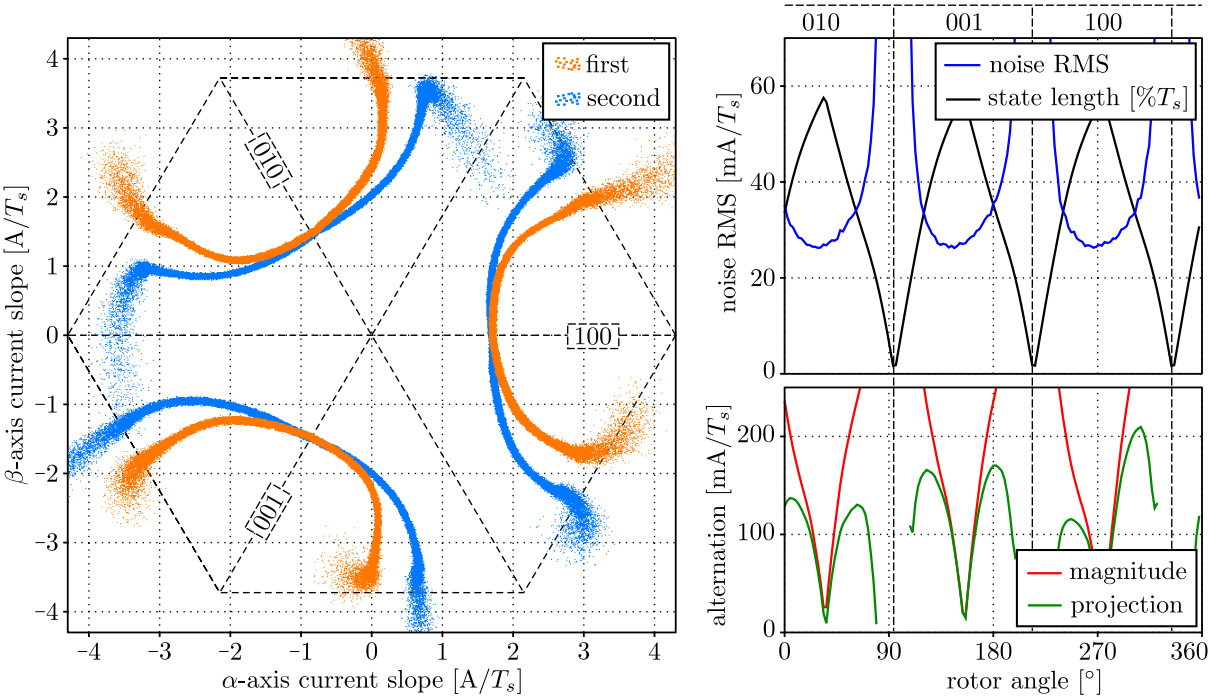

Figure 5.12: *Current slope during positive ASS distorted by EMF at nominal speed.*

ASS being applied as first or as second ASS within the PWM half-interval. Hence, this time those two cases comprise the exact same switching state that only differs in its past – a clear evidence for later derivations.

Again, the noise content increases with decreasing switching state length. However, at certain sector bounds, the ASS length becomes zero, which, as indicated in the upper right graph of Fig. 5.12, causes a huge increase of the noise content. In the left hand side graph of Fig. 5.12 this increase in noise causes the burst at the trajectory ends.

Also the magnitude alternation increases strongly towards the trajectory ends – much stronger than for the PSS, as can be seen by the red graph in Fig. 5.12. It is, however,

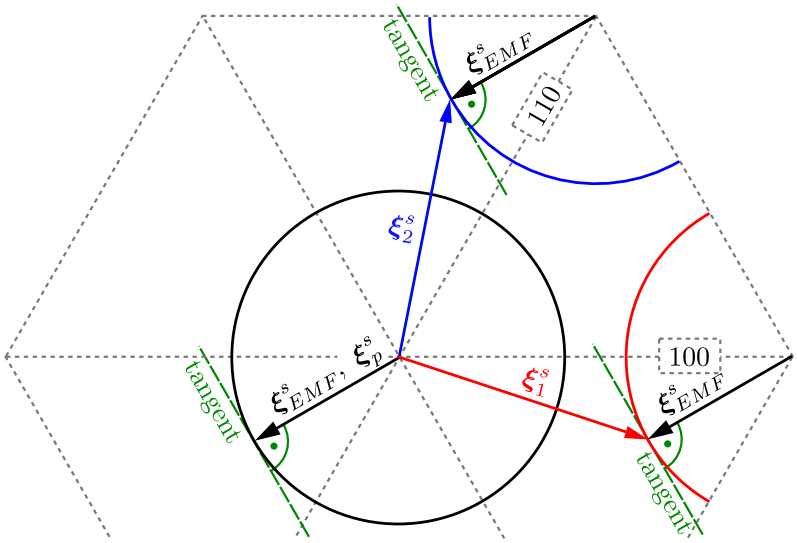

Figure 5.13: *Projection on the tangential direction of the measured current slope.*

interesting to note that the projection of the alternation on the relevant direction is in the same scale as the alternation of the PSS slope.

The phrase *relevant direction* refers to the tangential component of the circular trajectory shape, because this eventually affects the EMF-based angle estimation. As indicated in Fig. 5.13, the EMF-induced current slope $\boldsymbol{\xi}^s_{EMF}$ is the only slope component during the PSS (approximately), and adds to one of the active slope vectors, represented by hexagon

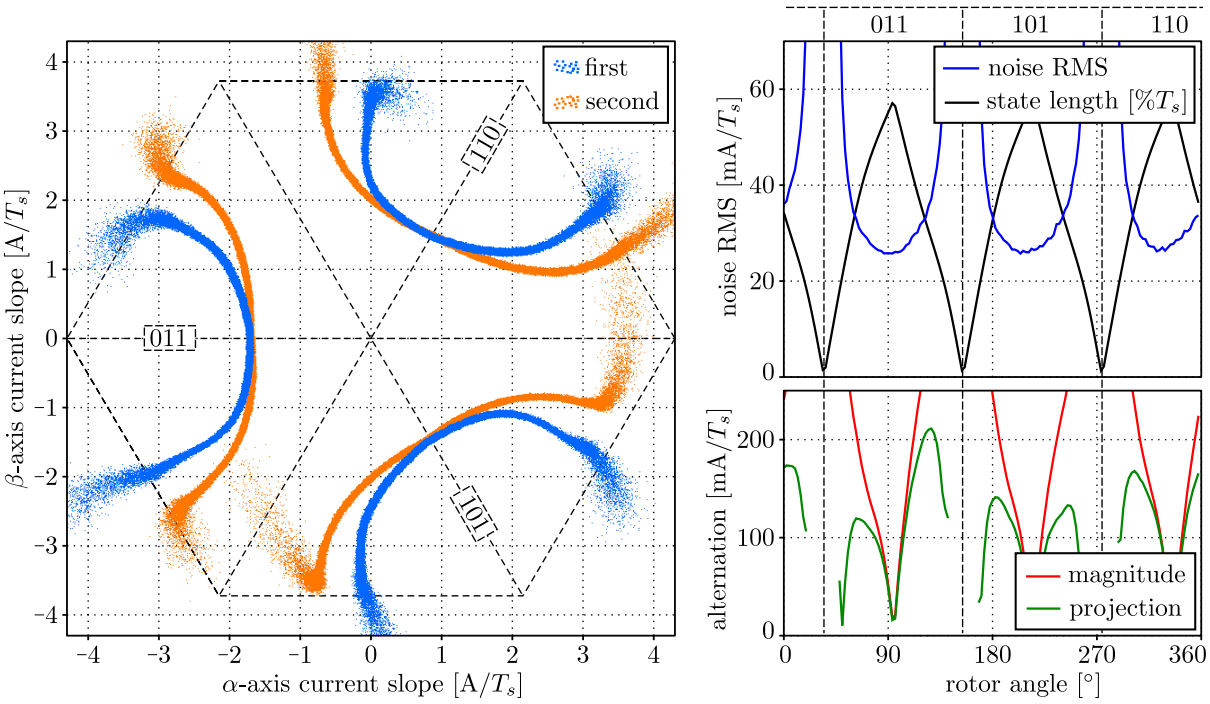

Figure 5.14: *Current slope during negative ASS distorted by EMF at nominal speed.*

corners, during the ASSs. Hence, ideally, the PSS slope trajectory forms an origin-centred circle and the ASS slope trajectories form shifted third-circles, centred around the hexagon corners. The relevant direction for the EMF angle evaluation is the perpendicular to the measured EMF slope and is indicated by the green dashed tangents in Fig. 5.13.

Fig. 5.14 shows the evaluation of the slope approximation for the negative ASSs (two phases at U_{DC}, one at ground potential) which, apart from the 180° shift of all quantities with respect to the electrical rotor angle, shows identical effects in comparison to the positive ASS.

However, one question remains: what causes this strong alternation? Since it is much stronger than the winding recharge currents, it must relate to a different physical effect. We already noted that the alternating cases are identical switching states that only differ in their past. This hints that dynamic effects, such as eddy currents, could be the reason. In order to investigate the influence of eddy currents on the linear approximation, the simple eddy current model from Ch. 2.6 is employed.

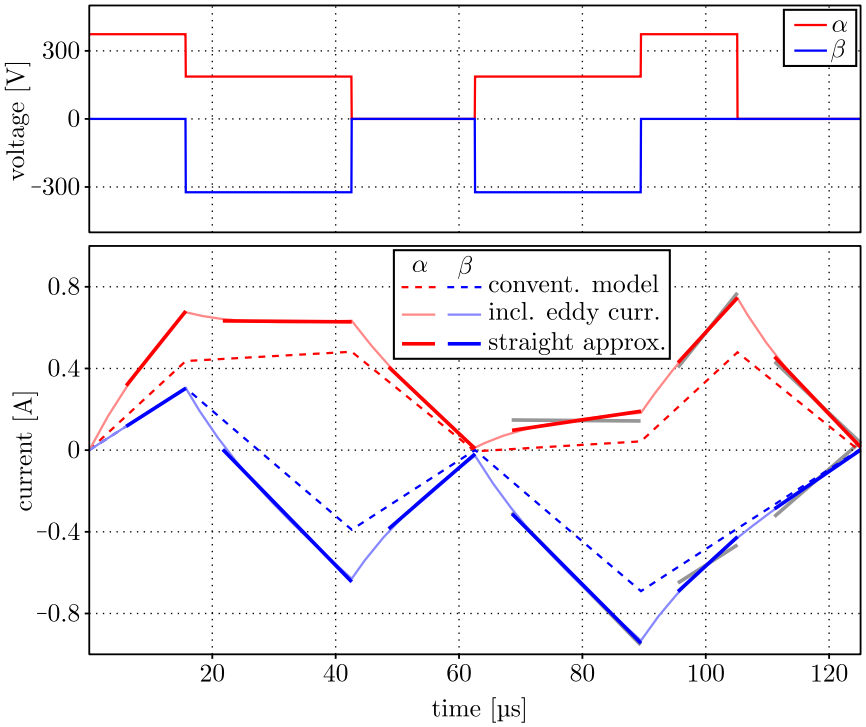

Figure 5.15: *One PWM cycle current simulation with conventional- and eddy current model, and resulting linear approximation.*

For each dot in Fig. 5.10, 5.12 and 5.14 the pulse widths have been recorded, from which the switching pattern could be reconstructed (top graph in Fig. 5.15). Using this voltage evolution, a simulation of one PWM cycle has been carried out for every angle interval, assuming that the applied voltage exactly compensates the EMF, i.e. that the current

eventually reaches its initial value again. As indicated in Fig. 5.15, the current simulated with a conventional machine model evolves on nearly straight lines, while the eddy current model, parametrized according to Ch. 4.2.4, shows clearly exponential evolutions. After blinding out the first 6 µs, the remaining current evolution of each switching state has been approximated with linear regression, resulting in the thickly drawn straights in Fig. 5.15. The slopes of the approximation straights are clearly different from the slopes of the conventional model current evolution. Moreover, the approximated slopes in the second half-period are different from the ones in the first-half period, which is demonstrated through the grey copies of first half-period slopes.

This difference results from the fact that the sequence of applying ASSs is interchanged in between the half-periods (see Fig. 5.11). Since for each switching state there is a specific steady state value that the eddy currents converge towards, the eddy current value at the end of a switching state is more or less fixed. The initial eddy current value at the beginning of a switching state, however, depends mainly on the previous switching state. Hence, the transition between initial and eventual value, and hence the approximated slope, depend on the excitation difference between the previous and the current switching state.

The above simulation (Fig. 5.15) has been carried out for 150 (evenly spaced) rotor positions, using the pulse widths that have been recorded during the above measurements

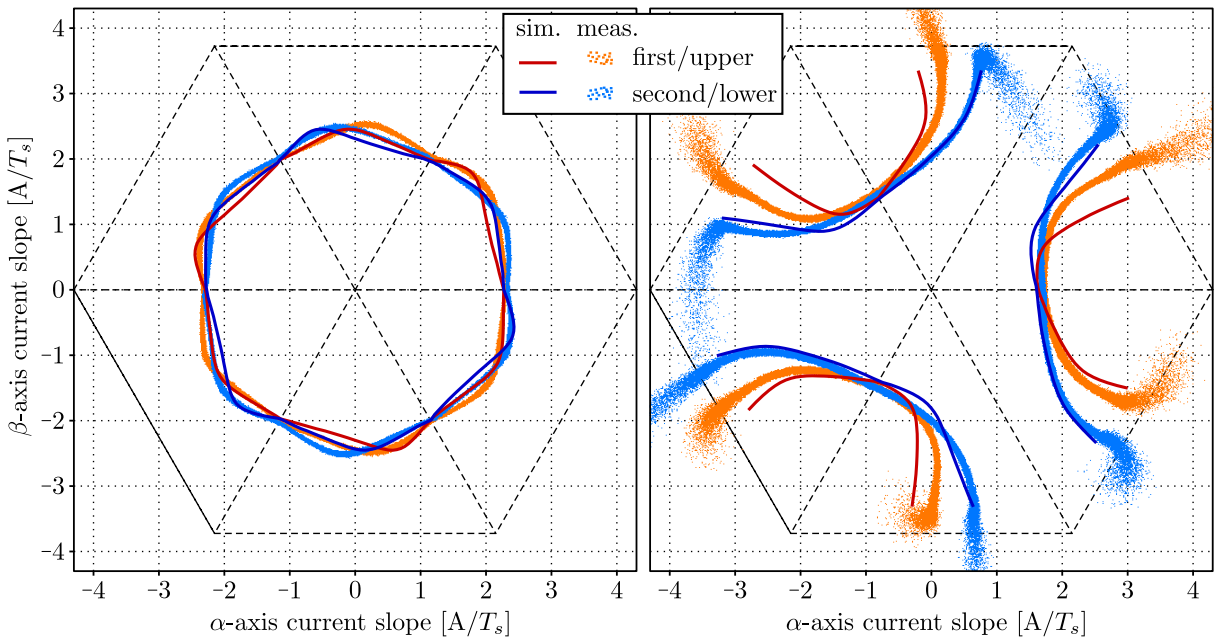

Figure 5.16: *Passive and positive active slopes in stator frame over one rotor revolution – comparison between measurement and eddy current simulation.*

(averaged for each angle interval) and the admittance and eddy current parameters from Ch. 4.2.4. The resulting simulated current slope trajectories in stator frame for the PSS and for the positive ASS are indicated in Fig. 5.16. For both switching states the simulation develops a qualitatively similar alternation to the measurements, but in a slightly different scale and also including a slight asymmetry. The scale can be explained by the simplicity of the eddy current model which does not include any distribution characteristics or the superposition of multiple fade out times, such that already in Fig. 4.10 a difference between the simulation and the measured slightly non-exponential fade out process could be noticed. The asymmetry results from the asymmetric excitation, also visible in the state length evolution in Fig. 5.10, 5.12 and 5.14. Here it is not clear why this asymmetry does not affect the measurement. However, since the purpose of the simulation is to scrutinize whether or not the presence of eddy currents could explain this strong alternation of the slope values, the qualitative conformance of both curves clearly affirms this hypothesis. Hence, a further model refinement to achieve also quantitative conformance, will not be pursued.

Finally, the evolution of noise and alternation of the slope approximation over rotor speed is analysed. Fig. 5.17 shows how both quantities evolve for two different surface

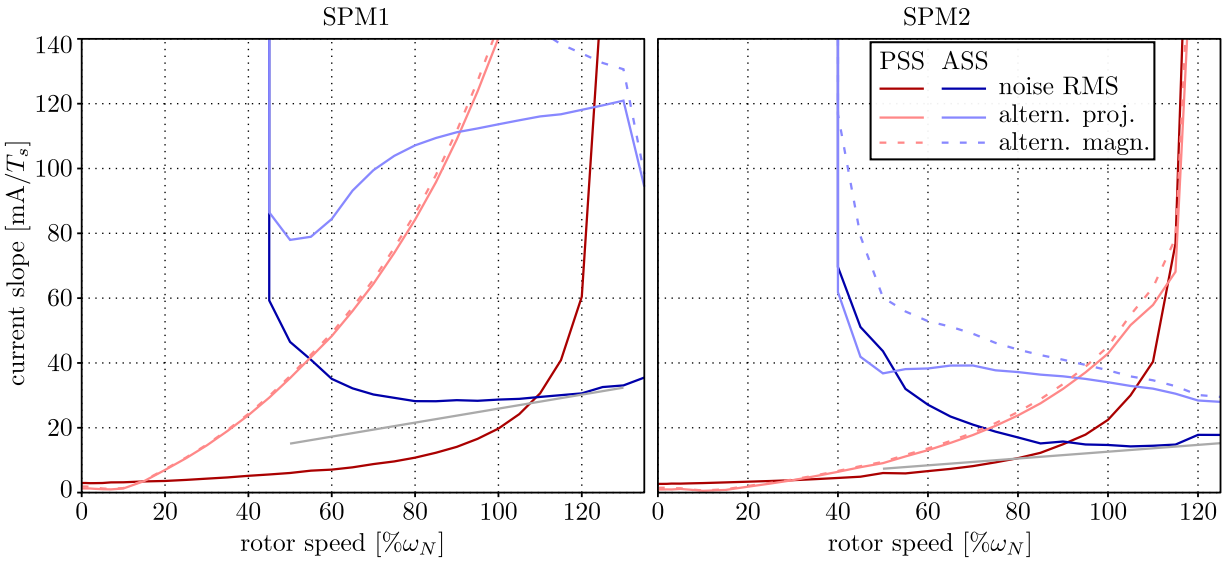

Figure 5.17: *Noise and alternation of PSS and ASS over rotor speed, within the range of feasible sinusoidal voltage generation.*

mounted PMSMs. By trend the PSS length decreases and the ASS length increases with increasing rotor speed, which explains the orientation of each hyperbolic noise curve. In particular, the analysis of the ASS has been carried out involving only one switching state at any instant: that one positive or negative ASS that has been applied the longest within

the considered PWM half-interval. Yet, the application time varies with the rotor position and hence does also the noise content, for which the overall RMS value is indicated here.

It is interesting to note that for both machines the PSS noise (dark red) curves are similar, whereas the ASS noise (dark blue) settles at different levels which are both markedly higher than the PSS noise at low speed. The left hand side graph eventually shows even an increase in ASS noise with increasing rotor speed, although then the ASS becomes longer and more current samples are involved. The reason for this effect lies in the ripple of the DC link voltage (caused by the diode bridge rectification) which induces a proportional variation of the ASS current slope. Since this variation is not accounted for, it is seen simply as a deviation from the average value by the RMS analysis and, hence, interpreted as noise. The DC link voltage ripple in free-wheeling condition showed a linear increase over speed, reaching $\pm 6\,\mathrm{V}$ at rated speed. Using the admittance of the machines, this voltage ripple is translated into an expected DC link induced current slope variation, the RMS of which is indicated by the grey curves in Fig. 5.17. The convergence of the ASS noise towards these expected grey curves affirms that a DC link induced slope variation explains the increased ASS noise content at high speed. Whilst in free-wheeling condition the ripple causes only a 0.6% RMS variation of the slope, in worst case load condition the much stronger ripple may cause up to 4% RMS variation. It is, hence, very important to take the DC link voltage into account when evaluating the ASS current slopes.

Furthermore, the second machine shows markedly less alternation than the first machine, which has to be regarded in relation to the different machine admittance. At rated speed the alternation of the first machine amounts 2.55% of the standstill ASS slope, whereas this relative value for the second machine is 1.66%. The remaining factor 1.5 in between both machines can be explained by different machine design or lamination thickness etc. and will not be investigated further. In summary, however, it is interesting to note that the alternation is mainly machine dependent, whereas the noise content seems nearly independent of the machine.

In particular, the noise content is expected to depend mainly on the switching state length since this designates the amount of current samples employed in the regression. Fig. 5.18 visualizes the relation between the switching state length and the noise content of the ASS and PSS. While the duration of the PSS around standstill can reach 100% of the sampling period T_s, no ASS of more than 77% length was required within the sinusoidal voltage range (no overmodulation). Hence, the ASS curve stops at this point.

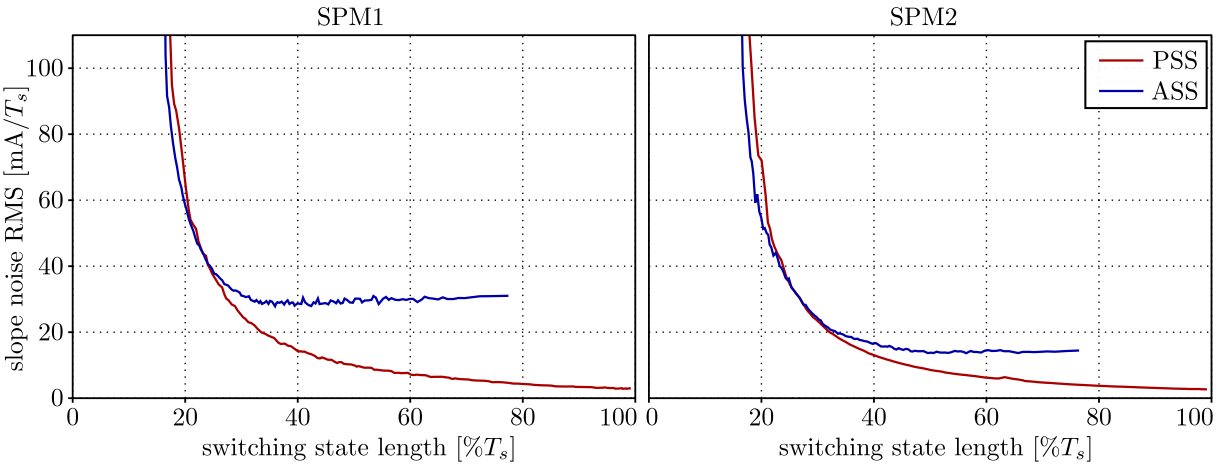

Figure 5.18: *Noise RMS of PSS and ASS current slope approximation depending on switching state length.*

5.4.4 Comparison to the theoretical expectation

According to the theoretical considerations in Ch. 5.3, the noise RMS of the straight offset should qualitatively scale by $\frac{1}{\sqrt{n}}$ with the switching state length and the noise RMS of the straight slope by $\frac{1}{n^{3/2}}$, where n is the number of involved samples. Quantitatively, the noise RMS of the straight offset should be $\frac{1}{33}$ times lower and the noise RMS of the straight slope should be $\frac{1}{10T_s}$ times lower than the noise of the sampled current if the switching state amounts the entire PWM half-period.

However, when analysing the measured noise curves in Fig. 5.9 and 5.18, we find the expected qualitative evolutions but not the expected quantitative values. As stated in Ch. 5.4.1, the measured full length noise reduction factor for the straight offset is $\frac{1}{7.3}$ and for the straight slope $\frac{1}{2.2T_s}$ which is both about 4.5 times higher than predicted by theory. This significant deviation from theory will be analysed and explained through the comparison of the following two Figs. 5.19 and 5.20.

The top graph of Fig. 5.19 shows a 1ms capture of the FPGA internal α-axis current signal (16,384 samples at 20 MHz) that has been recorded while the current sensor was *disconnected* from the ADC. Then only the A/D-conversion noise [88] is measured which had an RMS value of 2.09 mA and a nearly white spectrum, as can be seen from the lower graph in Fig. 5.19. The red curve in the upper graph is the result of a moving average filter with a window width of 1100 samples (entire PWM half-period minus blind-out time), showing a reduced RMS value of only 0.097 mA. The ratio between both is 21.45 which is nearly two thirds of the noise reduction factor predicted by theory.

The top graph of Fig. 5.20 shows the same α-axis current signal that has been recorded after the current sensor was re-connected to the A/D-converter (normal drive setup but

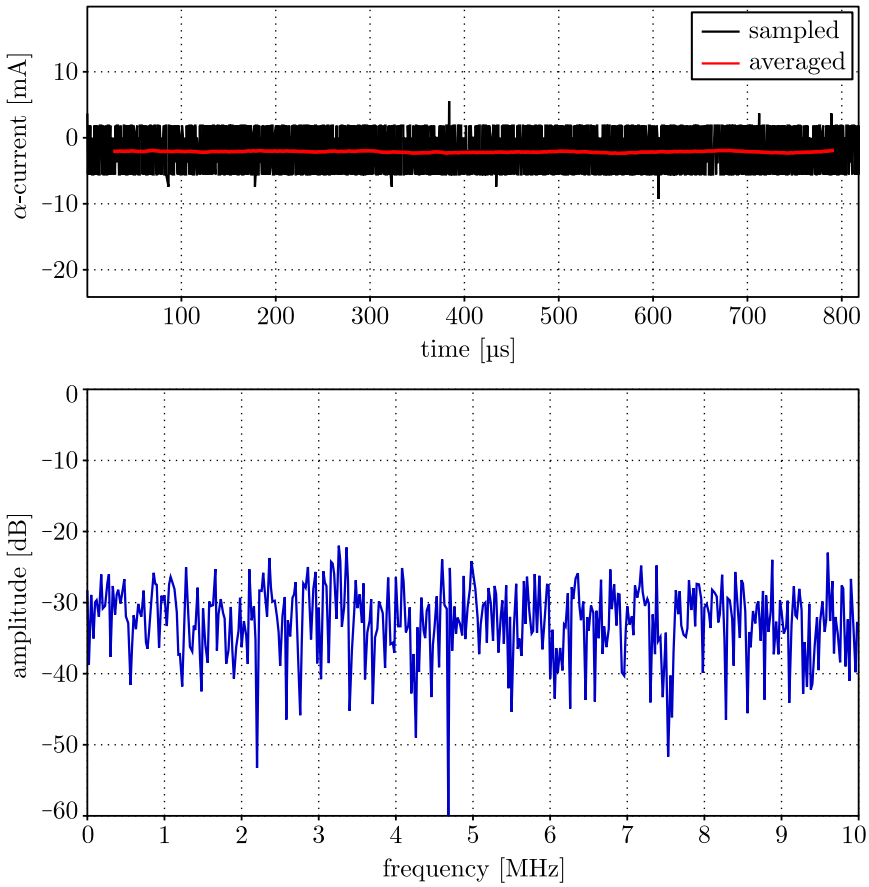

Figure 5.19: *Current measurement with current sensors disconnected.*

without PWM). Apart from the 114 mA offset, now the noise band is increased with respect to the disconnected case, showing an RMS value of 4.13 mA. This additional noise is consequently caused by the current transducer. It is, however, more interesting to note that the frequency spectrum of this current signal (bottom graph) is not white anymore but shows a peak around 6 MHz and an even bigger increase towards low frequencies, while the other frequency bands appear nearly unchanged. This constitutes a major deviation from the assumptions made in Ch. 5.4.1.

The disproportionate increase in the low frequency range deteriorates the noise filtering potential. Practically spoken, the averaging process over one PWM half-period is unable to suppress frequency components below PWM frequency. As a result, the red graph in Fig. 5.20 still comprises a nearly unchanged low frequency variation with 0.57 mA RMS. Hence, in this non-white case the noise reduction factor is only 7.25 which conforms to the experimentally determined value.

In a simplified summary, the resulting noise RMS of the linear approximation can be considered as a combination of the suppressible noise of the A/D conversion and the unsuppressable signal variation of the current transducer (see Fig. 5.21). Without

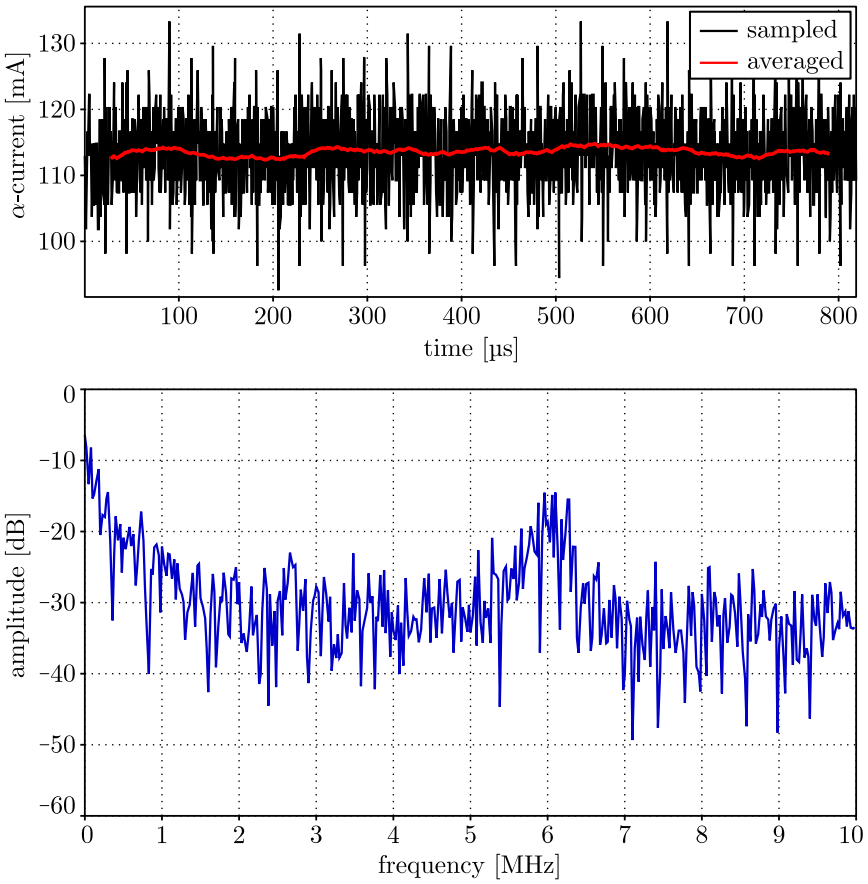

Figure 5.20: *Current measurement with current sensors connected, same frequency plot normalization as in Fig. 5.19 (*2.09 mA*).*

averaging, the ADC noise is much stronger than the sensor signal variation, such that the latter is negligible for conventional sampling techniques and has not been noticed during the analysis in Ch. 4.2. For high OSRs, however, the ADC noise can be suppressed to such an extent that the resulting linear approximation noise is solely generated by the sensor signal variation.

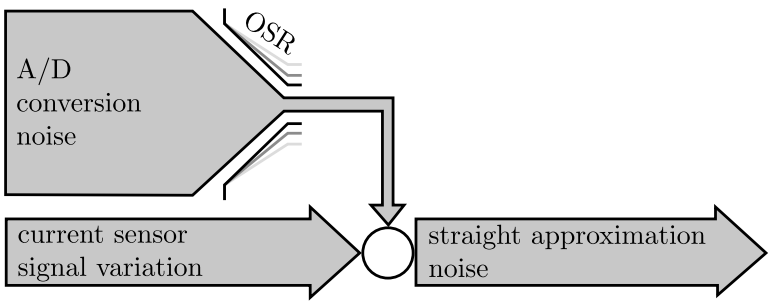

Figure 5.21: *Illustration of the simplified summary.*

The factor 4.5 between theoretical and experimental RMS in this work indicates that the 20 MHz oversampling reduces the ADC noise already 4.5 times below the sensor signal variation and that a further increase of the OSR would not improve the signal quality anymore. In fact, the noise dependency on $\frac{1}{\sqrt{n}}$ (see Ch. 5.3) would allow a reduction of the OSR by factor $4.5^2 = 20.25$ – i.e. down to 1.0 MHz. Only then would the ADC noise be in the scale of the sensor signal variation, which could be considered as economically reasonable dimensioning.

It is at this point important to note that in the test bench of this work, magneto-resistive current transducers CMS3015 from SENSiTEC have been employed. Not at least due to their new appearance on the market, these sensors are still somewhat more expensive than hall-compensation based transducers. However, during the hardware design phase of this work the output signals of various current sensor types and brands have been compared empirically, where the above mentioned magneto-resistive transducers showed clearly the best signal quality and bandwidth. As has been shown in this section, this aspect is very important to take into consideration when designing the hardware of a high performance sensorless control drive. In composition with oversampling-based techniques, mainly the signal quality of the current sensor is what restricts the possible injection magnitude reduction.

Chapter 6

Position estimation

As deduced in the previous chapters, the phase currents of a VSI driven synchronous machine are oversampled and approximated by one stator frame straight for each switching state. Hence, for the three switching states in one PWM half-period, there will be up to three two-dimensional low-noise slope $\boldsymbol{\xi}_s^s$ and offset $\boldsymbol{i}_o^s$ coefficients available per control interval – one pair for every sufficiently long switching state.

In this chapter different techniques will be proposed to deduce the rotor position from the approximated straight coefficients and their relation to the applied voltage. At low speed the anisotropy of the inductance will be exploited using the Arbitrary Injection method. As will be shown, this is only reasonable when reconstructing the ASS slope from the PSS information using the so-called PSS extension. At high speed the rotor position will be deduced from the EMF orientation which for SPMSMs can be obtained in a parameter-free way from the PSS current slope $\boldsymbol{\xi}_p^s$. In this case an (inverse) extension will deduce the PSS slope from the ASS coefficients, in order to allow for operation at very high speed (very short PSSs) as well.

All derived position estimation techniques will be validated by experiments, where especially the resulting signal to noise ratio (SNR) will be essential. In literature there are different definitions of the SNR. One [88, p. 92] is power-based and defined as the ratio between the squared signal magnitude and the variance of the signal μ^2/σ^2. The other one [88, p. 969] is magnitude-based and defined as the ratio between the effective value of the signal and the noise RMS (for Gaussian noise the standard deviation)

$$s = \frac{\mu}{\sigma}. \tag{6.1}$$

Since in the context of A/D conversion rather the second one is used, this work will align with this convention. This definition will be relevant for the interpretation of the SNR

graphs in this section and especially for the derivation of the fusion technique in Ch. 7.1.

In the following, firstly the position estimation for low speed and standstill will be derived and validated experimentally, after which the different options for position estimation in the presence of rotor speed will be considered and discussed. The logical conclusion leads to the selection of one source of information, for which an extended estimation technique will be derived and validated experimentally as well. The eventual selection of oversampling-based position estimation techniques and their experimental validations will form the basis for the later estimate fusion techniques proposed in Ch. 7 and the resulting entire speed range sensorless control.

6.1 Position estimation close to standstill

Sensorless control for low speed and standstill is based on the (assumedly) rotor fixed inductance anisotropy. As described in Ch. 3.2.1, Arbitrary Injection methods [16, 71] extract the anisotropy position information from the current response to an active voltage. Hence, the current slope $\boldsymbol{\xi}_z^s$, obtained from the regression during an ASS, should contain the required information.

However, as discussed in Ch. 4.2.2 and also in [12], in the first phase after a switching state transition, cable recharging currents distort the slope calculation, resulting in the decision to ignore the first 120 current samples. Thus, for ASSs shorter than 8.8% of the sampling time T_s, the ASS regression does not provide any results. An injection of this magnitude would, however, in many drives be sufficient for position estimation based on SCS, which would defeat the idea of utilizing the oversampling-based gain in signal quality to lower the injection magnitude.

Yet, the current slope during the ASS can be reconstructed from the approximation straights of the surrounding PSSs when taking the respective switching times into account. At low speed and low injection magnitude the PSS amounts almost the complete sampling period, assuring a high number of current samples being employed for the linear approximation.

Hence, at first the theory for this PSS extension will be derived, after which this section will explain how to incorporate the high quality PSS-regression based current slopes into an Arbitrary Injection scheme.

6.1.1 The passive switching state extension

In creating relations between the regression data of different sampling intervals and the voltage reference that leads to the respective switching instances, we are technically considering the point where the FPGA data is merged into the CPU. It is herein indispensable to take the particular timing relations of the RTS into account. Besides the actual derivation of the passive switching state (PSS) extension, this section will therefore devote high attention to the placements of the signals in time.

Fig. 6.1 exemplifies the PWM reference signals, the current measurement and the regression results over two and a half sampling periods T_s. The time $t = 0$ is defined as the instant where the current CPU control interrupt is triggered by the peak of the PWM triangle counter (situated in the FPGA). This is the point where the actual synchronous current samples $\boldsymbol{i}^s_{s0}$ are taken, where the encoder angle θ_0 would be captured and from where on the voltage $\boldsymbol{u}^s_{s0}$ will be applied. This voltage $\boldsymbol{u}^s_{s0}$ has been the control result of the previous period, based on the current samples $\boldsymbol{i}^s_{s1}$, taken at $t = -T_s$. Hence, an additional subscript will be used to indicate how many sampling cycles T_s a certain quantity is located in the past.

As a didactical simplification, the slight dead time in between voltage and current measurement (see Ch. 4.2.1) will be neglected in this section. Apart from complicating the illustration, it would, if considered, anyhow be cancelled out during the mathematical derivation and therefore not affect the results of this section.

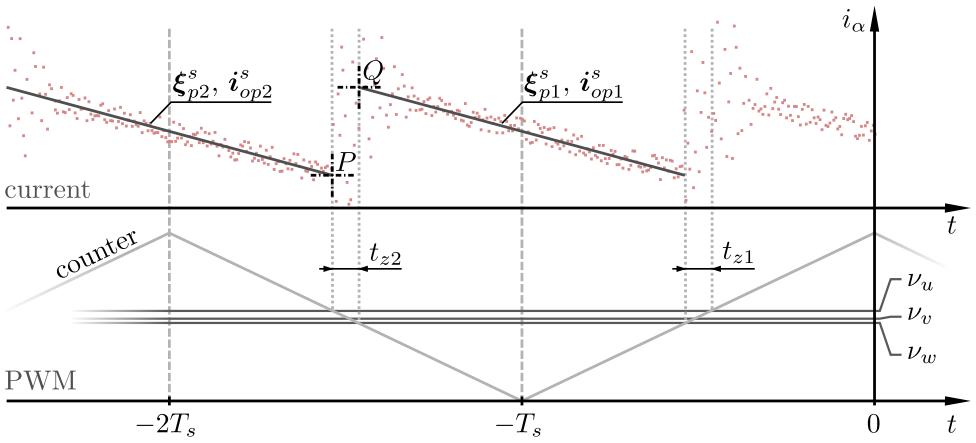

Figure 6.1: *ASS current slope reconstruction from PSS parameters.*

The close placement of the terminal pulse widths ν_u, ν_v and ν_w make Fig. 6.1 a low voltage situation in which there are no regression results for the ASSs. There is also no regression result for the current PSS, located around $t = 0$, since the respective regression process will only be finished around $\frac{1}{2}T_s$ in the future. Hence, the youngest available

regression result belongs to the PSS located around $t = -\mathbf{T}_s$, represented by the grey straight within the red dots for the current samples. These youngest results comprise of the current slope $\boldsymbol{\xi}^s_{p1}$ and the offset $\boldsymbol{i}^s_{op1}$, in which the subscript p denotes the assignment to the PSS.

The idea of the PSS extension is to reconstruct the ASS current slope during t_{z2} by utilizing the surrounding PSS regression results. While under low voltage condition the ASSs are too short, the PSS amounts almost the complete sampling period T_s. Hence, with the present system, more than 1,000 current samples are incorporated, resulting in very accurate PSS straight parameters $\boldsymbol{\xi}^s_p$ and $\boldsymbol{i}^s_{op}$.

In order to reconstruct the ASS current slope $\boldsymbol{\xi}^s_{z2}$, the points $P = [t_P,\ \boldsymbol{i}^s_P]^\top$ and $Q = [t_Q,\ \boldsymbol{i}^s_Q]^\top$ are introduced (see Fig. 6.1) which represent the intersections between the accurately known PSS straights and the unknown ASS straight. The locations in time of those points P and Q are determined from the pulse width reference for the respective intervals

$$t_{z2} = \max(\nu_{u2}, \nu_{v2}, \nu_{w2}) - \min(\nu_{u2}, \nu_{b2}, \nu_{w2}) \tag{6.2}$$

$$t_P = -\tfrac{3}{2}T_s - \tfrac{1}{2}t_{z2} \tag{6.3}$$

$$t_Q = -\tfrac{3}{2}T_s + \tfrac{1}{2}t_{z2}, \tag{6.4}$$

implying the assumption that the ASS phase is placed centric within the PWM half-interval[1].

Considering that the point P is located at the end of the regression window 2 and Q at the beginning of the regression window 1, the ordinates are obtained from the respectively parametrized straight equations

$$\boldsymbol{i}^s_P = \boldsymbol{\xi}^s_{p2}\left(T_s - \frac{t_{z2} + t_{z3}}{2}\right) + \boldsymbol{i}^s_{op2} \tag{6.5}$$

$$\boldsymbol{i}^s_Q = \boldsymbol{\xi}^s_{p1}\ 0 + \boldsymbol{i}^s_{op1}. \tag{6.6}$$

Finally, the mean current slope during the presence of the ASSs, $\boldsymbol{\xi}^s_{z2}$, is reconstructed

[1]This assumption is inherently fulfilled at low and medium voltage conditions when using a standard SVM. However, it does not hold for the more simple sinus-triangle based PWM generation techniques and not under voltage limitation or especially flat top modulation. For applying the PSS extension without this assumption, the exact switching times of the first and the last phase must be computed.

using the difference between the points P and Q

$$\boldsymbol{\xi}_{z2}^{s} = \frac{\boldsymbol{i}_{Q}^{s} - \boldsymbol{i}_{P}^{s}}{t_Q - t_P} \tag{6.7}$$

$$= \frac{\boldsymbol{i}_{op1}^{s} - \boldsymbol{i}_{op2}^{s} - \boldsymbol{\xi}_{p2}^{s}\left(T_s - \frac{t_{z2}+t_{z3}}{2}\right)}{t_{z2}}. \tag{6.8}$$

Due to the high number of current samples involved in the approximation of the passive straight parameters, this reconstructed ASS current slope $\boldsymbol{\xi}_{z2}^{s}$ has very low noise content and is able to resolve current differences far below the quantization of the ADC.

6.1.2 Elimination of the fundamental current slope

According to the nonlinear model (2.38), the current slope measured through (6.8) is the result of all voltage components, the terminal voltage, the resistive voltage and the extended EMF

$$\boldsymbol{\xi}_{z2}^{s} = \mathbf{Y}_{s}^{s}\boldsymbol{u}_{z2m}^{s} - \mathbf{Y}_{s}^{s}\left(R_s\boldsymbol{i}_{s}^{s} + \mathbf{J}\omega\boldsymbol{\psi}_{s}^{s} - \mathbf{L}_{s}^{s}\mathbf{J}\omega\boldsymbol{i}_{s}^{s}\right), \tag{6.9}$$

where $\boldsymbol{u}_{z2m}^{s}$ is the average voltage during the ASSs. Since this average value results from a weighted geometrical summation of two active vectors, the magnitude of $\boldsymbol{u}_{z2m}^{s}$ is within the range $\frac{\sqrt{3}}{3}U_{dc} \leq |\boldsymbol{u}_{z2m}^{s}| \leq \frac{2}{3}U_{dc}$. Its exact value can simply be calculated from the reference voltage $\boldsymbol{u}_{s}^{s}$ when considering that the overall voltage-time-face $\boldsymbol{u}_{s2}^{s}\mathbf{T}_s$ is imposed only within the active time t_{z2}

$$\boldsymbol{u}_{z2m}^{s} = \frac{T_s}{t_{z2}}\boldsymbol{u}_{s2}^{s}. \tag{6.10}$$

In order to estimate the anisotropy position, the first term of (6.9) must be segregated. As described in Ch. 3.2.1, Arbitrary Injection [67] assumes the right hand side term, referred to as fundamental model (FM) current slope, to be constant within two sampling intervals and eliminates it by subtracting two consecutive equations (6.9).

However, when using current oversampling, this right hand side term can be directly measured during the PSS, as it equals the current slope equation (6.9) for zero voltage

$$\boldsymbol{\xi}_{FM}^{s} = \frac{\boldsymbol{\xi}_{p1}^{s} + \boldsymbol{\xi}_{p2}^{s}}{2} \tag{6.11}$$

$$= -\mathbf{Y}_{s}^{s}\left(R_s\boldsymbol{i}_{s}^{s} + \mathbf{J}\omega\boldsymbol{\psi}_{s}^{s} - \mathbf{L}_{s}^{s}\mathbf{J}\omega\boldsymbol{i}_{s}^{s}\right). \tag{6.12}$$

In particular, (6.11) implies that the FM current slope value at the exact time of the ASS

$z2$ should be averaged from the values of the surrounding PSSs.

By subtracting this FM slope (6.11) from (6.8), an EMF free current slope $\boldsymbol{\xi}^s_{u2}$ is obtained that only relates to the terminal voltage $\boldsymbol{u}^s_s$ and the anisotropic admittance $\mathbf{Y}^s_s$

$$\boldsymbol{\xi}^s_{u2} = \boldsymbol{\xi}^s_{z2} - \boldsymbol{\xi}^s_{FM} \tag{6.13}$$

$$= \frac{\boldsymbol{i}^s_{op1} - \boldsymbol{i}^s_{op2} - \boldsymbol{\xi}^s_{p2}\left(T_s - \frac{t_{z2}+t_{z3}}{2}\right) - \frac{t_{z2}}{2}\boldsymbol{\xi}^s_{p2} - \frac{t_{z2}}{2}\boldsymbol{\xi}^s_{p1}}{t_{z2}} \tag{6.14}$$

$$= \mathbf{Y}^s_s \frac{T_s}{t_{z2}} \boldsymbol{u}^s_{s2}. \tag{6.15}$$

By cancelling the denominator t_{z2} and summarizing the numerator, (6.14) is rewritten in a more intuitive way

$$\Delta\boldsymbol{i}^s_{u2} = \mathbf{Y}^s_s T_s \boldsymbol{u}^s_{s2} = \left[\boldsymbol{i}^s_{op1} - \boldsymbol{\xi}^s_{p1}\frac{t_{z2}}{2}\right] - \left[\boldsymbol{i}^s_{op2} + \boldsymbol{\xi}^s_{p2}\left(T_s - \frac{t_{z3}}{2}\right)\right]. \tag{6.16}$$

Eq. (6.16) represents the current difference between the two PSS straight equations that are both solved for the middle of the ASS (see blue marks in Fig. 6.2). This difference relates exactly to the flux linkage imposed through $\boldsymbol{u}^s_{s2}T_s$.

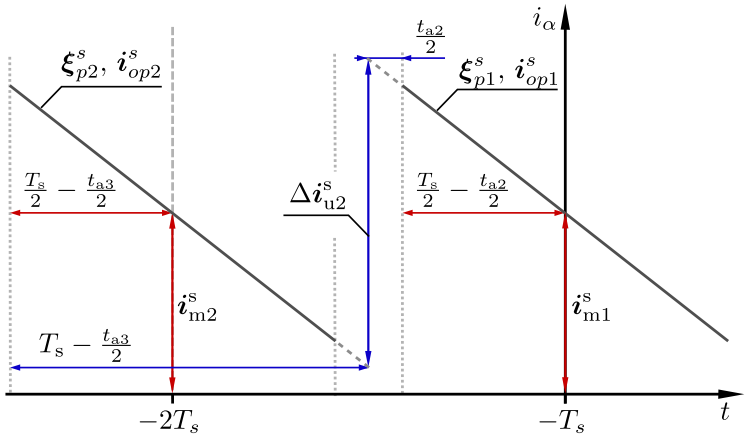

Figure 6.2: *Illustration of* (6.16) *and* (6.17).

Another intuitive way of rewriting (6.16) is

$$\Delta\boldsymbol{i}^s_{u2} = \underbrace{\left[\boldsymbol{i}^s_{op1} + \boldsymbol{\xi}^s_{p1}\frac{T_s - t_{z2}}{2}\right]}_{\boldsymbol{i}^s_{m1}} - \underbrace{\left[\boldsymbol{i}^s_{op2} + \boldsymbol{\xi}^s_{p2}\frac{T_s - t_{z3}}{2}\right]}_{\boldsymbol{i}^s_{m2}} - T_s\frac{\boldsymbol{\xi}^s_{p1} + \boldsymbol{\xi}^s_{p2}}{2}, \tag{6.17}$$

where the terms in brackets (red marks in Fig. 6.2) represent the current values at the synchronous sampling points $-2T_s$ and $-T_s$ and the last term equals the FM current difference over one sampling period T_s.

6.1.3 Experimental evaluation of the regression based anisotropy identification

The Arbitrary Injection algorithm described in Ch. 3.2 identifies the anisotropy from the current response to an arbitrary voltage excitation. Fig. 6.3 shows the results of this identification for a triangular injection with 1.6% magnitude (5.9V), where the same current evolution has been evaluated with the same algorithm, but using different current sampling techniques.

The conventional technique, synchronous current sampling (SCS), results in the red point clouds which for both the mean admittance estimate $[\hat{Y}_{\Sigma x}\ \hat{Y}_{\Sigma y}]^\top$ and the anisotropic current progression $\Delta \boldsymbol{i}_a^s$ show a relatively wide distribution. Due to the scaling of (3.29), the noise in the anisotropic current response $\Delta \boldsymbol{i}_a^s$ directly corresponds to the current measurement noise, while its signal strength varies proportionally with the applied voltage. Hence, the regression based results in Fig. 6.3 (black and blue clouds) show the same diameter/mean value, but a less wide spread distribution.

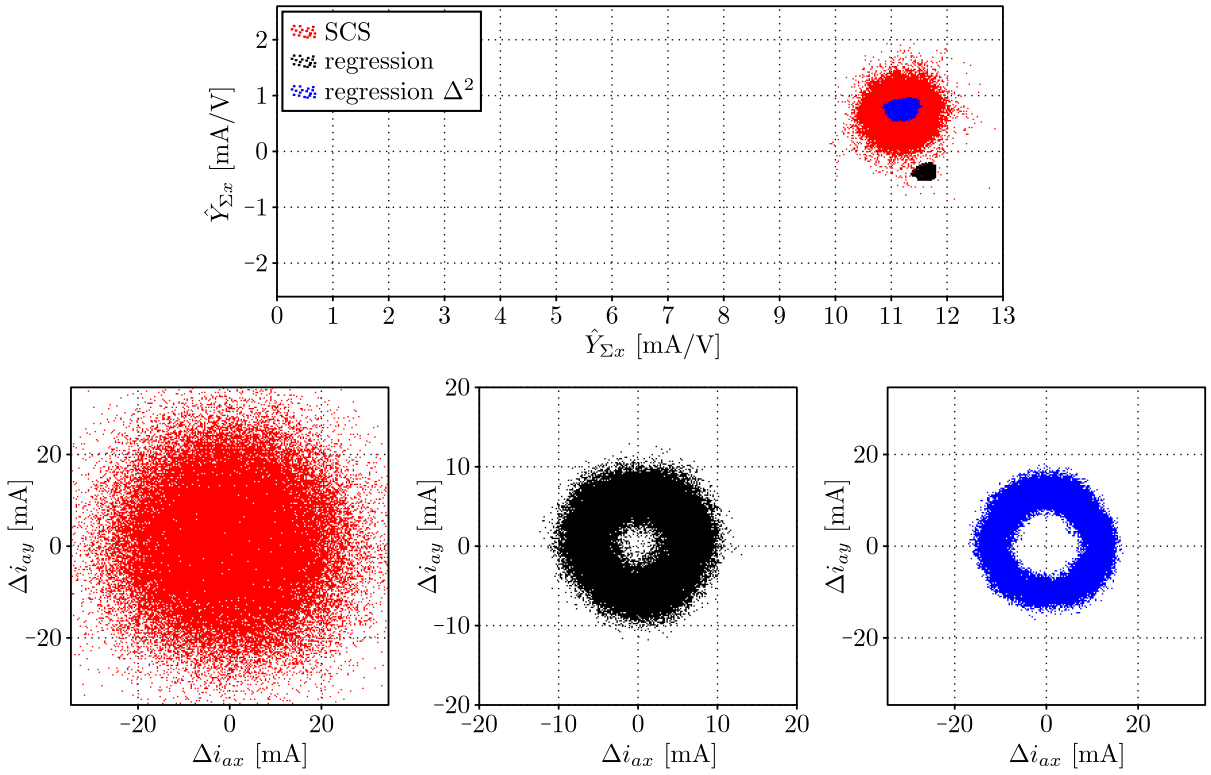

Figure 6.3: *Anisotropy Information at 1.6% injection.*

According to the noise scaling laws introduced in Ch. 5.3, the Δ^2 approach (3.16) for resistance and EMF elimination causes the following scaling of the current signal strength

and noise RMS

$$\mu_{a\Delta^2} = \sqrt{3} Y_\Delta u_{inj} \tag{6.18}$$

$$\sigma_{a\Delta^2} \overset{(3.16)}{=} \sqrt{\sigma_i^2 + (2\sigma_i)^2 + \sigma_i^2} \approx 2.45\sigma_i, \tag{6.19}$$

where σ_i is the current sampling noise RMS and $\sigma_{a\Delta^2}$ and $\mu_{a\Delta^2}$ are the noise RMS and signal strength of the anisotropic current response. Using the results of the current sampling noise analysis in Ch. 5.4.1, the SCS based $\Delta \boldsymbol{i}_a^s$ noise should hence be 13.2 mA. The actual RMS of the red cloud in Fig. 6.3 is 12.7 mA, resulting in an SNR of 0.89.

The regression based anisotropy identification (black cloud) eliminates the EMF by means of (6.17) which results in a different signal and noise scaling

$$\mu_{areg} = Y_\Delta u_{inj} \tag{6.20}$$

$$\sigma_{areg} \overset{(6.17)}{=} \sqrt{2\sigma_m^2 + 2\left(\frac{\sigma_\xi T_s}{2}\right)^2} \approx 0.71\sigma_\xi, \tag{6.21}$$

where σ_ξ and σ_m are the noise RMS values of the approximated current slope and offset, respectively. According to Ch. 5.3 and 5.4.1, the offset noise is markedly smaller than the slope noise $\sigma_m \ll \sigma_\xi T_s$, which justifies the rough simplification at the end of (6.21). Using the results of the approximation noise analysis in Ch. 5.4.1, the regression based noise in $\Delta \boldsymbol{i}_a^s$ should hence have 2.73 mA RMS. The actual RMS of the black cloud in Fig. 6.3 is 2.25 mA, i.e. significantly weaker than the SCS based result. However, as the regression based signal strength is 1.73 times weaker as well (respective scaling of the bottom centred graph in Fig. 6.3), the resulting SNR of 2.85 is consequently (only) 3.2 times higher than the SCS based SNR. In other words, the noise content of the slope value that contributes through (6.17), does not allow to achieve the expected noise reduction potential of about factor 6 that has been predicted in Ch. 5.4.

However, when eliminating the EMF in the regression results by means of the Δ^2 technique (instead of using the PSS slope), the stronger noise of the slope values does not aggravate the anisotropy identification. Then the following signal strength and noise RMS can be expected:

$$\mu_{areg\Delta^2} = \sqrt{3} Y_\Delta u_{inj} \tag{6.22}$$

$$\sigma_{areg\Delta^2} \approx 2.45\sigma_m. \tag{6.23}$$

As the signal strength is identical to the SCS and according to Ch. 5.4.1, the offset noise

$\sigma_m = 0.62\,\mathrm{mA}$ is 6.2 times smaller than the SCS noise $\sigma_i = 3.83\,\mathrm{mA}$, the regression based Δ^2 technique should increase the SNR by factor 6.2. The blue cloud in Fig. 6.3 shows a noise RMS of 2.1 mA, resulting in an actual SNR of 5.35 which is 6.0 times larger than the SCS value.

However, the above relations are only valid for triangular injection without an FOC voltage, because the Δ^2 technique evaluates only the difference between voltages, whereas Eq. 6.17 utilizes mean voltage components as well. Hence, when the FOC provides an additional voltage, the SNR of the pure regression may exceed the Δ^2 results. Yet, when aiming a minimum acoustical noise emission, the regression based Δ^2 will be advantageous.

Fig. 6.4 shows the signal and noise content of the anisotropic current progression $\Delta \boldsymbol{i}_a^s$ depending on the injection magnitude. As explained above, the Δ^2 based EMF elimi-

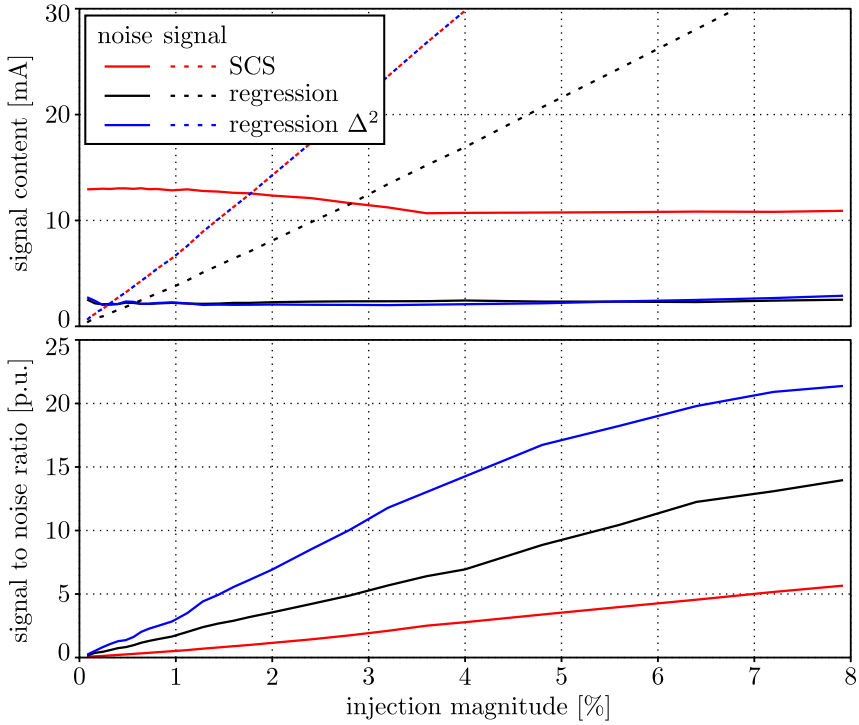

Figure 6.4: *Signal and noise content of the anisotropy information over injection magnitude.*

nation yields a 1.73 times stronger signal. In all cases the signal content scales linearly with the injection magnitude and the noise RMS appears nearly independent of the injection magnitude, where the SCS noise is significantly higher than the regression based techniques. When looking closer, however, the regression based noise increases slightly towards the right hand side of Fig. 6.4. As a result, the regression based SNR scales with the injection magnitude first, but eventually saturates above 20. Hence, it is less beneficial to aim for a gain in SNR at the same injection magnitude than for a reduction

of injection magnitude at the same SNR – which supports the motivation of this thesis.

Apart from the above discussed noise relations, also the signal content of the different quantities shows an interesting evolution over the injection magnitude. Fig. 6.5 shows the signal content of the above Arbitrary Injection estimates, mean admittance $[\hat{Y}_{\Sigma x}\ \hat{Y}_{\Sigma y}]^\top$ and anisotropic current progression $\Delta\boldsymbol{i}_a^s$, where the latter is indicated in its relative magnitude $Y_\Delta = \frac{|\Delta\boldsymbol{i}_a^s|}{|\Delta\boldsymbol{u}_s^s|}$ and its angle error with respect to the rotor angle $\arg(\Delta\boldsymbol{i}_a^s) - \theta$.

As indicated in Fig. 6.5, the signal content of the SCS (red) and of the regression with Δ^2 evaluation (blue) evolve similar, while the regression with PSS-based EMF elimination (6.17) shows a different, partly oppositional behaviour. Note that these evolutions depend

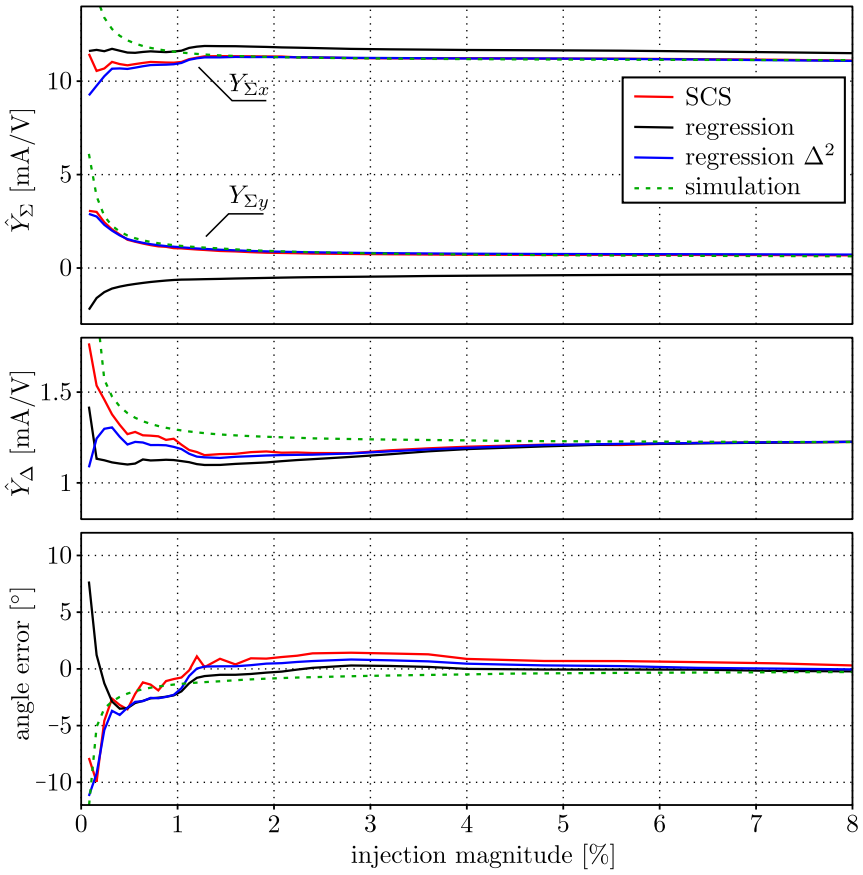

Figure 6.5: *Signal properties of the anisotropy information over injection magnitude.*

on the injection pattern which in this case has been triangular with positive rotational direction. In case of a negative rotation, for instance, the curves for $\hat{Y}_{\Sigma x}$ and the angle error are flipped vertically.

According to the conventional machine model (Ch. 2.3), all quantities in Fig. 6.5 should not depend on the injection magnitude. Moreover, the mean admittance should not have a quadrature component, $Y_{\Sigma y} = 0$ – i.e. the typical anisotropy circle of Fig. 3.8 should lie

on the x-axis. However, as can be seen in Fig. 6.5, the mean admittance has a quadrature component $Y_{\Sigma y} \neq 0$ (see also Fig. 6.3) and towards very low injection magnitudes all quantities evolve with a nearly hyperbolic shape. This evolution could be recreated in simulation by considering eddy currents (see Ch. 2.6) and a small IGBT (diode) voltage drop of 0.3 V in the machine model. The resulting dotted green curve in Fig. 6.5 matches the Δ^2 based evolutions relatively well (except for the parallel component of the mean admittance $\hat{Y}_{\Sigma x}$).

The particular influence of both effects is segregated by the comparison shown in Fig. 6.6. The blue and the dotted green curve are identical to Fig. 6.5 and contain both

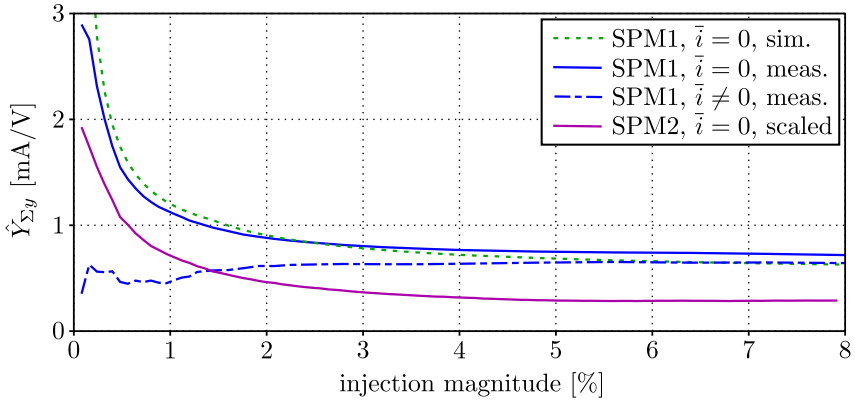

Figure 6.6: *Comparison of the hyperbolic behaviour in different conditions.*

the influence of the eddy currents and the diode voltage at zero average current $\bar{i} = 0$. At zero average current the injection forces the current to cross different sectors, leading to a varying diode voltage which influences the anisotropy identification. The dotted blue curve has been measured with an imposed current offset, such that under injection the current stayed in one sector. In this condition the diode voltage is constant and does not influence the anisotropy estimation. As a result, the dotted blue curve loses its hyperbolic shape, but not its offset. In conclusion, the hyperbolic shape is the result of an IGBT (diode) voltage drop, the constant magnitude of which affects the admittance estimation inversely proportional to the injection magnitude.

The purple curve in Fig. 6.6 demonstrates the opposite case: zero average current with the SEW CFM71S (SPM2) which in Ch. 5.4 showed less influence by eddy currents. After the purple curve has been scaled by the ratio between the admittances of the two machines (the same voltage magnitude induces only about half the current slope in this second machine), the hyperbolic shape matches the blue curve, but the purple curve shows a smaller offset. As the magnitude of the eddy currents scales with the injection, their effect on the admittance estimation is found as a constant offset. In particular, not the magnitude of

the eddy currents but the fade out time (i.e. the losses) influences this quadrature component. According to simulation, a very high stator resistance value (increase by factor 50) would have the same effect. This investigation, however, considered the Δ^2-based EMF elimination. As shown in Fig. 6.5, the PSS slope based EMF elimination by (6.17) has a different sensitivity to both effects.

In conclusion, the influence of eddy currents and for very low injection magnitudes especially the influence of the IGBT diode voltage affect the admittance identification and makes an estimation of the quadrature component of the mean admittance inevitable. Below 0.3% injection the diode voltage does also have a significant[2] effect on the admittance angle estimation if the current is zero in average (unloaded standstill). Under load this angle error will appear only close to the current sector boundaries where the injection forces one phase current to frequently cross zero. Hence, while from an SNR point of view the injection magnitude can be reduced relatively by factor 3.2 when using regression with PSS-based and by factor 6.2 when using regression with Δ^2 based EMF elimination, there is an SNR independent absolute minimum for the injection magnitude due to diode voltage which for the inverter of the used test bench setup lies at about 0.3% (1.1 V).

6.2 Position estimation in presence of rotor speed

When a sufficient amount of rotor speed is present, then three other sources of information (in addition to the anisotropy information from the above PSS extension) become available: Firstly, the EMF generates a PSS current slope that can be measured precisely at low speed already. Within this slope, however, the influence of the resistance and other distorting factors must be eliminated. If the rotor speed exceeds a certain threshold, given by the regression blind-out time, the regression results for the ASS become available as well. Since here an active voltage is applied to the machine, the slope during the ASS comprises both, the anisotropy orientation and the EMF angle.

	Anisotropy	EMF
PSS	(see Ch. 6.1)	at low speed already
ASS	if ASS long enough	if ASS long enough

Table 6.1: *Position information in active and passive switching states.*

Tab. 6.1 summarizes which additional information is available in the presence of rotor speed. Both, the anisotropy and the EMF information are present in both, the ASS and

[2] An error of more than 5 electrical degrees has been considered significant in this case.

the PSS, where the anisotropy angle extraction from the PSS has been derived in Ch. 6.1. By means of Arbitrary Injection the anisotropy information can also be extracted from the ASS slope at high speed, where we must, however, firstly raise the question: is this even reasonable?

After discussing this question and drawing a conclusion, the respective position estimation methods will be derived and experimentally validated in the following subsections. These estimation methods will then form the basis for the fusion techniques described in Ch. 7.

6.2.1 Passive switching state EMF evaluation

The basic idea of this section is that the PSS leads to a simplified voltage equation in which the input voltage is zero. Then the current slope is generated mainly by the electromotive force (EMF). In particular, the usual current trajectory of SPMSMs allows to neglect the influence of the resistance, which makes this a very simple and parameter-free direct EMF estimation approach. Moreover, the IGBT interlock time does generally not affect the PSS current slope and hence the angle estimation. However, as will be shown, the approach entails some simplifications and assumptions that affect the estimation accuracy.

6.2.1.1 Derivation of the estimation approach

The latest PSS regression results received from the FPGA are the values $\boldsymbol{\xi}_{p1}^{s}$ and $\boldsymbol{i}_{op1}^{s}$ which for the reason of simplicity are noted without temporal information (index $_1$) in this section. These values $\boldsymbol{\xi}_{p}^{s}$ and $\boldsymbol{i}_{op}^{s}$ correspond to the general voltage equation (2.19) for zero input voltage

$$\boldsymbol{u}_s^s = R_s \boldsymbol{i}_s^s + \frac{\mathrm{d}\boldsymbol{\psi}_s^s}{\mathrm{d}t} = 0. \tag{6.24}$$

As mentioned before, this approach is suited best for SPMSMs, since their maximum torque per ampere (MTPA) target current trajectory is located on the q-axis. Assuming

the flux of an SPMSM to be linear and isotropic[3]

$$\boldsymbol{\psi}_s^s = L_s \boldsymbol{i}_s^s + \boldsymbol{\psi}_{pm}^s \tag{6.25}$$

$$\text{with} \quad \boldsymbol{\psi}_{pm}^s = \mathbf{T}_r \boldsymbol{\psi}_{pm}^r = \mathbf{T}_r \begin{bmatrix} \psi_{pm} \\ 0 \end{bmatrix}, \tag{6.26}$$

the voltage equation consists only of three terms, the resistive and the inductive voltage and the EMF

$$0 = R_s \boldsymbol{i}_s^s + L_s \frac{\mathrm{d}\boldsymbol{i}_s^s}{\mathrm{d}t} + \mathbf{J}\omega\boldsymbol{\psi}_{pm}^s. \tag{6.27}$$

The current derivative $\frac{\mathrm{d}\boldsymbol{i}_s^s}{\mathrm{d}t}$ in the inductive term is measured through the regression result $\boldsymbol{\xi}_p^s$ which is provided by the FPGA. It is, hence, substituted in Eq. 6.27

$$0 = R_s \boldsymbol{i}_s^s + L_s \boldsymbol{\xi}_p^s + \mathbf{J}\omega\boldsymbol{\psi}_{pm}^s. \tag{6.28}$$

In the next step we introduce the estimated rotor frame (denoted by the circumflex $\hat{}$) that is aligned with the angle $\hat{\theta}$ and that can be accessed from stator frame using the transformation matrix $\hat{\mathbf{T}} = \mathbf{T}(\hat{\theta})$. Hence, the angle error with respect to the real rotor frame (see Fig. 6.7) is defined by $\tilde{\theta} = \hat{\theta} - \theta$ and the respective transformation matrix between the real and the estimated rotor frame is $\tilde{\mathbf{T}} = \hat{\mathbf{T}}\mathbf{T}^{-1}$.

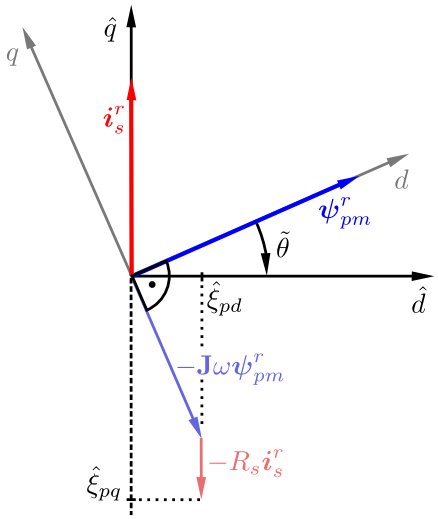

Figure 6.7: *Current slope components in estimated and real rotor frame.*

[3]The absence of a geometrical saliency in SPMSMs and, hence, their low saliency ratio justify this assumption. It is, however, not fully valid and results in an estimation error which is discussed and compensated in Ch. 6.2.1.2.

Based on this definition, the voltage equation is rewritten in estimated rotor frame

$$0 = \hat{\mathbf{T}}^{-1} R_s \boldsymbol{i}_s^s + \hat{\mathbf{T}}^{-1} L_s \boldsymbol{\xi}_p^s + \hat{\mathbf{T}}^{-1} \mathbf{J} \omega \mathbf{T} \boldsymbol{\psi}_{pm}^r \tag{6.29}$$

$$= R_s \boldsymbol{i}_s^{\hat{r}} + L_s \hat{\mathbf{T}}^{-1} \boldsymbol{\xi}_p^s + \tilde{\mathbf{T}} \mathbf{J} \omega \boldsymbol{\psi}_{pm}^r, \tag{6.30}$$

with $\boldsymbol{i}_s^{\hat{r}}$ being the current in estimated rotor frame. Since the FOC works in estimated reference frame, the d-component of $\boldsymbol{i}_s^{\hat{r}}$ is controlled to zero (for an SPMSM below rated speed). This allows to rewrite (6.30) in the following way

$$\boldsymbol{\xi}_p^{\hat{r}} = \hat{\mathbf{T}}^{-1} \boldsymbol{\xi}_p^s = -\frac{R_s}{L_s} \begin{bmatrix} 0 \\ i_q \end{bmatrix} - \frac{\omega \psi_{pm}}{L_s} \begin{bmatrix} \sin \tilde{\theta} \\ \cos \tilde{\theta} \end{bmatrix}. \tag{6.31}$$

Hence, after transforming the PSS current slope $\boldsymbol{\xi}_p^s$ from stator- to estimated rotor frame, the d-component consists of only one term that scales with the deviation between the estimated and the real rotor angle $\tilde{\theta}$. Note that this quantity $\boldsymbol{\xi}_p^{\hat{r}}$ is the stator frame current derivative value $\boldsymbol{\xi}_p^s$ that has been transformed to estimated rotor frame, which is different from the rotor frame current derivative

$$\boldsymbol{\xi}_p^{\hat{r}} \neq \frac{\mathrm{d}\boldsymbol{i}_p^{\hat{r}}}{\mathrm{d}t} = \hat{\mathbf{T}}^{-1} \left(\frac{\mathrm{d}\boldsymbol{i}_s^s}{\mathrm{d}t} - \mathbf{J} \omega \boldsymbol{i}_s^s \right). \tag{6.32}$$

However, in order utilize this d-component as a control error for a phase locked loop (PLL) structure, it must be normalized in such a way that it loses its dependence on the rotor speed ω. As shown in [89], this can for instance be achieved by dividing the d-component by the q-component

$$e_{\theta p} = \frac{\xi_{p\hat{d}}}{\xi_{p\hat{q}}} = \frac{\omega \psi_{pm} \sin \tilde{\theta}}{R_s i_q + \omega \psi_{pm} \cos \tilde{\theta}} \tag{6.33}$$

$$\approx \frac{\omega \psi_{pm} \sin \tilde{\theta}}{\omega \psi_{pm} \cos \tilde{\theta}} = \tan \tilde{\theta}, \tag{6.34}$$

where the simplification (6.34) applies for sufficient EMF magnitude $|\omega \psi_{pm}| \gg |R_s i_q|$. Due to the tangent, this normalization does, however, entail a 180° periodicity and hence a polarity uncertainty that has to be coped for when merging the position estimates. Moreover, the progressive nonlinearity of the tangent aggravates the weighted fusion of the estimates in Ch. 7.1 and its infinite output values for angle errors around $\tilde{\theta} \approx \pm 90°$ can lead to instability in discrete-time systems.

However, the derivation of (6.34) made clear that for an SPMSM the PSS slope based

EMF estimation does completely pass on machine parameters. Considering that the slope is obtained from a single switching state, it is moreover unaffected by the IGBT interlock time. Hence, this EMF estimation technique exhibits essential advantages, but requires reconsideration regarding the normalization strategy.

Therefore, as a further development with respect to [89], this work uses a different normalization strategy that overcomes the above drawbacks. Using the atan2(y, x) function which calculates the angle of a vectorial quantity $[x\ y]^\top$ within the range $-\pi \dots \pi$, the EMF angle in estimated rotor frame is calculated by: atan2$\Big(-\xi_{p\hat{q}},\ -\xi_{p\hat{d}}\Big)$. Since in real rotor frame the EMF is always aligned with the q-axis, error angle $\tilde{\theta}$ between the reference frames is obtained from the deviation of the above term from $\pm 90°$

$$e_{\theta p} = \text{atan2}\Big(-\xi_{p\hat{q}},\ -\xi_{p\hat{d}}\Big) + \tfrac{\pi}{2}\,\text{sign}\,\omega \tag{6.35}$$

$$= \text{atan2}\Big(R_s i_q + \omega\psi_{pm}\cos\tilde{\theta},\ \omega\psi_{pm}\sin\tilde{\theta}\Big) + \tfrac{\pi}{2}\,\text{sign}\,\omega \tag{6.36}$$

$$\approx \text{atan2}\Big(\omega\psi_{pm}\cos\tilde{\theta},\ \omega\psi_{pm}\sin\tilde{\theta}\Big) + \tfrac{\pi}{2}\,\text{sign}\,\omega = \tilde{\theta}, \tag{6.37}$$

where (6.37) implies the same simplification as (6.34). In contrast to (6.34), however, (6.37) does not entail a polarity uncertainty and depends linearly on the estimation error $\tilde{\theta}$ (without resistive influence), which eases the later fusion of the estimates. Yet, also here only the d-component $\xi_{p\hat{d}}$ affects the control error $e_{\theta p}$ (for small errors $\tilde{\theta}$) which is still unaffected by the resistive term and consequently allows to disregard the resistance in the EMF based angle estimation technique.

In order to account for the relatively strong alternation between the approximated slope values, discussed in Ch. 5.4.3, the particular implementation of (6.35) employs the average slope value of the rising and the falling PWM interval

$$e_{\theta p} = \text{atan2}\Big(-\xi_{p\hat{q}1} - \xi_{p\hat{q}2},\ -\xi_{p\hat{d}1} - \xi_{p\hat{d}2}\Big) + \tfrac{\pi}{2}\,\text{sign}\,\omega, \tag{6.38}$$

which increases the relative dead time of the estimate by $\frac{1}{2}T_s$. Hence, for the PSS evaluation the dead time is increased from $1.0T_s$ to $1.5T_s$ (and for the later ASS evaluation from $0.5T_s$ to $1.0T_s$) with respect to the current sampling instant. However, as a result, the alternation is completely eliminated and only the (white) noise will remain in the position estimate which due to the averaging is reduced by factor $\frac{1}{\sqrt{2}}$ (see Ch. 5.3).

Finally, the influence of the simplification between (6.36) and (6.37) should be investigated since the implied assumption $|\omega\psi_{pm}| \gg |R_s i_q|$ does not apply at very low speed. Therefore, the unity factor $V_{R\Psi}$ is introduced that constitutes the (speed and current

dependent) ratio between resistive and EMF induced q-axis voltage

$$V_{R\Psi} = \frac{R_s i_q}{\omega \psi_{pm}}. \tag{6.39}$$

At medium and high speed, when the above assumption holds, this ratio is nearly zero. Then the simplification is possible, such that $e_{\theta p} = \tilde{\theta}$. However, when operating at low speed this ratio will become $V_{R\Psi} > 0$ in motoring condition and $V_{R\Psi} < 0$ in generating condition.

Fig. 6.8 illustrates the effect of this growing factor $V_{R\Psi}$ on the analytical relation between estimation error $\tilde{\theta}$ (actual difference between estimated and real rotor angle) and control error $e_{\theta p}$ (detected error, used for the angle correction). While the relation is

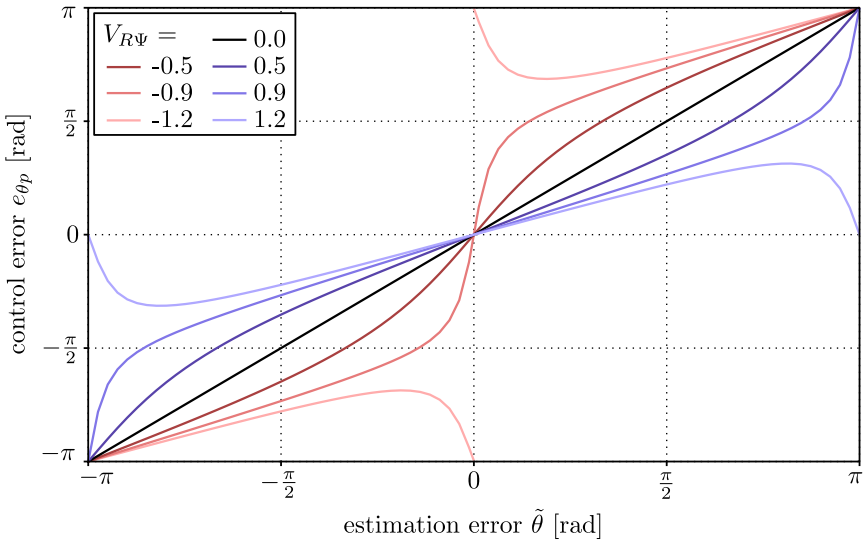

Figure 6.8: *Influence of the resistive term on the relation between estimation error and control input error.*

completely linear for $V_{R\Psi} = 0$, it is more and more distorted when this factor grows. The distortion in motoring condition (blue lines) is disadvantageous but not critical, as the slope around zero decreases by trend and for $V_{R\Psi} > 1.0$ (resistive voltage stronger than EMF) the end of the line flips over to zero. Both effects only result in a slower control performance but not in stability problems. In generating condition, however, the slope around zero error $\tilde{\theta}$ increases by trend, phasing over into a step for $V_{R\Psi} \leq -1.0$. Since this step constitutes an infinite slope around zero, the tracking controller will adopt bang-bang behaviour. However, since all graphs are located only in the first and the third quadrant, they exhibit a globally increasing behaviour with sign change at $\tilde{\theta} = 0$. This means that in all cases the tracking behaviour should be stable and the steady state tracking error should be zero.

In conclusion, the resistive voltage may influence the control behaviour at low speed, such that the tracking might become slower or oscillate, but it should be feasible and not cause instability. In order to maintain a predictable tracking behaviour, $V_{R\Psi}$ should be lower than 0.5, i.e. $|\omega\psi_{pm}| > 2|R_s i_q|$, which for the selection of SPMSMs used in this work (see Appx. B) does apply above 10% rated speed. However, although below this threshold the particular tracking behaviour will vary, it should be stable and without steady state error.

6.2.1.2 Influence of a present anisotropy

The previously described EMF estimation technique is based on the assumption that the machine is isotropic. Then the current slope at zero voltage will only consist of a q-axis component, if the estimation error is zero. However, most SPMSMs show an anisotropy in the scale of $Y_\Delta/Y_\Sigma \approx 10\%$ which is essential for the application of HF injection techniques.

Considering the presence of an anisotropy, the current slope in estimated rotor frame (6.31) becomes more complex

$$\boldsymbol{\xi}_p^{\hat{r}} = -R_s \tilde{\mathbf{T}}^{-1} \mathbf{Y}_s^r \tilde{\mathbf{T}} \boldsymbol{i}_s^{\hat{r}} - Y_q \omega \tilde{\mathbf{T}} \mathbf{J} \boldsymbol{\psi}_{pm}^r - \omega \tilde{\mathbf{T}}^{-1} \left(\mathbf{Y}_s^r \mathbf{J} \mathbf{L}_s^r - \mathbf{J} \right) \tilde{\mathbf{T}} \boldsymbol{i}_s^{\hat{r}}, \tag{6.40}$$

for which the particular derivation can be found in Appx. D. If a q-axis current is controlled by the FOC in estimated reference frame, then the last term in (6.40) causes a d-axis component of the current slope which, according to (6.35), will cause an estimation error. As shown in Fig. 6.9, this error scales progressively with the saliency ratio and degressively with the q-axis current.

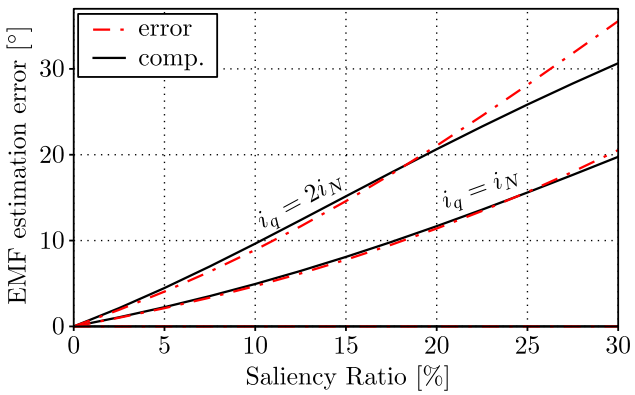

Figure 6.9: *Estimation error due to saliency neglect (red) and influence of compensation term* (6.42) *(black).*

However, when knowing the saliency ratio, this estimation error can be compensated by subtracting a current dependent d-axis slope component. Targeting ideal compensation,

the subtraction is assumed to be carried out in actual rotor frame ($\hat{\mathbf{T}} = \mathbf{T},\ \tilde{\mathbf{T}} = \mathbf{I}$), which simplifies eq. (6.40)

$$\boldsymbol{\xi}_p^{\hat{r}} = -R_s \mathbf{Y}_s^r \boldsymbol{i}_s^{\hat{r}} - Y_q \mathbf{J}\omega\boldsymbol{\psi}_{pm}^r - \omega\left(\mathbf{Y}_s^r \mathbf{J}\mathbf{L}_s^r - \mathbf{J}\right)\boldsymbol{i}_s^{\hat{r}} \tag{6.41}$$

such that the disturbing d-component of the last term can be rewritten as a simple current dependent compensation term

$$\xi_d = -\omega\frac{L_d - L_q}{L_d} i_q = \omega\frac{2Y_\Delta}{Y_\Sigma - Y_\Delta} i_q. \tag{6.42}$$

The different reference frames explain the slight difference between the influence of the compensation (6.42) and the original closed loop estimation error in Fig. 6.9. Yet, (6.42) is the analytically correct compensation term which must be subtracted from the PSS current slope $\boldsymbol{\xi}_p^{\hat{r}}$ in order to eliminate the estimation error.

Since the mean and the differential admittance, Y_Σ and Y_Δ, are estimates within the HF injection method (see Ch. 3.2.2), this compensation can be carried out without preliminary knowledge of a machine parameter. However, due to dynamic effects in the flux-current-relation (mostly eddy currents), the effective differential admittance for the HF injection method differs by $10 - 20\%$ from the fundamental one [90]. This entails a respective remaining estimation error that, according to Fig. 6.9, should however be within an acceptable scale.

6.2.2 Active switching state current slope evaluation

According to the current derivative equation (2.76) of the linear anisotropic PMSM model, the measurable current slope during an active switching state (ASS) is described by

$$\boldsymbol{\xi}_z^s = \mathbf{Y}_s^s\left(\boldsymbol{u}_z^s - R_s\boldsymbol{i}_s^s - \mathbf{J}\omega\boldsymbol{\psi}_{pm}^s - \left(\mathbf{J}\mathbf{L}_s^s - \mathbf{L}_s^s\mathbf{J}\right)\omega\boldsymbol{i}_s^s\right), \tag{6.43}$$

where $\boldsymbol{u}_z^s$ is one of the six fixed ASS voltage vectors with $\frac{2}{3}U_{dc}$ magnitude. Eq. (6.43) can be separated into an excitation term and the PSS current slope known from (6.40)

$$\begin{aligned}\boldsymbol{\xi}_z^s &= \mathbf{Y}_s^s\boldsymbol{u}_z^s + \mathbf{Y}_s^s\left(-R_s\boldsymbol{i}_s^s - \mathbf{J}\omega\boldsymbol{\psi}_{pm}^s - \left(\mathbf{J}\mathbf{L}_s^s - \mathbf{L}_s^s\mathbf{J}\right)\omega\boldsymbol{i}_s^s\right) &(6.44)\\ &= \mathbf{Y}_s^s\boldsymbol{u}_z^s + \boldsymbol{\xi}_p^s. &(6.45)\end{aligned}$$

Hence, the ASS current slope is capable of providing both information, the anisotropy orientation in the first term and the EMF angle in the remaining part. As mentioned at

the beginning of this section, it is firstly to be scrutinized which of those two information is reasonable to extract from the ASS current slope: the anisotropy, the EMF or both?

Considering the usual scale of the saliency ratio of an SPMSM, only about a tenth of the anisotropic current slope is actually position dependent, while the EMF based slope fully depends on the rotor position. So the consideration starts with an (assumed) factor 10 between the magnitudes of the position dependent terms of EMF and anisotropy response. Since the anisotropic term rotates twice per electrical rotor revolution, in contrast to the EMF term rotating exactly with the electrical position, the resulting factor between the *sensitivity* of both slope components with respect to the rotor angle is only 5. Finally, we must consider that both information are induced and thus scaled by different voltage sources: While the EMF information scales with the EMF-voltage term (and hence with rotor speed), the anisotropy information is, according to (3.24), induced directly by the terminal voltage which has a fixed magnitude of $\frac{2}{3}U_{DC}$ during the ASS. This is the maximal voltage magnitude, corresponding to 100% pulse width which the EMF will not exceed in any condition. However, according to Fig. 5.18, the noise content of the ASS allows a reasonable evaluation only above 30% ASS-length which in normal operation is applied because of a respective amount of EMF. Thus, the above factor 5 must be be scaled by those 30% in order to derive the overall worst case sensitivity factor 1.5 between both current slopes components. In other words, even in worst case condition (when the ASS is still much shorter than the PSS), the EMF slope term is already 1.5 times more sensitive to the rotor position, than the anisotropy information. Towards very high rotor speed, where only it is advantageous to evaluate the ASS instead of the PSS slope, this factor converges towards 5. Note that this factor is based on a 10% saliency ratio assumption.

In conclusion, it is not reasonable to evaluate the anisotropy information within the ASS current slope in addition to the EMF information. Since it is much weaker, it would be inherently disregarded by the later SNR based fusion approach (see Ch. 7.1).

6.2.2.1 EMF evaluation from the ASS current slope

According to (6.45), the ASS current slope is the vectorial sum of the PSS current slope and an anisotropic excitation term. This relation is illustrated in Fig. 6.10, where two ASS current slopes $\boldsymbol{\xi}^s_{z+}$ and $\boldsymbol{\xi}^s_{z-}$ are exemplified that would be measured in the same PWM half-period. The respective excitation terms of this period, $\mathbf{Y}^s_s\boldsymbol{u}^s_{z+}$ and $\mathbf{Y}^s_s\boldsymbol{u}^s_{z-}$, are indicated in black colour, while the 4 remaining excitation possibilities are indicated in grey. Due to the anisotropy, the voltage hexagon is skewed during the transition to the

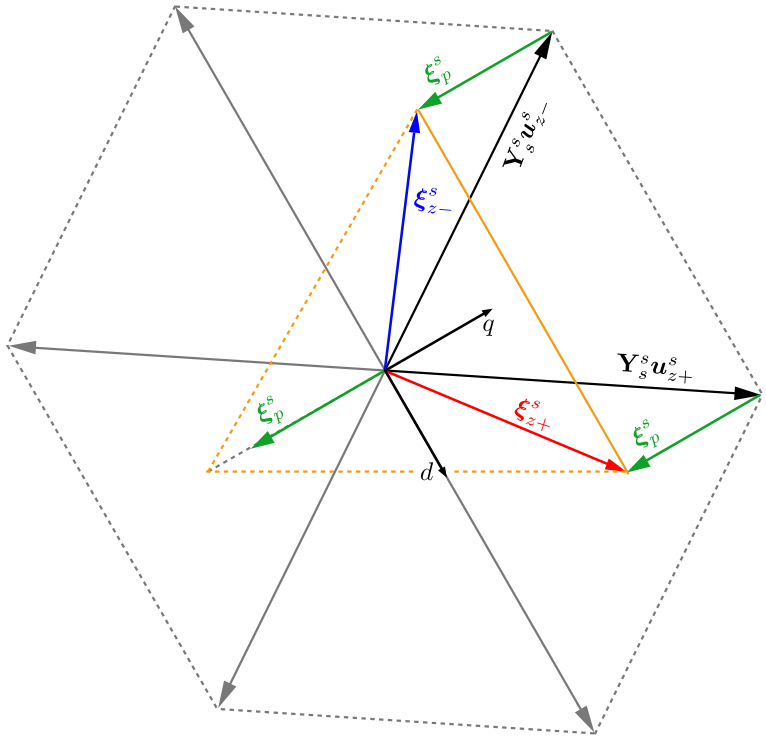

Figure 6.10: *Geometrical relation between PSS and ASS current slope.*

excitation terms, which is important to take into account in the following derivation.

Since eliminating the excitation term in the ASS current slope (6.45) would reveal the PSS current slope

$$\boldsymbol{\xi}_z^s - \mathbf{Y}_s^s \boldsymbol{u}_z^s = \boldsymbol{\xi}_p^s, \tag{6.46}$$

for which the EMF based position estimation has already been solved in Ch. 6.2.1, the ASS-based angle estimation is seen as an extension to Ch. 6.2.1 that only determines the PSS slope from the ASS. The particular challenge, however, is that the admittance matrix $\mathbf{Y}_s^s$ in (6.46) is not known and may moreover change rapidly under varying load conditions. Hence, the key point of the ASS-based EMF estimation is the identification of the relevant admittance.

The proposed idea of this section is to obtain the admittance information from the difference between the slopes $\boldsymbol{\xi}_{z1}^s$ and $\boldsymbol{\xi}_{z2}^s$

$$\left|\boldsymbol{\xi}_{z+}^s - \boldsymbol{\xi}_{z-}^s\right| = \left|\left(\mathbf{Y}_s^s \boldsymbol{u}_{z+}^s + \boldsymbol{\xi}_p^s\right) - \left(\mathbf{Y}_s^s \boldsymbol{u}_{z-}^s + \boldsymbol{\xi}_p^s\right)\right| \tag{6.47}$$

$$= \left|\mathbf{Y}_s^s (\boldsymbol{u}_{z+}^s - \boldsymbol{u}_{z-}^s)\right|, \tag{6.48}$$

which is indicated by the orange line in Fig. 6.10.

In the next step, the magnitude and the direction of the voltage difference ($\boldsymbol{u}^s_{z+} - \boldsymbol{u}^s_{z-}$) are considered: Since the voltage hexagon is composed of equilateral triangles, the magnitude of the difference equals the magnitude of each single vector – i.e. $\frac{2}{3}U_{dc}$. The direction of the voltage difference is roughly aligned with the d-axis (see Fig. 6.10), which is a result of the EMF mostly determining the voltage sector and hence the selected ASSs. Moreover, the slope approximation noise (see Fig. 5.18 in Ch. 5.4) demands a minimum length (ca. 25%) of *both* ASSs within one PWM half-period, which is only given within the white areas in Fig. 6.11. Since even on the outside edges of the hexagon (maximum

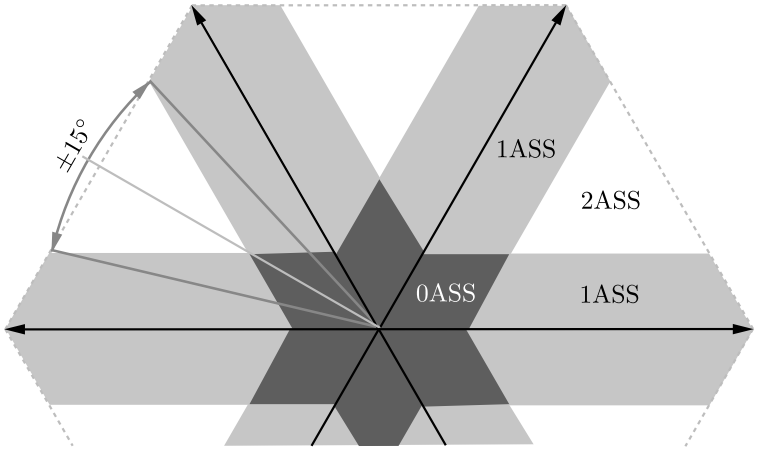

Figure 6.11: *Voltage regions with minimum 25% ASS length.*

voltage) these areas are only 30° wide, the orientation of ($\boldsymbol{u}^s_{z+} - \boldsymbol{u}^s_{z-}$) will vary for max. ±15° from the d-axis. Hence, the effective admittance for this difference ($\boldsymbol{u}^s_{z+} - \boldsymbol{u}^s_{z-}$) is nearly Y_d.

According to the above considerations, (6.48) can be rewritten as

$$\left|\boldsymbol{\xi}^s_{z+} - \boldsymbol{\xi}^s_{z-}\right| = Y_d \left|\boldsymbol{u}^s_{z+}\right| = Y_d \left|\boldsymbol{u}^s_{z-}\right| \tag{6.49}$$

$$= Y_d \left|\boldsymbol{u}^s_{z}\right|, \tag{6.50}$$

and be used to define a low pass filtered estimation variable $\hat{Y}_d$

$$\frac{\mathrm{d}\hat{Y}_d}{\mathrm{d}t} = k_{Yd}\left(\frac{3\left|\boldsymbol{\xi}^s_{z+} - \boldsymbol{\xi}^s_{z-}\right|}{2\ U_{dc}} - \hat{Y}_d\right), \tag{6.51}$$

that is always updated when both switching states $\boldsymbol{u}^s_{z+}$ and $\boldsymbol{u}^s_{z-}$ are applied long enough within one PWM half-period. The tuning factor k_{Yd} adjusts the estimation bandwidth and can be defined adaptively, e.g. depending on the length of the shortest ASS involved.

Once $\hat{Y}_d$ has reached its steady state $\hat{Y}_d = Y_d$, it can be multiplied with the direction

of the applied ASS voltage and then be subtracted from the measured ASS current slope

$$\boldsymbol{\xi}_z^s - \hat{Y}_d \boldsymbol{u}_z^s \overset{(6.45)}{=} \mathbf{Y}_s^s \boldsymbol{u}_z^s + \boldsymbol{\xi}_p^s - \hat{Y}_d \boldsymbol{u}_z^s \tag{6.52}$$

$$= \boldsymbol{\xi}_p^s + \left(\mathbf{Y}_s^s - Y_d \mathbf{I}\right) \boldsymbol{u}_z^s. \tag{6.53}$$

The benefit of the above derivation is revealed when transforming (6.53) to rotor frame

$$\mathbf{T}^{-1} \left(\boldsymbol{\xi}_z^s - \hat{Y}_d \boldsymbol{u}_z^s\right) = \boldsymbol{\xi}_p^r + \left(\mathbf{Y}_s^r - Y_d\, \mathbf{I}\right) \boldsymbol{u}_z^r \tag{6.54}$$

$$= \boldsymbol{\xi}_p^r + \begin{bmatrix} Y_d - Y_d & 0 \\ 0 & Y_q - Y_d \end{bmatrix} \boldsymbol{u}_z^r \tag{6.55}$$

$$= \boldsymbol{\xi}_p^r + \begin{bmatrix} 0 \\ (Y_d - Y_q)\, u_q \end{bmatrix}, \tag{6.56}$$

where a possible deviation between rotor and anisotropy frame has been neglected. According to (6.56) and according to the geometrical derivation by the orange dashed lines in Fig. 6.10, the directed subtraction (6.52) results in the wanted PSS current slope with an additional q-axis term. As both the admittance difference $(Y_d - Y_q)$ and the q-axis term of the ASS voltage are roughly constant, this additional term should result in a fixed increase in apparent signal strength, without position information. However, since the accuracy of the angle estimation from the PSS slope $\boldsymbol{\xi}_p^r$ only depends on the d-axis component (see Ch. 6.2.1.1), the estimation law (6.51) and the directed subtraction (6.52) are sufficient for the extraction of the PSS slope from the ASS

$$\hat{\boldsymbol{\xi}}_p^s = \boldsymbol{\xi}_z^s - \hat{Y}_d \boldsymbol{u}_z^s. \tag{6.57}$$

The subsequent angle estimation from $\hat{\boldsymbol{\xi}}_p^s$ is carried out according to Ch. 6.2.1 and results in the control error angle e_{θ_z} of the ASS-based EMF evaluation.

6.2.3 Experimental validation of the current slope based EMF estimation

In the above sections a parameter-free FM based rotor position estimation technique has been derived that identifies the EMF from the PSS current slope $\boldsymbol{\xi}_p^s$. An extension allows to deduce the PSS slope orientation from the ASS results such that the ASS approximation straight can be employed for rotor position estimation as well. Both position estimation techniques have been implemented on the test bench setup described in Ch. 4.1 and will

be validated by experiments with the SPM1 in this section.

Firstly, a general impression of the signal evolutions is provided by the graph array in Fig. 6.12 which compares the PSS-based EMF estimation with the ASS-based one at different rotor speeds. The upper row shows the estimation of the d-axis admittance

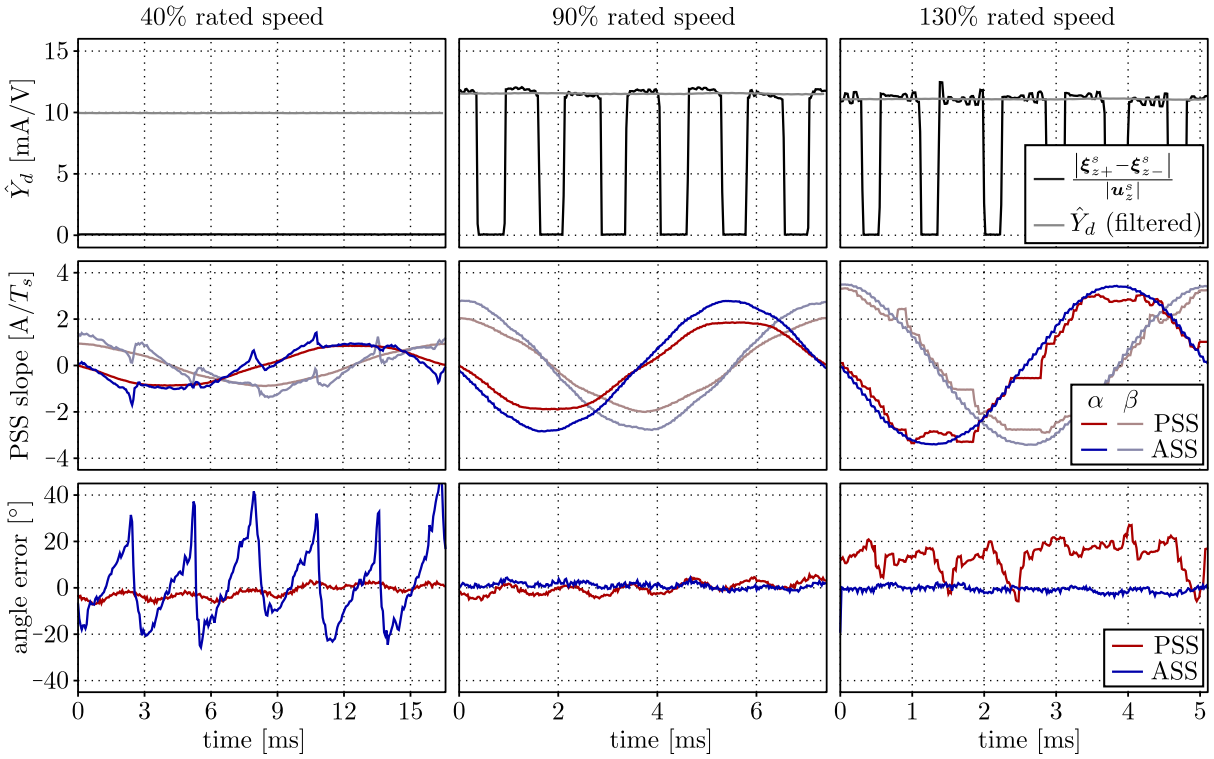

Figure 6.12: *EMF based rotor position estimation from the approximated PSS and ASS current slope during one electrical revolution.*

through (6.51). Only if this value $\hat{Y}_d$ is known, the PSS slope can be deduced from the ASS results. At 40% rated speed (left column) the FOC voltage is too low for both the positive and the negative ASS being applied for longer than 25% of the PWM half-period (see Fig. 6.11). Hence, there is no calculation result for $\left|\boldsymbol{\xi}^s_{z+} - \boldsymbol{\xi}^s_{z-}\right|$ (black graph always zero) and the low pass filtered value $\hat{\xi}_d$ is stuck at a wrong value (deduced from the Arbitrary Injection based admittance estimation, see Ch. 3.2.2). As a result, the PSS slope computation from the ASS approximation results (blue colour) shows strongly oscillating deviations from the actual PSS slope (red colour), as can be seen in the second row of Fig. 6.12. The last row shows the resulting angle estimation error that for the ASS is too large to allow for closed loop rotor position estimation. The direct PSS slope approximation (red colour), however, only comprises the EMF harmonics of SPM1, but does otherwise exhibit a high signal quality that can easily be employed for position estimation.

The second column in Fig. 6.12 shows the results at 90% rated speed where both techniques provide nearly the same signal quality. As can be seen in the first row, in the majority of times there are calculation results for $\left|\boldsymbol{\xi}^s_{z+} - \boldsymbol{\xi}^s_{z-}\right|$ and the low pass filtered estimate $\hat{Y}_d$ has reached a valid steady state value. As a result, the ASS-based PSS slope computation (second row, blue colour) provides a high signal quality as well. As predicted by Fig. 6.10 and (6.56), the anisotropy of the machine increases the magnitude of the ASS-based PSS slope estimation (blue colour) with respect to the actual PSS slope (red colour), while the angle (see last row) is not affected. It is, however, interesting to note that the harmonics in the ASS-based angle estimate are smaller than the actual EMF harmonics of the machine.

The last column in Fig. 6.12 shows the estimation close to the limits of sinusoidal voltage excitation where the ASSs are applied for relatively long times (see large areas of $\left|\boldsymbol{\xi}^s_{z+} - \boldsymbol{\xi}^s_{z-}\right|$ results in the first row). On the other hand, especially in the middle of the voltage sectors, the PSS is too short for an approximation of the current slope. As a result, the ASS-based PSS slope estimation (blue colour) is very clean, whereas the actual PSS slope signal (red colour) shows strong distortions and does partially freeze, as can be seen in the second row. Also the resulting angle signals in the last row demonstrate that at these very high speeds it is clearly advantageous to employ the ASS instead of the PSS for rotor position estimation.

In order to further analyse the discovered EMF harmonics reduction in the ASS-based estimation, Fig. 6.13 shows a comparison of the rotor frame PSS slope values, obtained through different techniques at rated speed with zero current. Firstly, the direct measurement by the PSS regression (red cloud) matches the known EMF harmonics of the

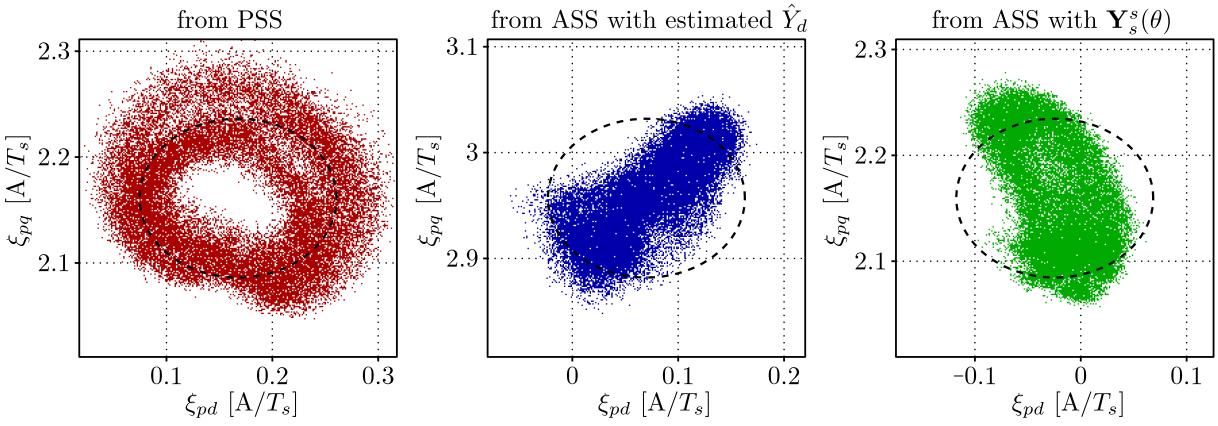

Figure 6.13: *Harmonic trajectory of the PSS current slope in rotor frame $\boldsymbol{\xi}^r_p$ – comparison between direct measurement and two different deductions from the ASS.*

machine (dashed black ellipse in all graphs). The trajectory of the ASS-based estimation according to Ch. 6.2.2 (blue cloud), however, evolves markedly different and particularly narrower in d-direction, which is relevant for the angle evaluation. Moreover, due to the anisotropy, the ASS-based estimation has an increased q-axis component (see ordinate values[4]), which additionally downscales the angle harmonics.

Since the EMF harmonics have sixth order of the electrical angle and the ASS-based trajectory does not split up in multiple paths, the distorting effects that shrink the ASS trajectory must also have order six (or integer multiples of six). According to the previous deduction of this thesis, there are two potential sources of error with order six:

(1.) The simplifications within the estimation of $\hat{Y}_d$: Firstly, depending on the angular width of the white areas in Fig. 6.11, a value slightly lower than Y_d is estimated. And secondly, this value is applied to an ASS voltage during $\pm 30°$ rotor movement.

(2.) The influence of eddy currents on the approximated ASS slope that has been disclosed in Fig. 5.16. The most evident effect, the strong alternation between the ASS being applied first and second in a PWM half-period, has been compensated by using the average value of both cases. Hence, the alternation is cancelled, but an effect on the average value may remain that would have order six and/or integer multiples as well.

In order to distinguish between both effects, the right hand side graph in Fig. 6.13 shows an ASS-based PSS slope trajectory in rotor frame, where not the estimate $\hat{Y}_d$, but the correctly parametrized admittance matrix $\mathbf{Y}_s^s$ including the measured rotor angle θ has been employed in (6.57) to deduce the PSS slope from the ASS approximation (see realistic ordinate values). Hence, the first source of error is eliminated and the difference between the blue and the green graph is concluded being the result of the simplification in the $\hat{Y}_d$ estimation. The difference between the green graph and the dashed ellipse (or the red graph) is concluded being the result of the ASS slope distortion by eddy currents.

However, in order to assess the PSS– and ASS slope-based estimation performance in the entire operating range, two more abstract comparisons are provided. Firstly, the overall evolutions of signal and noise content of the PSS and ASS current slope based EMF angle estimation over rotor speed are shown in Fig. 6.14 for two different SPMSMs, where the graphs of the SPM2 are generally lower because of its higher inductance values and slightly shorter because of its higher PM flux linkage. Obviously, the signal strength

[4]Apart from the ordinate values, the overall d-axis shift of the trajectories results from the fact that the PSS approximation is located $1.5T_s$ and the ASS approximation $1.0T_s$ in the past (see Ch. 6.2.1.1), with respect to the encoder angle used for the rotor frame transformation. This dead time is considered in the eventual angle estimation and compensated for by using the filtered rotor speed estimate.

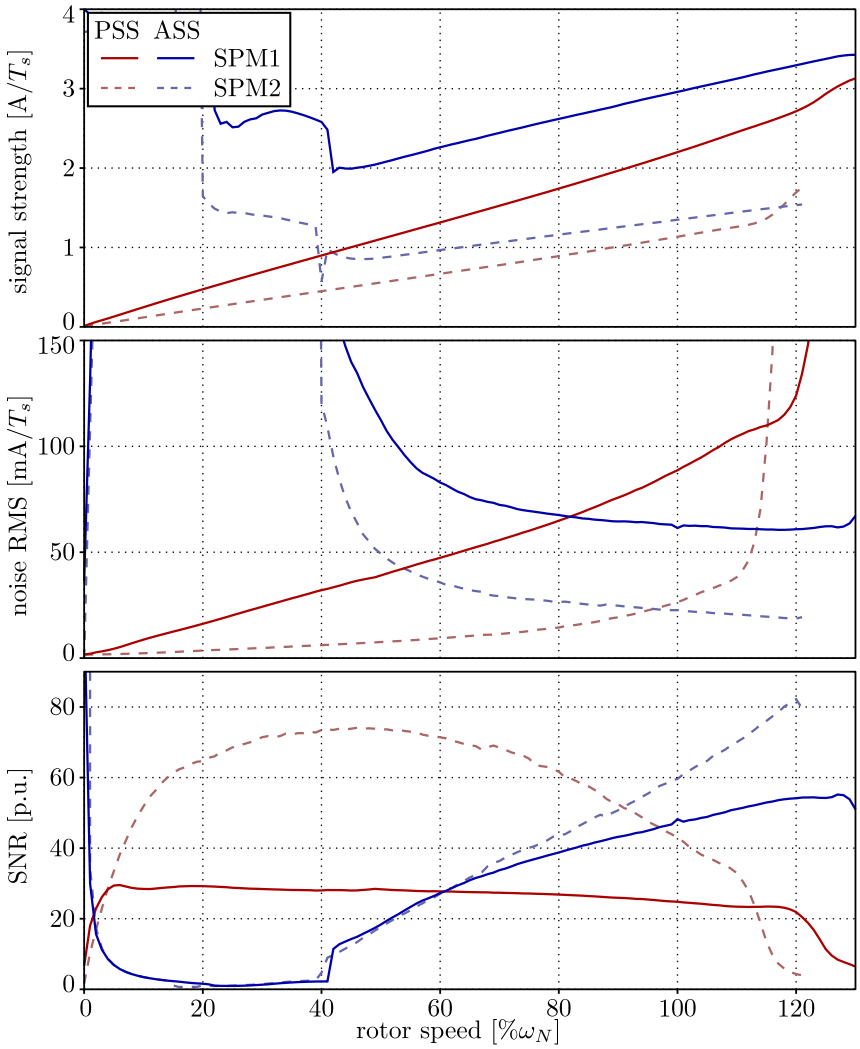

Figure 6.14: *Properties of the EMF signal detected from the PSS and the ASS slope – for two different SPMSMs.*

of all signals increases linearly over speed. The strong increase of the ASS at low speed and the slight increase of the PSS at very high speed are erroneous detections because of the very strong noise content in these regions. As predicted by (6.56), the anisotropy of the machine leads to an increase of the interpreted ASS signal strength with respect to the PSS. The slightly decreasing difference between both results from the fact that at high speeds (and voltages) the estimate $\hat{Y}_d$ is obtained over a wider angle area (see Fig. 6.11) and does hence decrease slightly with respect to the actual d-axis admittance Y_d. The noise RMS of all curves shows the expected hyperbolic evolution. It is, however, interesting to note that the ASS and the PSS curves intersect about 20% earlier for SPM1 than for SPM2. This can be explained by both higher EMF harmonics and stronger eddy currents in SPM1 which increase the detected PSS noise and decrease the detected ASS noise, respectively. In conclusion, SPM1 reaches a markedly lower PSS-based signal to noise

ratio (SNR) than SPM2, whereas the ASS-based SNR of both machines is in comparable scale. Yet, in all cases the SNR provides a sufficient representation of the respective signal quality and reaches a similar scale as the anisotropy evaluation in Fig. 6.4. At very low speed, however, the wrong interpretation of the ASS-based SNR must be avoided when aiming to employ the SNR for an estimate fusion.

Finally, the load-dependence of the proposed EMF angle estimation is analysed in Fig. 6.15, where the upper graphs show the estimation error average and the lower graphs the estimation error noise RMS over speed. In the left column the estimation is based on

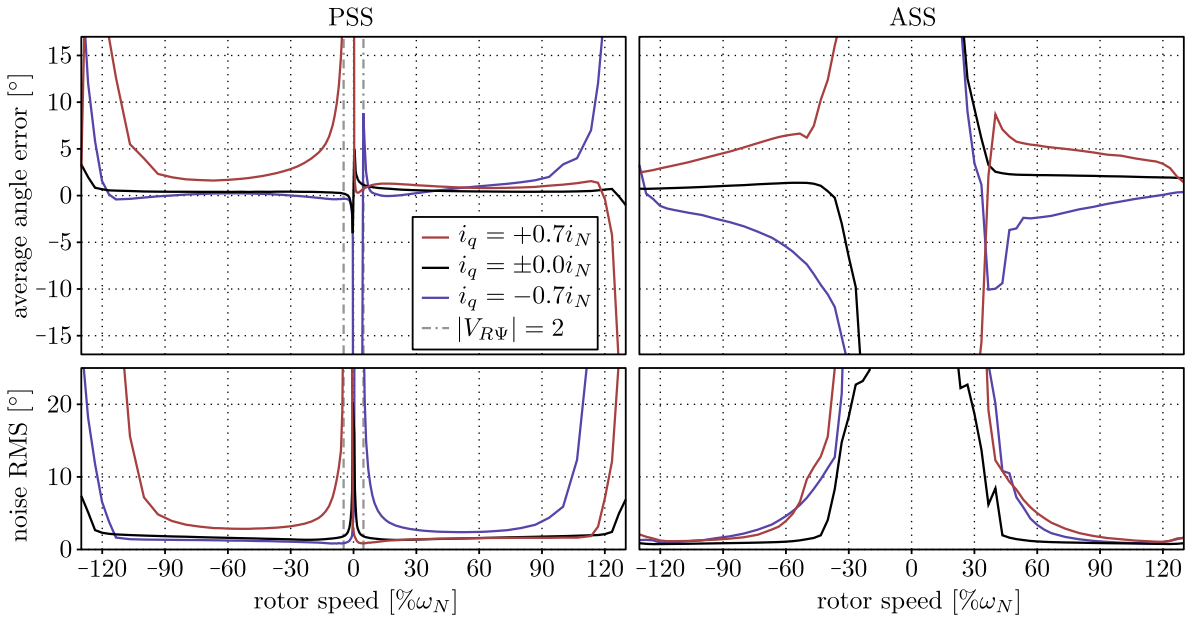

Figure 6.15: *Average error and noise content of the PSS and the ASS-based EMF angle estimation.*

the PSS, in the right column on the ASS approximation. The graph colours indicate the load conditions as either unloaded (black), 70% positive rated load (red) or 70% negative rated load (blue).

According to Ch. 6.2.1.1 and especially to Fig. 6.8, this EMF based angle estimation approach should not show an average estimation error at low speed and high load, although the particular tracking behaviour may vary. However, as can be seen in the upper left graph of Fig. 6.15, for a very low speed-to-load ratio of $|V_{R\Psi}| < 2$ (defined in Ch. 6.2.1.1), this only applies to the motoring condition (same sign of speed and current). The generating condition (opposite sign of speed and current) causes a relatively large angle error which is not suitable for position estimation. Between 10% and 100% rated speed, however, the average error is in a sufficiently low scale. It is noted but not clear why the average error of the positive load generating case evolves different. Regarding the PSS-

based noise, idle and motoring condition evolve similar while the generating condition is increased. In conclusion, the PSS-based estimation is good-natured in idle and motoring conditions, but shows worse properties in generating condition. However, in all cases the SNR is a good indication for the overall quality and reliability of the PSS-based signal.

Apart from the lack of estimation results below medium speeds, the ASS-based estimation shows a markedly bigger (but still acceptable) load-dependence on the right hand side of Fig. 6.15. As the final parts of both estimation techniques (the PSS evaluation) are identical, the load-dependence must result from the ASS-based PSS slope deduction by Eq. (6.51) and (6.57). Motoring and generating cases do, however, evolve similar and again, in all cases the SNR appears to be a good indication for the signal quality of the ASS-based EMF angle estimation.

Chapter 7

Fusion of the position estimates

After the current oversampling data, described in Ch. 4, has been approximated by a straight for each switching state in Ch. 5, three linear approximation based position estimation techniques have been derived in Ch. 6. According Ch. 6, the single position estimates have their optimal SNR in different speed ranges, which concludes in the common decision to design the eventual sensorless control scheme for the entire speed range by using a hybrid fusion of all estimates.

Summarizing the two main advantages of the oversampling-based position estimation techniques proposed in Ch. 6,

(1.) their independence of machine parameters and

(2.) the injection magnitude reduction potential around standstill,

two oppositional fusion techniques will be proposed in this chapter, each aiming at the best possible realization of one advantage in an overall sensorless control structure.

The first scheme, proposed in Ch. 7.1, targets an entirely machine parameter-free hybrid sensorless control scheme for SPMSMs, using three key techniques: the online SNR determination, the injection magnitude controller and the initial anisotropy displacement test. The second scheme, proposed in Ch. 7.2, disregards the parameter consideration while aiming at an optimal estimation performance using minimal injection magnitude. The key techniques herein are the flux stabilization with anisotropy information and the compensation of non-static effects in the current-flux relation.

7.1 Parameter-free hybrid sensorless control for SPMSMs

Both the anisotropy-based and the EMF-based position estimation techniques of Ch. 6 have been derived without the implication of any machine parameter. In order to maintain that advantage for the complete hybrid method, the fusion of and phase-over between the estimates is based on a signal quality consideration – namely the signal to noise ratio (SNR) which, according to Ch. 6, is a viable indication for the overall signal quality.

Following the idea of the Kalman Filter, the single position estimates (Anisotropy, PSS-EMF and ASS-EMF) which inhere different amounts of white noise, should be weighted and merged in such a way that the SNR of the resulting hybrid position estimate is minimized at all times. Therefore, the SNR of each estimate must be determined online and fed into a fusion scheme that fulfils the above goal.

In this section, firstly the online SNR determination technique will be derived such that for all position estimates the SNR value is available. Based on these values, an SNR minimization strategy is employed to derive an adaptive fusion law for the position estimates. Moreover, it will be shown that, based on this SNR consideration, also the injection magnitude can be adjusted. The result is an overall hybrid sensorless control scheme for SPMSMs that does not require the preliminary knowledge of any machine parameter. Finally, this scheme will be validated by experimental results.

7.1.1 Online SNR determination

As analysed in Ch. 5.4, noise imposed through the current transducer and the analogue to digital converter (ADC) leads to a variation of the approximated straight coefficients with the properties of white noise. Moreover, the influence of eddy currents led to an alternation between the slope values of the rising and the falling PWM half-period that has been eliminated in the angle estimate by using the average of both PWM half-periods. However, as shown in Ch. 6, the approximation noise can be found in all position estimates. The eventual PLL filter structure will suppress this noise only to a certain extent, as the filtered signal also needs to fulfil certain dynamic requirements. Hence, the signal to noise ratio (SNR) of the direct position estimate is an essential information regarding the feasibility and the performance of closed loop sensorless control. As shown in Ch. 6.2.3 it does, moreover, correlate with the reliability of the estimate that in certain operating conditions can be impaired by other influences (e.g. the resistance).

The easiest way to determine the SNR online would be a noise analysis of the angle

estimate itself, as the angle signal can be considered to have a constant "signal strength" that does not need to be determined. In case the signal strength of an estimation source variable ($\Delta\boldsymbol{i}_a^s$, $\boldsymbol{\xi}_p^{\hat{r}}$ or $\hat{\boldsymbol{\xi}}_p^{\hat{r}}$) increases while its noise content is constant, the resulting noise in the angle estimate would drop and the SNR would be determined higher. The difficulty herein is that the SNR determination should be both fast and accurate in order to correctly weight the estimates in the fusion process and to be employed in a control cycle as in Ch. 7.1.3. An accurate noise determination, however, requires a long analysis interval, such that also the low frequency content of the noise is included. This long analysis interval allows only a low estimation bandwidth. On the other hand, the signal strength can be determined rapidly. In summary, the signal strength can vary quickly and be determined rapidly, whereas the noise content mostly stays constant and can only be determined slowly. In order to fulfil both above requirements to the SNR determination, it is hence reasonable to determine signal strength and noise content separately for the estimation source variable and to calculate the SNR as the ratio between both.

According to the Sections 3.2.1, 6.2.1 and 6.2.2, all position estimation techniques result in a two-dimensional source signal $\Delta\boldsymbol{i}_a^s$ (Anisotropy-based estimation), $\boldsymbol{\xi}_p^{\hat{r}}$ (PSS-based estimation) and $\hat{\boldsymbol{\xi}}_p^{\hat{r}}$ (ASS-based estimation) from which the rotor angle is directly deduced. According to the sections 6.1.3 and 6.2.3, all these signals scale with the respective source of information (injection or speed), whereas the noise content depends mostly on the (operating point specific) average length of the employed type of switching state. Moreover, the PSS slopes in estimated rotor frame, $\boldsymbol{\xi}_p^{\hat{r}}$ and $\hat{\boldsymbol{\xi}}_p^{\hat{r}}$, and the anisotropic current response transformed with twice the estimated rotor angle

$$\Delta\boldsymbol{i}_a^{\hat{r}r} = \mathbf{T}^{-1}(2\hat{\theta})\Delta\boldsymbol{i}_a^s \tag{7.1}$$

form stationary (not moving) point clouds. Fig. 7.1 shows an exemplification of these clouds at rated speed for the EMF-based signals (left hand side) and at 4% injection for the anisotropy-based signal (right hand side). Although both graphs were measured over several electrical rotor revolutions, the anisotropy-based signal $\Delta\boldsymbol{i}_a^{\hat{r}r}$ is located stationary on the d-axis and the EMF-based signal nearly on the q-axis, only showing the harmonics and the dead time related shift described in Ch. 6.2.3. The dark grey vectors indicate the

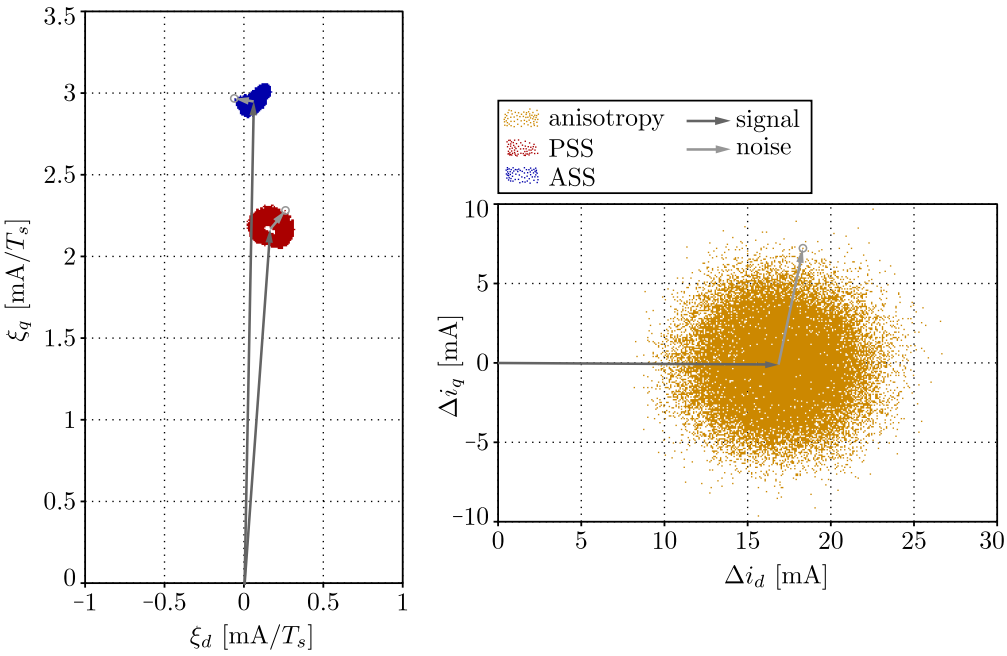

Figure 7.1: *Stationary point clouds of the position estimation source data.*

signal content of each cloud that is obtained by low pass filtering the source signals

$$\frac{\mathrm{d}}{\mathrm{d}t}\Delta\boldsymbol{i}_{a,lpf}^{\hat{r}r} = k_{\mu a}(\Delta\boldsymbol{i}_{a}^{\hat{r}r} - \Delta\boldsymbol{i}_{a,lpf}^{\hat{r}r}) \tag{7.2}$$

$$\frac{\mathrm{d}}{\mathrm{d}t}\boldsymbol{\xi}_{p,lpf}^{\hat{r}} = k_{\mu p}(\boldsymbol{\xi}_{p}^{\hat{r}} - \boldsymbol{\xi}_{p,lpf}^{\hat{r}}) \tag{7.3}$$

$$\frac{\mathrm{d}}{\mathrm{d}t}\hat{\boldsymbol{\xi}}_{z,lpf}^{\hat{r}} = \begin{cases} k_{\mu z}(\hat{\boldsymbol{\xi}}_{z}^{\hat{r}} - \hat{\boldsymbol{\xi}}_{z,lpf}^{\hat{r}}), & \text{if} \quad \max(\nu_{z+}, \nu_{z-}) \geq 0.25 \\ -k_{\mu z}\hat{\boldsymbol{\xi}}_{z,lpf}^{\hat{r}}, & \text{else} \end{cases} . \tag{7.4}$$

In order to prevent the erroneous detection of a high ASS signal strength at low speed (see Fig. 6.14 in Ch. 6.2.3), the ASS signal content vector $\hat{\boldsymbol{\xi}}_{z,lpf}^{\hat{r}}$ in (7.4) converges to zero in case no ASS is applied for longer than $25\%T_s$ (see also Fig. 6.11). The low pass filtering is particularly important for the detection of very low signal strengths (low injection or speed) in order to avoid noise being interpreted as signal. However, in order to ensure a sufficient detection bandwidth, the cut-off frequency should be chosen higher than the bandwidth of the speed controller (e.g. $k_\mu = 200/\mathrm{s}$) and the injection magnitude controller (Ch. 7.1.3), respectively.

Based on the above approximation of the signal content vectors, the signal strength μ

is defined as the magnitude of each content vector

$$\mu_a^2 = \boldsymbol{i}_{a,lpf}^{\hat{rr}\ T}\ \boldsymbol{i}_{a,lpf}^{\hat{rr}} \tag{7.5}$$

$$\mu_p^2 = \boldsymbol{\xi}_{p,lpf}^{\hat{r}\ T}\ \boldsymbol{\xi}_{p,lpf}^{\hat{r}} - \mu_{p0}^2 \tag{7.6}$$

$$\mu_z^2 = \hat{\boldsymbol{\xi}}_{z,lpf}^{\hat{r}\ T}\ \hat{\boldsymbol{\xi}}_{z,lpf}^{\hat{r}} - \mu_{p0}^2 \tag{7.7}$$

where the offset value μ_{p0}^2 accounts for the influence of the resistance on the PSS current slope that especially at standstill should not be misinterpreted as signal strength. μ_{p0}^2 can be determined as the maximum value of μ_p^2 during the macroscopic current pulses in the initial polarity check for the anisotropy-based method. The particular implementation must ensure that the result of this subtraction does not become negative. The anisotropy-based signal strength μ_a, however, does not need such a correction.

The noise content σ is determined as the RMS value of the distance between the single source signal measurements $\Delta\boldsymbol{i}_a^{\hat{rr}}$, $\boldsymbol{\xi}_p^{\hat{r}}$ and $\hat{\boldsymbol{\xi}}_p^{\hat{r}}$, and their respective signal content

$$\frac{\mathrm{d}}{\mathrm{d}t}\sigma_a^2 = k_{\sigma a}\left(\left(\Delta\boldsymbol{i}_a^{\hat{rr}} - \Delta\boldsymbol{i}_{a,lpf}^{\hat{rr}}\right)^\top\left(\Delta\boldsymbol{i}_a^{\hat{rr}} - \Delta\boldsymbol{i}_{a,lpf}^{\hat{rr}}\right) - \sigma_a^2\right) \tag{7.8}$$

$$\frac{\mathrm{d}}{\mathrm{d}t}\sigma_p^2 = k_{\sigma p}\left(\left(\boldsymbol{\xi}_p^{\hat{r}} - \boldsymbol{\xi}_{p,lpf}^{\hat{r}}\right)^\top\left(\boldsymbol{\xi}_p^{\hat{r}} - \boldsymbol{\xi}_{p,lpf}^{\hat{r}}\right) - \sigma_p^2\right) \tag{7.9}$$

$$\frac{\mathrm{d}}{\mathrm{d}t}\sigma_z^2 = k_{\sigma z}\left(\left(\hat{\boldsymbol{\xi}}_z^{\hat{r}} - \hat{\boldsymbol{\xi}}_{z,lpf}^{\hat{r}}\right)^\top\left(\hat{\boldsymbol{\xi}}_z^{\hat{r}} - \hat{\boldsymbol{\xi}}_{z,lpf}^{\hat{r}}\right) - \sigma_z^2\right), \tag{7.10}$$

where the low pass filtering is an approximation of the averaging process in the actual RMS algorithm that gives higher relevance to recent and gradually "forgets" old information. The bandwidth of this low pass filter (LPF) should be markedly lower (e.g. 1 Hz) than the signal strength filter bandwidth because of the reasons given at the beginning of this section.

Finally, the SNR is defined as the quotient of signal over noise

$$s_a^2 = \frac{\mu_a^2}{\sigma_a^2}, \qquad s_p^2 = \frac{\mu_p^2}{\sigma_p^2}, \qquad s_z^2 = \frac{\mu_z^2}{\sigma_z^2}, \tag{7.11}$$

where, as in all previous derivations, the square root to actually obtain the SNR value has not been accomplished consciously, because only the squared values are relevant for the subsequent estimate fusion.

However, all signal, noise and SNR graphs shown in this thesis, have been determined according to the above techniques (but using averaging instead of an LPF), where the square root has been accomplished and the linear value has been shown.

7.1.2 Adaptive fusion technique for noise minimization

Knowing the SNR of each position estimate through the techniques proposed in Ch. 7.1.1, the goal of this subsection is to scale and merge the estimates in such a way that the overall noise of the hybrid position estimation is minimized.

This is realized through the adaptive parametrization of the weighting factors k_a, k_p and k_z in Fig. 7.2 which weight the output signals of the different position estimators according to their SNR before feeding them into a PLL structure.

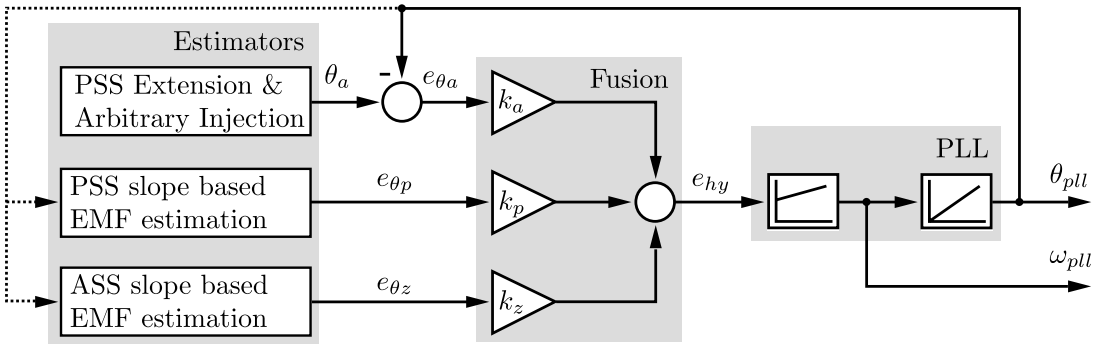

Figure 7.2: *Fusion of the position estimates in the error of a shared PLL structure.*

The particular weighting factor adaptation law is

$$k_a = \frac{s_a^2}{s_a^2 + s_p^2 + s_z^2} \tag{7.12}$$

$$k_p = \frac{s_p^2}{s_a^2 + s_p^2 + s_z^2} \tag{7.13}$$

$$k_z = \frac{s_z^2}{s_a^2 + s_p^2 + s_z^2}, \tag{7.14}$$

which generally gives an estimate with more SNR a bigger influence on the PLL. According to the derivation of this law in Appx. E, it leads to the minimization of the noise σ_{hy} in the PLL input signal e_{hy}

$$\sigma_{hy} = \sqrt{\frac{1}{\frac{1}{\sigma_a^2} + \frac{1}{\sigma_p^2} + \frac{1}{\sigma_z^2}}} \tag{7.15}$$

$$= \sqrt{\frac{\sigma_a^2 \sigma_p^2 \sigma_z^2}{\sigma_a^2 \sigma_p^2 + \sigma_p^2 \sigma_z^2 + \sigma_a^2 \sigma_z^2}}, \tag{7.16}$$

such that the hybrid noise RMS σ_{hy} is always lower (or equal) than the lowest noise of all single estimates. Moreover, the inherent property $k_a + k_p + k_z = 1$ maintains the dimension (electrical radians) for the hybrid error e_{hy}, allowing a straightforward tuning

of the PLL.

In summary, the complete set of equations for the PLL is given by

$$e_{pll} = \frac{s_a^2(\theta_a - \theta_{pll}) + s_p^2 e_{\theta p} + s_z^2 e_{\theta z}}{s_a^2 + s_p^2 + s_z^2} \tag{7.17}$$

$$\omega_{pll} = k_P e_{pll} + k_I \int e_{pll}\ \mathrm{d}t \tag{7.18}$$

$$\theta_{pll} = \int \omega_{pll}\ \mathrm{d}t, \tag{7.19}$$

where the tuning factors k_P and k_I can be used to adjust the bandwidth and the dynamic behaviour of the PLL. Whenever the SNR decreases or increases due to speed, injection magnitude or the availability of a regression result, the influence of the respective estimate in the PLL is automatically adapted. So will, for instance, at low speed no regression result for the ASS be available and the PSS inhere low signal magnitude and hence a low SNR. In this case, the injection-based angle estimate θ_a may have the highest SNR and hence the biggest influence on the PLL – depending on the anisotropy and the injection magnitude.

7.1.3 Injection magnitude controller

Normally, the injection magnitude (amount of pulse width used for injection) constitutes a machine specific parameter in the sensorless control scheme that depends on the admittance difference $|Y_d - Y_q|$, the sampling time T_s and the quality of the current measurement (resolution and noise). As a result, the injection magnitude has to be adjusted for every machine in order to yield a sufficient estimation quality. Moreover, the injection is switched off when the EMF estimator takes over at higher speed.

The idea behind the injection magnitude controller is that the SNR, as a reasonable measure for the angle estimation quality, can be raised or lowered by changing the injection magnitude. In particular, not only the anisotropy-based SNR s_a but the overall hybrid SNR

$$s_{hy} = \sqrt{s_a^2 + s_p^2 + s_z^2} \tag{7.20}$$

is considered since all terms s_a, s_p and s_z contribute to (7.17) and do therefore determine the overall estimation quality. Yet, s_a has a direct influence on s_{hy}, which makes s_{hy} a viable control variable, actuated by the injection magnitude ν_{inj}.

Based on the above definition of the control variable s_{hy}, the control law

$$u_{inj} = k_{inj} \int (s^*_{hy} - s_{hy}) \, \mathrm{d}t \tag{7.21}$$

is introduced which constitutes a simple integral controller with one tuning parameter k_{inj}. Hence, the so-called injection magnitude controller actually controls the hybrid SNR at low speed, using the injection magnitude as actuation variable.

For the choice of the hybrid SNR target value s^*_{hy} we rely on the empirical experience that 15-17 electrical degrees noise RMS in the direct angle estimate (before filtering) is sufficient for a PLL parametrization that allows for closed loop sensorless control with relatively high quality and dynamic stiffness. This value in degrees corresponds to 0.26 rad and hence to a hybrid SNR target value $s^*_{hy} = 4.0$ which has been validated for a variety of tested machines. The injection magnitude ν_{inj} has moreover been limited between 0 and 10% since no tested machine required more than 5%.

When the EMF-based SNR values s_p and s_z increase with increasing rotor speed, ν_{inj} will be reduced and eventually, at sufficient EMF magnitude, it is switched off completely due to the lower limit of 0%.

7.1.4 Initial identification of the load-dependent saliency displacement

Now that the machine parameter-free EMF-based sensorless method, proposed in Ch. 6.2, has been combined with the machine parameter free anisotropy-based sensorless method Arbitrary Injection, using a machine parameter free SNR-based fusion technique and injection controller, an overall parameter-free hybrid sensorless control technique has been obtained that will be applicable to any SPMSM without preliminary configuration. However, one crucial aspect within the fusion has been neglected: the cross saturation induced anisotropy displacement under load which requires a machines specific compensation.

Anisotropy-based methods rely on the alignment of the inductance anisotropy with the rotor position which is the result of both the geometrical saliency (if present) and the saturation of the stator iron due to the PM flux. However, the saturation state of the machine changes with the torque-producing current. Particularly, cross saturation effects (reduction of d-axis flux with increasing q-axis current) lead to cross coupling entries $L_{dq} \neq 0$ in the rotor fixed inductance matrix $\mathbf{L}^r_s$. Hence, the (uncoupled) anisotropy frame (see Ch. 2.3.2) shows a displacement with respect to rotor frame. After disclosing this displacement in [91, 92], a load-dependent angle compensation has become one of the

standard elements in anisotropy-based sensorless control which improves the efficiency and extends the feasible load range at low speed. This compensation, however, is a machine-specific curve over load and constitutes a set of machine parameters that has to be known.

Recently, different approaches have been proposed to identify this curve without using a position sensor. For instance in [93] the curve is obtained from a limited number of FE computations, while [94] utilizes a polynomial approximation of the machine flux curves. In [86] and [95] the comparison to an FM-based method is employed for the identification of this curve during operation. However, all these methods require either FEM results or the machine working in several operating points with speed and load. Nevertheless, some applications demand that all relevant machine parameters are obtained in an initial self commissioning process during which the rotor must not move. This is fulfilled by the initial anisotropy shift identification technique proposed in [96].

The idea behind [96] is that in idle (current-free) condition the flux linkage of a PMSMs is aligned with the rotor fixed d-axis. According to the flux linkage equation for a linear machine in rotor frame (2.67), an increasing pure q-axis current would result in a straight flux trajectory, indicated by the light blue dotted line in Fig. 7.3(a). In practice, however, magnetic cross-saturation leads to a reduction of the d-axis flux linkage with increasing q-axis current magnitude. As a result, a saturating machine will show the dark blue dotted flux trajectory in Fig. 7.3(a) in response to a pure q-axis current which is always slightly bent towards the current.

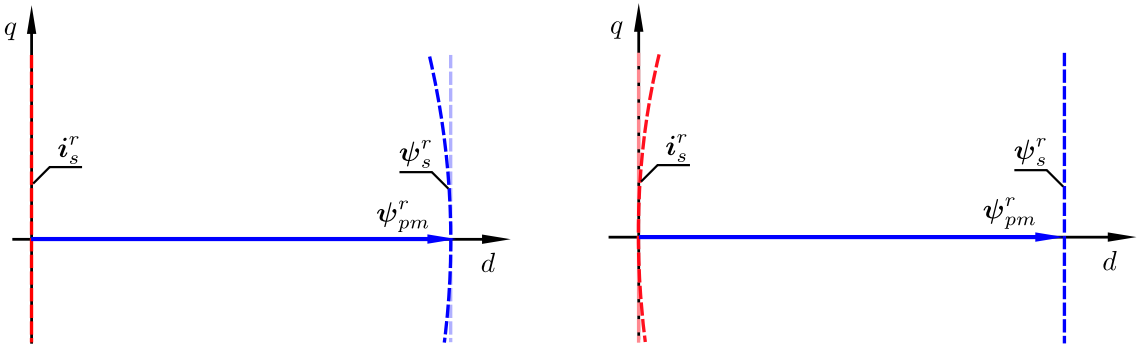

(a) Flux trajectory resulting from a pure q-axis current.

(b) Current trajectory resulting from a pure q-axis voltage.

Figure 7.3: *Current and flux responses to pure q-axis excitation in linear and cross-saturating case.*

In order to identify the anisotropy displacement, the inverse relation is employed: the current trajectory resulting from a pure q-axis flux imposition. During an initiation sequence, a short voltage injection phase identifies the orientation of the rotor frame

(with 180° uncertainty) after which a strong test voltage pulse is applied into the q-axis. If the rotor does not move ($\omega \approx 0$) and if the applied voltage is much stronger than the resistive term ($|u| \gg R_s|i|$), then the voltage equation in rotor frame is simplified

$$\frac{d\boldsymbol{\psi}_s^r}{dt} = \boldsymbol{u}_s^r - \cancel{R_s \boldsymbol{i}_s^r} - \cancel{\mathbf{J}\omega\boldsymbol{\psi}_s^r} \tag{7.22}$$

$$\approx \boldsymbol{u}_s^r. \tag{7.23}$$

Thus, a pure q-axis voltage pulse will force the machine flux to evolve on a straight vertical trajectory, indicated by the blue dotted line in Fig. 7.3(b).

While an ideal linear machine would respond with pure q-axis current (light red dotted line in Fig. 7.3(b)), a real saturating machine will show a current evolution that is bent towards the PM-flux (dark red dotted line in Fig. 7.3(b)) – a parabolic trajectory with an always positive d-component

$$i_d = \frac{Y_\Delta k_1}{Y_Q}\, i_q^2 \tag{7.24}$$

$$= a_2\, i_q^2, \tag{7.25}$$

where k_1 is the linear anisotropy displacement factor

$$\theta_a = \theta + k_1 i_q. \tag{7.26}$$

Hence, when knowing the saliency ratio Y_Δ/Y_Q (e.g. from the initial injection sequence), the load-dependence of the saliency displacement k_1 can be concluded from the curvature of the parabolic d-axis current response a_2 to a macroscopic q-axis voltage pulse.

Fig. 7.4 shows this initial test with SPM1, using a suitable voltage pattern that leads to an overall momentum-free[1] current evolution. The q-axis current response to the constant voltage pulses is linear, whereas the d-axis current develops the predicted parabolic shape. Three zero voltage phases have been inserted in order to obtain three clean current samples for the accurate computation of the squared coefficient

$$a_2 = \frac{i_{d3} - i_{d1}}{(i_{q3} - i_{q1})(i_{q3} - i_{q2})} - \frac{i_{d2} - i_{d1}}{(i_{q2} - i_{q1})(i_{q3} - i_{q2})}. \tag{7.27}$$

The magnitude of this coefficient is subsequently used to deduce the load dependence of

[1] As the q-axis current produces torque, the total area underneath the q-axis current graph must be zero in order to finish the pattern without remaining rotor speed. As shown in [96], the entailed rotor movement during this test is in the range of about 0.1 mechanical degrees.

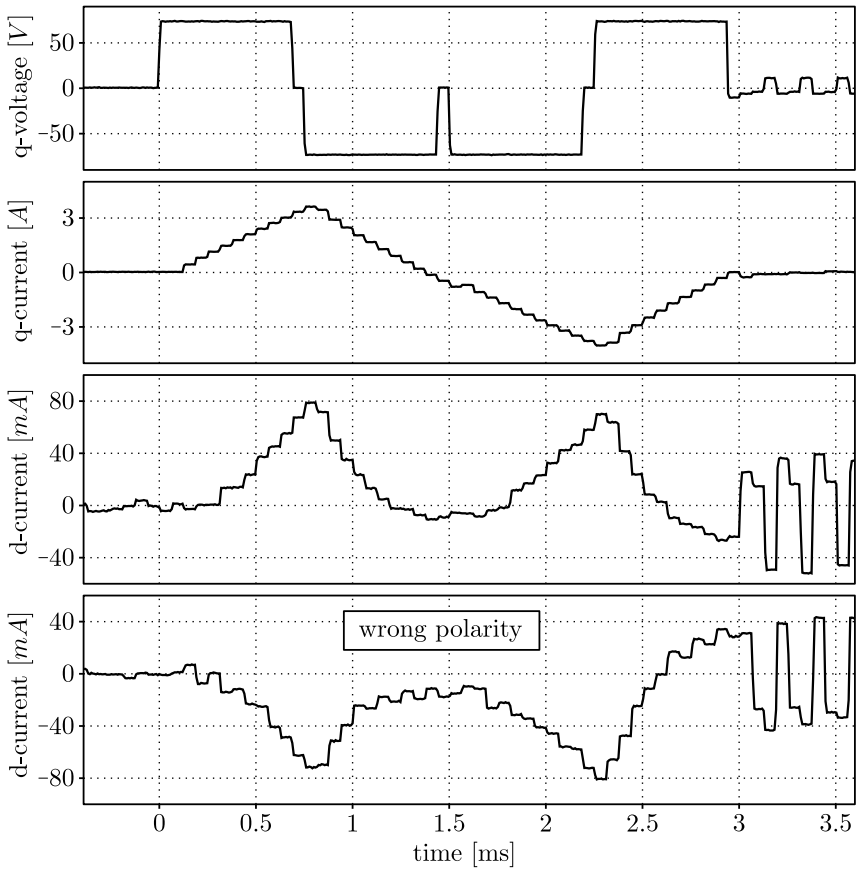

Figure 7.4: *Measured current response to pure q-axis voltage.*

the anisotropy

$$k_1 = \frac{Y_Q}{Y_\Delta}|a_2|. \tag{7.28}$$

As shown by the bottom graph of Fig. 7.4, the sign of a_2 can additionally be employed for the rotor polarity identification which is normally realized by a d-axis pulse [97].

7.1.5 Experimental validation of the parameter-free hybrid scheme

Apart from particular investigations, the proposed hybrid sensorless control schemes will be investigated and compared using closed loop sensorless speed control as the key challenge. As indicated in Fig. 7.5, the speed feedback signal is obtained from the time derivative of the hybrid position estimate. The respective noise amplification is damped by means of a first order LPF, the bandwidth $1/T_\omega$ of which must exceed the speed controller bandwidth by at least factor 2 (stability). Hence, in this test scenario the

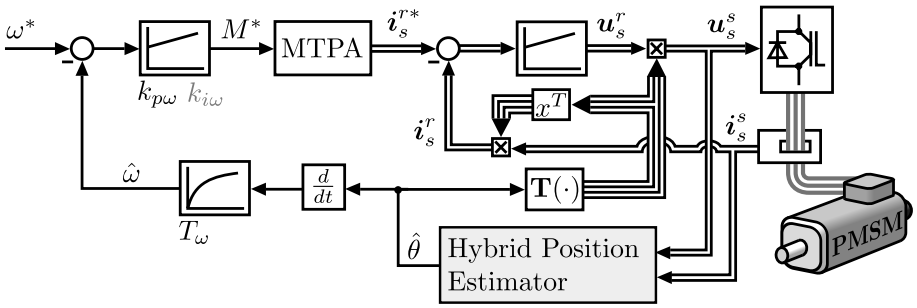

Figure 7.5: *Cascaded FOC and speed control structure for the validation of the proposed sensorless control techniques.*

bandwidth-noise trade-off problem is markedly aggravated, such that the resulting dynamic stiffness in combination with the cleanness of the estimation and actuation signals is a good indication for the achievable performance of a sensorless control approach. For this reason, the scheme indicated in Fig. 7.5 will be used as the superordinate control structure for the experimental performance validation in both this section and the following section 7.2.

During a slow acceleration from standstill to the voltage limit (in closed loop sensorless speed control) the single and hybrid SNR values of Fig. 7.6 have been recorded with SPM1. As a result of the subtraction of the signal strength offset in (7.6) and (7.7),

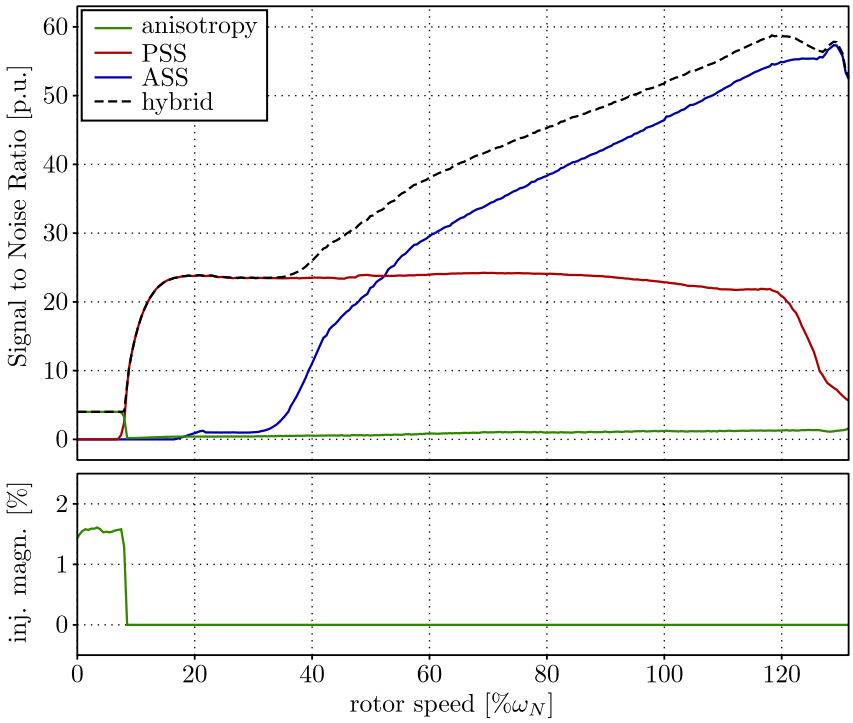

Figure 7.6: *Online identified individual and hybrid SNR with injection magnitude control over speed.*

the PSS-based estimation has nearly zero SNR below 10% rated speed. In this area the injection magnitude controller actuates with about 1.6% injection in order to maintain the overall hybrid SNR of $s_{hy} = 4.0$ and thus sufficient signal quality for sensorless control around zero speed. Between 20-40% rated speed the PSS evaluation has its optimal SNR. Beyond 50% rated speed the ASS evaluation reaches very high SNR values as it combines the increasing signal (EMF) strength with the growing ASS length. However, the PSS signal quality remains further on reasonable and contributes to the hybrid SNR until 120% rated speed (where the PSS finally becomes too short for being evaluated).

In order to validate the dynamic properties of the proposed machine parameter-free hybrid scheme, Fig. 7.7 shows its response in speed control to reference and load variations. The step-shaped speed reference adopts the values 0%, 30% and 110% rated speed. Ac-

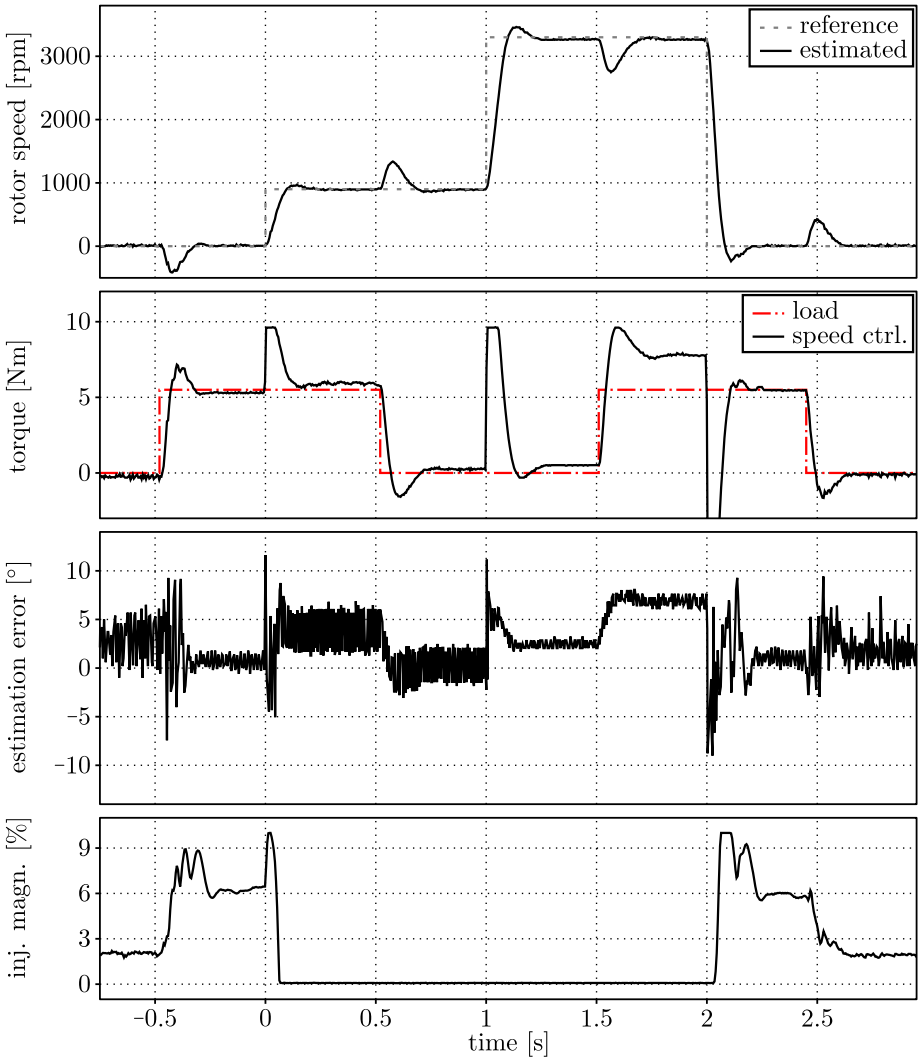

Figure 7.7: *Reference and load step response of the parameter-free hybrid scheme with SPM1.*

cording to Fig. 7.6, each of these values results in a different position estimate (anisotropy, PSS-, or the ASS-based) being dominant in the hybrid fusion. During the constant speed phase a load of roughly[2] two thirds rated torque has been applied. The initial injection and pulse sequence identified the saliency ratio being $Y_\Delta/Y_Q = 12.94\%$ and an anisotropy displacement factor $k_1 = 1.76°/\text{A}$, respectively. Based on these values the compensations for both the PSS-based and for the anisotropy-based angle estimation are carried out.

During load free standstill the SNR target value $s^*_{hy} = 4.0$ results in 1.8% injection magnitude[3], using the Δ^2 evaluation of the regression results. When a load torque is applied, the noise content increases such that the injection magnitude controller actuates with 6.0%. During torque transients the noise in the estimation error reaches peak values of up to 11°before the injection magnitude is respectively adapted.

During the load free phases the idle estimation error of each estimate can be seen, where (as noted before in Ch. 6.2.3) the PSS-based estimation shows larger harmonics than the ASS-based estimation. The difference between load free and loaded operation at each speed demonstrates the effectiveness of the compensation techniques of Ch. 6.2.1.2 and 7.1.4. The compensation of the anisotropy displacement (Ch. 7.1.4) is satisfactory, whereas the compensation of the load error of the EMF-based techniques (Ch. 6.2.1.2) is only partially successful, leaving 4° estimation error difference under load. This results mainly from the fact that the initial injection sequence determines a 30% lower HF saliency ratio than given by the tangential inductances of this machine – i.e. by the slope of the flux curves in Fig. 2.8(a) which are particularly relevant for the compensation of these fundamental effects. According to the investigations in [90], this difference may result from hysteresis and eddy currents.

In order to prove the machine parameter independence of the proposed SNR-based hybrid sensorless scheme, Fig. 7.8 shows the same experiment repeated with a structurally different machine: an IPMSM of almost double size. Since the proposed scheme presumes in two points (Ch. 6.2.1 and 7.1.4) that the reference current trajectory is located on the q-axis (which makes it suitable only for SPMSMs), IPM1 is not operated on its actual MTPA. Moreover, with this test bench setup no load could be applied.

The initial injection and pulse sequence identified a saliency ratio $Y_\Delta/Y_Q = 46.1\%$ and an anisotropy displacement factor $k_1 = 1.38°/\text{A}$. Due to the different rated speed value,

[2]Due to the configuration limits of the load inverter (induction machine saturation behaviour), the load torque is speed dependent. Hence, the load reference graph only indicates the time of the load steps. The actual load magnitude can be seen from the steady state value of the speed controller actuation torque.

[3]For this dynamic experiment the speed controller gains have been increased with respect to Fig. 7.6, which increases the overall noise level in the estimation signals and leads to this slightly increased injection magnitude.

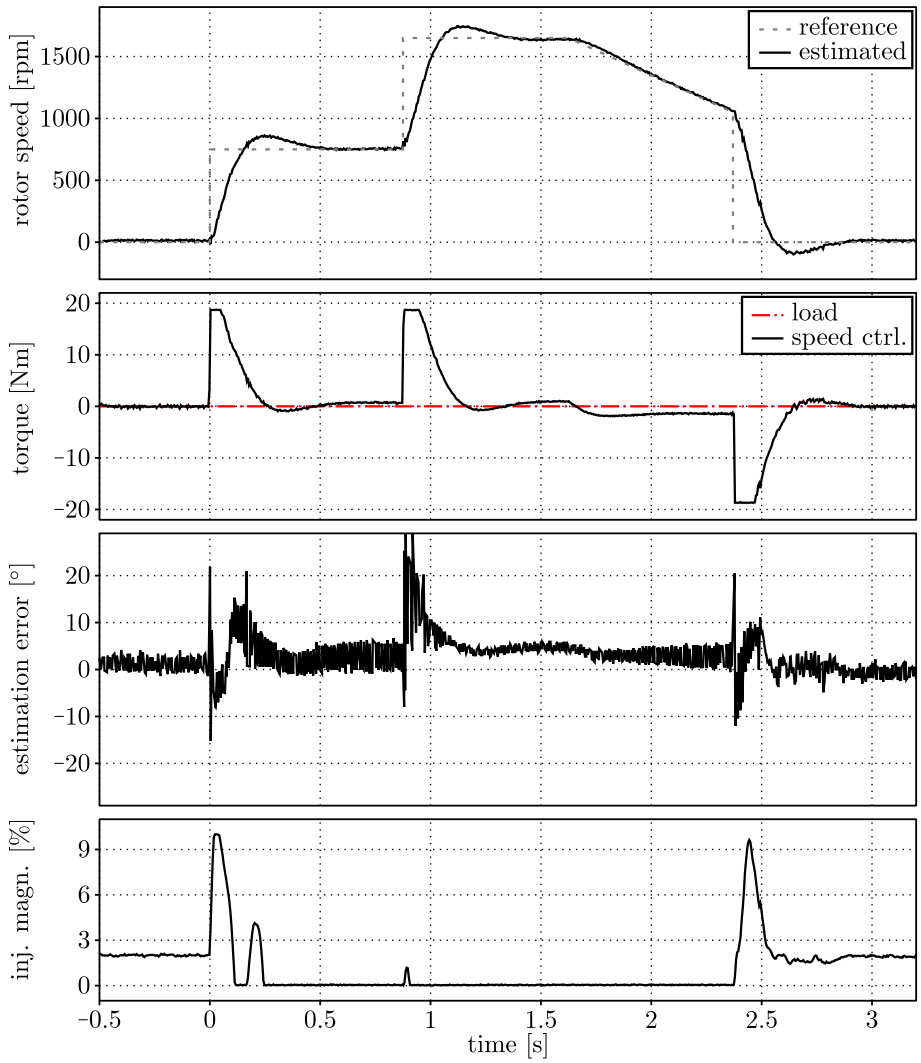

Figure 7.8: *Parameter-free hybrid scheme controlling IPM1.*

the reference steps are lowered respectively. Still, a full stop from rated speed was not possible with the big inertia of the machine (see Tab. B.1) and the passive front end of the inverter. With this very different and unsuited machine the sensorless control performance is worse than in Fig. 7.7, showing larger estimation errors and even slight injection peaks at high speed (due to a temporarily low SNR), but still acceptable in comparison to other results in literature. All in all, this experiment demonstrates that, although designed for SPMSMs, the proposed scheme can be applied to PMSMs of different structure and size without a change to its configuration or parametrization. Hence, in contrast to any other hybrid sensorless control method in literature, this method can be considered machine parameter independent.

7.2 Generic high performance hybrid sensorless control

The second fusion method, proposed in this section, has oppositional properties to the one of the previous section. By demonstrating both extremes, the author aims to provide a scope of the capabilities of oversampling-based sensorless control. This method will, on one hand, contain several machine parameters. On the other hand, it will provide very high estimation dynamics and good signal quality while still having low injection magnitude requirements. It is therefore considered to exhibit one of the best sensorless performances available in recent literature.

The basis of this hybrid sensorless control technique is the simple flux estimator, described in Ch. 3.1.2 and indicated in Fig. 7.9 again. Its design without any filtering

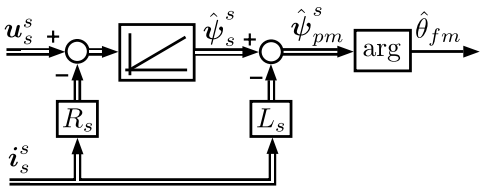

Figure 7.9: *Basic flux estimator.*

provides theoretically unlimited estimation bandwidth while the (physical) integrator ensures low noise content in the estimated flux $\boldsymbol{\psi}_s^s$ and hence in the estimated angle $\hat{\theta}_{fm}$. As a result, this FM-based position estimator can be employed to design a closed loop sensorless control with very high dynamic stiffness.

However, as mentioned in Ch. 3.1.2, its major drawback is the open loop integration which (due to inevitable parameter errors or offsets of the input signals) will show a drift problem – i.e. $\hat{\boldsymbol{\psi}}_s^s$ will drift towards a random direction and over time lose its angle information.

Consequently, practical implementations of this technique always include a feedback structure for drift compensation where, as mentioned in Ch. 3.1.2, the intelligence of this feedback determines the lower speed limit for the flux estimator.

Most sources in literature employ a feedback controller that either targets zero flux [46, 47] or the internal voltage[4] angle [45, 48], which both entails a lower speed limit. Consequently, it is necessary to switch over to anisotropy-based angle estimation at low speed. These methods, however, provide only limited dynamics which in particular depend on the injection magnitude.

[4]The EMF directly calculated from the voltage equation. Its relatively high noise content is still sufficient for the drift compensation.

7.2.1 Intelligent feedback design

The feedback approach employed in this work is rather seldomly used in literature [40, 50, 51]. As indicated in Fig. 7.10, the anisotropy-based angle information is utilized within the drift feedback structure to create a reconstruction of the PM flux $\tilde{\boldsymbol{\psi}}^s_{pm}$. This value is

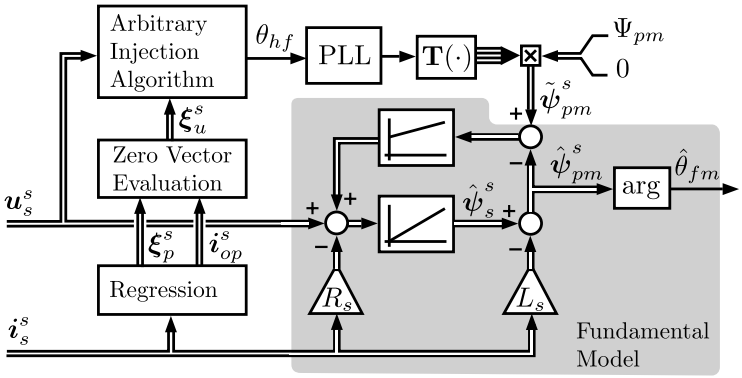

Figure 7.10: *Arbitrary Injection Scheme used for stabilization of a flux estimator.*

more or less noisy but does, in average, provide a valid representation of the real PM flux $\boldsymbol{\psi}^s_{pm}$ – also at standstill. By feeding the difference $\tilde{\boldsymbol{\psi}}^s_{pm} - \hat{\boldsymbol{\psi}}^s_{pm}$ into the PI drift controller, the estimated flux $\hat{\boldsymbol{\psi}}^s_{pm}$ is gradually "pulled" towards the centre of the noisy reconstruction $\tilde{\boldsymbol{\psi}}^s_{pm}$ and does, hence, also at standstill match the real PM flux $\boldsymbol{\psi}^s_{pm}$.

As a result, the output angle of the flux estimator $\hat{\theta}_{fm}$ can be used as a reliable position estimate also at low speed and standstill such that a switch over to using the anisotropy angle is not necessary anymore. Hence, the very good estimation properties of the flux estimator, especially its very high dynamics, are now also available at standstill.

Moreover, the noise content in θ_a and the subsequent PLL tuning must now only suffice the bandwidth of the drift compensation which is usually much lower than the demanded bandwidth of the output angle estimate. This allows an additional reduction of the injection magnitude compared to the direct usage of the PLL filtered anisotropy angle θ_a.

Fig. 7.11 shows the results of the proposed hybrid sensorless control scheme employed in closed loop speed control, i.e. the low pass filtered derivative of the position estimate is fed back to a superordinate PI speed controller (see Fig. 7.5). This derivative feedback aggravates the tradeoff between quality and bandwidth of the estimated signal and is therefore considered a good demonstration of the dynamical capabilities of a sensorless control scheme. The low noise content in the unfiltered position estimate $\hat{\theta}_{fm}$ allowed to use a relatively fast speed filter time constant $T_\omega = 1.25\,\mathrm{ms}$, resulting a very short delay in the speed estimate. For medium and low speed controller bandwidths (usual in sensorless control) this delay is negligible. Then the speed control plant can be considered

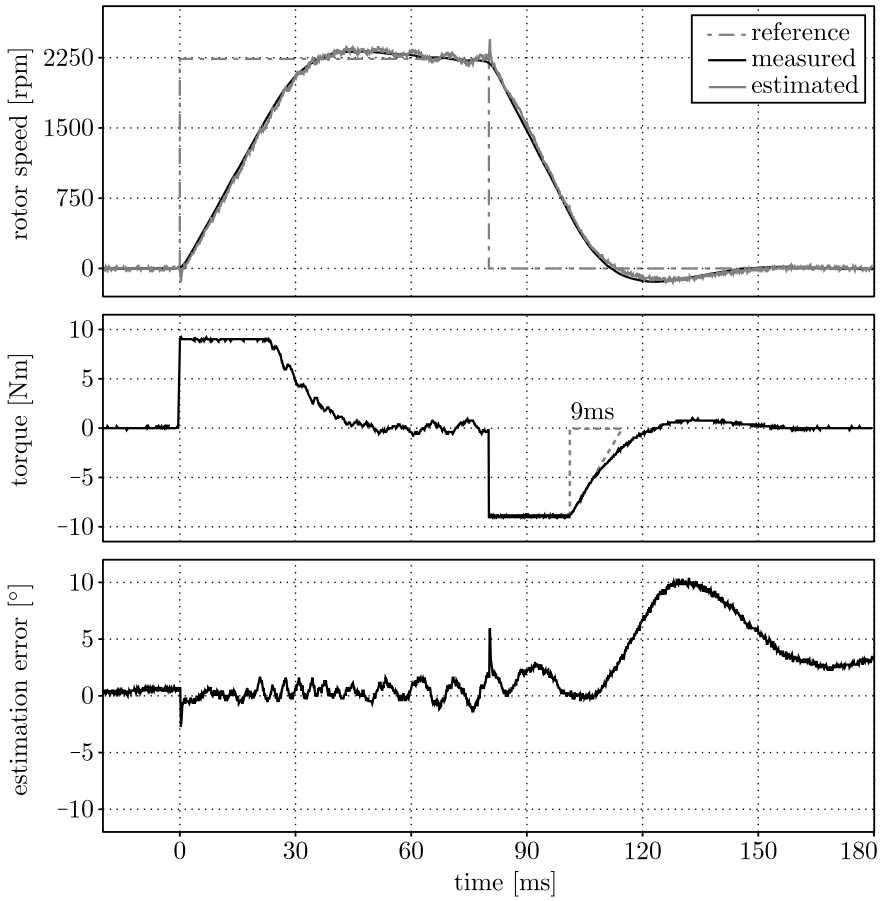

Figure 7.11: *Response of the stabilized flux estimator in speed control to a reference speed steep from standstill to 75% rated speed and back.*

as a simple integrator which is generally suitable for high gain control. Hence, the only expected restriction for the speed controller bandwidth k_ω is

$$k_\omega \approx \frac{k_{p\omega}}{\Theta} \ll \frac{1}{T_\omega} = 800/\mathrm{s}, \tag{7.29}$$

with Θ being the inertia of the rotor and all directly connected revolving parts.

However, the experimental results in Fig. 7.11 have been obtained with the highest possible P-Gain of the speed controller $k_{p\omega} = 0.047\,\mathrm{Nm/rpm}$ which, according to the torque decay time after limitation, results in an overall speed controller bandwidth of $k_\omega = 111/s$. This bandwidth is high in comparison to the hybrid methods proposed in literature [39–42], but still 8 times lower than the expected limitation. As described before in [98], a further increase of $k_{p\omega}$ results in an oscillation and later in the instability of the speed control loop.

7.2.2 Dynamic limitation due to eddy currents

This phenomenon, only arising for very stiff tuning of the superordinate speed controller, has neither been documented nor investigated in literature [45, 46, 48]. Yet, the relatively large distance to the expected bandwidth limitation hints that there could be potential for a further increase of the sensorless dynamics.

In order to scrutinize this limitation, the experiments indicated in Fig. 7.12 have been carried out. The top right graph shows a the response of the current control loop to a reference step of 70% rated current which could be the command of the speed controller. The light green graph in Fig. 7.12 shows what could already be seen in Fig. 7.11: during fast current transients an oppositional peak appears in the estimation error (estimated minus measured position). This peak propagates (amplified by the time derivative and damped by the LPF) into the estimated speed signal $\hat{\omega}$ that is fed back to the speed controller. The speed controller will consequently demand a higher current in order to counter this negative estimated speed, which explains the emerging instability for sufficiently high speed controller gains.

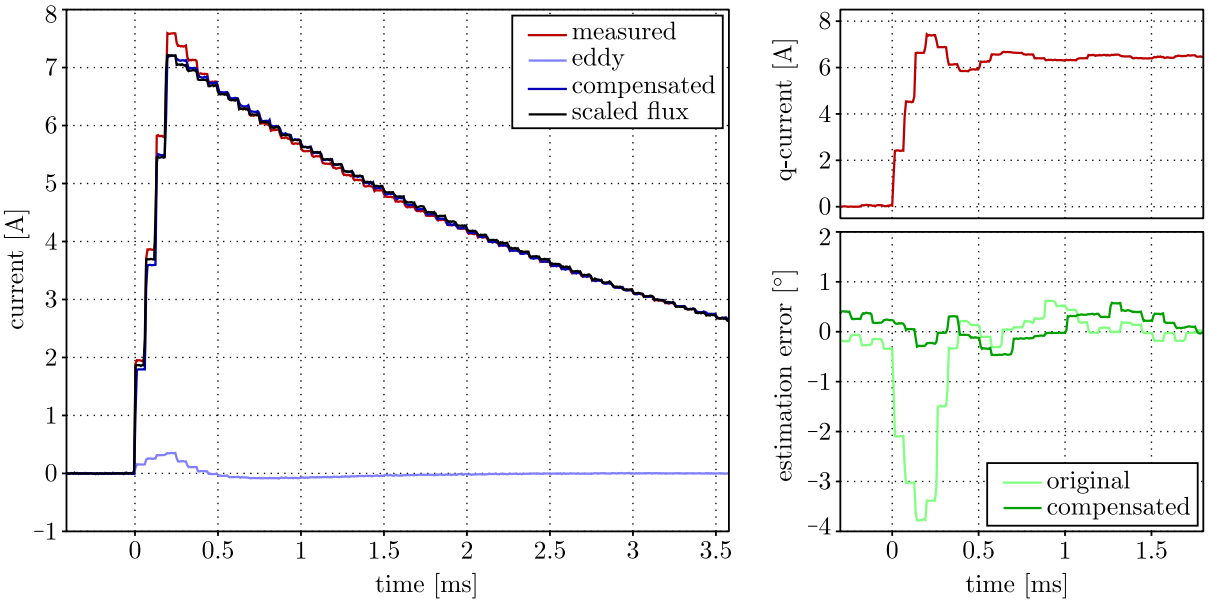

Figure 7.12: ***left:*** *Non-static relation between flux and current and compensation through eddy current model.*
right: *Peak in estimation error during current transients before and after eddy current compensation.*

Yet, the questions remains: What causes this peak in the estimation error during currents transients if the flux estimator though exhibits a theoretically unlimited bandwidth?

The answer lies in the left hand side graph of Fig. 7.12 that displays the current and flux response to a to a short, strong voltage pulse. The flux has been obtained through voltage

integration using (3.7) and scaled by the admittance in order to facilitate the comparison to the current. If the relation between flux and current was static[5], as assumed for the subtraction of the inductive flux term $L_s \boldsymbol{i}_s^s$ in (3.6), then the measured current and the scaled flux curve in Fig. 7.12 would match perfectly for this nearly linear SPMSM. However, in the time during and short after the voltage pulse those two curves differ, re-coinciding only about 0.2 ms after the voltage pulse. Hence, a strong voltage excitation causes a short-time non-static relation between flux and current.

Using the simple eddy current model from Ch. 2.6, this dynamic deviation could be emulated, resulting in the light blue curve in Fig. 7.12. Subtracting this simulated eddy current from the measured current results in the compensated current which, as indicated by the dark blue curve in Fig. 7.12, shows a nearly static relation to the flux again. Hence, this compensated current value inheres the properties required for the subtraction of the inductive term $L_s \boldsymbol{i}_s^s$ and is hence employed within (3.6).

It is, however, interesting to note that the simple eddy current model, used in various sections of this thesis, had to be parametrized differently here in order to match the measured deviation from the static behaviour: The eddy current admittance has been set to $\mathbf{Y}_{ed}^s = 0.17 Y_\Sigma$ (26% of the usual value) and the eddy current fade out time has been set to $T_{ed} = 4.0\ T_s$ (27 times the usual value). Since the differently parametrized model does, however, precisely match the measured non-static behaviour, we conclude that eddy currents are a valid explanation for this dynamical phenomenon, but that there must be different locations of the eddy currents in the machine material (laminated iron, copper, permanent magnets) with different quantitative characteristics. A further validation of this explanation would require an FEA and is not part of the scope of this thesis.

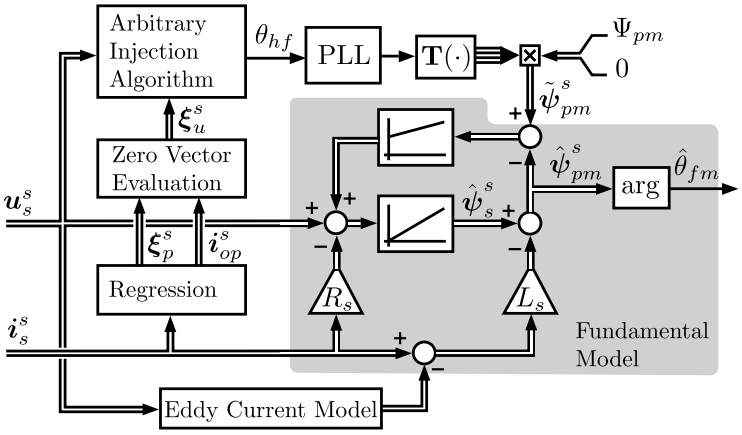

Figure 7.13: *Stabilized flux estimator with eddy current compensation.*

[5] A fixed (time-independent) relation between current and flux, representable by a linear or nonlinear curve.

Finally, the hybrid sensorless control scheme is extended by the eddy current model, as indicated in Fig. 7.13. The additional block reads in only the terminal voltage, based on which it simulates the eddy currents. This current value is subtracted from the measured current in order to obtain the compensated current with static relation to the flux.

As indicated by the dark green line in the bottom right graph of Fig. 7.12, the output angle of this extended hybrid scheme does not show the short time peak during current transients anymore, which allows to further increase the speed controller P-gain without causing an oscillation or instability of the speed control loop. A reasonable[6] value for the P-gain has been found empirically at $k_{P\omega} = 0.265\,\mathrm{Nm/rpm}$ which is 5.6 times higher than the limitation of the uncompensated scheme and about twice as high as a simple 1024 line encoder evaluation would allow.

Fig. 7.14 demonstrates the resulting high bandwidth closed loop speed control that is possible with this compensated hybrid sensorless control scheme. The increased inertia

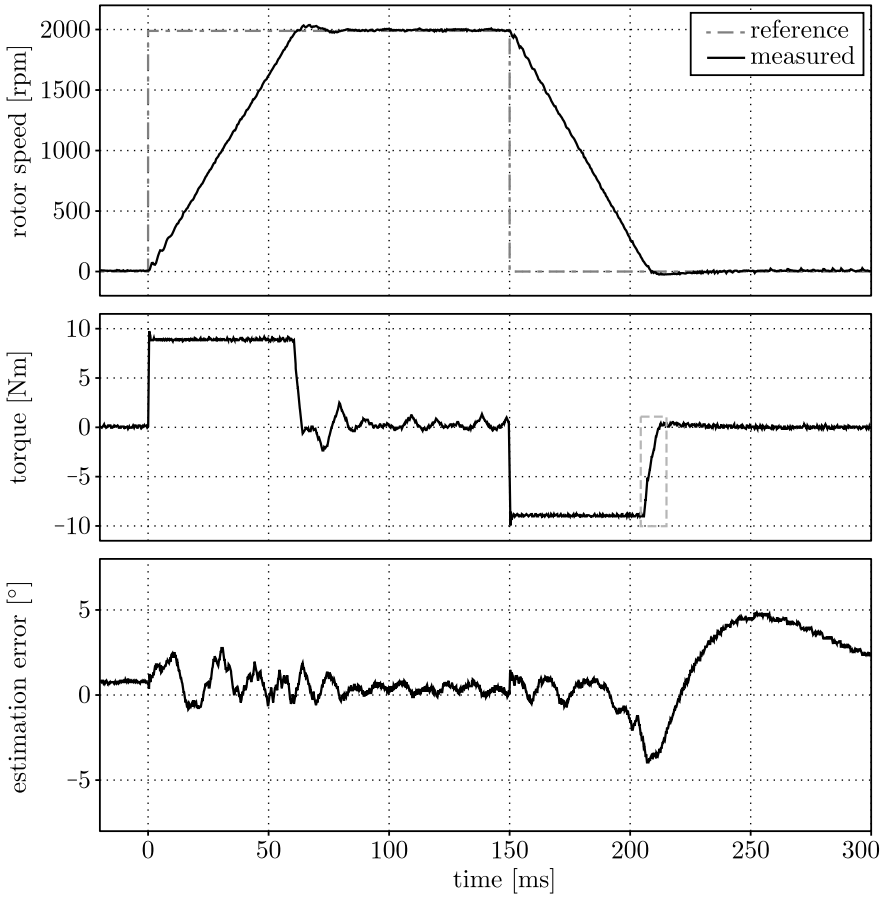

Figure 7.14: *Response of the stabilized flux estimator with eddy current compensation in speed control to a reference speed steep from standstill to 66% rated speed and back.*

[6] As stiff as possible, without relevant acoustic noise emission.

(bigger load machine coupled) leads to a longer acceleration time during the current limitation, but the torque decay phase is markedly shorter than in Fig. 7.11. Despite this high speed controller gain, the torque signal is relatively smooth – especially during the standstill phases where the acoustic noise emission is of increased importance. The estimation error does not show the transient peaks anymore and stays within ±3 electrical degrees (1 mechanical degree) – apart from the slow transient after reaching standstill again which can also be seen in Fig. 7.11. This transient is the result of the drift compensation adapting to the specific steady state errors (interlock time error voltage, diode voltage, etc.) belonging to the new sector that the deceleration phase ended in.

However, in order to furthermore analyse the achievable dynamic stiffness of the compensated hybrid scheme, Fig. 7.15 shows a zoom into the torque decay phase, indicated by

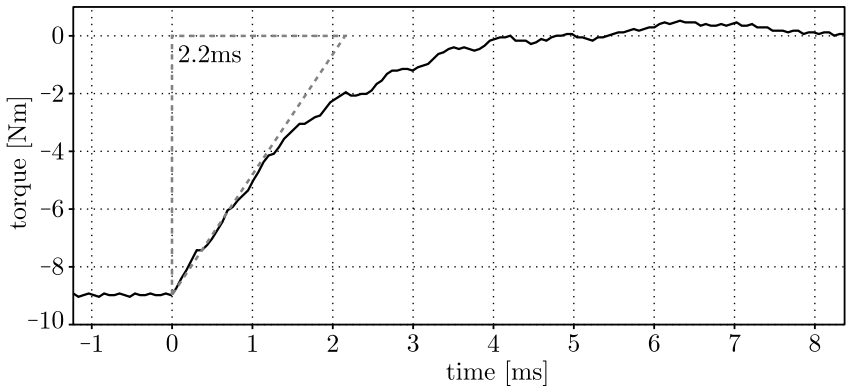

Figure 7.15: *Zoom into torque transient for control bandwidth evaluation.*

the dotted grey frame in Fig. 7.14. The tangent of the decaying toque reaches zero after 2.2ms which corresponds to a speed controller bandwidth of $k_\omega = 450/\mathrm{s}$ or 72 Hz. This bandwidth is much higher than the results shown in literature for sensorless control and rather ranks into the bandwidth scale of speed control with advanced sensors. Moreover, this bandwidth is achieved without employing an observer for the mechanical system and hence, without requiring structural and parametric knowledge of the mechanical system.

However, it is important to note that the analysis and the results demonstrated in this section have been carried out using SPM1 while they do depend on the specific machine geometry and the used material lamination. Hence, for other machine types and sizes, the influence of eddy currents will be quantitatively different. Yet, the qualitative relations deduced in this section should remain the same.

Finally, the disturbance response of the hybrid scheme is validated by applying a step of about two thirds rated load at standstill, accelerating the machine to 2000 rpm and releasing the load. In contrast to Fig. 7.14, the acceleration phase takes 120 ms due to the

load, but does otherwise not give new insight. Hence, in order to analyse the contracted speed distortion (due to the high speed controller bandwidth) in detail, Fig. 7.16 shows a zoom into the instants of load imposition.

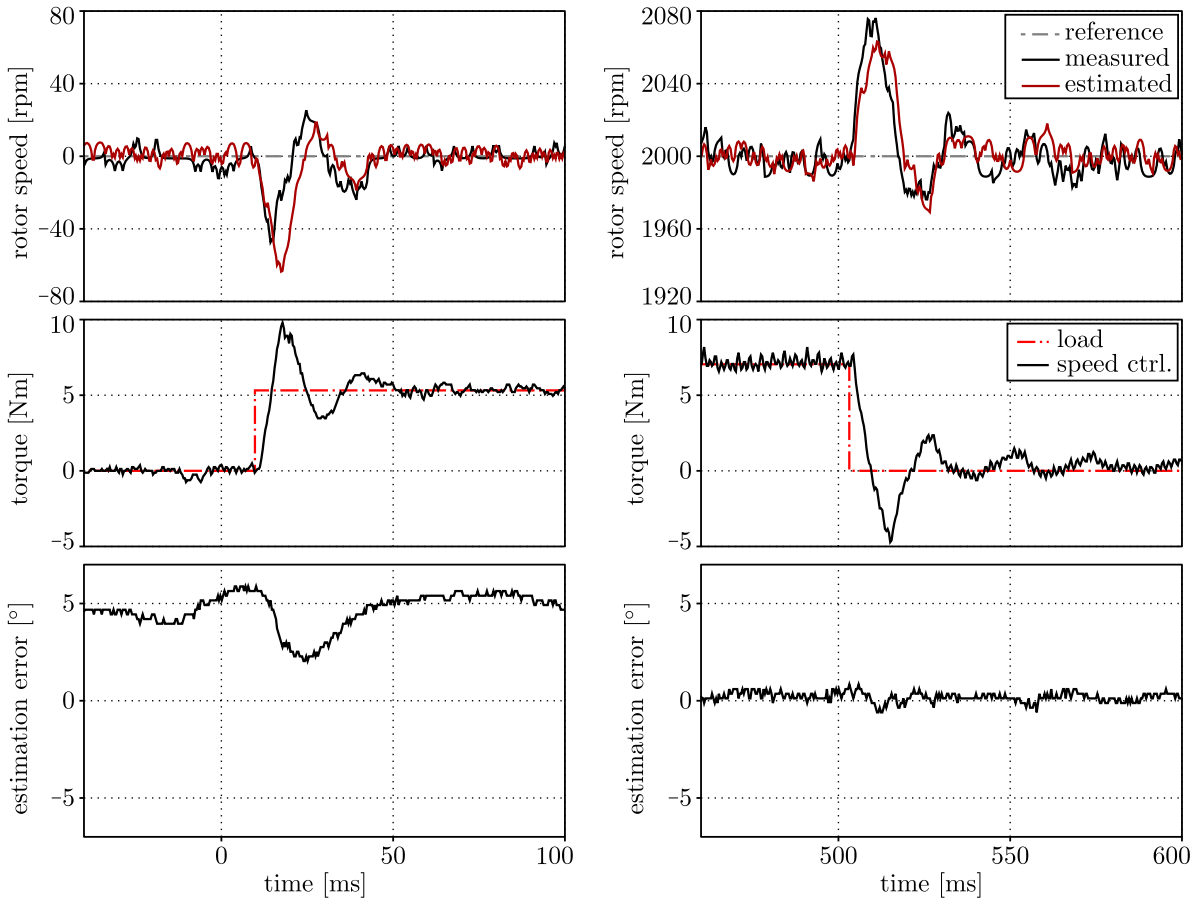

Figure 7.16: *Load step response of the stabilized flux estimator with eddy current compensation in speed control targeting standstill and 66% rated speed.*

Due to load inverter programming restrictions the applied load is speed dependent (as explained before in Ch. 7.1.5). Hence, the reconstructed load torque graphs do rather indicate the time of the load imposition than the actual height or shape. The high zoom factor of the speed signal (range $\pm 2.6\%\omega_N$) amplifies noise and variations that are barely visible in Fig. 7.14, such that the load-induced speed disturbance can be seen. This disturbance reaches peak values of 45 rpm at standstill and 70 rpm at high speed (both measured). The estimated speed signal, based on which the speed controller actuates, shows a partially different amplitude and a delay of about 2 ms. Within 4 ms after the step the load torque is compensated, after which it takes about 30 ms for the oscillations to calm down. At high speed, this transient process does not entail an estimation error. At standstill, (uncompensated) anisotropy harmonics cause an initial estimation error that

varies by about ±2° during the transient and settles, due to the anisotropy displacement compensation, at nearly the same error value again.

All in all, it is interesting to note that this quick detection of this tiny speed variation at standstill (overall rotor movement less than 1 mechanical degree) can only be realized by the eddy current compensated flux estimator that, as described in Ch. 7.2.1, provides the position estimate at all speeds. The necessary filtering behind the anisotropy angle estimation (or any other sensorless technique) would not allow to counter a load torque that rapidly – especially not at standstill.

The injection magnitude required for the high bandwidth settings of the above experiments is indicated in Fig. 7.17. Using SCS, a relatively smooth (calmness of the shaft)

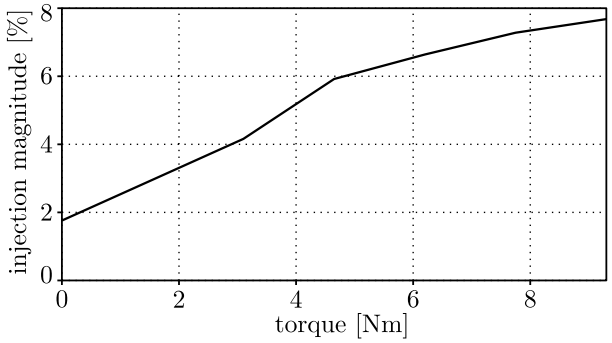

Figure 7.17: *Injection magnitude required for speed control with* 20 rpm *reference.*

sensorless low speed operation of the hybrid scheme could be reached with 10% injection magnitude. This subjective calmness corresponds to a speed controller actuation noise[7] RMS of 0.3 Nm which has been taken as a reference value. In order to reach these 0.3 Nm with the regression-based anisotropy evaluation, 1.8% injection magnitude (3.3 V) have been required in idle condition, corresponding to a reduction by factor 5.7. As found before in Ch. 7.1.5, under load the injection magnitude needs to be increased in order to retain the SNR of the anisotropy identification. However, those specific injection magnitude values depend on the particular hardware setup (DC link voltage, anisotropy of the machine and quality of the current transduction) and on the required estimation and control bandwidth. The still high dynamics of Fig. 7.11, for instance, required only 0.7% injection magnitude, resulting in a barely perceivable acoustic noise emission.

[7]The noise of the anisotropy angle feeds through the drift feedback (see Fig. 7.13) into the flux estimator. The resulting FM angle estimation noise propagates through the time derivative and the high bandwidth LPF into the speed signal (see Fig. 7.5) where it is amplified by the speed controller proportional gain $k_{p\omega}$ into a reference torque noise that can be felt at the shaft.

7.2.3 Stabilized flux estimator for the RSM

Finally, this highly dynamic concept for full speed range position estimation will be applied to the reluctance synchronous machine (RSM). Since EMF-based schemes for the RSM [53, 54] suffer from estimation noise around standstill, they are not suitable for this concept. It must be a flux estimation based approach which shows a drift problem around standstill. A well known generalised flux estimator is the Active Flux concept [45] which is also applicable to the RSM. However, its application to the RSM requires the permanent presence of a d-axis current. This is in conflict with the claim of anisotropy based schemes to always pre-saturate the q-axis of the RSM by means of a slight q-axis current in order to make the anisotropy visible [52]. Since combining both requirements does not leave any torque-free operating point, the Active Flux concept is not suitable for the design of a stabilized hybrid estimator.

The fundamental saliency based approach, proposed in [52] and described in Ch. 3.1.3, also employs a flux integration but does not presume the presence of a d-axis current. A torque-free operating point is hence possible on the q-axis. The drift problem of [52] can be stabilized by means of an anisotropy-based feedback structure similar to Ch. 7.2.1. Then the high bandwidth of the flux estimation is also available at standstill.

Since the current-flux relation of an RSM is highly nonlinear (see. Fig. 2.8), the flux reconstruction in the feedback structure requires a rotor fixed nonlinear assignment $f_{\psi i}(\cdot)$ which in this work has been realized by interpolating a 2D LUT. As indicated in Fig. 7.18, the anisotropy-based angle estimation θ_a is employed to transform the measured stator fixed current $\boldsymbol{i}_s^s$ to (estimated) rotor frame where the assignment $f_{\psi i}(\cdot)$ is realized. Then the resulting flux value $\tilde{\boldsymbol{\psi}}_s^{\hat{r}}$ is transformed back to stator frame using the same angle θ_a.

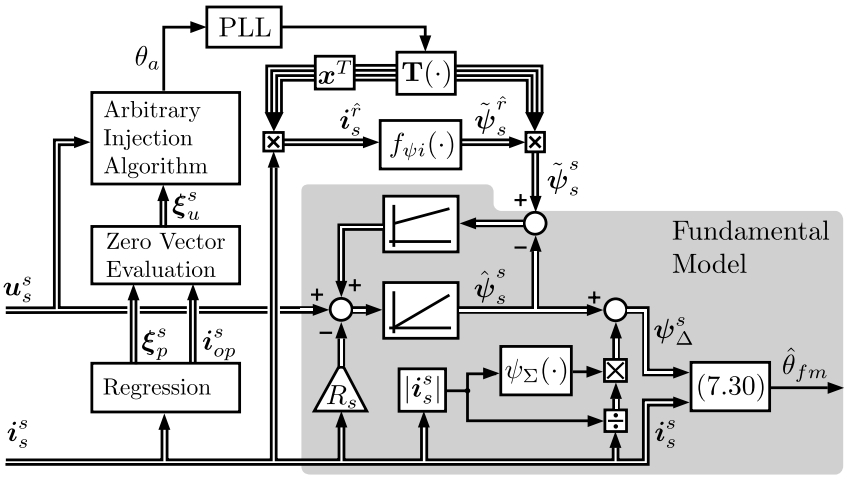

Figure 7.18: *Stabilized flux estimator for the RSM.*

Due to the noise in the anisotropy estimation, this stator fixed reconstructed stator flux $\tilde{\boldsymbol{\psi}}_s^s$ is noisy but drift free, and hence, a suitable reference value to gradually "pull" the estimated flux $\hat{\boldsymbol{\psi}}_s^s$ towards $\boldsymbol{\psi}_s^s$ (using a PI controller).

In order to utilize the full dynamic potential of the flux estimation, the eventual PLL structure of the scheme in Fig. 3.5 is replaced by a direct resolution of the rotor angle out of the relation between the salient flux component $\boldsymbol{\psi}_\Delta^s$ and the current $\boldsymbol{i}_s^s$

$$\hat{\theta}_{fm} = \frac{1}{2}\text{atan2}(i_\alpha\psi_{\Delta\beta} + i_\beta\psi_{\Delta\alpha},\ i_\alpha\psi_{\Delta\alpha} - i_\beta\psi_{\Delta\beta}) \tag{7.30}$$

which corresponds to the saliency angle equation of Arbitrary Injection (3.27). In this way, there is no filter structure included in the position estimation such that the estimation bandwidth is theoretically unlimited. Yet, due to the physically justified integration, the noise content in the angle estimate $\hat{\theta}_{fm}$ is sufficiently low to allow for a direct usage of $\hat{\theta}_{fm}$ in the FOC. The time derivative for the speed controller feedback, however, requires low pass filtering (see Fig. 7.5). It should, moreover, be noted that for good estimation accuracy both the anisotropy-based and the fundamental saliency based scheme require a load compensation which, for simplicity reasons, is not indicated in Fig. 7.18 but described in [96] and [52], respectively. In the following experimental results this compensation has been realized based on the current-flux LUTs (Fig. 2.8(b)).

Firstly, Fig. 7.19 demonstrates the dynamic properties of the stabilized flux estimation based hybrid sensorless control scheme for the RSM. In contrast to the results for the PMSM in Fig. 7.14, only a much lower bandwidth of the speed controller could be achieved which in Fig. 7.19 is about 14/s. Although this is far below the theoretical bandwidth of the flux estimator, an increase of the speed controller gain or the LPF bandwidth of the speed feedback (see Fig. 7.5) would cause an oscillation in idle (torque-free) condition. Again, peaks in the estimation error during torque transients, now in the scale of $\pm 10°$, indicate that the assumed static current-flux relation is not valid in transient conditions. In this case, however, an eddy current model could not solve the problem. Closer investigations indicated that this non-static relation shows the properties of magnetic hysteresis, the presence of which has been identified for this particular machine before in [90]. The extent of this hysteretic behaviour strongly depends on the saturation state of the machine, showing effect mainly in idle condition (i.e. current free; under load the speed controller bandwidth could be increased). As compensating for this effect would require a markedly more complex model which is outside the scope of this thesis, the development will be concluded with these medium performance results. Yet, these results demonstrate the general feasibility of the design of a stabilized flux estimator for the RSM and its

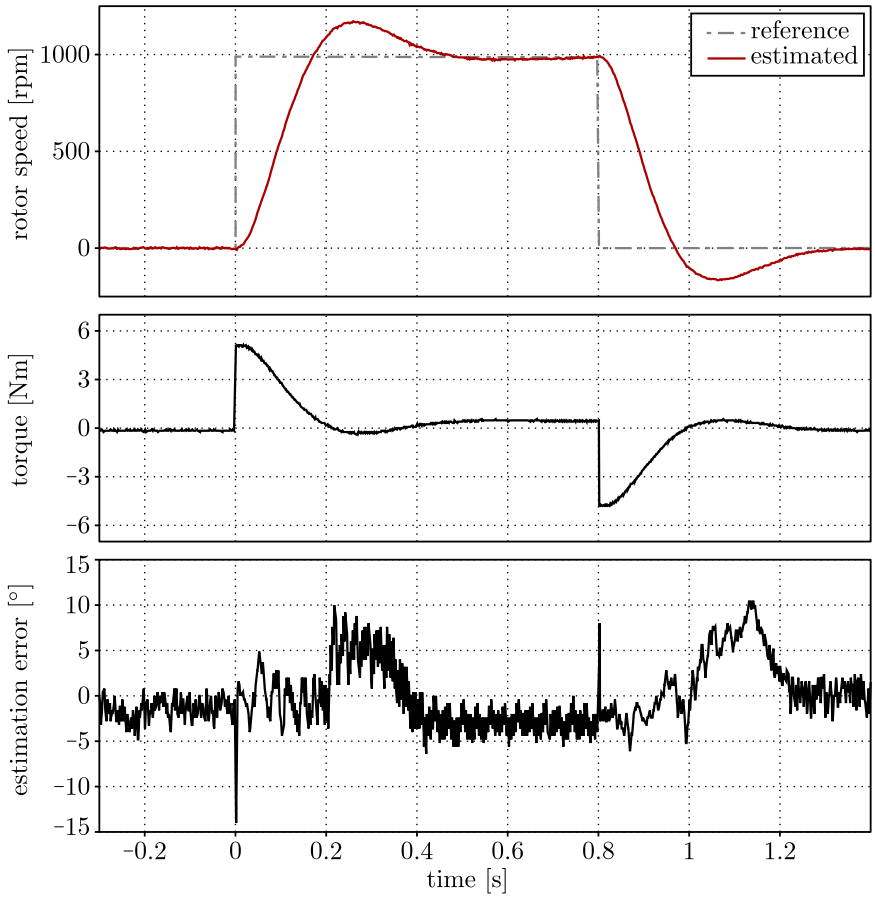

Figure 7.19: *Response of the stabilized RSM flux estimator in speed control to a speed step from standstill to 66% rated speed and back.*

potential limitations.

Fig. 7.20 shows the response of the hybrid scheme for the RSM to a load step. As the load has been passive, only a load release could be shown at standstill. Due to the low bandwidth of the speed controller, the speed deflection is markedly worse than in Fig. 7.16. Yet, the estimation error stays within ±5° at high speed and within ±10° at standstill. Moreover, all signals show an overall good-natured and stable behaviour, because for the above reasons load has a rather stabilizing effect.

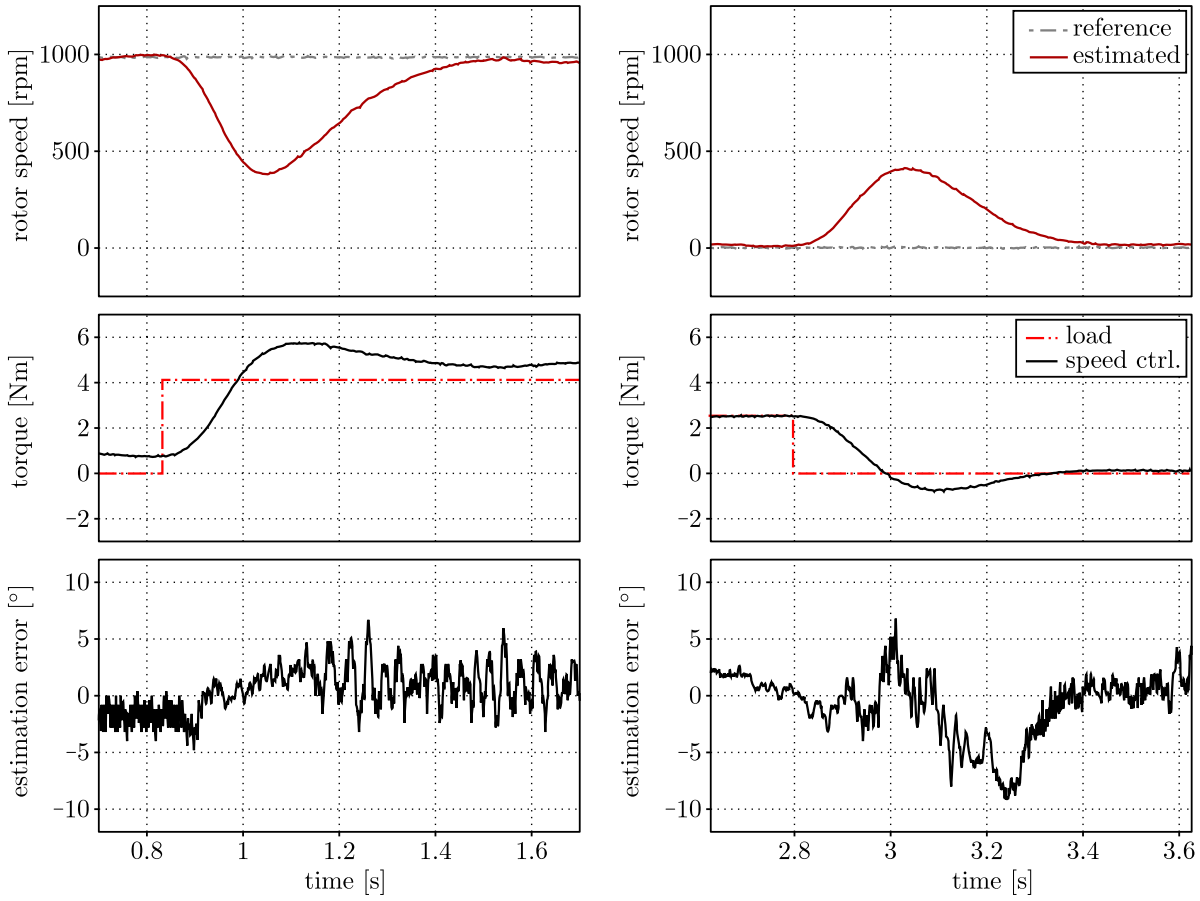

Figure 7.20: *Load step response of the stabilized RSM flux estimator in speed control targeting standstill and 66% rated speed.*

Chapter 8

Conclusion

In this work, the potential of current oversampling for the sensorless control of synchronous machines has been examined. In contrast to synchronous current sampling (SCS), the analogue to digital converter (ADC) is operated close to its maximum sampling frequency – a change in software configuration, possible in most conventional drive hardware. Using a least squares based method "linear regression", the oversampled current evolution is approximated by one straight per PWM switching state. The results are a few slope and offset coefficients (up to 3 pairs) per control interval that contain less noise and have a higher resolution than the current samples, and that can easily be employed in a sensorless control algorithm. Moreover, the slope value represents the time derivative of the current, which is essential for anisotropy-based methods and not measured in conventional drive hardware.

8.1 Summary

In order to experimentally validate the proposed oversampling-based sensorless control techniques, an academic control hardware setup has been designed for this work that employs a fast ADC (operated at 20 MHz), an FPGA and a Pentium CPU. The conscious over-dimensioning of this system in comparison to industrial hardware allows to determine the effects and restrictions of the approach itself, while the way of presentation in many cases enables a respective downscaling of the results.

The initial thorough analysis of the oversampled current response revealed that the actual current evolution within the time scale of one PWM period differs significantly from the conventional model. Apart from the well known switching transients that necessitate an initial regression blind-out time in every switching state, two minor and one major

effects have been identified: The minor effects are an easily compensatable 1.7 µs dead time between the PWM reference and the current response, and an anisotropic recharging process of the winding capacitance that at zero voltage causes a very slight, position dependent alternation of the approximation signals. Both minor effects do not have a relevant effect on the subsequent parts of this work. The major effect, however, is an overall significantly nonlinear evolution of the current during the constant voltage of a switching state. It could be identified that this perturbation is caused by the presence of eddy currents (in the magnetic material) that are excited by the active switching state (ASS) and decay during the passive switching state (PSS). This machine specific phenomenon cannot simply be compensated and does, hence, affect the results in later parts of this work – in certain cases necessitating adaptations.

The linear approximation has been realized on the FPGA, since the high current data rate cannot be communicated to or be processed by the CPU. In order to avoid memory problems and distribute the computational effort over time, the linear regression has been derived and implemented in a recursive way. Before validating the approximation properties experimentally, the noise suppression potential of linear regression has been determined theoretically: Considering the oversampling ratio (OSR) of this work, the SCS noise should be reduced by factor 33 in the offset and by factor 20 in the slope, if the switching state spans the entire PWM half-period. A reduction of the OSR scales the noise of both offset and slope by $\frac{1}{\sqrt{n}}$, with n being the number of involved current samples. A reduction of the switching state duration (e.g. due to pulse width), however, still scales the offset noise by $\frac{1}{\sqrt{n}}$ but the slope noise by $\frac{1}{n^{3/2}}$, making an evaluation of the slope for switching states shorter than 30% unreasonable. However, the experimental evaluation showed different results: At idle standstill the anisotropic recharging of the winding capacitance causes a slight, position dependent alternation of the coefficients, that does not need further consideration. More importantly, the SCS noise is only reduced 7.3 times in the offset and 2.2 times in the slope, which has been identified to result from an increased (unsuppressable) low frequency content in the current sensor output noise. In the presence of rotor speed, the dominant effect is a strong alternation of all (PSS and ASS) slope values between consecutive PWM half-intervals, much stronger than the actual noise content. It could be shown that this is the result of the ASSs being scheduled differently for increasing and decreasing PWM counter, leading to a different eddy current excitation. The hence machine specific alternation itself can be eliminated by averaging two consecutive slope results, which would however not eliminate an eddy current related average error in the slope value.

Based on the identified properties of the approximated straight coefficients, three oversampling-based position estimation techniques have been proposed. At low speed, the anisotropy information is obtained from the relation between ASS voltage and current slope using the Arbitrary Injection method. Since for low injection magnitudes the ASSs are too short for the approximation, the average ASS current slope is reconstructed from the surrounding PSS approximation results and the switching time reference by means of the proposed PSS extension. The experimental validation showed that the relatively high slope noise, feeding into the PSS extension, leads to a noise reduction by only factor 3.2 with respect to SCS. Using the Δ^2 technique (e.g. from Arbitrary Injection) for the EMF elimination allows for a noise reduction by factor 6.2, which is consequently chosen for the later parts of this work. However, apart from the above relative factors, an absolute lower limit for the injection magnitude of 0.3% (1.1 V) has been determined, below which the IGBT voltage drop distorts the anisotropy estimation by more than 5° (electrical). The second and third oversampling-based position estimation technique work in the presence of rotor speed and employ the current slope values for EMF estimation. Assuming a pure q-axis reference current trajectory (suited for SPMSMs), the second technique obtains the rotor angle information from the PSS current slope without requiring any machine parameter. The third technique is an extension to the second one. It deduces the PSS current slope from the ASS regression results, such that at very high speed (when the PSSs are too short) still a clean EMF-based position estimate is available. Although both techniques employ the PSS slope (either measured or deduced) and should, hence, result in similar position estimates, the third technique showed weaker harmonics – smaller than the actual EMF. This deviation has been identified to result from the above mentioned average influence of eddy currents on the slope value and may for a different machine cause an increase of harmonics.

Finally, the oversampling-based position estimates have been merged by means of two oppositional hybrid techniques, each supporting one essential advantage of the oversampling-based position estimation. The first technique realizes the machine parameter independence of all oversampling-based position estimates in an overall parameter-free hybrid technique: An online SNR determination is employed to merge the position estimates and to regulate the injection magnitude – independent of any machine parameter and, moreover, independent of the estimated speed signal, avoiding the usual phase-over problem. Furthermore, an initial macroscopic q-axis pulse is imposed to identify and compensate the load-dependent saliency displacement. In the experimental results this parameter-free hybrid technique showed a reasonable performance and could also be ap-

plied to a differently structured machine, as long as the current trajectory is located on the q-axis. The second proposed hybrid technique exhibits oppositional qualities, involving several machine parameters while providing a high performance compared to literature. The position signal of the oversampling-based Arbitrary Injection method is employed to stabilize a flux estimator which then provides the overall position estimate at all speeds (including standstill). Hence the theoretically unrestricted dynamics of the (filter-free) flux estimator are available in the entire speed range, while allowing for a further reduction of the injection magnitude. However, the experimental results revealed a dynamic restriction that could be identified being the result of eddy currents. A simple eddy current model, employed for compensation, allowed for an increase of the speed controller bandwidth by factor 4 to an absolute value of 450/s (72 Hz) which cannot be achieved by means of a simple encoder evaluation and exceeds the sensorless results, shown in literature, by far. It has furthermore been shown that this generic hybrid approach is also applicable to the reluctance synchronous machine (RSM), where hysteretic effects in the used machine, however, only allowed for achieving medium performance.

8.2 Outlook

In order to maintain the scope of this thesis, at several points throughout its course the development of techniques or investigation of effects had to be concluded. Those could be the starting points for further works and shall therefore be recalled in this final section.

Firstly, in contrast to the assumptions underlying this thesis, the current evolution during short-time constant voltage phases has been shown being strongly nonlinear, inter alia, resulting from the influence of eddy currents and an anisotropic winding recharging process. When not approximating the current evolution by a straight but by a higher order polynomial, those effects could possibly be segregated in corresponding coefficients. A possible position dependence of those coefficients could moreover be employed for sensorless control, which for the anisotropic recharging process would be feasible at standstill without applying injection.

Secondly, there were several indications that the eddy current fade-out evolution is not entirely exponential, but rather the superposition of several exponential evolutions with different fade-out times. A better mapping of this behaviour by an improved dynamic eddy current model could allow for one parametrization, valid for all parts of this thesis. Moreover, this could improve the eddy current prediction and compensation in the hybrid flux estimator and thereby possibly allow for a further increase of the speed controller

bandwidth.

Thirdly, the hybrid sensorless control of the RSM allowed only for a relatively low bandwidth due to the influence of magnetic hysteresis. In analogy to the above eddy current compensation, a dynamic hysteresis model could possibly solve this problem. Hence, the author suggests the development of a preferably simple dynamic hysteresis model and its incorporation into the fundamental saliency based flux estimator for the RSM.

Appendix

A Abbreviations

AC alternating current
A/D analogue to digital
ADC analogue to digital converter
ANN artificial neuronal network
ASS active switching state
BPF band pass filter
CPU central processing unit
DAC digital to analogue converter
DC direct current
eEMF extended electromotive force
EMF electromotive force
EMI electro magnetic interference
FEA finite element analysis
FEM finite element methods
FM fundamental model
FOC field oriented control
FPGA field programmable gate array
HF high frequency
IGBT insulated gate bipolar transistor
INFORM Indirect Flux detection by online Reactance Measurement
IPMSM interior permanent magnet synchronous machine
IPM1 Yaskawa SSR1-43P7AFN
JTAG Joint Test Action Group
LPF low pass filter
LR linear regression

LUT look-up table
MRAS model reference adaptive system
MTPA maximum torque per ampere
OSR oversampling ratio
P proportional
PC personal computer
PI proportional-integral
PLL phase locked loop
PM permanent magnet
PMARSM permanent magnet assisted reluctance synchronous machine
PMSM permanent magnet synchronous machine
PSS passive switching state
PWM pulse width modulation
RLR recursive linear regression
RMS root mean square
RSM reluctance synchronous machine
RSM1 Stellenbosch V1.0
RTS real time system
SNR signal to noise ratio
SPMSM surface mounted permanent magnet synchronous machine
SPM1 Merkes MT4-0750
SPM2 SEW CFM71S
SCS synchronous current sampling
SI systeme international d'unites
SVM space vector modulation
VHDL Very High Speed Integrated Circuit Hardware Description Language
VSI voltage source inverter

B Machines used in the experiments of this work

For the experimental investigations and validations within this work four different machines have been used: one RSM, one IPMSM and two SPMSMs from different manufacturers. Tab. B.1 summarizes the properties of those four machines which within the chapters of this thesis are referred to by their abbreviations. All experiments without explicit statement of the machine type are carried out with the default machine SPM1.

Abbreviation	**SPM1** (default)	**SPM2**	**RSM1**	**IPM1**
Designative information				
Manufacturer	Merkes	SEW	Stellenbosch University	Yaskawa
Type	MT4-0750	CFM71S	V1.0 (bridged&unskw.)	SSR1-43P7AFN
Picture				
Structural information				
Rotor	surface mounted PM	surface mounted PM	transversely laminated	interior PM
Windings	distributed	distributed	distributed	distributed
Pole pairs	3	3	2	3
Name plate nominal data				
Power	2.0 kW	1.6 kW	1.1 kW	3.7 kW
Speed	3000 rpm	3000 rpm	1500 rpm	1750 rpm
Torque	7.5 Nm	5.0 Nm	7.0 Nm	20.2 Nm
Voltage	373 V	400 V	400 V	369 V
Current	4.8 A	3.3 A	3.5 A	6.8 A
Frequency	150 Hz	150 Hz	50 Hz	87.5 Hz
Electrical phase parameters				
Resistance R_{ph}	1.6 Ω	3.2 Ω	5.1 Ω	1.2 Ω
Inductance L_{ph}	12.3 mH	23.0 mH	50-500 mH (nonlin.)	35.3 mH
Saliency ratio	16%	9%	0-70% (nonlin.)	27%
PM flux Ψ_{pm}	240 mVs	260 mVs	0 mVs	670 mVs
Mechanical parameters and dimensions				
Total inertia	ca. 15 kgcm^2	ca. 6 kgcm^2	ca. 34 kgcm^2	ca. 270 kgcm^2
Machine size	221×98 mm, ca. 10 kg	201×105 mm, 8.0 kg	220×160 mm, 24 kg	240×190 mm, 31 kg

Table B.1: *Description of the machines used for the experimental validations in this work.*

C Direct admittance matrix identification

A voltage difference $\Delta \boldsymbol{u}_s^s$ and a current progression difference $\Delta_2 \boldsymbol{i}_s^s$ obtained through (3.19) are free of resistive and EMF related content and do therefore directly relate through the admittance matrix $\mathbf{Y}_s^s$

$$\Delta^2 \boldsymbol{i}_s^s[n] = \mathbf{Y}_s^s \; \Delta \boldsymbol{u}_s^s[n-1]. \tag{C.1}$$

According to the machine model described Sec. 2.3.1 this matrix $\mathbf{Y}_s^s$

$$\mathbf{Y}_s^s = \begin{bmatrix} Y_\Sigma + Y_\Delta \cos 2\theta & Y_\Delta \sin 2\theta \\ Y_\Delta \sin 2\theta & Y_\Sigma - Y_\Delta \cos 2\theta \end{bmatrix} \tag{C.2}$$

comprises 3 unknowns Y_Σ, Y_Δ and θ, that cannot be identified through the two dimensional vector equation (C.1). Thus, in order to directly calculate the rotor angle, at least two current voltage relations have to be employed. Several particular solutions have been proposed for the angle calculation [42, 68–70], which basically constitute only mathematical variations of the same principle, carrying the same restrictions:

Following [68] for instance, two consecutive vectors $\Delta^2 \boldsymbol{i}_s^s[n]$, $\Delta^2 \boldsymbol{i}_s^s[n-1]$ and $\Delta \boldsymbol{u}_s^s[n-1]$, $\Delta \boldsymbol{u}_s^s[n-2]$ are employed to construct the matrices

$$\Delta \mathbf{I}_s^s = \begin{bmatrix} \Delta^2 i_\alpha[n] & \Delta^2 i_\alpha[n-1] \\ \Delta^2 i_\beta[n] & \Delta^2 i_\beta[n-1] \end{bmatrix} \qquad \Delta \mathbf{U}_s^s = \begin{bmatrix} \Delta u_\alpha[n-1] & \Delta^2 u_\alpha[n-2] \\ \Delta^2 u_\beta[n-1] & \Delta^2 u_\beta[n-2] \end{bmatrix}, \tag{C.3}$$

which, assuming that the rotor position did not change, are connected by one admittance matrix $\mathbf{Y}_s^s$

$$\Delta \mathbf{I}_s^s = \mathbf{Y}_s^s(\theta) \; \Delta \mathbf{U}_s^s. \tag{C.4}$$

However, now that the admittance matrix forms the connection between two matrices, it can in reverse be obtained through inversion of the voltage matrix

$$\Delta \mathbf{I}_s^s \Delta \mathbf{U}_s^{s-1} = \mathbf{Y}_s^s(\theta) \tag{C.5}$$

which from mathematical point of view is feasible, if the $\Delta \mathbf{U}_s^s$ has full rank - or in other words, if the two voltages $\Delta \boldsymbol{u}_s^s[n-1]$ and $\Delta \boldsymbol{u}_s^s[n-2]$ have not been parallel or anti-parallel $\Delta \boldsymbol{u}_s^{sT}[n-1] \; \mathbf{J} \; \Delta \boldsymbol{u}_s^s[n-2] \neq 0$. This however constitutes a restriction to the targeted arbitrary-ness, since all consecutive voltage vectors must have different directions. When

in practice noise and resolution affect the current measurement, the SNR of the matrix' entries and hence of subsequent angle estimation

$$\hat{\theta} = \frac{1}{2}\text{atan2}(Y_{\alpha\beta} + Y_{\beta\alpha},\ Y_{\alpha\alpha} - Y_{\beta\beta}) \tag{C.6}$$

scales with the value of the cross product $\Delta\boldsymbol{u}_s^{sT}[n-1]\ \mathbf{J}\ \Delta\boldsymbol{u}_s^s[n-2]$. This concludes to the fact, that all methods which aim to estimate the angle through direct inductance identification from only a few current samples [42, 68–70] need to employ an injection pattern with continuously large voltage direction differences.

D PSS current slope in presence of an anisotropy

We start with Eq. (2.76) for the stator frame current derivative of the linear anisotropic PMSM, which we rewrite for the conditions of the PSS - i.e. with $\boldsymbol{u}_s^s = 0$ and $\dot{\boldsymbol{i}}_s^s = \boldsymbol{\xi}_p^s$

$$\boldsymbol{\xi}_p^s = -\mathbf{Y}_s^s \left(R_s \boldsymbol{i}_s^s + \mathbf{J}\omega\boldsymbol{\psi}_{pm}^s + \omega \left(\mathbf{J}\mathbf{L}_s^s - \mathbf{L}_s^s\mathbf{J} \right) \boldsymbol{i}_s^s \right). \tag{D.7}$$

This stator frame current slope $\boldsymbol{\xi}_p^s$ is transformed to estimated rotor frame by multiplication with $\hat{\mathbf{T}}^{-1}$

$$\begin{aligned} \boldsymbol{\xi}_p^{\hat{r}} &= \hat{\mathbf{T}}^{-1}\boldsymbol{\xi}_p^s && \text{(D.8)} \\ &= -\hat{\mathbf{T}}^{-1}\mathbf{Y}_s^s R_s \boldsymbol{i}_s^s - \hat{\mathbf{T}}^{-1}\mathbf{Y}_s^s \mathbf{J}\omega\boldsymbol{\psi}_{pm}^s - \hat{\mathbf{T}}^{-1}\mathbf{Y}_s^s \omega \left(\mathbf{J}\mathbf{L}_s^s - \mathbf{L}_s^s\mathbf{J} \right) \boldsymbol{i}_s^s. && \text{(D.9)} \end{aligned}$$

The inductances, admittances and the PM flux are rewritten using their rotor fixed values (as their are given by the rotor orientation) and the current is rewritten in estimated rotor frame (as the FOC controls it in this frame)

$$\begin{aligned} \boldsymbol{\xi}_p^{\hat{r}} = &- \hat{\mathbf{T}}^{-1}\mathbf{T}\mathbf{Y}_s^r\mathbf{T}^{-1} R_s \hat{\mathbf{T}}\boldsymbol{i}_s^{\hat{r}} - \hat{\mathbf{T}}^{-1}\mathbf{T}\mathbf{Y}_s^r\mathbf{T}^{-1}\mathbf{J}\omega\mathbf{T}\boldsymbol{\psi}_{pm}^r \\ &- \hat{\mathbf{T}}^{-1}\mathbf{T}\mathbf{Y}_s^r\mathbf{T}^{-1}\omega\mathbf{T} \left(\mathbf{J}\mathbf{L}_s^r - \mathbf{L}_s^r\mathbf{J} \right) \mathbf{T}^{-1}\hat{\mathbf{T}}\boldsymbol{i}_s^{\hat{r}}. \end{aligned} \tag{D.10}$$

Using the rules $\hat{\mathbf{T}}\mathbf{T}^{-1} = \tilde{\mathbf{T}}$, $\hat{\mathbf{T}}^{-1}\mathbf{T} = \tilde{\mathbf{T}}^{-1}$ and $\mathbf{T}\mathbf{T}^{-1} = \mathbf{I}$, Eq. (D.10) is summarized

$$\boldsymbol{\xi}_p^{\hat{r}} = - \tilde{\mathbf{T}}^{-1}\mathbf{Y}_s^r\tilde{\mathbf{T}} R_s \boldsymbol{i}_s^{\hat{r}} - \tilde{\mathbf{T}}^{-1}\mathbf{Y}_s^r\mathbf{J}\omega\boldsymbol{\psi}_{pm}^r - \tilde{\mathbf{T}}^{-1}\mathbf{Y}_s^r\omega \left(\mathbf{J}\mathbf{L}_s^r - \mathbf{L}_s^r\mathbf{J} \right) \tilde{\mathbf{T}}\boldsymbol{i}_s^{\hat{r}}. \tag{D.11}$$

$\boldsymbol{\psi}_{pm}^r$ has only a d-axis component, which through $\mathbf{J}$ excites only the q-axis admittance in the second term. Hence, the matrix $\mathbf{Y}_s^r$ in the second term can be replaced by the scalar Y_q. Moreover, considering $\mathbf{Y}_s^r = \mathbf{L}_s^{r-1}$ the third term in Eq. (D.11) can be summarized,

which results in the equation

$$\boldsymbol{\xi}_p^{\hat{r}} = -R_s\tilde{\mathbf{T}}^{-1}\mathbf{Y}_s^r\tilde{\mathbf{T}}\boldsymbol{i}_s^{\hat{r}} - Y_q\omega\tilde{\mathbf{T}}^{-1}\mathbf{J}\boldsymbol{\psi}_{pm}^r - \omega\tilde{\mathbf{T}}^{-1}\left(\mathbf{Y}_s^r\mathbf{J}\mathbf{L}_s^r - \mathbf{I}\right)\tilde{\mathbf{T}}\boldsymbol{i}_s^{\hat{r}}, \tag{D.12}$$

that has been stated in Sec. 6.2.1.

E Minimum noise signal merging

The problem of merging three different sources of information, that all share the same expected value μ, but inhere different amounts of noise, is indicated in Fig. E.1. The

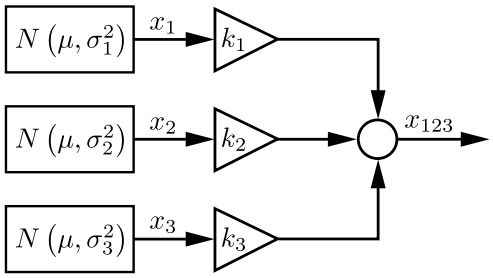

Figure E.1: *Scaled addition of noisy quantities.*

target is the minimization of the noise in the output signal x_{123} by means of an optimal choice of the weighting factors k_1, k_2 and k_3. However, maintaining the expected value μ in the output signal x_{123} requires a unity sum of the weighting factors

$$k_1 + k_2 + k_3 = 1. \tag{E.13}$$

In order to derive this optimum analytically, the two-dimensional optimization is split up into two one-dimensional optimization sub-problems. As indicated in Fig. E.2, firstly x_1 and x_2 are scaled and merged, targeting minimal noise in the intermediate variable

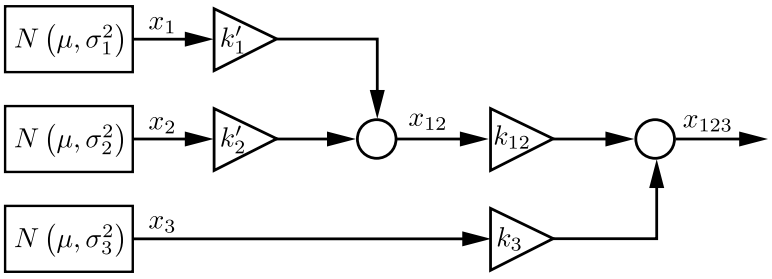

Figure E.2: *Varied addition of noisy quantities.*

x_{12}. In a second step x_{12} and x_3 are merged analogously. Herein the substitutes k_1' and

k_2' are defined as

$$k_1 = k_1' k_{12} \qquad \text{and} \qquad k_2 = k_2' k_{12} \tag{E.14}$$

and the maintenance of the expected value μ in the output signal x_{123} is ensured by

$$k_1' + k_2' = 1 \tag{E.15}$$

$$k_{12} + k_3 = 1. \tag{E.16}$$

Moreover, we substitute the noise RMS by the inverse SNR

$$\sigma = \frac{\sigma}{1} = \frac{1}{s} \tag{E.17}$$

since the merged values $x_1..x_3$ are angles, which all have unity signal strength.

According to the above considerations, merging x_1 and x_2 is described by

$$x_{12} = k_1' N\left(\mu, \frac{1}{s_1^2}\right) + \left(1 - k_1'\right) N\left(\mu, \frac{1}{s_2^2}\right) \tag{E.18}$$

$$= N\left(k_1'\mu, \frac{k_1'^2}{s_1^2}\right) + N\left(\left(1 - k_1'\right)\mu, \frac{\left(1 - k_1'\right)^2}{s_2^2}\right) \tag{E.19}$$

$$= N\left(\mu, \frac{k_1'^2}{s_1^2} + \frac{\left(1 - k_1'\right)^2}{s_2^2}\right) \tag{E.20}$$

$$= N\left(\mu, \frac{s_2^2 k_1'^2 + s_1^2\left(1 - k_1'\right)^2}{s_1^2 s_2^2}\right), \tag{E.21}$$

where the noise is minimized by solving the first derivative of the numerator in Eq. (E.21) with respect to k_1'

$$0 = \frac{d}{dk_1'}\left(s_2^2 k_1'^2 + s_1^2\left(1 - k_1'\right)^2\right) \tag{E.22}$$

$$= 2 s_2^2 k_1' - 2 s_1^2\left(1 - k_1'\right) \tag{E.23}$$

$$k_1' = \frac{s_1^2}{s_1^2 + s_2^2}, \qquad k_2' = 1 - k_1' = \frac{s_2^2}{s_1^2 + s_2^2}. \tag{E.24}$$

The optimized (squared) SNR s_{12}^2 of the merged quantity x_{12} is consequently

$$s_{12}^2 = \frac{s_1^2 s_2^2}{s_2^2 k_1'^2 + s_1^2 k_2'^2} \tag{E.25}$$

$$\overset{(E.24)}{=} s_1^2 + s_2^2. \tag{E.26}$$

Following the same steps for the second merging process of x_{12} and x_3 results in

$$x_{123} = k_3 N\left(\mu, \frac{1}{s_3^2}\right) + (1 - k_3)\, N\left(\mu, \frac{1}{s_{12}^2}\right) \tag{E.27}$$

$$= N\left(\mu, \frac{s_{12}^2 k_3^2 + s_3^2 (1 - k_3)^2}{s_{12}^2 s_3^2}\right), \tag{E.28}$$

with the minimization of the numerator resulting in

$$k_3 = \frac{s_3^2}{s_{12}^2 + s_3^2} = \frac{s_3^2}{s_1^2 + s_2^2 + s_3^2} \tag{E.29}$$

$$k_{12} = \frac{s_{12}^2}{s_{12}^2 + s_3^2} = \frac{s_1^2 + s_2^2}{s_1^2 + s_2^2 + s_3^2}. \tag{E.30}$$

Hence, the original factors k_1 and k_2 are

$$k_1 \overset{(E.14)}{=} \frac{s_1^2}{s_1^2 + s_2^2} \frac{s_1^2 + s_2^2}{s_1^2 + s_2^2 + s_3^2} = \frac{s_1^2}{s_1^2 + s_2^2 + s_3^2} \tag{E.31}$$

$$k_2 \overset{(E.14)}{=} \frac{s_2^2}{s_1^2 + s_2^2} \frac{s_1^2 + s_2^2}{s_1^2 + s_2^2 + s_3^2} = \frac{s_2^2}{s_1^2 + s_2^2 + s_3^2} \tag{E.32}$$

and the overall (squared) SNR is

$$s_{123}^2 = s_{12}^2 + s_3^2 = s_1^2 + s_2^2 + s_3^2. \tag{E.33}$$

Due to the requirement (E.13) this solution is a special case of the maximum-ratio combining technique known from telecommunications and information technology [99].

Bibliography

[1] D. H. Meadows, D. Meadows, and J. Randers, *The Limits to Growth: The 30-Year Update*. Chelsea Green Pub Co, 2004.

[2] N. Hanley, J. F. Shogren, and B. White, *Environmental Economics: In Theory and Practice*. Palgrave Macmillan, 2007.

[3] E. B. Barbier, *Economics, Natural-Resource Scarcity and Development*. Routledge Chapman & Hall, 2013.

[4] R. Perman, Y. Ma, J. McGilvray, M. S. Common, and D. Maddison, *Natural Resource and Environmental Economics*. Financial Times Prent., 2011.

[5] C. de Jong and K. Walet, *A Guide to Emissions Trading: Risk Management and Business Implications*. Risk Books, 2004.

[6] F. Briz, D. Diaz-Reigosa, M. Degner, P. Garcia, and J. Guerrero, "Current sampling and measurement in pwm operated ac drives and power converters," *IEEE Conf. IPEC*, pp. 2753–2760, 2010.

[7] P. Nussbaumer and T. Wolbank, "Saliency tracking based sensorless control of ac machines exploiting inverter switching transients," *IEEE Conf. SLED*, pp. 114–119, 2010.

[8] ——, "Using oversampling techniques to extract ac machine saliency information," *IEEE Conf. IECON*, pp. 1035–1040, 2010.

[9] ——, "Using switching transients to exploit sensorless control information for electric machines," *IEEE Conf. SLED*, pp. 35–40, 2011.

[10] S. Bolognani, S. Calligaro, R. Petrella, and M. Sterpellone, "Sensorless control for ipmsm using pwm excitation: Analytical developments and implementation issues," *IEEE Conf. SLED*, pp. 64–73, 2011.

[11] Y. Duan and M. Sumner, "A novel current derivative measurement using recursive least square algorithms for sensorless control of permanent magnet synchronous machine," *IEEE Conf. IPEMC*, pp. 1193–1200, 2012.

[12] D. Hind, M. Sumner, and C. Gerada, "Use of an artificial neural network for current derivative estimation," *Conf. EPE*, pp. 1–10, 2013.

[13] T. Matsuo and T. Lipo, "Rotor position detection scheme for synchronous reluctance motor based on current measurements," *IEEE Trans. on Industry Applications*, vol. 31, pp. 860–868, 1995.

[14] M. Schroedl, "Operation of the permanent magnet synchronous machine without a mechanical sensor," *Conf. Power Electronics and Variable-Speed Drives*, pp. 51–56, 1990.

[15] Y. Hua, M. Sumner, G. Asher, and Q. Gao, "Sensorless control for a pm machine with reduced current distortion using space vector pwm excitation," *Conf. EPE*, pp. 1–10, 2009.

[16] D. Paulus, P. Landsmann, and R. Kennel, "Saliency based sensorless field- oriented control for permanent magnet synchronous machines in the whole speed range," *IEEE Conf. SLED*, pp. 1–6, 2012.

[17] I. N. Bronstein, K. A. Semendyayev, G. Musiol, and H. Muehlig, *Handbook of Mathematics*. Springer, Berlin, 2007.

[18] D. Schroeder, *Elektrische Antriebe - Regelung von Antriebssystemen*. Springer Berlin, 2001.

[19] N. Mohan, *Electric Drives*. Mnpere Minneapolis, 2003.

[20] S.-K. Sul, *Control of Electric Machine Drive Systems*. John Wiley & Sons, 2011.

[21] R. D. Doncker, D. W. J. Pulle, and A. Veltman, *Advanced Electrical Drives*. Springer, 2011.

[22] F. W. Garbrecht, H.-J. Schaad, and R. Lehmann, *Workshop der professionellen Antriebstechnik*. Franzis Feldkirchen, 1996.

[23] H. Abu-Rub, A. Igbal, and J. Guzinski, *High Performance Control of AC Drives with Matlab / Simulink Models*. John Wiley & Sons, 2012.

[24] K. Meerkoetter. (2011, August) Skript lineare netze. Universitaet Paderborn. [Online]. Available: http://nachrichtentheorie.de/skripten/linearenetze.pdf

[25] S. Kuehl, P. Landsmann, and R. Kennel, "Bivariate polynomial approximation of cross-saturated flux curves in synchronous machine models," *IEEE Conf. ENERGYCON*, pp. 219–224, 2012.

[26] M. Chunting, G. Slemon, and R. Bonert, "Modeling of iron losses of permanent-magnet synchronous motors," *IEEE Trans. on Industry Applications*, vol. 39, pp. 734–742, 2003.

[27] N. Urasaki, T. Senjyu, , and K. Uezato, "Relationship of parallel model and series model for permanent magnet synchronous motors taking iron loss into account," *IEEE Trans. on Energy Conversion*, vol. 19, pp. 265–270, 2003.

[28] P. Sergeant, F. De Belie, L. Dupre, and J. Melkebeek, "Losses in sensorless controlled permanent-magnet synchronous machines," *IEEE Trans. on Magnetics*, vol. 46, pp. 590–593, 2010.

[29] A. Hannalla and D. Macdonald, "Numerical analysis of transient field problems in electrical machines," *Proceedings of the Institution of Electrical Engineers*, vol. 123, pp. 893–898, 1976.

[30] T. Renyuan, L. Feng, G. Zhenhong, and L. M. Jianguo, "Computation on transient nonlinear electromagnetic field by an improved space-time finite element method," *IEEE Trans. on Magnetics*, vol. 35, pp. 1426–1429, 1999.

[31] C. Kaehler and G. Henneberger, "Transient 3-d fem computation of eddy-current losses in the rotor of a claw-pole alternator," *IEEE Trans. on Magnetics*, vol. 40, pp. 1362–1365, 2004.

[32] Q. Gao, G. Asher, M. Sumner, and P. Makys, "Position estimation of ac machines over a wide frequency range based on space vector pwm excitation," *IEEE Trans. on Industrial Applications*, vol. 43, pp. 1001–1011, 2007.

[33] R. Morales-Caporal and M. Pacas, "Encoderless predictive direct torque control for synchronous reluctance machines at very low and zero speed," *IEEE Trans. on Industrial Electronics*, vol. 55, p. 4408, 2008.

[34] J. Choi and S. Sul, "Inverter output voltage synthesis using novel dead time compensation," *IEEE Trans. on Industrial Electronics*, vol. 11, p. 221, 1996.

[35] S. Bolognani and M. Zigliotto, "Self-commissioning compensation of inverter non-idealities for sensorless ac drives applications," *IEEE Conf. PEMD*, p. 30, 2002.

[36] S. Bolognani, M. Ceschia, P. Mattavelli, A. Paccagnella, and M. Zigliotto, "Improved fpga-based dead time compensation for svm inverters," *IEEE Conf. PEMD*, pp. 662–667, 2004.

[37] F. Alrifai and N. Schofield, "Control of pm machines with non-contact measured torque feedback," *IEEE Conf. EPE-PEMC*, pp. 71–78, 2010.

[38] M. J. Corley and R. D. Lorenz, "Rotor position and velocity estimation for a salient-pole permanent magnet synchronous machine at standstill and high speeds," *IEEE Trans. on Industrial Applications*, vol. 34, pp. 784–789, 1998.

[39] M. Schroedl, M. Hofer, and W. Staffler, "Combining inform method, voltage model and mechanical observer for sensorless control of pm synchronous motors in the whole speed range including standstill," *Elektrotechnik und Informationstechnik, Springer Wien*, vol. 123, Nr. 5, pp. 183–190, 2006.

[40] C. Silva, G. Asher, and M. Sumner, "Hybrid rotor position observer for wide speed-range sensorless pm motor drives including zero speed," *IEEE Trans. on Industrial Electronics*, vol. 53, pp. 373–378, 2006.

[41] S.-C. Agarlita, I. Boldea, and F. Blaabjerg, "High-frequency-injection-assisted active-flux-based sensorless vector control of reluctance synchronous motors, with experiments from zero speed," *IEEE Trans. on Industry Applications*, vol. 48, pp. 1931–1939, 2012.

[42] K. Wiedmann and A. Mertens, "Self-sensing control of pm synchronous machines for the entire speed range with reduced computational effort based on a novel mras approach," *IEEE Conf. PEMD*, pp. 1–6, 2012.

[43] O. Wallmark and L. Harnefors, "Sensorless control of salient pmsm drives in the transition region," *IEEE Trans. on Industrial Electronics*, vol. 53, pp. 1179–1187, 2006.

[44] T. Furuhashi, S. Sangwongwanich, and S. Okuma, "A position-and-velocity sensorless control for brushless dc motors using an adaptive sliding mode observer," *IEEE Trans. on Industrial Electronics*, vol. 39, pp. 89–95, 1992.

[45] I. Boldea, M. Paicu, and G.-D. Andreescu, "Active flux concept for motion-sensorless unified ac drives," *IEEE Trans. on Power Electronics*, vol. 23, pp. 2612–2618, 2008.

[46] D. Yousfi, A. Halelfadl, and M. E. Kard, "Review and evaluation of some position and speed estimation methods for pmsm sensorless drives," *IEEE Conf. ICMCS*, pp. 409–414, 2009.

[47] F. Demmelmayr, M. Susic, and M. Schroedl, "Sensorless control at high starting torque of a 4000 nm traction drive with permanent magnet synchronous machine," *Conf. EPE*, pp. 1–8, 2011.

[48] A. Eilenberger and M. Schroedl, "Extended back emf model for pm synchronous machines with different inductances in d- and q-axis," *Conf. EPE-PEMC*, pp. 945–948, 2008.

[49] A. Piippo, M. Hinkkanen, and J. Luomi, "Sensorless control of pmsm drives using a combination of voltage model and hf signal injection," *IEEE Conf. IAS*, pp. 964–970, 2004.

[50] W. Hammel and R. Kennel, "High-resolution sensorless position estimation using delta-sigma-modulated current measurement," *IEEE Conf. ECCE*, pp. 2717–2724, 2011.

[51] P. Landsmann, D. Paulus, A. Doetlinger, and R. Kennel, "Silent injection for saliency based sensorless control by means of current oversampling," *IEEE Conf. ICIT*, pp. 398–403, 2013.

[52] P. Landsmann, R. Kennel, H. de Kock, and M. Kamper, "Fundamental saliency based encoderless control for reluctance synchronous machines," *IEEE Conf. ICEM*, pp. 1–7, 2010.

[53] T. Tuovinen, M. Hinkkanen, L. Harnefors, and J. Luomi, "A reduced-order position observer with stator-resistance adaptation for synchronous reluctance motor drives," *IEEE Conf. EPE/PEMC*, pp. T5/174–179, 2010.

[54] J.-F. Stumper, D. Paulus, P. Landsmann, and R. Kennel, "Encoderless field-oriented control of a synchronous reluctance machine with a direct estimator," *IEEE Conf. SLED*, pp. 18–23, 2010.

[55] N. Bianchi, S. Bolognani, J. Ji-Hoon, and S. Sul, "Advantages of inset pm machines for zero-speed sensorless position detection," *IEEE Trans. on Industry Applications*, vol. 44, pp. 1190–1198, 2008.

[56] M. W. Degner and R. D. Lorenz, "Position estimation in induction machines utilizing rotor bar slot harmonics and carrier-frequency signal injection," *IEEE Trans. on Industrial Applications*, vol. 36, pp. 736 – 742, 2000.

[57] D. Paulus, P. Landsmann, S. Kuehl, and R. Kennel, "Arbitrary injection for permanent magnet synchronous machines with multiple saliencies," *IEEE Conf. ECCE*, pp. 511–517, 2013.

[58] M. Schroedl, "Detection of the rotor position of a permanent magnet synchronous machine at standstill," *IEEE Conf. ICEM*, pp. 51–56, 1988.

[59] M. Schroedl, D. Hennenbichler, and T. Wolbank, "Induction motor drive for electric vehicles without speed- and position sensors," *Conf. EPE*, pp. 271–275, 1993.

[60] M. Schroedl and P. Weinmeier, "Sensorless control of reluctance machines at arbitrary operating conditions including standstill," *IEEE Trans. on Power Electronics*, vol. 9, p. 225, 1994.

[61] M. Schroedl, "Sensorless control of ac machines at low speed and standstill based on the "inform" method," *IEEE Trans. on Industrial Applications*, vol. 34, pp. 270–277, 1996.

[62] Y.-D. Yoon, S.-K. Sul, S. Morimoto, and K. Ide, "High-bandwidth sensorless algorithm for ac machines based on square-wave-type voltage injection," *IEEE Trans. on Industrial Applications*, vol. 47, pp. 1361–1370, 2011.

[63] P. L. Jansen and R. D. Lorenz, "Transducerless position and velocity estimation in induction and salient ac machines," *IEEE Trans. on Industrial Applications*, vol. 31, pp. 240–247, 1995.

[64] M. Linke, R. Kennel, and J. Holtz, "Sensorless speed and position control of synchronous machines using alternating carrier injection," *IEEE Conf. IEMDC*, pp. 1211–1217, 2003.

[65] J. Holtz, "Acquisition of position error and magnet polarity for sensorless control of pm synchronous machines," *IEEE Trans. on Industrial Applications*, vol. 44, pp. 1172–1180, 2008.

[66] W. Hammel and R. Kennel, "Integration of alternating carrier injection in position sensorless control without any filtering," *IEEE Conf. ECCE*, pp. 3830–3836, 2009.

[67] D. Paulus, P. Landsmann, and R. Kennel, "Sensorless field- oriented control for permanent magnet synchronous machines with an arbitrary injection scheme and direct angle calculation," *IEEE Conf. SLED*, pp. 41–46, 2011.

[68] S. Kim, Y.-C. Kwon, S.-K. Sul, J. Park, and S.-M. Kim, "Position sensorless operation of ipmsm with near pwm switching frequency signal injection," *IEEE Conf. ICPE - ECCE Asia*, pp. 1660–1665, 2011.

[69] F. De Belie and J. Melkebeek, "Seamless integration of a low-speed position estimator for ipmsm in a current-controlled voltage-source inverter," *IEEE Conf. SLED*, pp. 50–55, 2010.

[70] F. De Belie, T. Vyncke, and J. Melkebeek, "Parameterless rotor position estimation in a direct-torque controlled salient-pole pmsm without using additional test signal," *IEEE Conf. ICEM*, pp. 1–6, 2010.

[71] P. Landsmann and R. Kennel, "Saliency based sensorless predictive torque control with reduced torque ripple," *IEEE Trans. on Power Electronics*, vol. 27, pp. 4311–4320, 2012.

[72] P. Landsmann, C. M. Hackl, and R. Kennel, "Eliminating all machine parameters in encoderless predictive torque control without signal injection," *IEEE Conf. IEMDC*, pp. 1259–1264, 2011.

[73] V. Blasko, V. Kaura, and W. Niewiadomski, "Sampling of discontinuous voltage and current signals in electrical drives: a system approach," *IEEE Trans. on Industry Applications*, vol. 34, pp. 1123–1130, 1998.

[74] A. Mertens and D. Eckardt, "Voltage and current sensing ind power electronic converters using sigma-delta a/d conversion," *IEEE Trans. on Industry Applications*, vol. 34, pp. 1139–1146, 1998.

[75] S. Song, J. Choi, and S. Sul, "Current measurement in digitally controlled ac drives," *IEEE Industry Application Magazine*, vol. 6, pp. 51–62, 2000.

[76] E. Persson, "Transient effects in application of pwm inverters to induction motors," *IEEE Trans. on Industrial Applications*, vol. 28, pp. 1095–1101, 1992.

[77] M. Kaufhold, H. Aninger, M. Berth, J. Speck, and M. Eberhardt, "Electrical stress and failure mechanism of the winding insulation in pwm-inverter-fed low-voltage induction motors," *IEEE Trans. on Industrial Electronics*, vol. 47, pp. 396–402, 2000.

[78] Z. Peroutka, "Requirements for insulation system of motors fed by modern voltage source converters," *IEEE Conf. PESC*, pp. 4383– 4389, 2004.

[79] W. Fengxiang, T. Laisheng, W. Guangning, and D. Tao, "Analysis of voltage waveform at the stator terminal of pwm inverter fed motors," *Conf. ISEIM*, pp. 382–385, 2005.

[80] C. Kaijiang, W. Guangning, Z. Liren, G. Xiaoxia, L. Kegang, and G. Bo, "Insulation life-span models for electrical and thermal aging under continuous high square impulses voltage," *IEEE Conf. ICPADM*, pp. 285–288, 2009.

[81] B. Muralidhara, A. Ramachandran, R. Srinivasan, and M. Reddy, "Experimental measurement of shaft voltage and bearing current in an inverter fed three phase induction motor drive," *Conf. ICECT*, pp. 37–41, 2011.

[82] M. Spencer and R. Lorenz, "Analysis and in-situ measurement of thermal-mechanical strain in active silicon power semiconductors," *IEEE Conf. IAS*, pp. 1–7, 2008.

[83] P. Nussbaumer, G. Stojicic, and T. Wolbank, "Exploiting switching transients for broken rotor bar detection in inverter-fed induction machines at all operating conditions," *IEEE Conf. IEMDC*, pp. 418–423, 2011.

[84] P. Nussbaumer, A. Mitteregger, and T. Wolbank, "Online detection of insulation degradation in inverter fed drive systems based on high frequency current sampling," *IEEE Conf. IECON*, pp. 1954–1959, 2011.

[85] R. W. Hamming, *Numerical Methods for Scientists and Engineers*. Dover Publications, 1987.

[86] P. Landsmann, D. Paulus, and R. Kennel, "Online identification of load angle compensation for anisotropy based sensorless control," *IEEE Conf. SLED*, pp. 80–84, 2011.

[87] L. Sachs and J. Hedderich, *Angewandte Statistik*. Springer, Berlin, 2010.

[88] U. Tietze and C. Schenk, *Halbleiter-Schaltungstechnik*, U. Tietze and C. Schenk, Eds. Springer, Berlin, 2010.

[89] P. Landsmann, D. Paulus, and R. Kennel, "Silent and parameter independent hybrid sensorless control for spmsm based on current oversampling," *IEEE Conf. SLED/PRECEDE*, pp. 1–8, 2013.

[90] J. Cordier, P. Landsmann, and R. Kennel, "The influence of magnetic hysteresis on hf injection based inductance calculation," *IEEE Conf. ECCE*, pp. 638–645, 2011.

[91] T. Frenzke, "Impacts of cross-saturation on sensorless control of surface permanent magnet synchronous motors," *Conf. EPE*, p. 10, 2005.

[92] P. Guglielmi, M. Pastorelli, and A. Vagati, "Cross-saturation effects in ipm motors and related impact on sensorless control," *IEEE Trans. on Industry Applications*, vol. 42, pp. 1516–1522, 2006.

[93] F. De Belie, P. Sergeant, T. Vandoorn, and J. Melkebeek, "Estimation errors in sensorless drives due to the magnetic interaction," *IEEE Conf. ICEM*, pp. 1–5, 2008.

[94] S. Kuehl, P. Landsmann, and R. Kennel, "Compensating angle estimation errors caused by magnetic saturation in anisotropy-based sensorless control schemes," *IEEE Conf. SLED*, pp. 1–6, 2012.

[95] K. Wiedmann and A. Mertens, "Self-sensing control of pm synchronous machines including online system identification based on a novel mras approach," *IEEE Conf. SLED*, pp. 21–22, 2012.

[96] P. Landsmann and R. Kennel, "Q-axis pulse based identification of the anisotropy displacement over load for surface mounted pmsm," *IEEE Conf. SLED/PRECEDE*, pp. 1–6, 2013.

[97] J. Holtz, "Initial rotor polarity detection and sensorless control of pm synchronous machines," *IEEE Conf. IAS*, pp. 2040–2047, 2006.

[98] P. Landsmann, D. Paulus, S. Kuehl, and R. Kennel, "Dynamische geberlose Regelung im gesamten Drehzahlbereich für PM-Synchronmaschinen," *Conf. SPS/IPC Drives*, pp. 1–8, 2013.

[99] D. Brennan, "Linear diversity combining techniques," *Proc. IRE*, vol. 47, pp. 1075–1102, 1959.